Theoretical Issues in Silicon Quantum Dot Qubits

by

Teck Seng Koh

A dissertation submitted in partial fulfillment of
the requirements for the degree of

Doctor of Philosophy
(Physics)

at the
University of Wisconsin – Madison
2012

Defended on 13 Nov 2012
Dissertation approved by the following members of the Final Oral Committee:

Susan N. Coppersmith · Professor of Physics
Mark G. Friesen · Senior Scientist of Physics
Mark A. Eriksson · Professor of Physics
Robert J. Joynt · Professor of Physics
Irena Knezevic · Associate Professor of
Electrical and Computer Engineering

Abstract

Electrically-gated quantum dots in semiconductors [1] is an excellent architecture on which to make qubits for quantum information processing [2]. Silicon is attractive because of the potential for excellent manipulability, scalability, and for integration with classical electronics [3].

This thesis describes several aspects of the theoretical issues related to quantum dot qubits in silicon. It may be broadly divided into three parts – (1) the hybrid qubit and quantum gates, (2) decoherence and (3) charge transport.

In the first part, we present a novel architecture for a double quantum dot spin qubit, which we term the hybrid qubit, and demonstrate that implementing this qubit in silicon is feasible. Next, we consider both AC and DC quantum gating protocols and compare the optimal fidelities for these protocols that can be achieved for both the hybrid qubit and the more traditional singlet-triplet qubit [4].

In the second part, we present evidence that silicon offers superior coherence properties by analyzing experimental data from which charge dephasing and spin relaxation times are extracted. We show that the internal degrees of freedom of the hybrid qubit enhance charge coherence, and demonstrate tunable spin loading of a quantum dot.

In the last part, we explain three key features of spin-dependent transport – spin blockade, lifetime-enhanced transport and spin-flip cotunneling. We explain how these features arise in the conventional two-electron as well as the unconventional three-electron regimes, using a theoretical model that captures the key characteristics observed in the data.

Acknowledgements

This thesis could not have been completed without the help and support from many people.

First and foremost, I would like to express my sincere gratitude to my advisor, Prof. Susan Coppersmith, who has been a constant source of insight and creative ideas. I thank Sue for her big idea of the hybrid qubit – a central theme of this thesis – without which this thesis would be considerably poorer. From her, I learnt to appreciate the importance of having the "big picture". I am especially grateful for the kindness and understanding that she showed me when I have had to fly back with my family to Singapore.

I would also like to express my gratitude to my co-advisor, Dr. Mark Friesen, for his constant encouragement and patient explanation of Physics. I am particularly indebted to Mark for his meticulous and careful reading of my manuscripts which took up much of his time. More importantly, my first publication, which gave me much confidence in my ability to perform quality research, would not have been possible without his guidance.

Much of this thesis is based on work done in collaboration with Prof. Mark Eriksson and members of his lab. I would like to express a heartfelt thank you to him, Christie Simmons and Shi Zhan, whose fine experimental data derived from painstaking hours of labwork informed much of my theoretical research. Working with excellent experimentalists like Mark, Christie and Zhan, was always pleasant and illuminating, and I am grateful to have had the opportunity to do so.

I would also like to thank the members of my thesis defense committee, Prof. Susan Coppersmith, Dr. Mark Friesen, Prof. Mark Eriksson, Prof. Robert Joynt and Prof. Irena Knezevic, for the time and effort put into improving this thesis.

I benefitted directly from collaborations with John Gamble and Yun-Pil Shim, whose theoretical calculations helped to put some of my work on firmer footing, and to whom I would like to say a big thank you. Also, to members of the Quantum Computing in Silicon group who have listened to the talks I presented, thank you! I also thank Saurabh Maiti, Christie Simmons, Shi Zhan, Jon Prance, John Gamble, Kenny Rudinger, Dushko Kuzmanovski, Fei Jianjia, Zhou Dong, Yun-Pil Shim, Nga Nguyen, Yeo Ye and Ho Shen

Yong for invaluable discussions about various topics of Physics.

I have been blessed with much goodwill and friendship during my time in Madison. Miao Jinlu, Noah Lim, Cindy Sim, Jennifer Lien, Gan Cheong Soon, Dr. and Mrs. Hu Kejing, Aree Manosuthikit, and many others, have helped make my time in Madison unforgettable. In particular, my wife and I are happy to count Jinlu, Noah and Cindy among some of our closest friends.

Last but certainly not the least, my journey would not be possible without the love and support of my wife, my parents, my parents-in-law and my children.

I am sincerely grateful for the unconditional love and unwavering support of my wife, Song Lye Kuan. Our journey "into the woods", as Lye Kuan described coming to live in Eagle Heights and University Houses, has been nothing short of magical. Coming from Singapore, a fast-paced city-state with one of the world's highest population densities, these peaceful and leafy neighbourhoods presented to us what seemed like luxuries of life. With our children, Koon Wee and Yik Wee, we treasured opportunities to admire the glowing dance of fireflies at dusk and to listen to the hooting of owls calling out to each other in the darkness. We peered through our telescope and saw the rings of Saturn and the faint smear of the Andromeda galaxy for the very first time. We had time to slow down and appreciate the colours of the seasons. We love the vibrant reds and yellows of Fall and the pristine whites of Winter – two seasons which contrasted starkly with the equatorial climate of Singapore. We travelled to Yellowstone, Yosemite, the Grand Canyon and the Canadian Rockies, and admired these awe-inspiring creations of Nature. These are our special memories and will always remain magical.

Our experiences have been so positive that our sons, Koon Wee and Yik Wee, secretly hoped that I will not graduate. Or at least, get my graduation delayed, so that they could stay in Madison for another semester or two. Fortunately, I am graduating, and I am very certain that their grandparents are glad for that.

I am grateful to my father, Koh Kim Beng, for his love, patience and wisdom. As I become older, I find that our interests converge. We have always been interested in "the

nature of reality", in terms of what Physics and Buddhist philosophy have to offer. I remember him reading Fritjof Capra's *"The Tao of Physics"* and explaining the double slit experiment and wave-particle duality to me. That was when I was in Primary School. I didn't think it made much sense then – in fact, I thought he probably explained it wrongly. I got *really* interested in Physics only in my last semester as a Physics major at the National University of Singapore (NUS). I was in the Science Library reading the Quantum Mechanics textbook by Bransden and Joachain, and came upon Bell's Theorem and the experiments which demonstrated the non-local nature of Quantum Mechanics. It gave me the goosebumps. As cliche as it may sound, it was the defining moment which made me believe that Physics may have something to offer in terms of real insight into the "nature of reality". That was in 1998; it gave me the desire to learn more about the foundations of Quantum Theory, a motivating factor that remained strong in the intervening decade between graduating from NUS and coming to graduate school.

That decade in-between was filled with many of life's ups and downs. I have nothing but gratitude and love for my late mother, Cheong Lee Ha, who passed away peacefully after a long battle with dementia during that period. I know that she would have been very proud of me today as I complete my PhD.

I would also like to express my sincere gratitude to my mother-in-law, Mak Yoke Leng, and my late father-in-law, Song Yong Hock. I am grateful to them for their love and patience. We always looked forward to receiving the packages of cooking spices, herbs and toys they mailed to us during our years here. Each package was not just a box of things – they were filled with their unconditional love for us. I only have one regret about our journey here – it is that I was not able to bring Lye Kuan and our boys back to Singapore in time to say our goodbyes to my late father-in-law. My consolation is that we had spent Chinese New Year together with him in Singapore this year.

I look forward to going home to Singapore. There will be more experiences to be shared and challenges to be overcome, and I await the next journey of life with my family.

I dedicate this thesis to the most important people in my life:

my lovely wife, Lye Kuan, for travelling this path with me,

my dearest sons, Koon Wee and Yik Wee, for filling the journey with much joy,

my beloved parents – my father, Koh Kim Beng, and my late mother, Cheong Lee Ha –

for helping me to find my path.

Contents

List of Figures

List of Tables

Chapter 1

Introduction

It may be said that the holy grail of the field of quantum computation [2] is the physical realization of a working quantum computer. In the past decade, there have been tremendous progress in the area of experimental implementations of the basic units of a quantum computer. While there exists different platforms on which to build the hardware of a quantum computer, silicon technology, with its status as the basis for classical computation for over half a century, holds the unique prospects of scalability and integration with classical electronics. Together with advances that have driven electronic devices continuously smaller, new generations of devices have emerged which are designed to make use of the quantum properties of charges and spins [3], making silicon technology uniquely placed as the platform of choice on which to realize quantum computer hardware.

It was first proposed in 1998 by Loss and DiVincenzo [1] to make use of electrically-gated quantum dots in semiconductor heterostructures to make qubits for quantum information processing. The development of silicon qubits has attracted substantial interest [5, 6, 7, 8] because spins in silicon have longer coherence times than spins in many other semiconductors. This is because of both the weak spin-orbit coupling and the low nuclear spin density in silicon [9, 10, 11].

Decoherence of a qubit arises from its interaction with the local environment. A key figure of merit for a quantum information processing device is the ratio of the quantum

coherence time to the time required to perform qubit gate manipulations [12, 13, 14]. In a semiconducting qubit, some interactions are intrinsic to the material in question, such as charge coupling to phonons [15]. Other sources of decoherence are extrinsic, such as charge noise [16, 17], which denotes the effects of fluctuating electric fields arising from sample defects and from the electronics and transmission lines used to control the qubit.

1.1 Outline of the thesis

This thesis describes several aspects of the theoretical issues related to quantum dot qubits in silicon. It may be broadly classified into three parts, (1) the hybrid qubit and quantum gates, (2) decoherence and (3) charge transport.

In the first part, we begin in Chapter 2 by detailing a new architecture for quantum dot qubits, which we term the hybrid qubit. We present evidence that implementing this qubit in silicon is feasible and that it is a relatively simple qubit architecture that could operate at high speeds with a higher figure of merit [18] than previous qubit designs [19, 20, 21].

In Chapter 3, we demonstrate how high fidelity and high speed quantum operations, called quantum gates, may be achieved using this architecture. We then compare different gating protocols for the hybrid qubit as well as for the more traditional singlet-triplet qubit [4], and analyze the optimal fidelities that can be achieved for each. We discuss how the highest possible fidelity should be achieved in the hybrid qubit using a gating protocol called STIRAP.

In the second part in Chapter 5, we present experimental data and theoretical analysis of coherent manipulation of a charge qubit in silicon. We show that long coherence times and high figures of merit can be achieved by exploiting the discrete electronic states of the qubit. We discuss the implications for the hybrid qubit.

We then present, in Chapter 6, data that demonstrate long spin lifetimes of a single spin in a silicon quantum dot, and show that the rate of loading of electron spins can be tuned over an order of magnitude, both of which are highly important for initialization and readout of spin qubits.

In the last part, in Chapters 7 and 8, we turn our attention to issues related to transport through double quantum dots in silicon. In particular, Chapter 7 focusses on transport in the two-electron regime, and describes how characteristic features of transport data can be explained by spin-dependent phenomena called spin blockade and lifetime-enhanced transport. Chapter 8 makes use of the same data, but focusses on transport in the less conventional three-electron regime. This is important because the hybrid qubit operates in that regime. In this Chapter, we show how the features of the data which have previously not been observed, can be explained by theory that makes use of the many-electron nature of the system.

We then summarize our main results in Chapter 9 and discuss the outlook of silicon quantum dot qubits.

1.2 Publications

Several papers form the basis of this thesis. Many people are responsible for the work described in each of the papers. Research, being a collaborative, synergistic process, makes it impossible to break down in detail, the contributions of each individual. Here, I will mention in brief, my primary contribition to each piece of work, as well as the contributions of the main authors.

Chapter 2 relies on the paper *"Fast hybrid silicon double quantum-dot qubit"* [18], in which I was responsible for the theoretical calculations and Zhan Shi was responsible for the experimental work performed.

Chapter 3 draws upon the work, *"Pulse-gated quantum dot hybrid qubit"* [22], to be published in Physical Review Letters, in which I was responsible for the idea of pulsed gating, and Mark Friesen completed the main theoretical calculations for single-qubit gates.

Chapter 4 comes from a recently completed piece of original work, *"High fidelity gates in quantum dot spin qubits"*, which is in the process of submission for peer-review. In this piece of work, I was responsible for developing the analytical and numerical approach to answer the central question of optimizing the fidelity of different quantum gating protocols.

Chapter 5 refers to another recently submitted paper, *"Enhanced coherence and high figure of merit in a silicon charge qubit"* [23]. In this work, Zhan Shi performed the experiment and I was responsible for the theoretical simulations.

Chapter 6 draws from the paper, *"Tunable spin loading and T_1 of a silicon spin qubit measured by single-shot readout"* [8]. Christie Simmons performed the experimental work underlying the paper, Bjorn van Bael and Jon Prance provided theoretical and computational support for the analysis of data, and I performed the numerical fitting necessary for the extraction of experimental spin rates.

Chapter 7 relies on the paper *"Pauli spin blockade and lifetime-enhanced transport in a Si/SiGe double quantum dot"* [24]. Christie Simmons performed the experimental work and I was responsible for performing the theoretical analyses based on the theoretical groundwork laid by Mark Friesen.

Chapter 8 draws upon the paper, *"Unconventional transport in the "Hole" regime of a Si double quantum dot"* [25], for which I was responsible for the theoretical work based on data obtained by Christie Simmons.

Chapter 2

Hybrid qubit: A new quantum dot spin qubit architecture

2.1 Introduction

Tremendous progress towards the development of working electrically-gated quantum dot qubits has been made over the past decade, and single-qubit operations have been demonstrated for logical qubits implemented in single [19], double [4], and triple [26] quantum dots in GaAs heterostructures. However, even with sophisticated pulse sequences that lead to coherence times up to 200 μs [27], the important figure of merit, the number of gate operations that can be performed within the qubit coherence time [12, 13, 14], needs to be improved significantly for quantum dot qubits to become useful. Moreover, it is highly desirable that a given implementation be as simple as possible.

In this chapter, we present a relatively simple double-dot qubit architecture in which a universal set of fast gate operations can be implemented. Each qubit consists of a double quantum dot with two electrons in one dot and one electron in the other. The qubit itself is the set of two low-lying electronic states with total spin quantum numbers $S = 1/2$ (square of the total spin of $3\hbar^2/4$) and $S_z = -1/2$ (z-component of total spin of $-\hbar/2$). These states form a decoherence-free subspace that is insensitive to long-wavelength magnetic flux noise;

moreover, decoherence processes that do not explicitly couple to spin or induce a transition of an electron to the reservoir do not induce transitions that go outside of the subspace of an individual qubit [28].

The gate operations are all implemented using purely electrical manipulations, enabling much faster gates than using ac magnetic fields [1, 19], inhomogeneous dc magnetic fields [20, 4, 27], or mechanisms using spin-orbit coupling [29, 30]. The qubit has the same symmetries in spin space as the triple-dot qubit proposed by DiVincenzo et al. [21], but is simpler to fabricate because it requires a double dot instead of a triple dot. The hybrid qubit proposed here also has significant advantages over the three-dot qubit for implementing multi-qubit operations: two hybrid qubits made of four dots in a linear array have higher effective connectivity than the similar linear array of dots considered in Ref. [21]. We show that this increased effective connectivity can reduce the number of manipulations required to implement two-qubit gates.

We present evidence that implementing this qubit in silicon is feasible. The development of silicon qubits has attracted substantial interest [5, 6, 7, 8] because spins in silicon have longer coherence times than spins in many other semiconductors, because of both the weak spin-orbit coupling and the low nuclear spin density in silicon [9, 10, 11]. Here, we measure a triplet-singlet relaxation time in a single silicon dot to be > 100 ms and demonstrate readout of the singlet and triplet states of two electrons in a silicon dot. We estimate dephasing times theoretically to be on the order of microseconds, long enough to achieve high fidelity quantum operations.

2.2 Qubit design

An important advantage of the qubit proposed here is that all qubit manipulations can be implemented using electric and not magnetic fields, resulting in fast operations [21]. To understand why electrical manipulation of our qubit is possible, we enumerate the possible transitions between spin states of three electrons that can be induced by spin-conserving manipulations. When three spin-1/2 entities are added, the resulting 8 total spin eigenstates

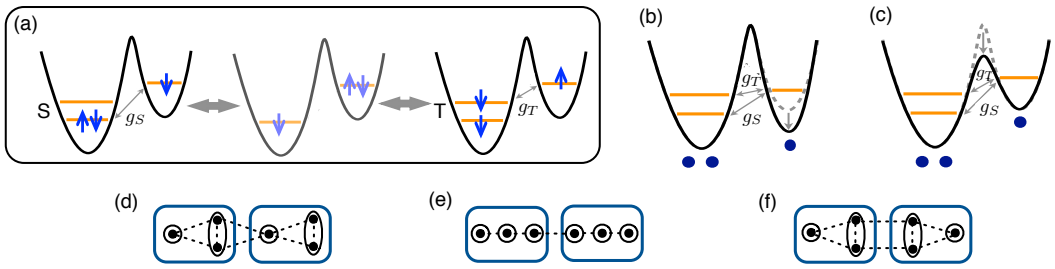

Figure 2.1: The logical qubit states of the hybrid qubit are $|0\rangle_L = |S\rangle|\downarrow\rangle$ and $|1\rangle_L = \sqrt{\frac{1}{3}}|T_0\rangle|\downarrow\rangle - \sqrt{\frac{2}{3}}|T_-\rangle|\uparrow\rangle$, where $|S\rangle$, $|T_-\rangle$, and $|T_0\rangle$ are two-particle singlet (S) and triplet (T) states in the left dot, and $|\uparrow\rangle$ and $|\downarrow\rangle$ respectively denote a spin-up and spin-down electron in the right dot. Fast qubit gate operations are performed by applying gate voltages that change the energy splittings between the singlet and triplet states in the left dot and that change the tunnel couplings g_S and g_T between the two dots. (a) Introducing tunneling between the dots induces transitions between $|0\rangle_L$ and $|1\rangle_L$. Starting from $|0\rangle_L$, in which the electrons in the left dot are in a singlet, if an electron tunnels from the left dot to the right dot, and then the other electron tunnels back to the left dot, the spins in the left dot will end up in a triplet. The actual process conserves the total spin quantum numbers S^2 and S_z and yields transitions between $|0\rangle_L$ and $|1\rangle_L$ (see Appendix A). (b) and (c): Schematic illustrating independent tuning of the coupling between the electron in the singly occupied dot and the singlet and triplet states in the doubly occupied dot via the barrier height and relative energies in the two dots, as described in the text. (d): Effective connectivity of two hybrid qubits composed of four dots in a linear geometry. Each connection is a tunable two-electron interaction. There are eight effective connections, compared to five effective connections in a linear array of six dots for the qubits considered in Ref. [21], shown in (e). For (d), a two-qubit gate equivalent to CNOT up to local (one-qubit) unitary operations can be implemented in 16 steps, compared to 18 for (e) [31] (see Appendix A). (f): Connectivity for which a fourteen-operation two-qubit gate equivalent to CNOT up to local unitary operations has been found (see Appendix A).

form a quadruplet with $S = 3/2$ and $S_z = 3/2,\ 1/2,\ -1/2,\ -3/2$, and two doublets, each with $S = 1/2$, $S_z = \pm 1/2$, where the total spin is $\hbar^2 S(S+1)$ and the z-component of the total spin is $\hbar S_z$. Only states with the same S and S_z can be coupled by spin-independent terms in the Hamiltonian. We choose to use the group of two states with $S = 1/2$, $S_z = -1/2$ for the states of the qubit.

As discussed in Ref. [21], the two states of the logical qubit with $S = 1/2$ and $S_z = -1/2$

can be written as

$$|0\rangle_L = |S\rangle|\downarrow\rangle, \tag{2.1}$$

$$|1\rangle_L = \sqrt{\frac{1}{3}}|T_0\rangle|\downarrow\rangle - \sqrt{\frac{2}{3}}|T_-\rangle|\uparrow\rangle. \tag{2.2}$$

In our case, $|S\rangle$ is the singlet $((|\uparrow\downarrow\rangle - |\downarrow\uparrow\rangle)/\sqrt{2})$, T_0 triplet $((|\uparrow\downarrow\rangle + |\downarrow\uparrow\rangle)/\sqrt{2})$, and T_- triplet $(|\downarrow\downarrow\rangle)$ in the left dot, and $|\uparrow\rangle$ and $|\downarrow\rangle$ respectively denote a spin-up and spin-down electron in the right dot. The essential difference between our system and that of [21] is that the singlet and triplet states are of two electrons in one dot instead of two different dots, as depicted in Fig. 2.1.

2.3 Single qubit gate operations

We now discuss how gate operations are implemented in this qubit in terms of the elementary operations implemented by changes of gate voltages in the device. A complete set of single-qubit manipulations consists of one that changes the energy splitting between the qubit states and another that drives transitions between the qubit states. The energy difference between the two qubit states is mainly the singlet-triplet splitting in the doubly occupied dot, and this splitting indeed can be tuned by changing gate voltages in both GaAs/GaAlAs [32] and in Si/SiGe dots [33]. In Si/SiGe systems, changing the voltage on a global top-gate should also change the singlet-triplet splitting [34, 35].

Transitions between the two states of the hybrid qubit can be induced by changing the off-diagonal terms in the reduced Hamiltonian. These terms are each proportional to $g_i^2/\Delta E_i$, where g_i is the relevant tunneling amplitude and ΔE_i is the energy difference between the relevant state with two electrons on the left dot and the virtual state in which an electron has tunneled from state i in the left dot onto the right dot. Explicit calculations of the effective spin Hamiltonian obtained by a canonical transformation that systematically eliminates higher energy states [36, 37, 38] demonstrate that increasing the tunnel couplings between the quantum dots indeed drives transitions between thetwo states of the qubit (see Appendix A). Therefore, gate modulations that change the g_i will induce transitions be-

tween the qubit states, and modulations of the energy difference ΔE_i will similarly induce transitions when the g_i are non-negligible. We note that when the singlet-triplet splitting E_{ST} is nonzero, Rabi flops are performed by modulating the off-diagonal terms at the angular frequency Ω satisfying $\hbar\Omega = E_{ST}$. This modulation is easier to achieve experimentally when E_{ST} is not too large. A singlet-triplet splitting of 0.05 meV, typical of splittings measured in quantum dots fabricated in Si/SiGe heterostructures [39, 40], corresponds to a frequency of ~ 10 GHz. Quantum dot gate operations have already been achieved at this speed [41], and efficient schemes exist for refocusing the fast rotations [42].

While the two manipulations obtained by changing the singlet-triplet splitting in one dot or the tunnel coupling between two dots described above are sufficient for achieving arbitrary single qubit gates, a larger set of elementary operations (or, equivalently, more fine-grained control of the terms in the effective Hamiltonian) is useful because it enables two-qubit gates to be implemented with fewer elementary operations. We note that g_S and g_T, the tunneling matrix elements that shift a single electron from the singlet or triplet state in the left dot to the lowest energy state in the right dot, can be tuned separately. Decreasing the tunnel barrier, as shown in Fig. 2.1(c), increases both tunnel rates, whereas changing the difference between the overall energies in the left and right dots, as in Fig. 2.1(b), can change the ratio of the two tunnel rates, because of energy-dependent tunneling [43, 24]. The tunable degrees of freedom (the singlet-triplet splitting and the tunnel rates into the singlet and into the triplet) are denoted schematically in Fig. 2.1(d) as dashed lines.

2.4 Two-qubit gates

The spin symmetries of the hybrid qubit are the same as in the three-dot qubit of Ref. [21] and two-qubit gates are implemented similarly; however, because the hybrid qubit has higher effective connectivity, two-qubit gates can be implemented with fewer elementary operations. The increased connectivity for dots in a linear array is illustrated schematically in Fig. 2.1(d-f). Fig. 2.1(d) shows two hybrid qubits with eight effective connections, while Fig. 2.1(e) shows the five effective connections of two triple-dots in a linear array.

Fig. 2.1(f) shows a different arrangement of two double-dots, also with eight effective connections (Appendix A shows how the hybrid qubit can achieve these connections). We have found sequences, presented in Appendix A, of 16 and 14 two-qubit operations that yield gates equivalent to CNOT up to local unitary operations for Fig. 2.1(d) and Fig. 2.1(f), respectively. In comparison, 18 operations are needed for Fig. 2.1(e) [31]. These shorter gate sequences provide strong evidence that increased effective connectivity can enable implementation of gates of two logical qubits with fewer elementary two-qubit operations.

2.5 Readout and initialization.

Readout of the qubit states can be performed by exploiting the difference in tunnel rates coupling the singlet and triplet states of the doubly occupied dot to the lead [44]. (See also Chapter 6.)

Fig. 2.2 shows charge sensing measurements of a Si/SiGe double quantum dot in which the ground state of the left dot when occupied by two electrons at low field is a singlet S, whereas at large magnetic field B the ground state is the triplet T_-. (All electron numbers refer to the effective electron number; the actual number may include a spin-zero closed shell of electrons in addition to the valence electrons we study here. Details of the measurements are presented in Appendix A.) To measure the tunnel rate into the dot, we start with one electron in the left dot. We apply a step increase in voltage to gate PL, causing an electron to tunnel from the lead into the dot, and changing the dot occupation from one to two. Fig. 2.2(a) shows an average of 300 measurements of the charge sensor current in response to the electron tunneling into the dot for $B = 1\,\mathrm{T}$ and $B = 3\,\mathrm{T}$, showing exponential decays corresponding to loading a single electron with tunneling rates $\gamma_{\mathrm{load}} = 81\,\mathrm{Hz}$ ($B = 1\,\mathrm{T}$, ground state S) and $\gamma_{\mathrm{load}} = 521\mathrm{Hz}$ ($B = 3\mathrm{T}$, ground state T_-) (See Appendix A). Fig. 2.2(c) shows analogous measurements of electrons tunneling out of the dot that yield tunnel rates $\gamma_{\mathrm{unload}} = 182\,\mathrm{Hz}$ (ground state S) and $\gamma_{\mathrm{unload}} = 645\,\mathrm{Hz}$ (ground state T_-). The difference in tunnel rates between the singlet and triplet states is thus large and suitable for both readout and initialization.

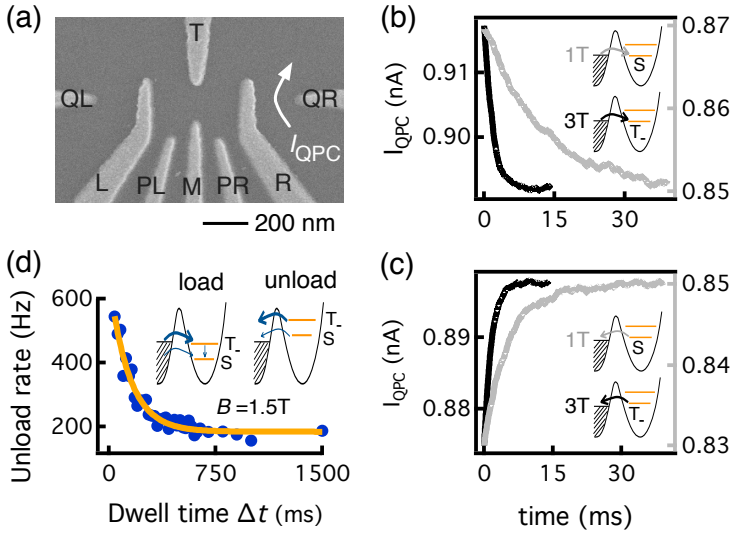

Figure 2.2: (a) Scanning electron micrograph of a top-gated Si/SiGe dot with the same gate structure as the one used in the experiment, which is described in [8]. (b) Measurement of the tunnel rate into the dot when the dot ground state is a singlet S (gray, $B = 1$ T) and a triplet T_- (black, $B = 3$ T). The measured charge sensor current I_{QPC} versus time after the voltage on gate PL is changed is fit to an exponential form, yielding tunnel rates $\gamma_{\rm load} = 81$ Hz and $\gamma_{\rm load} = 521$ Hz, respectively. (c) Analogous measurement of the tunnel rates out of the dot, yielding $\gamma_{\rm unload} = 182$Hz (ground state S) and $\gamma_{\rm unload} = 645$Hz (ground state T_-). The different singlet and triplet tunnel rates enable qubit initialization and readout. (d) Measurement of the triplet T_- to singlet S relaxation time. The gate voltages on the dot are changed to allow the triplet or singlet state to load, and the unloading rate is measured as a function of the duration of the loading pulse Δt. Fitting the unloading rate versus dwell time to an exponential form (shown as the solid line) yields $T_1 = 141 \pm 12$ ms.

2.6 Coherence properties

While the spin symmetries of the hybrid qubit are identical to those of the three-dot qubit in Ref. [21], the coherence properties are different because the singlet and triplet states have different spatial wavefunctions. An essential component of this qubit is a long lifetime for the triplet state of the dot with two electrons. We measure this lifetime by applying a step in voltage to gate PL large enough that both the ground state singlet S and the triplet T_- excited state are energetically accessible at magnetic field $B = 1.5$ T. States S and T_- each load with some probability. After a dwell time Δt, the voltage is returned to its previous value, and an electron tunnels out of the dot. As Δt is increased, the probability that the

electrons remain in the T_- state decreases exponentially with a characteristic time T_1, and the tunnel rate to the lead decays with the same characteristic time. Fig. 2.2(d) shows the result of such a measurement; it yields $T_1 = 141 \pm 12$ ms. This slow relaxation time is significantly longer than the value of ~ 3 ms measured in GaAs [44] and is consistent with theoretical estimates that account for Rashba spin-orbit coupling and phonon-assisted hyperfine coupling [45, 46].

The different charge distributions of the two qubit states gives rise to dephasing due to electron-phonon coupling [47, 48] and charge noise [49]. Our calculations indicate that for realistic states, the intervalley component of the electron-phonon dephasing term is the most important, and leads to $T_2 \sim 1$ μs [15]. Dephasing due to charge noise is suppressed in the hybrid qubit compared to charge qubits [50] because the changes in charge distributions are confined to a single quantum dot, making the effective dipole moment much smaller (indeed, the dipole moment vanishes in the limit of harmonic dot potentials) [15]. Therefore, charge fluctuation-induced decoherence is greatly suppressed in the hybrid qubit compared to double dot charge qubits. Simple estimates indicate that decoherence rates induced by nuclear spins will be similar to those in singlet-triplet qubits [27].

2.7 Summary

To summarize, we have proposed a solid state qubit architecture which we term hybrid qubit. It consists of three electrons in two quantum dots. Compared to previous proposals, this new qubit has the important advantages of fast gate operations and relative simplicity of fabrication. Experimental data are presented that support the feasibility of constructing the qubit architecture using Si/SiGe quantum dots. Details of theoretical calculations and experimental work that support the claims of this chapter are given in Appendix A.

We also proposed single-qubit gate operations which make use of the fast AC modulations of the tunnel coupling. In general, fast AC control over experimental parameters can be experimentally more challenging compared to DC control. In this light, we present an alternative protocol for single-qubit gates using DC pulses in the next chapter, and show

that it is possible to achieve high fidelity with such a scheme.

Chapter 3

Quantum gates I: DC pulsed gating of the hybrid qubit

3.1 Introduction

A key figure of merit for a quantum information processing device is the ratio of the quantum coherence time to the time required to perform qubit gate manipulations [12, 13, 14]. The hybrid quantum dot qubit [18] introduced in Chapter 2 is a relatively simple qubit architecture that could operate at high speeds with a higher figure of merit [18] than previous qubit designs [19, 20, 21].

Chapter 2 (Ref. [18]) proposes to implement gate operations using high-frequency ($\sim 10 - 40$ GHz) resonant RF pulses, which is feasible [51, 52], but significantly more complicated to implement experimentally than the pulse-gating methods used for charge qubits [50, 53, 54, 55, 56] and for spin qubits [4, 26, 57, 58, 59]. Here we show how to implement pulse-gating of the quantum dot hybrid qubit by exploiting the level crossings where the qubit becomes charge-like. We develop one- and two-qubit gates that require a modest number of non-adiabatic voltage pulses (five and eight, respectively). We obtain closed-form solutions for the control sequences and show that the gates are fast (sub-nanosecond) and can achieve high fidelities.

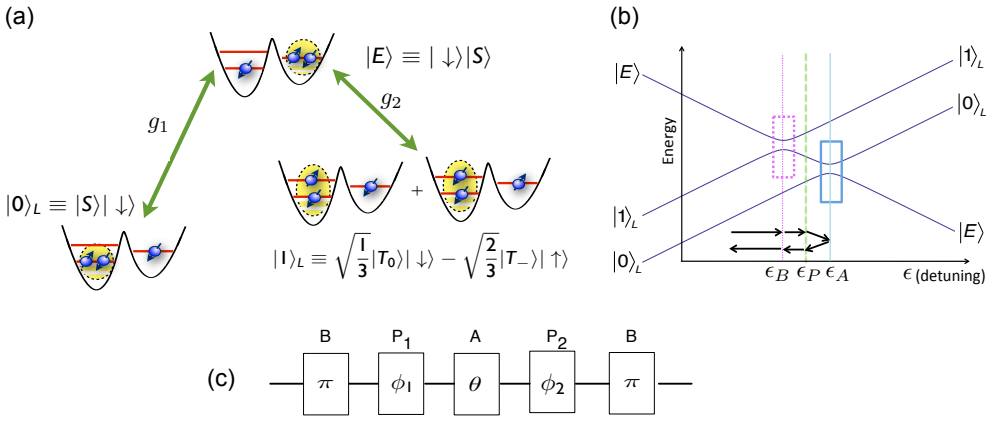

Figure 3.1: (a) Schematic of the quantum dot hybrid qubit and of the physics underlying gate operations. The logical qubit states are $|0\rangle_L = |S\rangle|\downarrow\rangle$ and $|1\rangle_L = \sqrt{\frac{1}{3}}|T_0\rangle|\downarrow\rangle - \sqrt{\frac{2}{3}}|T_-\rangle|\uparrow\rangle$, as first defined in Eqs. 2.1 and 2.2 in Chapter 2. Introducing tunneling amplitudes g_1 and g_2 to a (1,2) excited state $|E\rangle$ induces transitions between $|0\rangle_L$ and $|1\rangle_L$. (b) Energies of $|0\rangle_L$, $|1\rangle_L$, and $|E\rangle$ versus detuning ϵ between the two dots. The ground state has charge occupation (2,1) when $\epsilon < \epsilon_A$ and (1,2) when $\epsilon > \epsilon_A$; the qubit operates mainly in the regime $\epsilon \leq \epsilon_A$. The energy difference between the qubit states $|0\rangle_L$ and $|1\rangle_L$ is large for all values of ϵ, but there is an avoided crossing between $|0\rangle_L$ and $|E\rangle$ at detuning ϵ_A (blue box), and another avoided crossing between $|1\rangle_L$ and $|E\rangle$ at ϵ_B (dotted magenta box). Pulse-gate transitions between $|0\rangle_L$ and $|1\rangle_L$ can be performed by using both avoided crossings. Pulses to the detuning ϵ_P are used to induce phase differences between the three states. A gating sequence to perform arbitrary rotations in the qubit Hilbert space is indicated with arrows; along the detuning axis, the pulse sequence is $\epsilon_i \rightarrow \epsilon_B \rightarrow \epsilon_P \rightarrow \epsilon_A \rightarrow \epsilon_P \rightarrow \epsilon_B \rightarrow \epsilon_f$. (c) The corresponding circuit diagram for the gate sequence, with time progressing from left to right. Gates P_1, A, and P_2 are tunable, with the control parameters ϕ_1, θ, and ϕ_2 given in Eqs. 3.2-3.4.

The two logical qubit states of the quantum dot hybrid qubit are given in Eqs. 2.1 and 2.2 of Chapter 2. Transitions between the logical states $|0\rangle_L$ and $|1\rangle_L$ are allowed when tunneling is introduced between the dots. Transitions between $|0\rangle_L$ and $|1\rangle_L$ occur via an intermediate state $|E\rangle$ that has charge occupation (1,2) and the same total S^2 and S_z. Fig. 3.1(a) shows the hybrid qubit and a physical process that yields transitions between $|0\rangle_L$ and $|1\rangle_L$. We assume that the right dot's singlet-triplet splitting is large enough that higher energy states of the right dot do not mix appreciably with the states considered explicitly here.

Quantum oscillations between two states $|\alpha\rangle$ and $|\beta\rangle$ are achieved by changing the

detuning suddenly to a value at which the energy difference between the states is smaller than the coupling between them. Very near the avoided crossing between two states, the time evolution is governed by the two-state Hamiltonian

$$H = \begin{pmatrix} \frac{1}{2}\tilde{\epsilon} & g_0 \\ g_0 & -\frac{1}{2}\tilde{\epsilon} \end{pmatrix} , \tag{3.1}$$

where g_0 is the coupling between $|\alpha\rangle$ and $|\beta\rangle$ and $\tilde{\epsilon}$ is the energy difference between $|\alpha\rangle$ and $|\beta\rangle$ in the absence of coupling. Significant mixing between the states occurs only when $\tilde{\epsilon} \lesssim g_0$. If one pulses the system suddenly to $\tilde{\epsilon} = 0$, so that the state at time $t = 0$ is $|\psi(0)\rangle = |\alpha\rangle$, then the time evolution of the two-state system is given by $|\psi(t)\rangle = \cos(\Omega_R t)|\alpha\rangle - i\sin(\Omega_R t)|\beta\rangle$, oscillating between $|\alpha\rangle$ and $|\beta\rangle$ with angular frequency $\Omega_R = g_0/\hbar$. A pulse of duration T rotates the state on the Bloch sphere by an angle $\Theta = 2\Omega_R T$ around the x-axis [2].

Fig. 3.1(b) shows the energies of the states $|0\rangle_L$, $|1\rangle_L$, and $|E\rangle$ as a function of detuning ϵ, which is controlled using gate voltages. The energy difference between $|0\rangle_L$ and $|1\rangle_L$, which is the singlet-triplet energy splitting in the left dot, typically is substantial ($\sim$ 0.1 meV, corresponding to a frequency $\sim$25 GHz) and depends only moderately on ϵ [33], so achieving an avoided crossing of $|0\rangle_L$ and $|1\rangle_L$ is typically not feasible. Therefore, pulse-gating is ineffective in inducing transitions directly between $|0\rangle_L$ and $|1\rangle_L$. However, there is a detuning ϵ_A where there is an avoided crossing between the states $|E\rangle$ and $|0\rangle_L$[1], and another detuning ϵ_B where there is an avoided crossing between the states $|E\rangle$ and $|1\rangle_L$. Transitions from $|0\rangle_L$ to $|1\rangle_L$ can be induced by pulsing first to ϵ_A and then to ϵ_B. Similarly, transitions from $|1\rangle_L$ to $|0\rangle_L$ can be induced by pulsing first to ϵ_B and then to ϵ_A.

3.2 Arbitrary single-qubit rotations

A pulse sequence that implements $U(\hat{\mathbf{n}}, \beta)$, a rotation of the logical qubit by an angle β about the rotation axis $\hat{\mathbf{n}} = (\sin\eta\cos\zeta, \sin\eta\sin\zeta, \cos\eta)$, where η and ζ are the polar and

[1] A π pulse at ϵ_A also enables fast spin-to-charge conversion for readout, since it changes the charge state of $|0\rangle_L$ but not $|1\rangle_L$.

azimuthal angles, is constructed from three primitive gates: A, B, and P. All detuning changes are assumed to be instantaneous. The B gate, implemented by pulsing the detuning to ϵ_B for a time that yields a π rotation about the x-axis in the $\{|1\rangle_L, |E\rangle\}$ subspace, converts $|1\rangle_L \rightarrow |E\rangle$ and $|E\rangle \rightarrow |1\rangle_L$. The A-gate, obtained by pulsing to ϵ_A for an interval that implements a rotation by an arbitrary angle θ about the x-axis in the $\{|0\rangle_L, |E\rangle\}$ subspace, changes the "latitude" of the qubit on the $\{|0\rangle_L, |E\rangle\}$ Bloch sphere. The "longitude" on the $\{|0\rangle_L, |E\rangle\}$ Bloch sphere is controlled using a phase gate P, whose detuning ϵ_P is roughly midway between the anticrossings at ϵ_A and ϵ_B, to avoid causing quantum oscillations. The P gate causes $|E\rangle$ to gain a phase ϕ relative to $|0\rangle_L$. By inserting two P gates that rotate the phase by angles ϕ_1 and ϕ_2 between the B and A-gates, any prescribed rotation on the $\{|0\rangle_L, |1\rangle_L\}$ Bloch sphere can be obtained. The full pulse sequence $U = BP_2AP_1B$ is shown at the bottom of Fig. 3.1(b) and as a circuit diagram in Fig. 3.1(c). The control parameters (θ, ϕ_1, ϕ_2) that yield rotation parameters (β, η, ζ) are derived in detail in Appendix B, and are given by

$$\theta = 2\arcsin[\sin(\eta)\sin(\beta/2)], \tag{3.2}$$

$$\phi_1 = \arctan[\cos(\eta)\tan(\beta/2)] - \phi_B - \zeta + \pi/2, \tag{3.3}$$

$$\phi_2 = \arctan[\cos(\eta)\tan(\beta/2)] - \phi_B + \zeta + \pi/2, \tag{3.4}$$

where ϕ_B is the incidental phase gained by state $|1\rangle_{\rm L}$ relative to $|0\rangle_{\rm L}$ while implementing the B-gate. For example, $U = BP_2(-\phi_B + \pi/2)A(\beta)P_1(-\phi_B + \pi/2)B$ yields an x-rotation by an angle β.

The speed of a pulsed gate in a quantum dot hybrid qubit can be estimated by noting that it is composed of five primitive gates, as shown in Fig. 3.1(c). The A and B-gates correspond to charge qubit rotations, and their speed is determined by the anti-crossing energy gaps [23, 41, 50, 53, 55, 56]. A $\pi/2$ rotation of a charge qubit can be implemented in a time $\lesssim$200 ps [23, 56]. The speed of the phase gates P_1 and P_2 is determined by the energy splitting between states $|0\rangle_{\rm L}$ and $|E\rangle$. For a splitting of 50 μeV, a single P-gate can be implemented in $\leq$ 80 ps. Thus, sub-nanosecond gating of a hybrid-qubit should be achievable with current technology. Sub-nanosecond coherent driven oscillations between

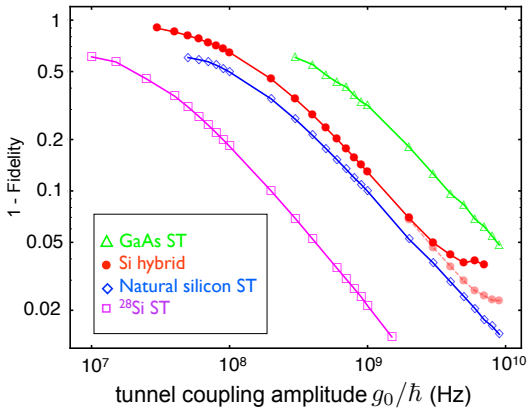

Figure 3.2: Numerically calculated infidelity (1-fidelity) caused by dephasing during qubit rotations without use of dynamical decoupling [60], as a function of the inter-dot tunnel coupling in a double quantum dot. Solid red circles show the results for a hybrid qubit, and open triangles, diamonds, and squares show the results for the exchange gate of singlet-triplet qubits [4, 59] for GaAs, natural Si and isotopically purified Si, with 28Si exhibiting the best overall gate fidelity. The two curves for the Si hybrid qubit represent different values of the singlet-triplet splitting (0.05 meV for the upper curve and 0.5 meV for the lower curve).

the (2,1) singlet and both of the low energy (1,2) states in a Si/SiGe double dot have been reported [23], providing further evidence that fast pulse-gating of hybrid qubits is feasible.

3.3 Gate fidelity

When hybrid qubits are not undergoing gate operations, their coherence properties benefit from their spin-like character, similar to singlet and triplet states in a two-electron quantum dot [15]. However, the gating procedures described above consist of sequential rotations of charge qubits, for which the decoherence rates are faster. The gating speeds are also faster, so realistic estimates for the gate fidelity require us to perform dynamical simulations of the gate sequence.

We model the dynamical evolution of the density matrix ρ using a master equation [2]:

$$\dot{\rho} = -\frac{i}{\hbar}[H, \rho] - D. \tag{3.5}$$

The Hamiltonian and decoherence terms are expressed in the $\{|0\rangle_L, |1\rangle_L, |E\rangle\}$ basis as

$$H = \begin{pmatrix} -\Delta E_{01}/2 & 0 & g_1 \\ 0 & \Delta E_{01}/2 & -g_2 \\ g_1 & -g_2 & -\epsilon \end{pmatrix}, \tag{3.6}$$

$$D = \begin{pmatrix} 0 & \gamma\rho_{01} & \Gamma\rho_{0E} \\ \gamma\rho_{10} & 0 & \Gamma\rho_{1E} \\ \Gamma\rho_{E0} & \Gamma\rho_{E1} & 0 \end{pmatrix}. \tag{3.7}$$

In the Hamiltonian, $\Delta E_{01} \simeq 0.1$ meV is the energy splitting between the logical qubit states [33], and g_1 and g_2 are the tunnel couplings. For valley-type excited states in Si, $g_2 = \sqrt{3/2}g_1$ [33]. The charge dephasing rate [61] $\Gamma = 1/T_2^* \simeq 0.2$ GHz is the experimentally measured value for charge qubits in GaAs [56], and the spin dephasing rate $\gamma \simeq 1$ MHz is the theoretical estimate for $1/T_2^*$ of the hybrid qubit far from the anti-crossings [15].

Fig. 3.2 shows the results of our dynamical simulation for an X-gate (a π rotation around the logical x-axis), using the gate sequence $U = P_2BA(\pi)BP_1$ (see Appendix B). Increasing the tunnel coupling improves the fidelity because it increases the gate speed, until the A and B anti-crossings overlap and the fidelity flattens out. The frequency at which this occurs increases as ΔE_{01} increases.

Fig. 3.2 also shows analogous fidelity calculations for the exchange gate that implements X-rotations of singlet-triplet qubits [4, 59] by pulsing to a value of ϵ at which the exchange coupling J dominates over the inter-dot magnetic field difference ΔB [4]. There are competing effects in the fidelity when $J \gg \Delta B$ (*i.e.*, when $|\epsilon|$ is small): the qubit becomes charge-like, and decoheres more quickly, but the gate speed increases. In Fig. 3.2, the value of ϵ is chosen to yield the optimum fidelity for every ΔB and g_1. Fig. 3.2 shows results for three physical systems: GaAs ($\gamma = 1/T_2^* = 0.14$ GHz, $\Delta B = 3.6$ mT [62]), natural Si ($\gamma = 1.5$ MHz, $\Delta B = 26$ μT [62]), and isotopically purified Si ($\gamma = 0.2$ MHz, $\Delta B = 1.2$ μT [62]). For fixed tunnel coupling, increasing ΔB reduces the fidelity of the exchange gate. However, better fidelities can be achieved by increasing ΔB and g_1 simultaneously.

Fig. 3.2 shows that for natural silicon, the fidelity of an X-gate in a hybrid qubit is comparable to the fidelity of an exchange-mediated gate (with $J \gg \Delta B$) in a singlet-triplet qubit. The fidelity of a Z-gate in a hybrid qubit is very high because it is a fast gate that is implemented far from any level crossings [33]. For a singlet-triplet qubit, the corresponding gate (with $\Delta B \gg J$) is also implemented away from level crossings, but inhomogeneous broadening places a materials-dependent lower bound on the fidelity [62]. Fast pulse sequences can be used to overcome this constraint [27] at the cost of gating complexity. Hybrid qubit gates are simple for both rotation axes since they do not require complicated gating sequences.

Pulse-gated quantum operation can also be performed by combining slow ramps and fast pulses to perform adiabatic passage through the B anticrossing between $|E\rangle$ and $|1\rangle_L$ [63] and quantum oscillations at the anticrossing A between $|0\rangle_L$ and $|E\rangle$. Starting from a large negative detuning, first the detuning is increased adiabatically through anticrossing B (which transforms $|1\rangle_L \rightarrow |E\rangle$ and has no effect on $|0\rangle_L$), then pulsed suddenly to anticrossing A (inducing quantum oscillations between $|0\rangle_L$ and $|E\rangle$), and finally decreased adiabatically through anticrossing B (which transforms $|E\rangle \rightarrow |1\rangle_L$ and has no effect on $|0\rangle_L$). This partially adiabatic protocol could be very useful if the energy splitting at anticrossing B is significantly larger than for anticrossing A, which is conceivable because of the large differences of tunnel rates from different orbital states that have been observed in a silicon quantum dot [8] (see Chapter 6). However, the time spent in $|E\rangle$ is likely to be longer than in the all-sudden protocol described above, rendering the gate much more susceptible to charge noise, because of the markedly different charge distribution in $|E\rangle$ than in $|0\rangle_L$ and $|1\rangle_L$ [15]. Thus it is likely to be more difficult to perform high-fidelity gate operations using a partially adiabatic process than using the sequence of quantum oscillations described above.

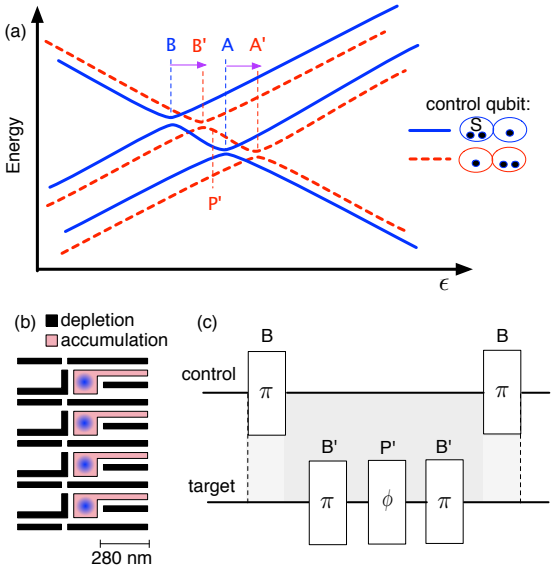

Figure 3.3: Pulse-gating protocol for a two-qubit controlled-phase gate. (a) The detunings of the avoided crossings A and B of the target qubit shift by $\delta\epsilon$ (horizontal arrows on the figure) when the state of the control qubit is changed from $|0\rangle_L$ to $|E\rangle$. (b) Realistic device geometry for a top-gated Si/SiGe heterostructure, described in (see Appendix B). 2D Thomas-Fermi modeling [64] of this device yields $\delta\epsilon \gtrsim 0.1$ meV, ample for operation of a conditional gate. (c) Gate sequence for a conditional rotation of the phase of the target qubit. First, a B-gate is applied to the control qubit, which leaves $|0\rangle_L$ unchanged and transforms $|1\rangle_L \rightarrow |E\rangle$. The target qubit is then pulsed to anticrossing B', then to P', and then again to B', which changes the phase of the target qubit only when it starts in state $|1\rangle_L$ and the control qubit is in state $|E\rangle$. Finally, applying a B-gate to the control qubit converts it back to a spin qubit. The gray shading denotes that the operations on the target qubit are conditional between application of the two B-gates to the control qubit. This gate sequence changes the phase of the target qubit only when the control qubit starts in state $|1\rangle_L$. The operations also perform a conditional phase rotation on the control qubit, which can be adjusted to be a multiple of 2π by appropriate choice of pulse parameters.

3.4 Two-qubit gates

Two-hybrid qubit gates can be implemented by exploiting capacitive coupling [58, 65, 66]. As shown in Fig. 3.3(a), the charge distribution in state $|E\rangle$ is substantially different than in $|0\rangle_L$, so there is a substantial Coulomb coupling that causes the location of the anticrossings A and B of the target qubit to depend on whether the control qubit is in state $|0\rangle_L$ or in state $|E\rangle$. Therefore, pulsing the target qubit to the detuning of anticrossing A converts the state $|1\rangle_L$ of the target qubit to $|E\rangle$ when the control qubit is in state $|0\rangle_L$ but not

in state $|E\rangle$. This dependence of the position of the anticrossings of the target qubit on the state of the control qubit enables the construction of a conditional two-qubit gate, as illustrated in Fig. 3.3(c). One first applies a B-gate to the control qubit, which transforms $|1\rangle_L \rightarrow |E\rangle$, and then applies a gate sequence that changes the phase of the target qubit only if the control qubit is in state $|0\rangle_L$. 2D Thomas-Fermi modeling [64] of the realistic device geometry, shown in Fig. 3.3(b) and described in Appendix B, yields shifts in the anticrossing energies of $\gtrsim 0.1$meV, which is ample for fast operations to be feasible.

3.5 Summary

To summarize, in this chapter, we presented a method for pulse-gating a quantum dot hybrid qubit. Even though the qubit states typically cannot be made energetically degenerate, pulsed gating can be implemented by exploiting avoided crossings at two different detunings between each of the two qubit states and an intermediate state. With an additional phase gate at a third detuning, arbitrary rotations of the logical qubit can be achieved. We have derived explicit expressions for the pulse sequences and performed dynamical simulations of the gates assuming realistic values for the dephasing rates. We also showed that two-qubit gates can be implemented by operating the control qubit in the charge regime to electrically enable or disable a rotation on the target qubit.

To understand how the fidelity of this method of pulse-gating gating fares when compared with the AC scheme of the previous chapter as well as the more traditional singlet-triplet qubit [4], we analyze the optimal fidelities achievable for both qubits using both DC and AC methods of gating and present our results in the next chapter.

Chapter 4

Quantum gates II: Optimal DC and AC fidelities

4.1 Introduction

A variety of logical qubits and quantum gates have been proposed for quantum computer architectures using top-gated quantum dots. Differences between the schemes can make meaningful comparisons of the resulting gate fidelities challenging.

In this chapter, we show that it is possible to evaluate many qubit-gate-decoherence combinations on an equal footing, once the gating protocols have been properly optimized. To demonstrate our procedure, we analyze optimal fidelities of single qubit gates for two types of double-dot qubits: the singlet-triplet [20, 4] and hybrid [18] qubits. Quantum gates involving transitions between the logical qubit states are controlled by the exchange interaction between the dots, J, which is itself a function of two experimental parameters, the tunnel coupling g and the detuning between the double-dots ϵ. We consider three types of gates involving transitions between qubit states: a DC pulsed gate, and two AC gates, based on logical qubit resonance (LQR) and stimulated Raman adiabatic passage (STIRAP). Remarkably, we find that after optimization, almost all the gate fidelities are quantitatively similar and and follow the same simple scaling law. The only exception is

the pulse-gated hybrid qubit, which is more difficult to optimize. Of the cases considered here, we find that the highest possible overall fidelity is achievable in a hybrid qubit using a STIRAP gating protocol.

4.2 Decoherence and gate speed

Performing prescribed quantum transformations of a qubit with an extremely high degree of quantum coherence is one of the several stringent criteria required for the realization of a working quantum computer [12, 13, 14]. However, inevitable interactions between the qubit and its environment result in "dephasing" [2], or the loss of coherence necessary for quantum information processing. For semiconducting qubits, charge fluctuations in the semiconductor environment comprise a fast noise source that causes rapid dephasing. One way to decrease the dephasing rate has been to encode qubits in spin degrees of freedom. Hyperfine coupling between nuclear magnetic moments and the electron spin comprises a slow noise source, allowing techniques such as spin echoes [67, 27] to mitigate their dephasing effects. Thus, quantum dot spin qubits [20, 4, 18, 1, 19, 21, 26, 59] possess longer coherence times than quantum dot charge qubits [50, 53, 56].

The state of the qubit can be fully characterized by its position on the unit Bloch sphere, where the $\pm\hat{z}$ directions correspond to the qubits states 0 and 1 [2]; single qubit operations can then be visualized as rotations on the Bloch sphere. The energy splitting ΔE between qubit states causes an accumulation of the phase difference between energy eigenstates of the qubit [67], which are rotations about the z-axis of the Bloch sphere. For quantum dot spin qubits, this "phase accumulation gate" is susceptible to slow dephasing with rate γ. Coherent transitions between the qubit states are x-axis rotations on the Bloch sphere, which in quantum dot spin qubits are performed by turning on the exchange interaction, so we denote performing x-rotations as "exchange gating". The exchange interaction is a strong interaction and enables fast ($>$ GHz) rotations. However, the exchange interaction brings the quantum dot spin qubit out of the qubit subspace, into a transient superposition of states with different charge distributions. This makes exchange gating susceptible to fast

dephasing Γ, as depicted in Fig. 4.1(c). The degree to which fast dephasing affects exchange gating increases with the strength of the interaction. Therefore, it is not obvious *a priori* whether running an exchange gate faster will result in better fidelity.

Experimentalists have a range of tools with which to control single qubit rotations. The exchange interaction J depends on the tunnel coupling between dots g and the detuning (energy difference between dots) ϵ, both of which have a wide range of tunability. On the other hand, the energy splitting ΔE between the qubit states is typically of limited tunability. In addition, there are different gating protocols to choose from. We consider a DC pulse-gating protocol, and two AC protocols – a resonance protocol we term Logical Qubit Resonance (LQR) and an adiabatic protocol termed stimulated Raman adiabatic passage (STIRAP) [68], which has been developed and exploited extensively in atomic systems [68, 69]. We show that for a given tunnel coupling, almost all the the maximum achievable fidelities are quantitatively similar, and they follow a simple scaling law. The limits on fidelity arise from experimental limits on the relevant parameters that prevent full optimization. Using realistic estimates of these limitations, we find that the highest-fidelity operations should be achieved in a hybrid qubit using a STIRAP gating protocol.

4.3 Single-qubit rotations

First we review the qubits and the methods for performing quantum operations that we will study in this chapter. We consider *logical* qubits [28] formed from multiple electrons in a double quantum dot, the singlet-triplet (ST) qubit [20, 4] with two electrons and the hybrid qubit [18], introduced in Chapter 2, with three electrons. Other schemes involving three or more quantum dots [21] are not considered here. There are some disadvantages in using two instead of one quantum dot, in terms of device complexity. However, we will demonstrate that the internal degrees of freedom provided by such logical qubits can also bring important benefits, because they allow us to optimize qubit performance.

We make use of two tunable parameters in these devices, both of which can be controlled experimentally by varying the voltages on the top-gates. These control knobs, shown in

Fig. 4.1, are the detuning ϵ, and the tunnel coupling g between the dots. Typically, $\epsilon = 0$ is defined as the degeneracy point between two charge occupation states. For the ST qubit, for example, $\epsilon = 0$ refers to the degeneracy point between the $(1,1)$ and $(0,2)$ states of the double dot, where a state (n,m) has n electrons in the left dot and m electrons in the right dot. The tunnel coupling g is tuned by changing the height of the tunnel barrier between dots. We also assume that there is a magnetic field difference ΔB between the two quantum dots. This field difference arises from naturally occurring nuclear magnetic moments, and can also be engineered by polarizing the nuclei [71, 72], or by fabricating external micromagnets [52] or striplines [19].

Singlet-triplet (ST) qubit

We first consider the ST qubit with two electrons in a double quantum dot. In the far-detuned (large, negative ϵ) regime, the ground state charge configuration is $(1,1)$. The low-lying eigenstates $|\uparrow,\downarrow\rangle$ and $|\downarrow,\uparrow\rangle$, which have energy splitting ΔE_B because of the magnetic field difference between the dots ΔB, define the ST logical qubit, as shown in Fig. 4.1. This energy splitting causes the relative phase between the qubit states to increase, which, by definition [2], is a z-rotation on the Bloch sphere. These rotations are subject to "slow" dephasing with rate γ_{ST}, which is ~ 2.5 MHz in natural silicon [59].

Hybrid qubit

The quantum dot hybrid qubit, introduced in Chapter 2, has three electrons in a double quantum dot [18]. In the far-detuned regime, the ground state charge configuration is $(2,1)$. We define the qubit states to be in the $S = 1/2$, $S_z = -1/2$ subspace, similar to [21]. We ignore the other low-lying energy levels with different spin quantum numbers because they can be reached only by processes which are non-spin-conserving. The logical qubit states are given by Eqs. 2.1 and 2.2 of Chapter 2. The energy splitting between the qubit states, ΔE_{01}, is dominated by the singlet-triplet energy splitting of the two-electron dot. As for ST qubits, this splitting causes z-rotations; however, ΔE_{01} is typically 0.1 meV [33], significantly larger than $\Delta E_B \sim 1-10$ neV [59, 62] for typical ST qubits, and the rotations are correspondingly faster. The "slow" dephasing rate for the hybrid qubit γ_{hy}, is determined by the dephasing

of the singlet and triplet states in the two-electron dot, and it has been calculated in [15] to be 1-10 MHz in Si/SiGe quantum dot qubits..

Exchange interaction

In both ST and hybrid qubits, when the absolute value of detuning $|\epsilon|$ is small, the qubit states are strongly coupled with an excited state with a different charge configuration (the $(0,2)$ state $|S_{02}\rangle$ for the ST qubit and the $(1,2)$ state $|E\rangle \equiv |\downarrow\rangle|S\rangle$ for hybrid qubit; see Fig. 4.1). This coupling gives rise to the exchange interaction, characterized by an energy J. In the presence of the exchange interaction, there are quantum oscillations between the qubit states, which represents an x-rotation on the Bloch sphere [2]. Because the exchange interaction brings the qubit into a transient superposition of different charge configurations, x-rotations are strongly affected by environmental charge fluctuations, leading to a "fast" dephasing rate Γ for both types of qubits, as shown schematically in Fig. 4.1(c).

4.4 Model

The dynamical evolution of the logical qubit density matrix ρ is governed by the master equation [73] which we made use of in Chapter 3 (Eq. 3.5). We repeat the master equation here:

$$\frac{d\rho}{dt} = -\frac{i}{\hbar}[H,\rho] - D, \tag{4.1}$$

where H is the Hamiltonian describing coherent evolution, and D is a phenomenological term that describes the fast and slow dephasing processes under the assumption of Markovian dynamics, as appropriate for the double quantum dot system [61].

The basis states of each of the Hamiltonians for the ST and hybrid qubits are the logical qubit states, as well as an excited charge state, to which each of the basis states is coupled. The basis states for the ST qubit are $\{|a\rangle \equiv |\uparrow,\downarrow\rangle, |b\rangle \equiv |\downarrow,\uparrow\rangle, |e\rangle \equiv |S_{02}\rangle\}$, and for the

hybrid qubit $\{|0\rangle_L, |1\rangle_L, |E\rangle\}$. The Hamiltonians are

$$H_{\rm ST} = \begin{pmatrix} -\Delta E_B/2 & 0 & g \\ 0 & \Delta E_B/2 & -g \\ g & -g & -\epsilon \end{pmatrix}, \tag{4.2}$$

$$H_{\rm hy} = \begin{pmatrix} -\Delta E_{01}/2 & 0 & g_1 \\ 0 & \Delta E_{01}/2 & -g_2 \\ g_1 & -g_2 & -\epsilon \end{pmatrix}. \tag{4.3}$$

The dephasing terms are given by

$$D_{\rm ST} = \begin{pmatrix} \frac{\gamma_{\rm ST}}{2}(\rho_{aa}-\rho_{bb}) & \frac{\gamma_{\rm ST}}{2}(\rho_{ab}-\rho_{ba}) & \Gamma\rho_{ae} \\ \frac{\gamma_{\rm ST}}{2}(\rho_{ba}-\rho_{ab}) & \frac{\gamma_{\rm ST}}{2}(\rho_{bb}-\rho_{aa}) & \Gamma\rho_{be} \\ \Gamma\rho_{ea} & \Gamma\rho_{eb} & 0 \end{pmatrix}, \tag{4.4}$$

$$D_{\rm hy} = \begin{pmatrix} 0 & \gamma_{\rm hy}\rho_{01} & \Gamma\rho_{0E} \\ \gamma_{\rm hy}\rho_{10} & 0 & \Gamma\rho_{1E} \\ \Gamma\rho_{E0} & \Gamma\rho_{E1} & 0 \end{pmatrix}. \tag{4.5}$$

Our numerical results were obtained by solving for the dynamical evolution of the density matrix (Eq. 4.1) in the interaction picture [74] with the rotating wave approximation [70]. (See Appendix C for details.)

4.5 Gating protocols for x-rotations

DC pulsed gates

As described in the previous sections, z-rotations are implemented in the limit $\Delta E \gg J$ and x-rotations are implemented in the opposite limit, $J \gg \Delta E$. In experiments, it is typical to keep the tunnel coupling fixed at $g = g_0$, and move between these limits by changing the detuning ϵ, as indicated in Fig. 4.1. In the pulsed gating protocol, the detuning should be switched instantaneously (non-adiabatically). The protocol is DC in the sense that the detuning changes only during switching events.

The protocols and considerations for pulsed gating differ slightly for ST and hybrid qubits. For ST qubits, the switching protocol is straightforward in principle. In practice, however, ΔE and J cannot be turned off completely. Hence, the rotation axis never points precisely along x or z. For the ST qubit, simple procedures can be adopted to correct for this problem. When $J \gtrsim \Delta E_B$, a three-step procedure given by Hanson and Burkard (HB) [75] yields exact x-rotations in the absence of dephasing. Such a procedure involves pulsing to the region of detuning which allows for x-rotations, then to the far-detuned regime for a z-rotation, followed by another x-rotation, with the corresponding detuning regions shown schematically in Fig. 4.1(a). When $J \gg \Delta E_B$, however, a simpler one-step pulse (to the detuning region for an x-rotation) [4, 59] suffices because the infidelity arising from the tilt of the rotation axis from the x-axis is smaller than that arising from the combination of fast and slow gates in the HB sequence. Which of the two procedures yields higher fidelity gates depends on precise system parameters, as is discussed below.

For the hybrid qubit, the energy splitting of the qubit states is much larger than that for the ST qubit, $\Delta E_{01} \gg \Delta E_B$, and it is also much larger than the tunnel couplings, $\Delta E_{01} \gg g$. As a result, the energy-versus-detuning diagram has two distinct anticrossings, as indicated in Fig. 4.1(b). The DC pulse-gating sequence that generates a rotation about an arbitrary axis in the x-z plane of the Bloch sphere by an arbitrary rotation angle has five steps, [22], and contains intervals at both the $|0\rangle - |E\rangle$ and $|1\rangle - |E\rangle$ anticrossings shown by the dotted lines in Fig. 4.1(b). This was been explained in detail in Chapter 3.

Logical qubit resonance (LQR)

Electron spin resonance (ESR) provides a robust AC method for generating x-rotations of individual electron spins [67]. In conventional ESR, a large DC magnetic field is applied in the z directions. An AC magnetic field is applied in the x direction at the resonant frequency $\omega = \Delta E/\hbar$, where ΔE is the Zeeman energy splitting, inducing transitions between states with different S_z. In the analogous LQR scheme, x-rotations are generated by modulating the tunnel coupling g at the resonant frequency $\Delta E/\hbar$. The speed of the x-rotation is determined by the AC component of the exchange coupling J_{AC}; the tunnel

coupling oscillates with an amplitude of g_0 on top of a DC offset of g_0. (See Fig. 4.1(e) and Appendix C.)

There are two complications to the analogy between LQR and conventional ESR, neither of which has a strong effect on the fidelity of the rotation. First, the effective coupling in the LQR protocol is a second order coupling as depicted in Fig. 4.1(e), rather than a direct coupling as in ESR. The resonant frequency thus is half of the Larmor frequency (see Appendix C). Second, while the magnitude of the exchange interaction can be modulated at high frequency, its sign cannot, so it is necessary here to implement the AC field using the positive-definite AC signal shown in Fig. 4.1, which contains an average DC component. As a result, the AC field points slightly away from the x-axis, in the x-z plane. A high fidelity x-rotation can still be achieved under these conditions, in the limits $g_0 \ll \sqrt{\Delta E|\epsilon|}$ and $g_0 \ll |\epsilon|$, as easily verified in the rotating wave approximation (see Appendix C).

Stimulated Raman adiabatic passage (STIRAP)

The STIRAP protocol [68] generates x-rotations on the Bloch sphere by causing transitions between the qubit states $|a\rangle$ and $|b\rangle$, via a third, the excited charge state $|e\rangle$. The tunneling processes $|a\rangle \leftrightarrow |e\rangle$ and $|b\rangle \leftrightarrow |e\rangle$ are controlled independently by applying modulated pulses that change the tunnel coupling g at the respective resonant frequencies $\omega_{ae} = \Delta E_{ae}/\hbar$ and $\omega_{be} = \Delta E_{be}/\hbar$. The value of tunnel coupling is positive-definite, and the amplitude of the pulses is $2g_0$, where g_0 is the average DC offset. Somewhat counter-intuitively, when the overlapping pulses are implemented sequentially and adiabatically, as shown in Fig. 4.1(d), the result is a smooth rotation between $|a\rangle$ and $|b\rangle$ that never actually populates the excited state $|e\rangle$, and therefore never encounters the fast dephasing effect described by Γ. The adiabatic limit corresponds to an infinite gate time however, and is not experimentally feasible. Finite (but realistic) gate times lead to a nonzero occupation of the excited state, which is susceptible to dephasing. Therefore, there is an optimum protocol speed that optimizes the overall fidelity of the gate.

4.6 Optimizing the fidelity

For all three x-rotation protocols considered here, the optimum gate fidelity is determined by a competition between fast and slow decoherence processes. Implementing the rotations too quickly causes excessive population of the excited charge state $|e\rangle$, which suffers from fast dephasing, with rate Γ. Slow rotations suffer from intrinsic dephasing of the logical qubit, with the slow rate γ. The optimal rate for implementing rotations lies somewhere between these two limits. Here, we determine the optimal gate parameters for maximizing the fidelity using a master equation approach that incorporates both the fast and slow dephasing rates. The optimal gate parameters are determined by maximizing the fidelity.

We calculate the relevant fidelities by solving a master equation that specifies the time evolution of the density matrix ρ that specifies the quantum system. The master equation [73], Eq. (4.1), incorporates both coherent evolution and dephasing. The coherent evolution is governed by the three-state Hamiltonian, H, in which the two logical qubit states, $|a\rangle$ and $|b\rangle$, are each coupled to an excited state, $|e\rangle$, and the three x-rotation protocols are implemented via the time dependence of the detuning and tunnel coupling parameters, $\epsilon(t)$ and $g(t)$. Dephasing is incorporated using a phenomenological term D that assumes Markovian dephasing [78], as is appropriate for our double dot system [61]. (See Appendix C for more details.)

To characterize the fidelity for a π rotation about the x-axis of the Bloch sphere, we assume that the system is in state $|a\rangle$ at time $t = 0$, so that the initial probability of finding the system in state $|a\rangle$, $\rho_{aa}(0)$, is 1. A perfect π rotation implemented in a time τ results in the system being rotated to state $|b\rangle$, in which case, the probability of observing state $|b\rangle$, $\rho_{bb}(\tau) = 1$. Therefore, we take as our fidelity measure the calculated value of $\rho_{bb}(\tau)$ from the master equation, Eq. (4.1) (see Appendix C). This measure is identical to the distance metric between two density matrices given in [79] and is detailed in the Appendix C. For the DC pulsed gating protocol, we investigate the one- [4, 59] and three-step [75] gating procedures for the ST qubit, and the five-step procedure [22] for the hybrid qubit. For the AC protocols, we solve Eq. (4.1) in the interaction picture [74] using the rotating wave

approximation [70].

The different rotation protocols incorporate several tunable parameters, including ϵ, g, and for STIRAP, the shapes of the pulses. The optimization procedures for LQR for both the ST and hybrid qubits, and DC pulsed gating for the ST qubit are all similar. For each value of g, the optimum value of ϵ that maximizes the fidelity can be determined numerically from Eq. 4.1. A typical result is shown in the inset of Fig. 4.2. For small $|\epsilon|^{-1}$, the fidelity is limited by the slow dephasing rate γ, while for large $|\epsilon|^{-1}$, the fidelity is limited by the fast dephasing rate Γ. The optimum detuning and the maximum fidelity are easily determined numerically. Analytic estimates described in the Appendix C agree well with the numerical results, as shown in Figs. 4.2 and 4.3. The analytic estimates for LQR gating yield

$$\left|\epsilon^{\rm opt}_{\rm ST,LQR}\right| \simeq g_0\sqrt{\Gamma/\gamma_{\rm ST}}, \tag{4.6}$$

$$\left|\epsilon^{\rm opt}_{\rm hy,LQR}\right| \simeq g_0\sqrt{2\Gamma/\gamma_{\rm hy}}, \tag{4.7}$$

with optimal fidelities in the limit of small $(\Gamma\gamma)^{1/2}/g_0$ of

$$f^{\rm opt}_{\rm ST,LQR} \simeq 1-2\pi\hbar\sqrt{\Gamma\gamma_{\rm ST}}/g_0 \simeq \exp\left(-2\pi\hbar\sqrt{\Gamma\gamma_{\rm ST}}/g_0\right), \tag{4.8}$$

$$f^{\rm opt}_{\rm hy,LQR} \simeq 1-2\pi\hbar\sqrt{\Gamma\gamma_{\rm hy}/2}/g_0 \simeq \exp\left(-2\pi\hbar\sqrt{\Gamma\gamma_{\rm hy}/2}/g_0\right), \tag{4.9}$$

where the exponential expression captures the expected asymptotic form of f for small g_0.

The optimal detuning of DC pulsed gating of the ST qubit, in the limit of zero energy splitting $\Delta E_B \to 0$, is

$$\lim_{\Delta E_B\to 0}\left|\epsilon^{\rm opt}_{\rm ST,DC}\right| \simeq 2g_0\sqrt{\Gamma/\gamma_{\rm ST}}, \tag{4.10}$$

with optimal fidelity in the limit $\sqrt{\Gamma\gamma_{ST}}/g_0 \ll 1$ of

$$\lim_{\Delta E_B\to 0} f^{\rm opt}_{\rm ST,DC} \simeq 1-\frac{\pi\hbar\sqrt{\Gamma\gamma_{\rm ST}}}{g_0} \simeq \exp\left(-\frac{\pi\hbar\sqrt{\Gamma\gamma_{\rm ST}}}{g_0}\right). \tag{4.11}$$

The exponential forms in Eqs. 4.8, 4.9, and 4.11 agree well with the numerical data for the entire range of $\hbar(\Gamma\gamma)^{1/2}/g_0$, as shown in Figs. 4.2 and 4.3.

For the STIRAP gating protocols for both the ST and hybrid qubits), the gate speed is determined by shaping of the pulses (see Fig. 4.1(d)) and not by the detuning parameter.

For each value of tunnel coupling g, pulse shape parameters $t_{\rm width}$ and $t_{\rm delay}$ are optimized for maximum fidelity. There are no simple analytical methods for treating the STIRAP problem. However, quite remarkably, the optimal fidelities obtained from numerical optimization of STIRAP appear to be identical to those for LQR, as we demonstrate in the Appendix C.

The results of the numerical optimization procedures for LQR and for STIRAP are shown in Fig. 4.2, along with the corresponding LQR analytical forms. The speeds of the various gates are indicated by the calibration bars at the top of the figure. Here, we have used the values $\gamma_{\rm ST} = 0.2$ MHz, $\gamma_{\rm hy} = 1$ MHz, assuming the host material to be isotopically purified silicon. The rates $\gamma_{\rm ST}$ and $\gamma_{\rm hy}$ are the quadrature sums of the dephasing rates from dominant noise sources in semiconductor materials, such as nuclear hyperfine coupling [62], electron-phonon coupling [15, 48] and charge noise [15, 76], the latter of which is more important for hybrid qubits [15]. In our calculations, we also used $\Gamma = 1$ GHz, based on experimental measurements of charge qubit dephasing times. [56, 50, 23].

We now discuss DC pulsed gating of the hybrid qubit, which has different optimization properties than the other gating schemes. Here, the pulse gating protocol prescribes the detuning at each point of the five-step procedure [22], and the excited charge state is fully populated, rather than virtually populated, by design. The only tunable parameter is the tunnel coupling g. The fidelity is always optimized by implementing the gate as fast as possible, by maximizing g. For this one protocol, there is no balance between slow and fast dephasing, and the optimization is trivial.

The optimal fidelities as a function of tunnel coupling g for DC pulsed gating of both ST and hybrid qubits are shown in Fig. 4.3. The main plot shows the optimal fidelities versus tunnel coupling for DC pulsed gating of the ST qubit at two interdot magnetic field differences ΔB, for a one-step pulse sequence [4, 59]. At small g, the fidelity is poor because the exchange energy J is smaller than the qubit energy splitting ΔE_B, and the rotation axis is tilted away from the x-axis. The fidelity increases as g is increased. The three-step HB sequence [75] that would yield an exact x-rotation improves the fidelity slightly at small

tunnel coupling but not at large g. Results for the HB sequence are plotted in detail in the Appendix C. At large tunnel coupling, where $J \gg \Delta E_B$, the one-step DC pulse tends to its optimal limit (Eq. 4.11) shown by the green line. In this limit, DC pulsed gating is superior to LQR and STIRAP, whose optimal fidelity is shown by the black line. The optimal DC pulsed gating fidelity for the hybrid qubit is plotted in the inset as teal triangles, and compared with the analytical LQR fidelity, shown as the blue line. DC pulsed gating of the hybrid qubit has inferior fidelity because it must be performed by pulsing to the anticrossings, where the dephasing effects of charge noise are large.

4.7 Discussion

We have characterized the optimal fidelities of several common quantum dot qubit gates. The fidelity of gates that perform z-rotations on the Bloch sphere that change the relative phase of the qubit states is determined by fluctuations in ΔE, the energy splitting between the two qubit states. The fidelity of the z-rotations can be improved by either increasing the gate speed, $\Delta E/h$, or suppressing the dephasing rate, γ. For ST qubits, ΔE corresponds to the Zeeman splitting, and it can be enhanced by polarizing the nuclei [71, 72], or by fabricating external micromagnets [52]. For hybrid qubits, ΔE corresponds to the ST energy splitting inside the two-electron dot; it is naturally large ($\sim 0.1-1$ meV), and it can be modified electrostatically [33]. Since the noise spectrum of the nuclear spins is dominated by low frequencies [80], the fidelity of z-rotations may be improved in ST qubits by applying pulse sequences similar to spin echos [27]. For hybrid qubits in Si, the noise spectrum of the optical phonons is dominated by higher frequencies [15] (the same is often true for charge fluctuations [17]), so that pulse sequences are probably less effective. In principle, the fidelity of the z-rotations can always be improved by increasing the sophistication of the pulse sequences; however in practice, they are constrained by dephasing that occurs during the x-rotations in the sequence.

We also consider x-rotations (transitions between the qubit states), of three distinct types: DC pulsed gates, and AC gates based on logical qubit resonance (LQR) and stim-

ulated Raman adiabatic passage (STIRAP) protocols. Perhaps surprisingly, for a given qubit type, the AC methods appear to attain the same fidelity, given by Eqs. 4.8 and 4.9. For ST qubits, the fidelity of DC pulsed-gating follows a similar scaling law (Eq. 4.11), while DC pulsed-gating for hybrid qubits has lower fidelity because the detuning cannot be optimized; it is fixed by the protocol itself.

The maximum achievable fidelity in experiments depends on whether the optimum parameter values can be achieved in a given gating scheme. Some important experimental considerations are: (i) DC gates should satisfy the "sudden" approximation. Typical fast pulses in quantum dot systems [23] should satisfy the condition on the rise time $t_{\rm rise}$ of the pulses, $\hbar/t_{\rm rise} \gg g_0$. (ii) DC pulsed gates for ST qubits and LQR are both optimized by choosing the detuning parameter given in Eqs. (4.6, 4.7). Since $|\epsilon|$ is bounded by a charging energy of ~ 1 meV in typical devices, this leads to an upper bound of $g_0 \ll 24$ GHz for a ST qubit, or 38 GHz for a Si hybrid qubit. These bounds give rise to an upper limit of 99.8% on the fidelity of DC pulsed gating in the (unrealistic) limit of zero interdot magnetic field difference ($\Delta E_B \to 0$), and to an upper limit of 99.6% on the fidelity of LQR gating. (iii) For the AC protocols, LQR and STIRAP, the x-rotation should be much slower than the z-rotation to avoid gating errors, as consistent with the rotating wave approximation, $g_0 \ll \sqrt{\Delta E|\epsilon|}$ and $g_0 \ll |\epsilon|$. For a GaAs ST qubit with $\Delta B = 10$ mT, this gives a bound of $g_0 \ll 0.4$ GHz, corresponding to an upper limit on the optimal fidelity of 80.1%, while for a hybrid qubit with $\Delta E_{01} = 0.5$ meV, the bound is $g_0 \ll 760$ GHz, corresponding to an upper limit on the optimal fidelity of 99.99%. We note that at present, classical electronics components limit the frequency of the electrical signal that are used to control tunnel coupling to ~ 40 GHz. This limit corresponds to an upper bound on the optimal fidelity of STIRAP for the hybrid qubit at 99.8%. Based on these criteria, the highest quality x-rotations should be possible in a hybrid qubit, using STIRAP gates. For Si devices, this is the preferable gating method, although ST qubits, and DC or LQR gating methods also provide high fidelity. For GaAs devices, in which the "slow" decoherence rate for a hybrid qubit is ~ 1 GHz [15], the highest quality x-rotations are achieved in DC pulsed gates.

It is worth noting that, unlike z-rotations, the x-rotations probably cannot be improved by implementing pulse sequences. This is because any pulse sequence would involve a mixture of fast and slow x-rotations, which would necessarily violate the optimization requirement.

Finally, we note that the highest overall fidelity that can be achieved in a given gating scheme should be defined as the smaller of the fidelities of the x and z-rotations. When pulse sequences are used to improve the fidelity of the z-rotations, the overall fidelity is constrained by g_0, as described above. In general, the fidelity is maximized when g_0 is very large. When one of these quantities is limiting, however, there is no significant advantage in increasing the other quantity.

4.8 Summary

We have analyzed the optimal fidelities for single-qubit gates for the ST and hybrid qubits using three different protocols (a DC pulse-gated scheme and two AC schemes) and showed that they can be evaluated on an equal footing. Using experimentally realistic constraints, we find that the maximum fidelity is 99.8% for both qubits. This fidelity is achievable for hybrid qubits using a STIRAP protocol, and for ST qubits using DC pulsed gating. However, the latter comes at the cost of an unreasonably slow z-rotation gate. These high fidelities are promising for using these qubits to build a scalable quantum processor.

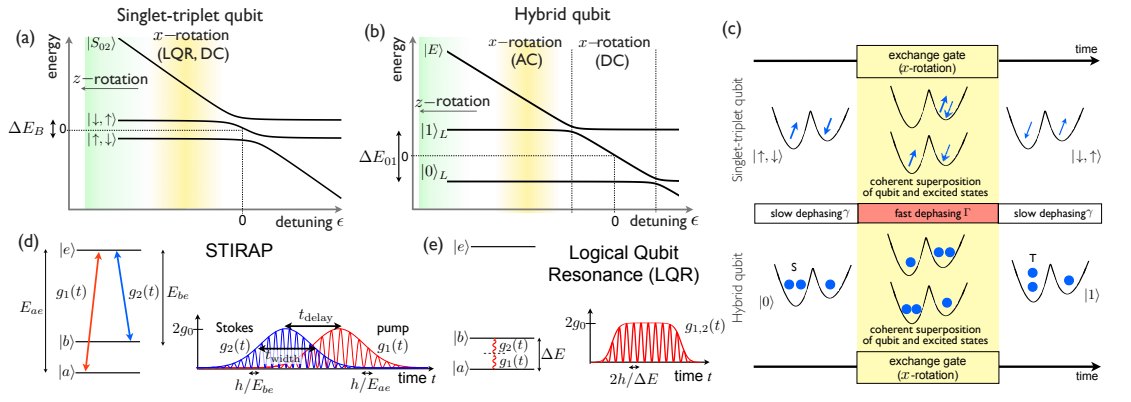

Figure 4.1: Schematic of the physics underlying the x- and z-rotations of the singlet-triplet (ST) and hybrid qubits. Transitions between qubit states yield x-rotations, while relative phase changes between the qubit states yield z-rotations. Panels (a) and (b) show plots of the energy versus detuning of the relevant energy levels for the ST and hybrid qubits. The energy splitting of the qubit states that drives the z-rotations is typically much smaller for the ST qubit than the hybrid qubit: $\Delta E_B \ll \Delta E_{01}$. In both cases, the qubit states are coupled to an excited charge state via the tunnel-coupling g. The resulting exchange interaction J is large when the absolute value of detuning $|\epsilon|$ is small. (a) Singlet-triplet qubit. For DC and LQR gate protocols, the optimal value of the detuning for x-rotations is close (but not too close) to $\epsilon = 0$ (yellow shaded region). STIRAP is performed on the right-hand-side of the detuning axis, where the exchange interaction J is small. (b) Hybrid qubit. For LQR, the optimal value of the detuning is again close (but not too close) to the energy level anticrossing, and STIRAP is performed on the right-hand-side of the detuning axis. However, for typical experiments, the energy splitting is much larger than the tunnel coupling, $\Delta E_{01} \gg g$, leading to two distinct anticrossings. For this arrangement, DC gating for an x-rotation requires a five-step sequence [22] in which some of the pulses are at anticrossings. (c) The excited state that mediates the exchange interaction has a substantially different charge configuration than the qubit states, so increasing the strength of the exchange interaction increases the gate speed but also increases the dephasing rate. There is therefore a balance between the gate speed and dephasing rate for which exchange gate fidelity is optimized. (d) STIRAP (stimulated Raman rapid adiabatic passage [70]) is implemented using shaped RF pulses that oscillate the tunnel coupling at the respective resonant frequencies, h/E_{ae} and h/E_{be}, modulated by overlapping Gaussian envelopes known as Stokes and pump pulses (see Appendix C). Here, the gate fidelity is optimized by choosing an appropriate combination of $t_{\rm width}$ and $t_{\rm delay}$, describing the shape of the pulse envelopes. (e) Logical Qubit Resonance is performed by oscillating the tunnel couplings at a frequency equal to half the Larmor frequency, $2h/\Delta E$. Here, the gate fidelity is optimized by choosing an appropriate value of the detuning, for a given tunnel coupling.

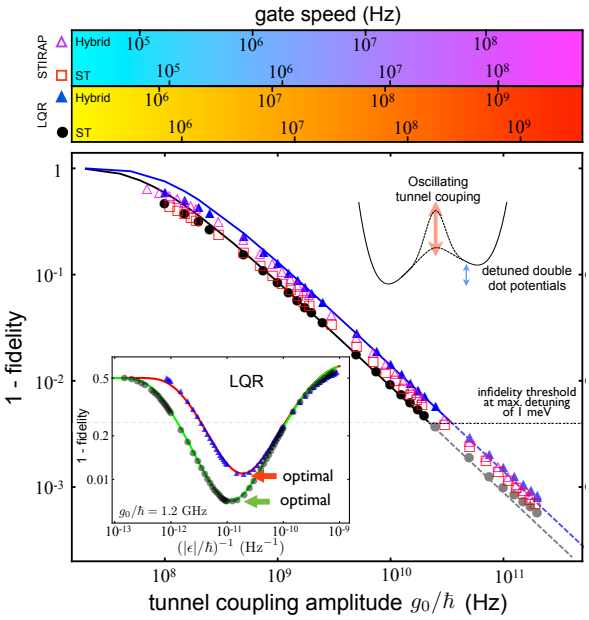

Figure 4.2: Comparison of the optimal fidelities of the LQR and STIRAP gating schemes for ST and hybrid qubits using the parameter values $\Gamma = 1$ GHz, $\gamma_{\rm ST} = 0.2$ MHz [76, 48, 62] and $\gamma_{\rm hy} = 1$ MHz [15, 62]. Inset: the minimum infidelity (1 - fidelity), as a function of detuning at a fixed tunnel coupling, gives the optimal detuning value for LQR. Numerical simulations for the ST (gray filled circles) and hybrid (blue filled triangles) qubits are in excellent agreement with analytical estimates for the respective qubits (Eqs. 4.6 and 4.7, shown as green and red curves respectively). Main panel: a plot of the infidelity for optimized gates versus the tunnel coupling amplitude $g_0/\hbar$. For both LQR and STIRAP, the gate speed (top panels) increases with tunnel coupling. In the main plot, the numerically optimized LQR and STIRAP fidelities for the ST qubit (black filled circles and red empty squares respectively) and for the hybrid qubit (blue filled triangles and magenta empty triangles respectively) are in excellent agreement with the analytical expression for the LQR fidelity, given by Eqs. 4.8 and 4.9. The dashed horizontal line represents the minimum infidelity when the detuning is constrained to be less than 1 meV, the charging energy in typical devices [77]. The fidelity for STIRAP, optimized for pulse parameters $t_{\rm delay}$ and $t_{\rm width}$ at each value of the tunnel coupling (see (see Appendix C)), is in excellent agreement with the scaling law for the fidelity of LQR.

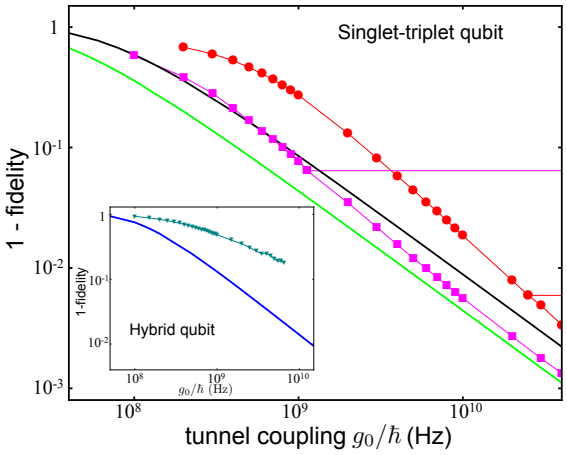

Figure 4.3: Main panel: optimal fidelities versus tunnel coupling g_0 for a DC pulse-gated x-rotation of the ST qubit for interdot magnetic field differences of $\Delta B = 0.03$ mT (magenta squares) and $\Delta B = 0.30$ mT (red circles), for a one step pulse sequence [4, 59]. At small g_0, the exchange energy J is smaller than the qubit energy splitting ΔE_B and the rotation axis is tilted away from the x-axis, reducing the fidelity. At large tunnel coupling, $J \gg \Delta E_B$, and the one-step DC pulse sequence tends to its optimal limit (Eq. 4.11) shown by the green line. In this limit, DC pulsed gating is superior to LQR and STIRAP whose optimal fidelity is shown by the black line. A three-step pulse-gating sequence [75] to implement an x-rotation improves the fidelity slightly at small g_0, but plateaus at large g_0 denoted by the horizontal lines, as discussed in the Appendix C. Inset: Gate fidelities versus tunnel coupling for the hybrid qubit. The optimal DC pulsed gating fidelity for the hybrid qubit is plotted as teal triangles, and compared with that for LQR and STIRAP as the blue solid line. Because pulsed gating for the hybrid qubit is implemented at the anticrossings between different charge states, dephasing effects are large and the fidelity of DC pulsed gating of the hybrid qubit is poorer than that for the other protocols. Assuming an experimental limitation on the maximum detuning of $\sim$ 1 meV, the maximum fidelity achievable for both qubits is ~ 0.998 using pulsed gating for the ST qubit, and using STIRAP for the hybrid qubit.

Chapter 5

Decoherence I: Coherent oscillations of a silicon charge qubit and enhanced dephasing time T_2

5.1 Introduction

Coherent manipulation of qubits is a fundamental challenge. Fast, coherent control of charge qubits has been demonstrated in both superconducting circuits[65, 81] and semiconductor quantum dots[50, 56]. Because charge states have relatively fast decoherence[56, 16, 17], it is essential to find ways to maximize the coherence of charge manipulation in semiconductor quantum dots. This is imperative for DC pulsed gating of the hybrid qubit, which utilizes the charge degree of freedom in order to perform single-qubit rotation about an arbitrary axis, as described in Chapter 3. By exploiting the discrete electronic states of the quantum dot qubit, we demonstrate that longer coherence times and higher figures of merit can be achieved in a three electron double dot qubit. We achieve a record figure of merit (number of oscillations per coherence time) for quantum dot charge qubits of 37. This result is important for both spin qubits as well as charge qubits. Manipulating spin qubits quickly is done by mixing spin with charge degrees of freedom (either through spin-orbit coupling[82]

or the exchange interaction[1, 5, 83, 21, 18, 22]), so charge coherence determines the ultimate fidelity of spin qubits.

Decoherence of a qubit arises from its interaction with the local environment. In a semiconducting qubit, some interactions are intrinsic to the material in question, such as charge coupling to phonons [15]. Other sources of decoherence are extrinsic, such as charge noise [16, 17], which denotes the effects of fluctuating electric fields arising from sample defects and from the electronics and transmission lines used to control the qubit. Fortunately, the decohering effects of both intrinsic and extrinsic sources depend on the properties of the charge qubit itself.

5.2 Coherent charge oscillations

We demonstrate coherent quantum oscillations between the (2,1) and (1,2) charge states of a qubit formed in a Si/SiGe double quantum dot. We observe coherent oscillations of the qubit in four different regimes, each of which has a different charge coherence time, with the longest and shortest differing by more than a factor of 20. We show that the variation in coherence properties can be understood quantitatively in terms of the internal properties of the qubit, including the tunnel coupling between the left and the right quantum dots, and the energy level structure within the right quantum dot itself. The longest coherence time we measure, $T_2^* = 3.7$ ns, is not observed at the typical operating point — the point where the (2,1) and (1,2) states have equal energy, where we find T_2^* is 2.1 ns — but rather occurs when the (1,2) state is the ground state. We explain this behavior based on Landau-Zener-Stuckleberg interference[84, 85, 86, 87] between the ground and first excited states within the right quantum dot. This effect gives rise to coherent rotations about the x-axis of the Bloch sphere for the charge qubit, yielding the highest figure of merit observed for a semiconductor charge qubit. The shortest coherence time, $T_2^* = 179$ ps, is measured when the charge qubit is operated at the point that is most sensitive to charge noise in the local environment. The oscillations observed in this regime are Ramsey fringes and reflect rotations about the z-axis of the Bloch sphere. The results demonstrate control of

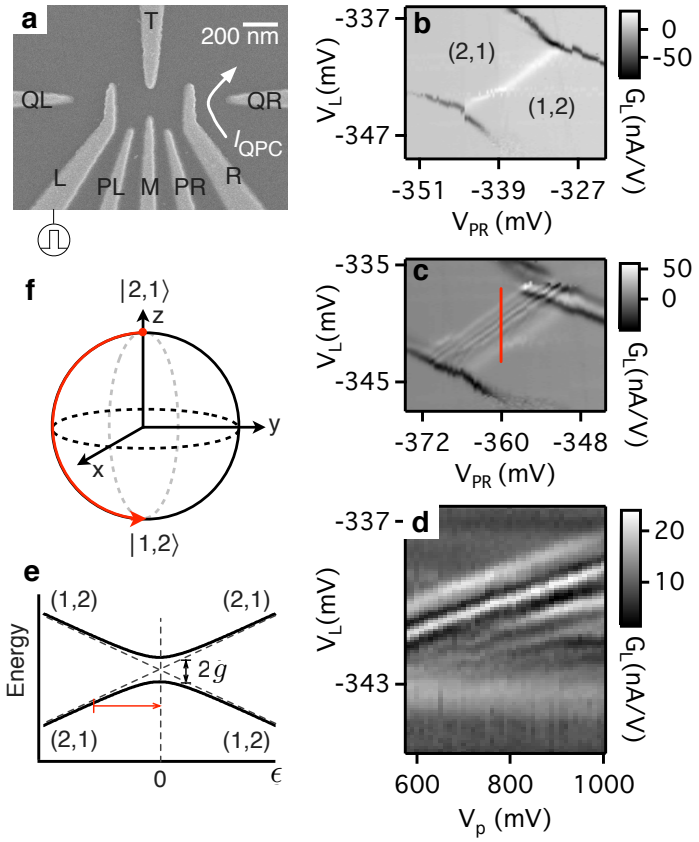

Figure 5.1: (a) SEM image of a device identical to the one used in the experiment. The charge state of the double dot was determined by measuring the current through the quantum point contact (QPC). Voltage pulses are applied to gate L. (b) Stability diagram of the double dot with effective charge occupation labeled. The transconductance $G_{\rm L} = \partial I_{\rm QPC}/\partial V_{\rm L}$ is shown as a function of the two gate voltages $V_{\rm L}$ and $V_{\rm PR}$; the lines in the diagram correspond to changes in the double dot charge occupation. The polarization line is white, and corresponds to a change in the effective electron occupation from (2,1) to (1,2). (c) Stability diagram in the presence of a pulsed voltage applied to gate L. (d) Charge resonance positions as a function of pulse amplitude. As expected for Larmor oscillations, the displacement in $V_{\rm L}$ of the peaks from the polarization line increases as the pulse amplitude $V_{\rm p}$ increases. (e) Diagram of energy levels versus detuning, showing the expected anticrossing of the (2,1) – (1,2) charge transition. The red arrow shows the effect of an applied voltage pulse with the dc detuning and pulse amplitude chosen to place the peak of the pulse at $\epsilon = 0$. (f) Bloch sphere of the charge qubit. The red arrow indicates a π-rotation about the x-axis.

a silicon charge qubit about two axes on the Bloch sphere, and they show how the internal properties of a semiconductor charge qubit can be exploited to improve its coherence and figure of merit.

A scanning electron microscope image of a device identical to the one measured in the experiment is shown in Fig. 5.1(a). The double quantum dot used here was fabricated in a Si/SiGe heterostructure as described in Refs. [88, 8]. Changes in the charge states of the left and right dots are observed through measurements of the current I_{QPC} through the nearby charge sensing quantum point contact (QPC), as shown in Fig. 5.1(a). The stability diagram in Fig. 5.1(b) shows the QPC transconductance $G_{\mathrm{L}} = \partial I_{\mathrm{QPC}}/\partial V_{\mathrm{L}}$, measured using a lock-in amplifier, as a function of the voltages on gates L and PR. Using magnetospectroscopy[33], we have determined that the white polarization line is where the effective charge state of the double dot changes between (2,1) and (1,2).

Near the charge degeneracy point, at which the energies of the (2,1) and (1,2) states are equal, the system is well-described by the Hamiltonian of a two-state system:

$$H = \begin{pmatrix} \epsilon/2 & g \\ g & -\epsilon/2 \end{pmatrix}, \tag{5.1}$$

where g is the tunnel coupling between the two states and ϵ is the detuning, the energy difference between the two states in the absence of tunnel coupling. Coherent oscillations between the two charge states can be observed when the detuning ϵ is changed abruptly. For example, just after the detuning is increased suddenly from a large negative value to $\epsilon = 0$, as shown in Fig. 5.1(e), the system Hamiltonian $H = \Delta\sigma_x$, where σ_x is the usual Pauli matrix, with the initial wavefunction being a position eigenstate. Subsequently, the system oscillates between the two position eigenstates at the Larmor angular frequency $2g/\hbar$. More generally, suddenly increasing the detuning ϵ to a larger value ϵ' induces oscillations at the angular frequency $\Omega_{\mathrm{R}} = \sqrt{\epsilon'^2 + 4g^2}/\hbar$; as one moves away from the polarization line, the oscillations increase in frequency and decrease in amplitude.

Larmor oscillations appear in the data of Fig. 5.1(c) , which shows the stability diagram in the presence of a 580 mV pulse (which after attenuation in the coax path is calibrated to

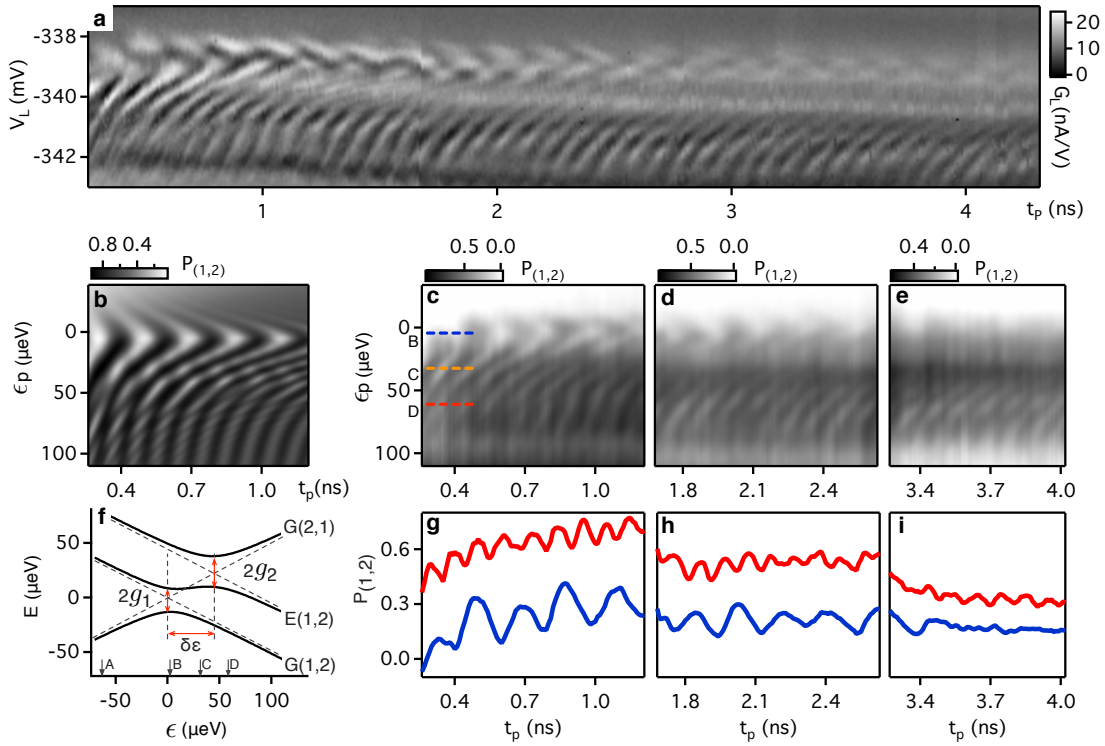

Figure 5.2: (a) Differential conductance G_{L} of the charge-sensing quantum point contact as a function of pulse duration t_{p} and gate voltage V_{L} for pulses of amplitude $V_{\mathrm{p}} = 800$ mV (5.27 mV on gate L). The signal oscillates as the duration of the pulses is increased, with a frequency that is a minimum when the pulse takes the state of the system to the polarization line (detuning $\epsilon = 0$). The coherence time T_2^* that governs the decay of the oscillations is longer at larger detunings. (b) Simulation of the Larmor oscillations as described in the main text. (c–e) Integration of the differential conductance yields the average charge state of the dot as a function of ϵ_{p}, as described in the text. The Larmor oscillation arising from the anticrossing of the (2,1) and (1,2) ground states is clearly visible at $\epsilon_{\mathrm{p}} = 0$. The data are acquired as a series of vertical sweeps, and in panels (c–e) each such sweep is offset to compensate for the increasing pulse duration with increasing t_{p}, so that the reference voltage V_{L} and thus ϵ_{p} is independent of t_{p}. The data in all three subpanels are smoothed by averaging over three diagonally adjacent pixels. (f) Energy level diagram showing two nearby anticrossings, as described in the main text. (g–i) Line cuts at two values of V_{L} indicated by the red and blue dashed lines labeled B and D in (c). The Larmor frequency is larger at larger detuning, as expected. The coherence time governing the decay of the oscillations is longer at nonzero detuning than when the detuning is zero. Because the Larmor frequency and the coherence time both increase as the detuning is increased, the number of oscillations that is observed is largest at large detuning, with 42 oscillations clearly apparent in (a).

be 3.82 mV on gate L) of duration 500 ps applied at a repetition rate of 40 MHz. A series of resonances parallel to the polarization line are clearly visible, corresponding to partial time-averaged occupation of the (1,2) charge state in the region in which the (2,1) charge state is the ground state. Fig. 5.1(d) shows a measurement of G_{L} along the red line in Fig. 5.1(c) as a function of the amplitude V_{P} of a voltage pulse of duration 375 ps. The positions of the resonances visible in Fig. 5.1(c) shift linearly with pulse amplitude, providing evidence that the oscillations result from pulsing the (2,1) charge state non-adiabatically into the vicinity of the charge-state anticrossing.

Fig. 5.2(a) shows Larmor oscillations between the (2,1) and (1,2) charge states: the transconductance G_{L} is plotted as a function of the duration of the pulse and of the voltage V_{L}, which determines the distance of the detuning from the polarization line. Oscillations of the signal are apparent out to several nanoseconds, and the oscillation frequency is faster towards the bottom of Fig. 5.2(a) , where the detuning ϵ at which the Larmor precession is occuring is largest. Surprisingly, the coherence time is longest when the oscillations are fastest, with more than 40 well-defined oscillations present in Fig. 5.2(a) .

5.3 Quantifying charge oscillation data

To characterize the oscillations quantitatively, we integrate the data presented in Fig. 5.2(a) from top to bottom to calculate the total change in dot charge, calibrated by using the fact that the total charge transferred across the polarization line is one electron, and we smooth by averaging over three adjacent pixels. The vertical axis is converted to ϵ_{p}, the detuning value at the peak of the pulse, by noting that the main, slowest oscillation corresponds to $\epsilon_{\mathrm{p}} = 0$, and by fitting the change in frequency as a function of V_{L} for small positive ϵ_{p}. Fig. 5.2(c) –e present the resulting gray-scale images; Fig. 5.2(g)–i show line cuts through the corresponding plots at the points labelled B and D, revealing clear oscillations of the average charge as a function of time. By fitting the amplitude of these oscillations to exponential decays, we extract a dephasing time T_2^* of 2.1 ± 0.4 ns near $\epsilon_{\mathrm{p}} = 0$ (label B) and, intriguingly, of 3.7 ± 0.6 ns when $\epsilon_{\mathrm{p}} = 59$ μeV (label D). This increase in coherence

time for $\epsilon > 0$ yields a T_2^* that is substantially longer than the value of ~ 0.3 ns measured by Petersson *et al.*[56] in a GaAs charge qubit far away from its charge degeneracy point. We return to a discussion of this increase below.

5.4 Ramsey experiment

We now demonstrate coherent rotations of the qubit about the z-axis of the Bloch sphere by performing a Ramsey fringe experiment[16, 89] using the procedure illustrated in Fig. 5.3(a) . First, a pulse is applied that rotates the Bloch vector around the x-axis by an angle $5\pi/2$, rotating it from being along z to along y (we use a $5\pi/2$ pulse of amplitude 400 mV and duration 300 ps instead of a $\pi/2$ pulse because of the difficulty of creating high-quality pulses as short as 60 ps). After a variable time, during which the system evolves at the base value of the detuning, a second pulse is applied that rotates the state about the x-axis on the Bloch sphere by $5\pi/2$. The charge measured at the end of this process oscillates as a function of the time between the two $5\pi/2$ pulses at a frequency $f = \sqrt{\epsilon^2 + 4g^2}/h$, where ϵ is the detuning in the absence of the pulse. Fig. 5.3(b) shows the differential conductance $G_{\rm L}$ measured through the charge sensor for a pulse amplitude of 400 mV (2.64 mV on gate L) as a function of the gate voltage $V_{\rm L}$ and τ, the time between the start of the first and second $5\pi/2$ pulses, with a repetition rate of 40 MHz. For very short τ, the $5\pi/2$ pulses overlap and one is essentially performing a Larmor oscillation experiment. At $\tau \sim 300$ ps (red dashed box in Fig. 5.3(c)) the time interval between the end of the first $5\pi/2$ pulse and the start of the second becomes nonzero, and the oscillations that are observed reflect the rotation of the Bloch vector between the two pulses. We have verified that the temporal period of the Ramsey fringes decreases if we decrease the detuning at which the Ramsey precession occurs (data not shown). To analyze these data quantitatively, we again integrate the differential conductance and normalize by noting that the total charge transferred across the polarization line is one electron (Fig. 5.3(c)). Fig. 5.3(d) shows a cut through the integrated data at the value of $V_{\rm L}$ marked by the blue arrow labeled A. After subtraction of a smooth background (smooth gray curve in Fig. 5.3(d)), the resulting oscillating curve is fit

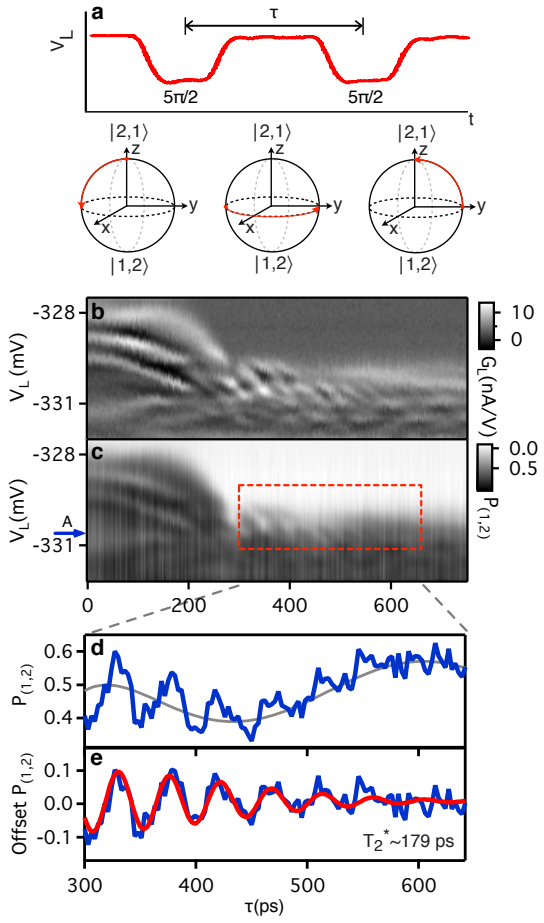

Figure 5.3: (a) Example measured pulse sequence for the Ramsey fringe experiment that demonstrates coherent control of oscillations about the z-axis of the Bloch sphere. A $5\pi/2$ pulse of duration 300 ps is applied to rotate the qubit Bloch vector around the x-axis into the $x-y$ plane. The system then evolves for a variable time τ, and a second $5\pi/2$ pulse is then applied. The oscillations observed as a function of the time between pulses reflect the rotation of the Bloch vector in the $x-y$ plane. (b) Differential conductance through the QPC as a function of the gate voltage $V_{\rm L}$ and of the pulse delay τ. The two pulses overlap for $\tau < 300$ ps; oscillations are observed for $\tau > 300$ ps, corresponding to Ramsey fringes arising from the rotation of the state about the z-axis of the Bloch sphere. (c) Integrated transconductance, normalized by noting that the total charge transferred across the polarization line is one electron. Red dashed box shows the location of the Ramsey fringes. (d) Blue: Line cut of the data in (c) at the detuning marked by the blue arrow. Gray: Smooth background that is subtracted from the line cut before fitting the data to a damped sinusoidal form. (e) Blue: data from (d) with background subtracted. Red: fit to the form $A\exp(-(t-t_0)^2/T_2^{*2})\cos(\omega t+\phi)+C$, which yields a value for the coherence time T_2^* of 179 ps.

to the product of a cosine function and a Gaussian. This procedure yields $T_2^* = 179 \pm 18$ ps, substantially longer than the value of 60 ps obtained by measuring Ramsey fringes for a GaAs charge qubit and using a similar fitting procedure [89]. Calculations following the methods of Ref. [15] show that the charge dephasing rate in GaAs from polar optical phonons is of order 1 GHz, whereas similar calculations for phonon-induced charge dephasing in Si yield values of order 0.5 MHz. Thus, in both materials, and particularly in Si, improvements may be possible through a reduction of excess charge noise.

5.5 Discussion

We now return to the increase in the coherence time T_2^* of the Larmor oscillations for $\epsilon_p > 0$. This behavior is in sharp contrast to the results that have been obtained for charge qubits in GaAs quantum dots and in superconducting charge qubits[56, 17]. Moreover, such an increase in T_2^* with increasing ϵ_p is generally unexpected, because the qubit is well protected from charge noise — that is, from environmental noise in the detuning ϵ — at the "sweet spot" corresponding to $\epsilon_p = 0$. The data of Fig. 5.2(c–e) contain an important clue to the origin of this behavior: the Larmor oscillations at larger detuning are faster than those near $\epsilon_p = 0$, yet the increase in Larmor frequency seems to saturate at about $\epsilon_p = 50$ μeV. In fact, the Larmor oscillations appear as an approximately parallel series of lines from $\epsilon_p = 50$ to 100 μeV.

The long-lived oscillations at large ϵ_p can be explained by the presence of an anticrossing between the (2,1) ground state G(2,1) and the (1,2) excited state E(1,2), as shown in Fig. 5.2(f). The effect of this second anticrossing is shown in the theoretical simulation plotted in Fig. 5.2(b) , which makes use of the following parameters (as defined in the figure): tunneling amplitude $g_1/h = 2.7$ GHz (determined directly from the Larmor oscillation period at $\epsilon = 0$), tunneling amplitude $g_2/h = 3.5$ GHz, detuning difference $\delta\epsilon = 45$ μeV, and a voltage pulse rise time of 80 ps. Dephasing is incorporated phenomenologically as described in Ref. [15]; additional details about the simulations and the choice of parameters are in Appendix D.

The second anticrossing has two effects. First, Larmor oscillations at the anticrossing between G(2,1) and E(1,2) lead to small distortions in both the measured and simulated oscillation patterns at small, positive $\epsilon_{\rm p}$; these are visible in the simulation shown in Fig. 5.2(f) and can be found in the data at the right side of Fig. 5.2(c) . More importantly, because the inverse rise time of the pulse is comparable to g_1 and g_2, for large $\epsilon_{\rm p}$ the voltage pulse takes the state G(2,1) into a superposition of G(1,2) and E(1,2) — that is, the transition through the two anticrossings is not fully abrupt. These two states G(1,2) and E(1,2) accumulate phase at different rates, leading to oscillations at the frequency $f_{GE} = 2\delta\epsilon/h$. Thus, the long-lived coherent oscillations at large $\epsilon_{\rm p}$ — the parallel lines in Fig. 5.2(c–e) the range $\epsilon_{\rm p} = 50$ to 100 μeV — arise from the interference between states G(1,2) and E(1,2).

Because the energies of states G(1,2) and E(1,2) have nearly the same dependence on ϵ at label D in Fig. 5.2(f) , these oscillations are protected from charge noise in a way that is similar but even better than the protection that occurs near label B and the energy level anticrossing at $\epsilon = 0$[18, 90]. For this reason, at point D we find a figure of merit of 37. In contrast, the Ramsey fringes of Fig. 5.3 arise from oscillations at a completely unprotected position on the energy level diagram, as can be seen at label A in Fig. 5.2(f). At this point, random fluctuations in ϵ directly change the energy gap, resulting in a short $T_2^* = 179 \pm 18$ ps. At point C in Fig. 5.2(f), in between the long coherence operating points B and D, we have extracted $T_2^* = 264 \pm 36$ ps; at this point the energy levels diverge almost as rapidly as at A. Thus, the anticrossings and internal electronic states of the two dots have a profound affect on the measured coherence times and figures of merit.

Implications for the hybrid qubit The demonstrated enhancement of charge coherence is also important for spin qubits[4, 27, 58, 59], including the hybrid qubit [18]. Spin qubits themselves have good coherence, and spins in silicon-based structures have especially long spin coherence times, because of the predominance of spin-zero nuclear isotopes and relatively weak spin-orbit coupling[9, 45, 62]. Recent experiments have demonstrated coherent quantum oscillations of singlet-triplet spin qubits in Si/SiGe[59] with substantially longer intrinsic spin T_2^* coherence times than singlet-triplet qubits in GaAs

heterostructures[4, 27, 58].

The importance of a long charge coherence time cannot be understated. Fast manipulation of spin qubits based on the exchange interaction relies on transient mixing of spin with charge. The hybrid qubit offers greater flexibility in coherent operations, through direct coupling to a different charge state, as explained in Chapter 3. Therefore, demonstrating a high figure of merit for Si/SiGe charge qubits increases the expected fidelity of spin qubit manipulation.

Chapter 6

Decoherence II: Tunable spin loading and relaxation time T_1 of a single spin

6.1 Introduction

Spin relaxation times in Si quantum dots have been measured by using time-averaged techniques [6, 91]. Readout of spin qubits requires single-shot spin measurement [92, 7], something that has not been demonstrated in gate-defined Si quantum dots. Furthermore, tunability enables control over coupling to both ground and excited states, which has the potential to enable rapid qubit initialization.

In this Chapter, we present experimental data and theoretical analysis of single-shot spin readout in a silicon quantum dot spin qubit, and we report single-shot measurement of the longitudinal spin relaxation time T_1. We further demonstrate that the rate of loading of electron spins can be tuned over an order of magnitude by using a gate voltage, that the spin state depends systematically on the loading voltage level, and that this tunability arises because electron spins can be loaded through excited orbital states of the quantum dot. The longitudinal spin relaxation time T_1 is found to be 3 s at a field of 1.85 T.

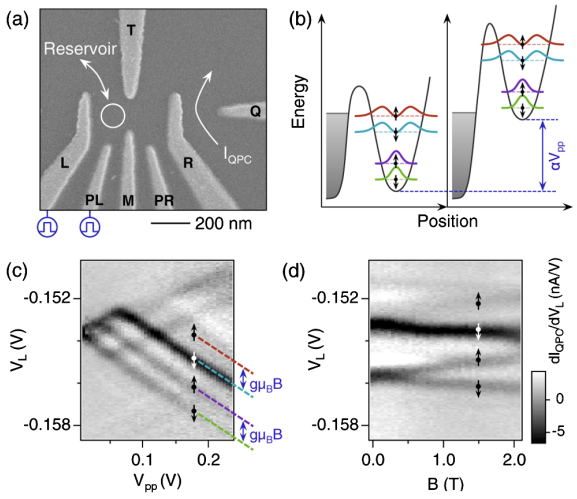

Figure 6.1: (a) Scanning electron micrograph of a device identical to that used here. The gates are tuned so that a single quantum dot exists at the location of the white circle and tunneling occurs to and from the left reservoir only. Charge sensing is performed by measuring the current I_{QPC}. (b) Voltage pulses of amplitude V_{pp}, applied to either gate L or PL, adjust the energy levels of the dot. The case shown corresponds to loading an electron during the positive phase of the pulse (left) through any of the four states $|\downarrow g\rangle, |\uparrow g\rangle, |\downarrow e\rangle$, and $|\uparrow e\rangle$ that are below the Fermi energy E_F and then unloading the electron during the negative phase of the pulse (right). (c), (d) Measurements of $dI_{\mathrm{QPC}} = dV_L$, in the presence of a pulsed voltage V_{pp} on gate L. Transitions to the three lowest eigenstates, $|\downarrow g\rangle, |\uparrow g\rangle, |\downarrow e\rangle$, are clearly visible in (c), where the magnetic field $B = 1.5$ T. The state $|\uparrow e\rangle$ is expected at the location shown by the red dashed line but is invisible due to the strong coupling of the excited state $|e\rangle$. As a function of B (and with $V_{pp} = 0.125$ V), the ground and first orbital excited states split linearly due to the Zeeman effect. (See Appendix E for details of the spectroscopy measurement and results for the electron spin g factor.)

The demonstration of single spin measurement as well as a long spin relaxation time and tunability of the loading are all favorable properties for spintronics and quantum information processing applications. Our results show that Si/SiGe quantum dots can be fabricated that are sufficiently tunable to enable single-electron manipulation and measurement and that long spin relaxation times are consistent with the orbital and/or valley excitation energies in these systems.

6.2 Single-shot spin readout

The measurements we report were performed in a dilution refrigerator with a parallel magnetic field on a gate-defined quantum dot fabricated from a Si/SiGe heterostructure, by using the methods outlined in Ref. [88]. The gate configuration is shown in Fig. 6.1(a), and the gates were tuned so that the device was in the few-electron, single-dot regime. The electron temperature was 143 ± 10 mK, measured by fitting the width of electronic transitions as the base temperature of the dilution refrigerator was raised.

As shown in Fig. 6.1(b), an electron can be loaded into one of four energy eigenstates; we denote the states, in order of increasing energy, as $|\downarrow g\rangle, |\uparrow g\rangle, |\downarrow e\rangle$, and $|\uparrow e\rangle$, where the first index refers to spin ($\downarrow$ having lower energy than $\uparrow$) and the second to the ground (g) and excited (e) orbital levels. We obtain an experimental map of the discrete energy spectrum by measuring the differential current $dI_{\mathrm{QPC}} = dV_L$ through a charge sensing quantum point contact while applying square voltage pulses to gate L. The gray-scale plots of $dI_{\mathrm{QPC}} = dV_L$ in Figs. 6.1(c) and 6.1(d) reveal dark lines corresponding to the onset of tunneling to the energy eigenstates when the transitions come into resonance with the Fermi energy E_F [93]. The measured calibration factor for gate L, $\alpha = 0.125 \pm 0.006$ eV/V, translates the positions of these lines into a spectroscopy of the dot energy levels.

In Fig. 6.1(c), the darkest line indicates the onset of transitions to the orbital excited state $|e\rangle$ of energy 311 ± 19 μeV. This relatively large energy splitting is favorable for applications in which spin coherence is desirable [9], and it is notable because the low-lying excited orbital states in Si/SiGe quantum dots have fundamental differences compared to those in GaAs [94], because of the role of valley degrees of freedom [95, 39, 96, 97, 98, 99, 100]. The Zeeman splitting of the ground and excited states is shown in Fig. 6.1(d).

6.3 Tunable spin loading

A main focus of this Chapter is to demonstrate that orbital excited states can be exploited to control both the rate of loading and the spin state of the electron loaded into the dot.

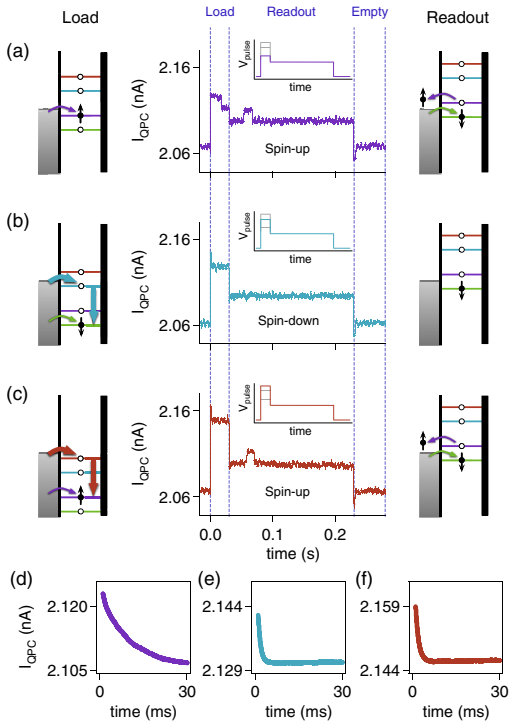

Figure 6.2: A 3-level gate voltage pulse sequence consisting of load, readout, and empty stages is applied to gate PL for single-shot spin readout. The loading rate and the probability for loading different spin states vary with the loading voltage level. (a), (b), and (c) correspond, respectively, to preferential loading of states $|\uparrow g\rangle$, $|\downarrow e\rangle$, and $|\uparrow e\rangle$ at load voltages $V_{\text{load}} = +175, +325$, and $+425$ mV. The single-shot traces in (a) and (c) are identified as spin-$\uparrow$ because of the current pulse during readout caused by a spin-$\uparrow$ tunneling off the dot and a spin-$\downarrow$ replacing it. Trace (b), which has no such pulse, is identified as spin-$\downarrow$. The schematics indicate the possible loading channels for each case. For all cases, $t_{\text{load}} = 30$ ms, $t_{\text{readout}} = 200$ ms, $V_{\text{readout}} = +75$ mV, $t_{\text{empty}} = 50$ ms, and $V_{\text{empty}} = -200$ mV. (d)–(f) Average of 500 time traces of electron loading events for the load voltages of (a)–(c), respectively. Loading at the excited orbital state [shown in both (e) and (f), with tunnel rates of 1186 ± 3 and 958 ± 2 Hz, respectively] is much faster than loading at the ground state [shown in (d), with a tunnel rate of 106.7 ± 0.2 Hz].

To measure the spin state of individual electrons, we use a 3-level pulsed-gate technique for single-shot readout pioneered in Ref. [92]. Starting with the electron unloaded, V_{PL} is rapidly changed to a load level. A downward step is visible in I_{QPC} during the load stage when an electron of either spin tunnels onto the dot. V_{PL} is then changed to the readout level. During the readout stage, a spin-$\uparrow$ electron can tunnel off the dot, and a spin-$\downarrow$ electron will tunnel on to replace it, resulting in a pulse in I_{QPC} that persists as long as the

dot is unloaded. In contrast, a spin-↓ electron will remain in the dot and no current pulse will occur during the readout phase. During the final, empty stage, the electron tunnels off the dot regardless of its spin orientation.

Three single-shot spin readout traces are shown in Figs. 6.2(a)–6.2(c). In each case, the voltage levels for the readout and empty stages are the same. As shown in the schematics, the load level is varied for preferential loading of states$|\uparrow g\rangle, |\downarrow e\rangle$, and $|\uparrow e\rangle$ in Figs. 6.2(a)–6.2(c), respectively. The data in (a) and (c) show that a spin-↑ was loaded, and the data in (b) show that a spin-↓ was loaded. (See Appendix. E for a description of the identification of loading and unloading events using a wavelet technique.) The loading rate can be determined by averaging many loading events together, resulting in an exponential decay of I_{QPC} from a magnitude corresponding to an unloaded electron to that corresponding to a loaded electron. Figures 6.2(d)–6.2(f) show that the loading rates into the excited orbital states are much faster than into the ground orbital states.

The rate at which an electron loads into the dot, as well as the spin state of that electron, both depend strongly on the voltage at which the electron is loaded. In Fig. 6.3, we show that these features are observed over a wide range in gate voltage. Figure 6.3(a) shows that the loading rate Γ_{load}, measured in the same way as in Figs. 6.2(d)–6.2(f), but now as a continuous function of loading level, increases by over an order of magnitude when the electron is loaded through an orbital excited state instead of through the orbital ground state. The loading rate shows two strong peaks as a function of loading voltage, corresponding to the excited states $|\uparrow e\rangle$ and $|\downarrow e\rangle$. Because orbital relaxation is very fast compared to the experimental time scale [101, 102], one expects any electron loaded into a spin-↑ state to be measured in the state $|\uparrow g\rangle$ and any electron loaded into a spin-↓ state to be measured in the state $|\downarrow g\rangle$.

The relative fraction of spin-↑ and spin-↓ loaded can be tuned, because the loading rate for each spin type is voltage-dependent. We demonstrate this directly by using single-shot spin readout to measure the spin-↑ fraction as a function of the loading level, as shown in Fig. 6.3(b). The fraction of spin-↑ electrons has two clear peaks as a function of the loading

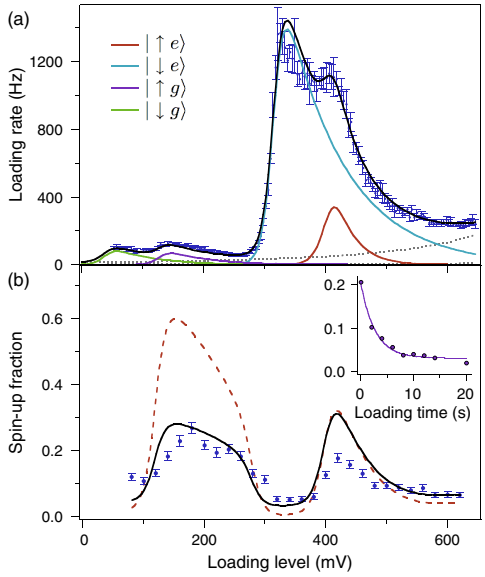

Figure 6.3: Spin selective loading and spin lifetime measurement. (a) Plot of electron loading rate Γ_{load} versus loading voltage V_{load} on gate PL at $B = 1.85$ T. Error bars are the standard deviation of four measurements. Peaks occur when levels in the dot are made available for loading, enabling tuning of both the loaded-spin fraction and the loading rate. The spin-split excited orbital levels $|\uparrow e\rangle$ and $|\downarrow e\rangle$ load 10 times faster than the ground state. The black solid line in (a) is a fit obtained by treating the loading rate contribution from each state as a convolution of a Fermi-Dirac distribution, a Lorentzian line shape, and a linearized energy-dependent tunneling function. (b) Spin-up fraction versus loading level measured by using single-shot readout (see Fig. 6.2), with $t_{\text{load}} = 100$ ms, $t_{\text{readout}} = 200$ ms, $t_{\text{empty}} = 50$ ms, $V_{\text{readout}} = +85$ mV, and $V_{\text{empty}} = -200$ mV. Each data point corresponds to an analysis of 1000 single-shot traces. The red dashed line is a fit using the same parameters as in (a); the black solid line is the same fit with corrections for the T_1 decay before measurement, a measurement fidelity less than unity, and a nonzero dark count rate (see Appendix E for additional details). Error bars are $\sqrt{M}$, where M is the number of readout events. Inset: Spin-up fraction versus loading time with $V_{\text{load}} = +425$ mV. The solid line is an exponential fit that yield $T_1 = 2.8 \pm 0.3$ s.

voltage, one corresponding to $|\uparrow g\rangle$ and a second to $|\uparrow e\rangle$. These peaks arise because loading rates into specific spin states in the dot are a maximum when the state is near resonance with the Fermi level.

6.4 Quantifying spin loading rates and relaxation times T_1

The variation in both the total loading rate and the spin-↑ fraction can be understood by calculating the loading rate for each spin state. The probability of loading a spin-↑ electron is $\Gamma_\uparrow/\Gamma_{\rm load}$, where $\Gamma_\uparrow$ is the total rate for all spin-↑ channels and $\Gamma_{\rm load}$ is the sum of the rates for all ways to load the dot. A global fit to the data in terms of loading through spin-split ground and excited states with Lorentzian broadening is shown in Figs. 6.3(a) and 6.3(b). The fit is to both the total loading rate and the fraction of spin-↑ electrons. We treat the loading rate contribution from each state as a convolution of a Fermi-Dirac distribution, a Lorentzian line shape, and a linearized energy-dependent tunneling function [103]:

$$\Gamma_i(V) = \int_{-\infty}^{\infty} \left(\frac{\Gamma_{0i}\, e^{-\alpha y/E_i}}{1 + e^{-\alpha y/k_B T}} \right) \frac{\gamma_i/2\pi}{(\gamma_i/2)^2 + (\delta V_i - y)^2}\, {\rm d}y, \tag{6.1}$$

where E_i is the linearized energy-dependent tunneling coefficient that relates to the transparency of the barrier [43]; γ_i is the full width at half maximum of the Lorentzian; Γ_{0i} is the amplitude; V is the loading voltage; and $\delta V_i = V - V_i$, where V_i is the position of the state (see Appendix E for additional details). The fit is in good agreement with the experimental measurements for the loading rates and the fractions of spin-↑ and spin-↓ electrons, supporting the interpretation of the data in terms of loading through specific spin states of the dot.

The black line in Fig. 6.3(b) is corrected for the finite spin lifetime T_1 of the electrons loaded into the dot. We determine T_1 by measuring the spin-↑ fraction as a function of the duration of the loading pulse, $t_{\rm load}$ [92]. The inset in Fig. 6.3(b) shows a typical result for a magnetic field of 1.85 T, with an exponential fit yielding the value $T_1 = 2.8 \pm 0.3$ s. For these data, $V_{\rm load} = +425$ mV, so that loading occurs predominantly through the excited orbital states. We have measured T_1 at different loading voltages and also measured T_1 for a four-step pulse sequence in which the dot is held at a fourth "wait" voltage. The values of T_1 were all of the order of seconds, except when both the load and wait voltages were set so the state $|\uparrow g\rangle$ was aligned just below E_F, where the value of T_1 is reproducibly much shorter: $T_1 = 136 \pm 22$ ms. In principle, virtual hopping of electrons from the dot

to the leads can limit T_1 [104], but the predicted magnitude is much too small to explain the observed effect, and this mechanism is not consistent with the behavior when the wait voltage is varied. The possibility that the excited orbital states are long-lived is ruled out by performing single-shot measurement with the readout level positioned such that $|\downarrow g\rangle$ and $|\uparrow g\rangle$ are below E_F and $|\downarrow e\rangle$ and $|\uparrow e\rangle$ are above E_F. In this situation, even for short loading times ($t_{\mathrm{load}} = 20$ ms), less than 0.5% of traces show events.

6.5 Discussion

It has been observed that T_1 can be limited by dipolar coupling to nearby spins [7]; we believe that the shorter T_1 time measured when the dot is loaded through the state $|\uparrow g\rangle$ is due to interaction with a nearby spin trap, which is suppressed by the deeper pulse associated with loading at the excited orbital states. The ability to load an electron into the dot through the excited state thus provides an immediate benefit, in that the additional tunability enables one to avoid sample imperfections that lead to a shorter spin relaxation time.

We have demonstrated the ability to manipulate and measure the spin state of individual electrons in a Si/SiGe quantum dot, and we report the first single-shot measurements of the longitudinal spin relaxation time T_1 in such devices. We have shown that loading into spin-split orbital excited states provides a fast channel for initializing spins into the ground orbital spin qubit states because of the coexistence of fast orbital relaxation and slow spin relaxation. The demonstrations of fast initialization and slow spin relaxation enhance the prospects for the development of Si/SiGe devices for spintronics and quantum information processing applications.

Chapter 7

Transport I: Spin blockade and lifetime-enhanced transport

7.1 Introduction

In this Chapter, we analyze electron transport data through a Si/SiGe double quantum dot in terms of spin blockade and lifetime-enhanced transport (LET), which is transport through excited states that is enabled by long spin relaxation times, T_1, which was measured to be of the order of 3 s in Chapter 6.

The Chapter is organized as follows. Sec. 7.2 introduces the phenomena of spin blockade and lifetime-enhanced transport in double quantum dots. Sec. 7.3 presents a simple argument for the existence of the LET tail based on data at small bias voltages and involves an absolute minimum of data analysis. Sec. 7.4 presents our experimental procedures. The methods used to fit the bias triangles are presented in Sec. 7.5, and the procedure used to position and scale the bias triangles are presented in Sec. 7.6. The phenomenon of energy-dependent tunneling is prominent in the data, and a theoretical model that describes this effect as it appears in the data is presented in Sec. 7.7. In Sec. 7.8, results from the model are compared to the experimental data, and important phenomenological parameters are reported. The Chapter concludes with a discussion in Sec. 7.9.

7.2 Spin blockade and lifetime-enhanced transport

Recent progress in GaAs quantum dots has enabled the manipulation of exchange coupling in a two-electron double dot [4] and has led to single-shot readout of one- [92] and two-electron [44] spin states in a single dot. The latter experiment makes use of energy dependent tunneling to provide high visibility in the measurement. The simplest explanation of this effect is that a larger tunnel barrier causes a slower tunneling rate. The effect is of fundamental interest for quantum phenomena, and can lead to very precise measurement techniques in the context of quantum information. Energy dependent tunneling effects in quantum dots have also been studied in several other recent experiments [105, 106, 107, 108, 43, 32]. Silicon-based devices should exhibit a strong energy dependence in tunneling, since the effective mass in silicon, on which the tunneling rate depends exponentially [109] is relatively large.

Semiconductor double quantum dots are tunable structures that enable the coupling of two small regions of bound electrons to each other and, often, to two leads, enabling measurement of an electron transport current through the system [110]. Double quantum dots can display an effect known as Pauli spin blockade [111, 112, 106] where current flow proceeds in a cycle that first loads either a two-electron singlet state with one electron in each dot, the $S_{1,1}$ state, or a two-electron triplet $T_{1,1}$ state that is nearly degenerate with the singlet. For the cycle to proceed without blockade in either case, both the singlet $S_{2,0}$ and the triplet $T_{2,0}$ states, where both electrons are on the left dot, must be lower in energy than their corresponding (1,1) states. There are regions in gate-voltage space where this is not true, and the striking absence of current that arises in such regions is known as spin blockade. Spin blockade makes double dots extremely useful for quantum dot spin qubits, because it provides a robust means to perform spin readout [20, 113, 4, 107, 82, 52].

Spin blockade has been reported in silicon quantum dots formed using both Si metal-oxide-semiconductor structures [114] and Si/SiGe heterostructures [115]. In both cases, the spin blockade results displayed many similarities with previous observations of spin blockade, most of which have been made in GaAs/AlGaAs-based double quantum dots.

In Ref. [115], we also reported measurements of current flow for the opposite voltage bias. In this regime, we observed unusual patterns in two-dimensional maps of the current as a function of a pair of gate voltages. The most striking observation was a strong 'tail' of current, which appeared in a supposedly blockaded portion of the current map. This behavior was attributed to the combined effects of slow triplet-singlet relaxation and strong energy dependent tunneling, the two of which together enable current to flow through long-lived excited states. For this reason, the phenomena were labeled 'lifetime-enhanced transport,' or LET. Recently, LET behavior has also been observed in transport through individual donors in silicon [116].

In this Chapter, we present a large quantity of additional data and analyze these data in detail, showing that they can all be fit using one consistent set of parameters. We analyze eight two-dimensional plots of current as a function of a pair of gate voltages, four different biases in each direction of current flow through the double dot. Spin blockade is observed in the direction of current flow in which it is expected. For the opposite voltage bias, the unusual current patterns associated with LET are observed, in agreement with our previous results [115]. To test the explanation that the 'tail' of current arises because of LET, we fit all eight sets of data in parallel, determining optimum values for the three slopes of the edges of the bias triangles, the lengths of the sides of the bias triangles, and the positions of those triangles. The results are shown to be consistent with both spin blockade and LET. In particular, it is shown that we cannot obtain consistent results for the length of the triangles if the current tails are included in the triangles. The fitting and the subsequent delineation of the bias triangles also enables us to improve our measurements of the singlet-triplet splittings in both the (2,0) state, corresponding to two electrons in the left dot, and the (1,1) state, corresponding to one electron in each dot.

Building on accurate fitting of the bias triangles, we investigate details of the strong dependence of the transport current on the gate voltages. Within the triangles, we obtain consistent and quantitative fits to the data by explicitly incorporating strong energy-dependent tunneling as well as tunneling through both singlet and triplet channels. Both

coherent [117, 118] and incoherent [119] processes contribute strongly to the energy dependence of the electron tunneling rates, and we develop a general model for transport in a double dot, including both inelastic and resonant effects, using the master equation approach. We show that this model can be used to perform a quantitative fit of the transport data and that relevant parameters can be extracted from the data.

Our success in interpreting a large body of experimental data with a single consistent set of fitting parameters is strong evidence in support of the interpretation of the current tail in terms of transport through the triplet channel, as first described in Ref. [115].

7.3 Simple Demonstration of LET

The key observable feature of LET is a strong tail of current protruding beyond the end of the base of the conventional bias triangle. Careful fitting of the triangles to many sets of data obtained with a variety of source-drain bias voltages, as we do below, is a good way to test for the existence of this tail. However, before embarking on such a detailed analysis, we first provide a simple argument for our LET interpretation of the data.

Figure 7.1(a-c) show plots of the current through a double quantum dot as a function of two gate voltages. The sample is described in Sec. 7.4 below, and the sign of the voltage bias is opposite to that in which spin blockade would be observed. Fig. 7.1(a) is obtained at very low bias, such that current flows only very near the triple points [110]. In particular, the bias voltage is smaller than the singlet-triplet splitting. Fig. 7.1(b) shows data at a slightly larger voltage. As expected, the region of current flow is correspondingly larger, and it has the same overall shape. Fig. 7.1(c) is acquired at a bias voltage slightly higher still. Again, the primary region of current flow is correspondingly larger. However, a new feature suddenly appears in the data: a tail of current that extends to the lower right. This tail completely changes the shape of the current pattern.

To be quantitative, we consider the lengths of the various current features visible in Fig. 7.1(a)-(c). The bias triangles, and therefore the lengths of these current features, should scale linearly with the applied bias voltage. Panel (d) shows in green the ratio of the

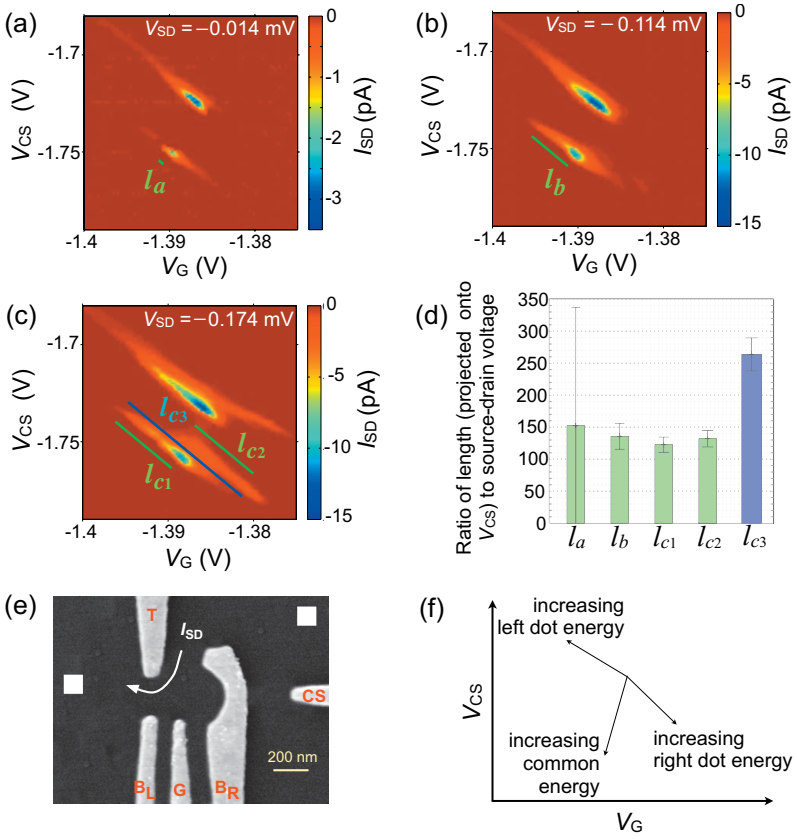

Figure 7.1: The transport current through a double quantum dot for a device with gate arrangement shown in the inset to (a) at three different source-drain biases V_{SD}: (a) -0.014 mV, (b) -0.114 mV, (c) -0.174 mV. Panel (c) shows the sudden appearance of a current tail. (d) Lengths, l_a, l_b and l_{c_1} in panels (a) to (c) are measured from the peak of the current to the upper left tip of a 1 pA contour around the peak. l_{c_2} is the length of the tail from its peak at the lower right to the tip of a 1 pA contour on the upper left. l_{c_3} is the length that would be extracted if the 'tail' were part of the conventional bias triangle. It is measured from the peak of the current in the tail to the tip of the upper left-most 1 pA contour; i.e., it is essentially the sum of l_{c_1} and l_{c_2}. The graph in (d) shows the ratio of the lengths, as measured by their projection onto the left-hand gate voltage axis, divided by V_{SD}. The four lengths l_a, l_b, l_{c_1}, and l_{c_2} are consistent with each other and with the description of the 'tail' in terms of LET. The blue length l_{c_3} is clearly too long, and thus the description of the physics in terms of LET and the concept of a current 'tail' extending out of the conventional bias triangle are necessary to understand the data in panels (a)-(c). (e) SEM image of the gate pattern with the gates labeled in red. The gates were tuned so that the device contained a double quantum dot [115]. (f) Schematic diagram of the energy axes for the double dot.

lengths of the main current features identified in panels (a)-(c), projected onto the left-hand voltage axis, to the applied bias voltage $V_{\rm SD}$. These lengths were measured, as indicated, from the point where the current peaks at the lower right, to the extremum at the upper left on a 1 pA contour. The LET interpretation predicts that the ratios of lengths l_a, l_b, and l_{c_1} to $V_{\rm SD}$ should be equal, as shown in panel (d). In particular, l_b and l_{c_1}, which have small error bars, are nearly identical. Further, the length of the tail is the same as the length of the main current region in Fig. 7.1(c): that is, $l_{c1} = l_{c2}$. This is also consistent with the LET interpretation presented below and in Ref. [115]. In contrast, if the base of the triangle were located at the end of the tail in Fig. 7.1(c), the length of the region of current flow would be as is shown in blue and labelled l_{c3}. As is clear from Fig. 7.1(d), such a length is incompatible with length l_b from Fig. 7.1(b). Note that the length l_a has a large error bar, because the source-drain voltage $V_{\rm SD}$ is so small that the uncertainty in that quantity is larger than its value; panel (a) is included in this discussion to emphasize that current is indeed visible at very low bias voltage, indicating that current flows at the triple points themselves. If the base of the bias triangle were located at the end of the tail in Fig. 7.1(c), no current would be observed at the triple point. In such an interpretation, the triple point would be located directly below the tail, and this would be incompatible with the observation of current at the triple point in Fig. 7.1(a).

These simple arguments make clear that the LET tail does indeed protrude beyond the base of the bias triangle. The rest of this Chapter presents an analysis of a large quantity of data, all of which is analyzed together and self-consistently. The results of our analysis provide a complete and quantitative understanding of the data in terms of spin blockade and LET.

7.4 Experiment

The data we discuss here were acquired from a double quantum dot formed in a top-gated $Si/Si_{0.7}Ge_{0.3}$ heterostructure [120, 121, 122]. The quantum well was nominally 12 nm thick, and it contained a two-dimensional electron gas of density $n = 4 \times 10^{11}$ cm^{-2} and mobility

$40,000\,\mathrm{cm}^2/\mathrm{Vs}$. The gate design for this device, reproduced from Ref. [115] as Fig. 7.2(e), has a single plunger gate. For the data presented here, a gate originally intended for charge sensing was pressed into service to tune the dot occupation, providing the second axis for manipulation of the double dot in gate-voltage space [115]. Here we focus on the region in gate-voltage space where the device exhibits the behavior of a double-dot; this region occurs between a regime in which the device acts as a single dot and a region in which no measurable current flows through the device [115]. Unlike more recent work, [123, 88] the absolute number of electrons in the dots is not known, and all references to the number of electrons refers to the valence number; there could be a closed shell underneath the valence electrons, and the existence of that shell would not be apparent in the data.

Figure 7.2 shows the current I through the double quantum dot as a function of gate voltages V_{G} and V_{CS}. Each of the panels in Fig. 7.2 contains two features that are similar to each other. These features are conventionally called the 'electron' and 'hole' triangles [110] and we adopt this language here. The 'electron' system is called so because it can be described in terms of the electron occupations (1,1), (2,0), and (1,0). The 'hole' system can be described in terms of the electron occupations (2,1), (2,0), and (1,1). However, these states result in energy level diagrams that are more complicated than those of the electron triangle. A complementary description of transport in terms of the hole states $(0,1)_h$, $(0,2)_h$, and $(1,1)_h$ allows us to draw a set of energy level diagrams that are analogous to the diagrams for the 'electron' system. This hole picture has proven useful in some situations [110]. However, it is difficult to include excited states of the zero-hole state in a simple way. Thus, we will stick with the three-electron diagrams here, in spite of their complexity [25]. Detailed plots of the chemical potentials relevant for modeling of transport with both positive and negative voltage bias are shown in Appendix F in Fig. F.1. We emphasize that, although for clarity and connection with the existing literature we retain the electron and hole terminology, the chemical potential diagrams for the latter in Fig. F.1 actually describe three-electron states, not hole states. In this Chapter, we refer to chemical potentials for electrons only, and never holes, and we explain in detail, transport in the

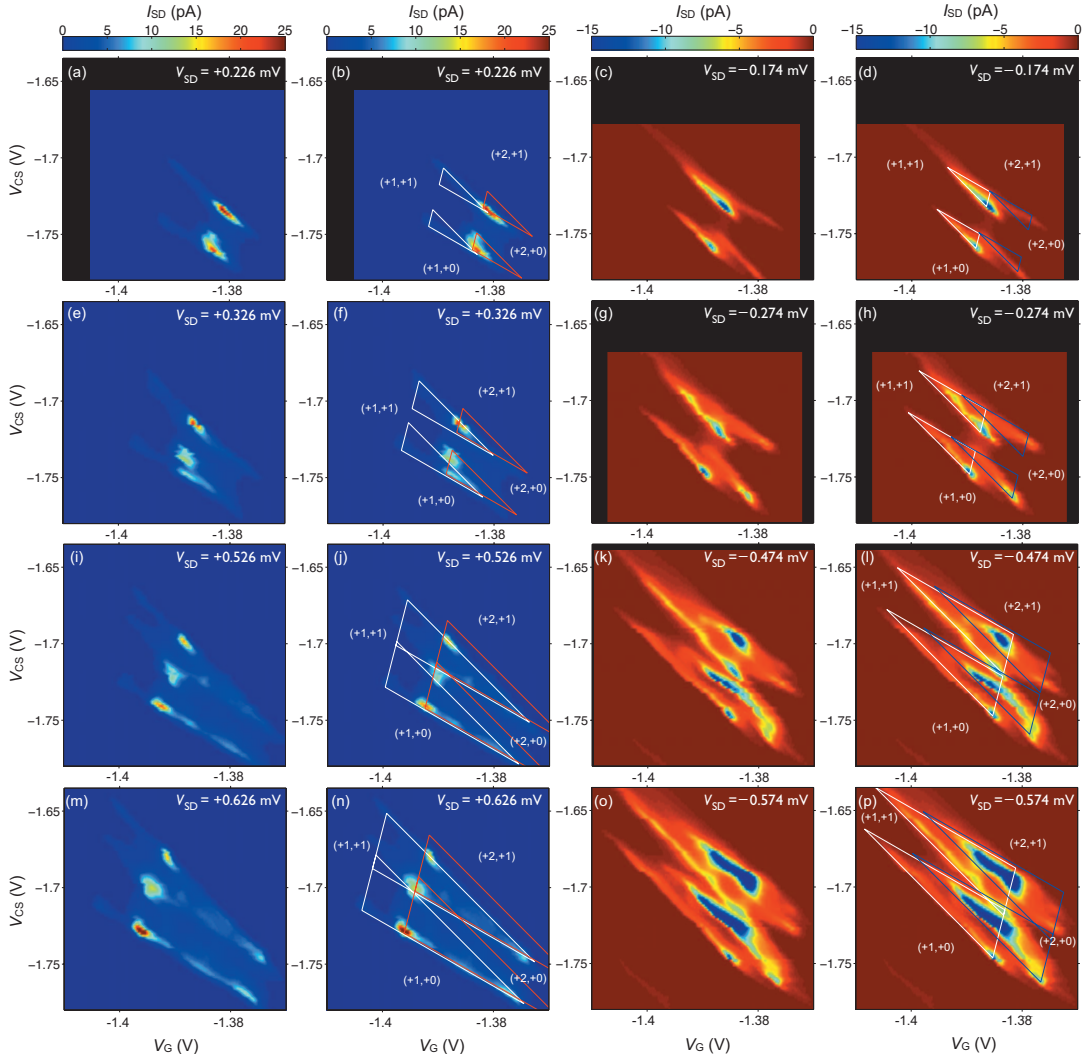

Figure 7.2: The current through the double quantum dot as a function of the gate voltages V_G and V_{CS}. Panels (a)–(p) correspond to eight different bias voltages V_{SD} as labelled. Column one shows data in the spin blockade regime (forward bias). Column three shows the data in the LET regime (reverse bias). Columns two and four show the same data as columns one and three, with the calculated bias triangle boundaries superimposed on the data, as explained in the main text. The data in panels (a) and (g) have been presented previously in Ref. [115].

three-electron regime in the following Chapter 8.

The data for positive source-drain bias (column one of Fig. 7.2) exhibit spin blockade. We refer to this bias direction as 'forward bias.' The data in this bias direction are largely understandable using the conventional concepts of Pauli spin blockade; indeed, the consistency of these data with classic spin blockade behavior provides strong evidence that our assignment of the valence electron occupancies is correct. There are, however, interesting resonances observable, e.g., where transport through the triplet channel of the electron triangle overlaps with transport though the singlet channel of the hole triangle. Also, the current in the spin blockade regime extends by small amounts past the conventional tips of the bias triangles. We discuss these features and others in Sec. 7.9 below.

The data for negative source-drain bias (column three of Fig. 7.2) show unusual patterns in the current as a function of gate voltages V_{G} and V_{CS}. We refer to this bias direction as 'reverse bias.' Consistent with the arguments in Sec. 7.3 above and in Ref. [115], there are regions of current extending outside the conventional bias triangle regions — the only regions in which transport is conventionally observed. We have argued that current is observed outside the bias triangles due to an effect named lifetime-enhanced transport, or LET. The essential prerequisite for observing this effect is that long relaxation times from an excited state, such as the (2,0) spin triplet state discussed below, can leave open a fast, energetically downhill current path. In order to check this argument and understand the features shown in the right two columns of Fig. 7.2, it is important to determine with a fair degree of precision the sizes and positions of the bias triangles.

The data sets in Fig. 7.2(a) and (g) were previously reported in Ref. [115]. The bias voltages were reported in that Chapter to be $+0.2\mathrm{mV}$ for the data in panel (a) and $-0.3\mathrm{mV}$ for panel (g), but these values were slightly affected by an offset in the current preamplifier. This offset was discovered when we analyzed four additional data sets taken at very small bias voltage V_{SD}. To determine the size of the offset, we examined several data sets with small V_{SD}, including Figs. 7.1(a) and (b). Cuts through the data were taken along a line connecting the two triple points (see explanation, below). The peak current, the full-width-

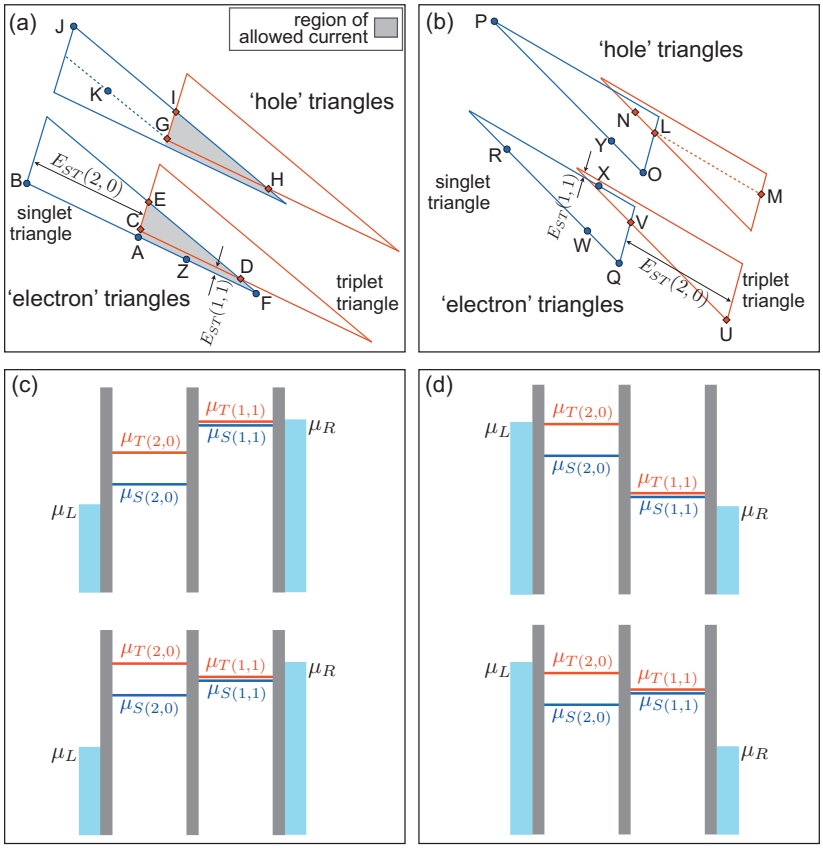

Figure 7.3: (a) Schematic diagrams showing the singlet and triplet triangles for forward bias. The gray areas show the region in which current is allowed in conventional spin blockade. In addition, current is expected along segments BA and JI, because on these lines the (1,1) singlet and triplet are aligned with the leads, and spin exchange is possible. In the data of Fig. 7.2, segments BF, which has low slope, and JH, which has a slightly higher slope, are strongly visible and thus good candidates for fitting. (b) Schematic diagrams showing the singlet and triplet triangles for reverse bias. Points U and M are outside the conventional bias triangle. (c), (d) Energy levels in a double quantum dot, with one fixed electron in the left-hand dot. Panel (c) corresponds to forward bias of the the double dot, while panel (d) corresponds to reverse bias. Electrons may transit via the singlet or triplet channels. The upper and lower plots show the chemical potentials at two example gate voltages. In the upper schematics of (c) and (d), electrons can transit through both the singlet and the triplet channels via an energetically downhill path. In the lower panel of (c), spin blockade is present, as the triplet channel is energetically uphill. The lower panel of (d) is the lifetime-enhanced transport (LET) regime, in which the singlet channel is energetically uphill, and current will be blockaded unless electrons tunnel preferentially through the triplet channel.

at-half-maximum, and the area under the sampled cuts were computed for each cut. Each of these quantities was assumed to depend linearly on $V_{\rm SD}$ at small bias, allowing us to determine a bias offset of 0.026 mV. We emphasize that the source-drain biases indicated in each figure in this Chapter have been corrected to reflect this offset.

7.5 Fitting

Overview

At infinitesimal bias voltages $V_{\rm SD}$, the Fermi levels of the left lead L and the right lead R are nearly equal, and current flows through the double dot only when the Fermi energies in both leads and the chemical potentials of both quantum dots are aligned, *i.e.*, when $E_{LF} \simeq E_{RF} \simeq E_1 \simeq E_2$. Here, $E_{LF}(E_{RF})$ refers to the Fermi energy of the left (right) lead and $E_1(E_2)$ refers to the chemical potential of the left (right) dot. When these energies are equal, the charge configurations of interest are degenerate, and a 'triple point' is observed in the data [110]. For the electron system, the degenerate double dot electron configurations are $(1,0)$, $(1,1)$, and $(2,0)$, while for the hole system these electron occupations are $(1,1)$, $(2,0)$, and $(2,1)$. The data in Fig. 7.1(a) were acquired at a small $V_{\rm SD}$. As $V_{\rm SD}$ is increased, plots of the current as a function of E_1 and E_2 (or, more conveniently, the gate voltages most directly controlling E_1 and E_2) reveal these triple points expanding into 'bias-triangles' arranged regularly in the well-known pattern known as a honeycomb diagram [110].

The conventional bias triangle is defined by the region in gate voltage space in which the double dot ground states (in this case the singlet states) are both energetically downhill and within the source-drain bias window. We refer to these as the 'singlet triangles.' There are analogous 'triplet triangles' defined by similar conditions for the excited triplet states. Separate singlet and triplet triangles can be defined for both the electron and hole systems. For electrons in forward bias, transport occurs through the sequence (1,0) $\rightarrow$ (1,1) $\rightarrow$ (2,0), while for the hole regime, in forward bias, transport occurs through the electron sequence (2,1) $\rightarrow$ (1,1) $\rightarrow$ (2,0). Figures 7.3(a) and (b) show schematic diagrams of these four distinct triangles for the cases of forward bias in panel (a) and reverse bias in panel (b).

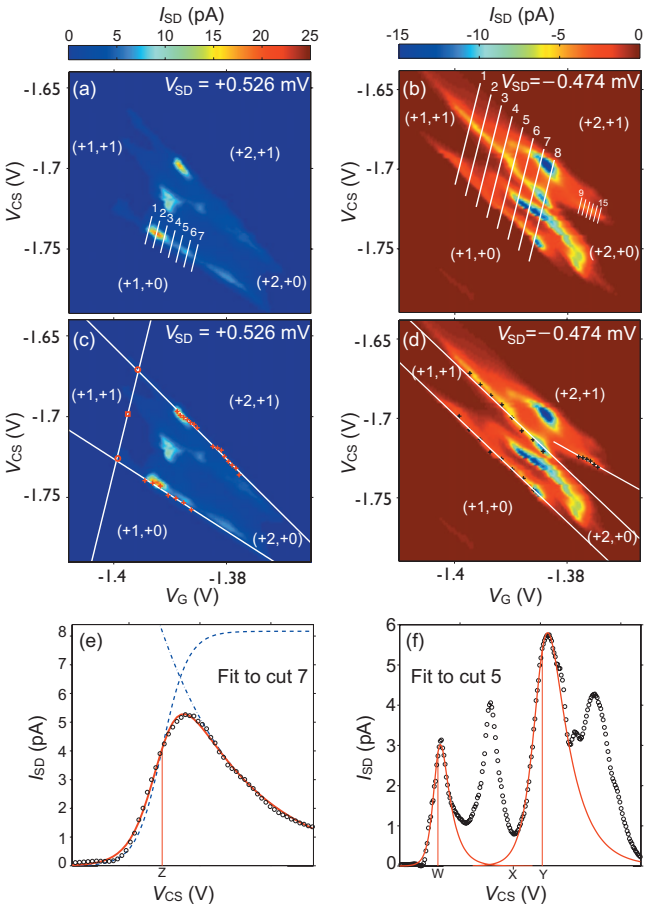

Figure 7.4: Examples showing how the triangle boundaries and slopes are determined from the data. (a) Forward bias: the positions of the data cuts (1-7) that we use to determine the low slope. (b) Reverse bias: the positions of the data cuts that we use to determine the high slope (1-8) and the low slope (9-15). (c) For the same data as panel (a), the red circles mark the points used to determine the base slope for this data set; their centroid is marked by the red square. A white line with the mean base slope is drawn through the centroid. The red crosses mark points used to determine low and high triangle slopes; the two white lines are obtained by linear fits through the crosses. (d) For the same data as panel (b), the black crosses mark points used to determine low and high triangle slopes; the three white lines are obtained by linear fits through the crosses. The separation between the triple points is labeled d. (e) Example fitting results for cut 7 in panel (a). The dashed lines correspond to the Fermi function and the energy dependent tunnel rate, and the red line corresponds to their product. The vertical red line indicates the triangle boundary. (f) Example of two independent fits to cut 5 in panel (b), and the corresponding triangle boundaries.

Note that the lengths BA and AC represent the singlet-triplet energy splittings in the (2,0) and (1,1) states, respectively. The magnitude of the measured current varies significantly across each triangle because of energy-dependent tunneling [105, 106, 107, 108, 43, 32]; the tunneling rate from the lead decreases as the tunnel barrier increases, which occurs as the energies of the relevant levels in the dots are lowered below the Fermi level. The effects of energy-dependent tunneling are more marked in Si/SiGe dots than in GaAs dots, because electrons in silicon have larger effective mass [109] and these effects are discussed in more detail below, in Sec. 7.7.

Points Q, R, X, W, and V in Fig. 7.3(b) lie within the conventional bias triangle. Point U lies outside this triangle, but within the triplet triangle. Fig. 7.3(d) shows example energy level arrangements for points within both the singlet and triplet triangles (upper cartoon), and points such as U, that lie outside the singlet triangle but within the triplet triangle (lower cartoon). In the conventional picture, without LET, the regions of strong current flow are the blue singlet triangles, while the regions of the red triplet triangles that do not overlap the singlet triangles are blockaded. A major point of this Chapter is to demonstrate that the current visible in the lower right hand corners of the panels in column three of Fig. 7.2 arises because significant current is flowing through the triplet states outside the conventional bias triangle. Because of its shape, we refer to this feature in the data as the triplet 'tail.' LET lifts the blockade condition, giving rise to the triplet tail when tunnel rates and triplet-singlet relaxation times are appropriate — specifically, the triplet must load enough faster than the singlet that a transport current is measurable, even though tunneling through the singlet channel is very slow [115].

In order to understand how electrons move from one lead to the other through the double dot system, it is necessary to know the chemical potentials of each quantum dot for particular occupancy states. Of particular significance are the chemical potentials associated with points labeled with uppercase letters in Fig. 7.3(a) and (b). The corresponding energy level diagrams are all presented in the appendix. To understand the data in columns one and three of Fig. 7.2, simultaneously and self-consistently, we aim to determine the size and

shape of the bias triangles, and to position these triangles as accurately as possible on the data. The end result of this analysis is shown in the second and fourth columns of Fig. 7.2.

Our procedure is as follows: first, using data for all biases and from both the electron and hole systems, we obtain the three slopes that define the edges of the bias triangles (see Fig. 7.2(f)); these are (i) the slope of the base of the triangle (base slope), which characterizes the direction in gate voltage space in which the chemical potentials of the two dots are held constant relative to each other, (ii) the low slope of one of the long edges (low slope), which characterizes the direction in gate voltage space in which the chemical potential of the right dot is held constant with respect to the Fermi level of the right lead, and (iii) the slightly higher slope of the other long edge (high slope), which characterizes the direction in gate voltage space in which the chemical potential of the left dot is held constant with respect to the Fermi level of the left lead. Second, we determine the separation between the electron and the hole triangles, as well as the scaling relation between the applied bias voltage and the size of the triangles. Finally, we position the triangles on the data sets in Fig. 7.2.

Determination of the base slope

The base slope joins the points B and J in Fig. 7.3(a) and, similarly, the points Q and O in Fig. 7.3(b). Points B and J are identified as small, solitary peaks in the left-hand region of the forward bias experimental data (column 1 of Fig. 7.2 and expanded in Fig. 7.7(a, b)). Note that the data were interpolated using the cubic spline procedure, [1] to more accurately identify the center of the points, while keeping the functional form of the data unchanged. The base slopes were obtained for each pair of points (B,J), in all four forward bias data sets, and the average value was calculated, with results summarized in Table 7.1. The base line for each forward bias data set is obtained by determining the centroid position of a given (B,J) pair, and then drawing a line with the average base slope through the centroid. An example of this procedure is shown in Fig. 7.4(c), with the centroid indicated as a red square and the points B and J indicated by the red circles.

[1] In fitting the data, two processing steps were performed: (i) cubic spline interpolation of five points for every single data point was used, and (ii) the average background current was determined and subtracted from each data set.

Table 7.1: Base slopes obtained from the spin blockade data of Fig. 7.2.

Bias (mV)	Base slope
0.226	15.3
0.326	11.2
0.526	15.5
0.626	14.8

Base slope mean = 14.2
Standard deviation = 2.02

Determination of the low slope

Both the forward and reverse bias data possess features that are useful for determining the low slope of the bias triangles. We first consider the forward bias data along the line segment AF shown in Fig. 7.3(a). Along this line, the chemical potential of the left dot is variable, while the chemical potential of the right dot is constant. The current flow is nearly constant along AF, except for the resonant peak, which we will discuss in Section 7.7. Thus, the current depends only weakly on the chemical potential of the left dot. We then take data cuts parallel to the base slope, crossing the line segment AF, as shown in Fig. 7.4(a). Along a given cut, the current does not flow uniformly and it does not fill up the whole bias triangle. The strong suppression of the current above AF is a signature of energy dependent tunneling. We conclude that the current depends most strongly on the chemical potential of the right dot, and that the right-hand tunnel barrier forms the transport bottleneck.

In Section 7.8 below, we provide detailed models for energy dependent tunneling. However, in order to delineate the edges of the bias triangle here, we simply point out that the dominant contribution to the current along the data cuts in Figs. 7.4(a) and (b) can be expressed as follows:

$$I/e = f_R \Gamma_R. \tag{7.1}$$

Here,

$$f_R = \left[e^{(E - E_{RF})/k_B T} + 1 \right]^{-1} \tag{7.2}$$

is the Fermi function for the right lead, where E is the chemical potential of the right dot, and E_{RF} is the Fermi level of the lead. The Fermi function defines the edge of the forward

bias triangle along the line AF, defined by the condition $E = E_{RF}$. The second function appearing in Eq. (7.1) is the effective tunneling rate Γ_R, from the right lead to the right dot. To capture the effect of energy dependent tunneling, we will apply approximations similar to those used in Refs. [43] and [32], and discussed in greater detail in Sec. 7.8, leading to the prescription

$$\Gamma_R = \Gamma_{R0} e^{(E-E_{RF})/E_{R0}}, \tag{7.3}$$

where Γ_{R0} is proportional to the attempt rate, and E_{R0} describes the scale for the energy dependent tunneling. This exponentially decaying function suppresses the current flow above line segment AF.

Equation (7.1) can be used to fit the data along the cuts shown in Fig. 7.4(a) by assuming a linear relation between the chemical potential of the right dot and the control voltages V_{CS} and V_{G}. The proportionality constants, the so-called 'lever-arms', are determined as part of the fit. A typical result of the fitting procedure is shown in Fig. 7.4(e). The vertical line on the plot represents the boundary of the bias triangle, corresponding to the condition $E = E_{RF}$. The boundary positions for each of the cuts in Fig. 7.4(a) were obtained in the same way, giving the points marked as red crosses in Fig. 7.4(c). The edge of the bias triangle was then determined by fitting a straight line through these points, with the result shown in Fig. 7.4(c)

The low slope can also be investigated in the hole system in the reverse bias regime, along the line segment LM shown in Fig. 7.3(b). Data cuts are again taken parallel to the base slope, as shown by the short lines on the right-hand-side of Fig. 7.4(b). A function similar to Eq. (7.1) was used to fit the data, to obtain the triangle boundary along each cut. The results are shown as black crosses superimposed on the right-hand side of Fig. 7.4(d). Again, we fit a straight line through these boundary points, obtaining the result shown in panel (d). The low slopes were obtained in this way for 8 different data sets, as summarized in Table 7.2.

Determination of the high slope and the triple point spacing

The high slope can also be determined from fits to both forward and reverse bias data. In

Table 7.2: Low slopes obtained from both forward and reverse bias data.

V_{SD} (mV)	Low slope	V_{SD} (mV)	Low slope
0.226	-2.25	-0.174	-1.94
0.326	-2.17	-0.274	-1.93
0.526	-2.24	-0.474	-1.97
0.626	-2.24	-0.574	-1.95

Low slope mean = -2.09
Standard deviation= 0.15

the case of forward bias, we take data cuts though the hole data, along lines parallel to the base slope. Along the line IH, indicated in Fig. 7.3(a), the chemical potential of the left dot is equal to the Fermi level of the left lead. For the hole triangle, the energy dependent tunneling is rather weak. The prominent features in the data along line segment IH are mainly attributed to the Fermi function for the left lead. We therefore adopt the following fitting form for data near line segment IH:

$$I/e = (1 - f_L)\Gamma_L, \tag{7.4}$$

where the Fermi function f_L and the energy dependent tunnel rate Γ_L are defined analogously to Eqs. (7.2) and (7.3). The data cuts are fit as described above, for source-drain biases $V_{SD} = 0.226$, 0.526, and 0.626 mV. The 0.326 mV data set in Fig. 7.2(e) exhibits a discontinuity along IH arising from a charging event. For that data set alone, the fitting procedure is performed in the vicinity of line segment JI rather than IH. The fitting results for the triangle boundaries are shown as red crosses in Fig. 7.4(c), for each data cut. The high slope is obtained from a linear fit through the boundary points, as given by the white line.

In the reverse bias regime, we also take data cuts parallel to the base slope. In this case, the cuts extend across the entire electron-hole system, as shown in Fig. 7.4(b). We use form

$$I/e = f_L\Gamma_L \tag{7.5}$$

to fit the data. In this case, however, independent fits are made to both the electron and the

hole peaks, giving typical results as shown in Fig. 7.4(f). Here, the vertical lines represent the inferred locations of both triangle boundaries. The resulting boundary locations are shown as black crosses in Fig. 7.4(d). By fitting straight lines, we obtain results for the high slope, as summarized in Table 7.3.

The fits to the reverse bias data provide a direct method for determining the separation between the electron and hole triangles along the direction parallel to the base slope. This separation is the triple point spacing, and it is indicated by the distance d in Fig. 7.4(d). It is also indicated, schematically, by the distance between points Q and O in Fig. 7.3(b). The triple point spacing is the same for all biases, and we therefore determine its value by averaging the individual extracted values for d.

Table 7.3: High slopes obtained from both forward and reverse bias data.

V_{SD} (mV)	High slope	V_{SD} (mV)	High slope
0.226	-3.32	-0.174	-3.86
0.326	-3.75	-0.274	-4.06
0.526	-3.47	-0.474	-3.37
0.626	-3.59	-0.574	-3.71

High slope mean = -3.64
Standard deviation= 0.25

7.6 Positioning and scaling the bias triangles

It is now possible to draw the singlet and triplet bias triangles. The shape of each triangle is known precisely in terms of the high, low, and base slopes. In this section, we explain how the sizes of the triangles are determined and how they are positioned on the data.

The size of the triangles is proportional to the source-drain bias. To determine the scaling, we focus on the forward bias data sets. By using the triple point spacing d, in combination with line fits of the type shown in Fig. 7.4, the triangles for the forward bias data are completely determined. We extract a gate voltage-to-energy proportionality constant for each forward bias data set for both V_{CS} and V_G, and we calculate the mean

values of each. We use these constants to set the size of the triangles for the reverse bias data. The sizes of the triangles drawn in column 4 of Fig. 7.2 are all obtained using these mean voltage-to-energy calibrations.

We now position the triangles in the forward bias regime. Since line segment CD cannot be easily distinguished from AF in the forward bias data, the triplet triangles are initially positioned by assuming that AF and CD overlap. That is, we assume zero $(1,1)$ singlet-triplet energy splitting. The actual $(1,1)$ singlet-triplet splitting is determined later. We then determine the base position of the triplet triangle by performing a Lorentzian fit to a data cut along line segment BF, placing the triangle corner at the peak of the Lorentzian.

To position the singlet triangles on the reverse bias data plots, we only need to determine a single point, which we take to be point Q in Fig. 7.3(b). This point is determined for each data set by fitting a Lorentzian to a data cut along line segment RQ. Similarly, the triplet triangles are positioned by performing a Lorentzian fit to point U along the line segment VU. This method of independently positioning the singlet and triplet triangles provides a means of estimating the (1,1) singlet-triplet splitting, which is observed as a slight shift in the edges of the triangles. Note that, due to the lack of a straight line of current for the two higher bias data sets, we use the coordinates of the strongest current peak in that vicinity to locate point U. This should lead to an overestimate of the (1,1) singlet-triplet energy splitting in those two cases.

The (2,0) singlet-triplet splitting is given by the distance between the bases of the singlet and triplet triangles. These voltages are converted to energies using our lever-arm calibrations. We then take a mean value from all eight data sets, obtaining the result $E_{ST}(2,0) = 0.173$ meV, as reported in Table 7.4. This value is interesting, because it corresponds to the lowest excited state that is not a spin excitation. In general, this degree of freedom will involve an orbital parameter, and specifically, it can correspond to the valley degree of freedom. As such, the mean value of $E_{ST}(2,0)$ provides a lower bound on the valley splitting [95, 124, 125, 126, 96, 39] in dot 1.

We can compute the singlet-triplet splittings $E_{ST}(1,1)$ in a similar manner. Such esti-

mates can only be obtained in the LET data sets, since the forward bias data sets do not provide a good signature of the splitting. We find that the standard deviation of $E_{ST}(1,1)$ is almost as large as its mean value. Such a large uncertainty in $E_{ST}(1,1)$ is not surprising, because its value is similar to the estimated electron temperature during these measurements, which is 145 mK. The resulting estimates for $E_{ST}(1,1)$ is reported in Table 7.4.

Table 7.4: Singlet-triplet energy splitting.

V_{SD} (mV)	$E_{ST}(1,1)$ (meV)	$E_{ST}(2,0)$ (meV)
-0.174	0.0078	0.170
-0.274	0.0044	0.174
-0.474	0.0306	0.148
-0.574	0.0345	0.193
0.226		0.200
0.326		0.178
0.526		0.155
0.626		0.162
Mean	0.019	0.173
Standard deviation	0.015	0.018

7.7 Theoretical model for energy-dependent tunneling effects

In this section, we investigate processes related to LET in the reverse bias regime, and we analyze energy-dependent tunneling and its impact on the transport. We focus specifically on the lower two triangles of Fig. 7.3(b). In this case, one valence electron is always present in the left dot, while a second valence electron transits the double dot from the left to the right, in the charging sequence $(1,0) \rightarrow (2,0) \rightarrow (1,1) \rightarrow (1,0)$. Note that a downhill energy path between the left and right dots corresponds to a positive value of the detuning parameter, $\epsilon \equiv (E_1 - E_2) > 0$, where E_1 and E_2 are the chemical potentials of the left dot (dot 1) and the right dot (dot 2), respectively.

Qualitative Discussion

In Ref. [115], a sequential tunneling model was used to analyze the reverse bias transport

currents. In the sequential tunneling approximation, the current through a particular transport channel can be expressed as $(I/e)^{-1} = \Gamma_L^{-1} + \Gamma_{12}^{-1} + \Gamma_R^{-1}$, where the L index refers to the $L \rightarrow 1$ tunnel process, the R index refers to the $2 \rightarrow R$ process, and the 12 index refers to tunneling between dots 1 and 2. As in previous sections, L and R refer to the left and right leads. In Ref. [115], two transport channels were studied: the singlet channel (S) and the triplet channel (T).

The sequential tunneling model provides a great deal of information. For example, it explains why the lower portions of the data in Fig. 7.2(c) and (g) take the distinctive form of two parallel lines, rather than a triangle: the two lines correspond to distinct transport processes through the singlet and triplet channels. For either channel, the current is effectively determined by the bottleneck process, which turns out to be Γ_L or Γ_{12}. Since the function Γ_L depends sensitively on the chemical potential of dot 1, due to energy dependent tunneling, we observe that I is exponentially suppressed when $E_1 < E_{LF}$, reducing the bias 'triangle' to a narrow line. Thus, the lower current feature in Fig. 7.3(b) actually consists of two overlapping triangles (a singlet triangle and a triplet triangle), each of which is reduced to a narrow line due to energy dependent tunneling.

Despite its success, the sequential tunneling model is over-simplified and cannot explain certain crucial features of the transport current. For example, the strong enhancements of the transport current at the points marked Q and U in Fig. 7.3(b) are resonances arising from the coherent delocalization of electrons in dots 1 and 2. Such effects cannot be explained by an incoherent tunneling model. The master equation approach of Nazarov and Stoof does incorporate resonant effects [117, 118]. However, it does not account for the inelastic, sequential tunneling processes that dominate the transport throughout most of the current map. We use a master equation technique that incorporates both resonant and inelastic tunneling effects to address this situation.

Quantitative Analysis

The theoretical model that we use for the quantitative analysis is presented in detail in Appendix F.3. This model treats the S and T transport channels independently, and treats the coupling to the environment within the Lindblad formalism [73, 2]. The analysis yields

an expression for the current I through a single channel in the two-electron dot:

$$I = e\Gamma_L\Gamma_R \frac{\begin{array}{l}\left\{4g^2(f_L - f_R)[\Gamma_L(1-f_L) + \Gamma_R(1-f_R) + \Gamma_i]\right. \\ \left. +\Gamma_i\left(4(\epsilon/\hbar)^2 + [\Gamma_L(1-f_L) + \Gamma_R(1-f_R) + \Gamma_i]^2\right)[f_L(1-f_R)\theta - f_R(1-f_L)\bar{\theta}]\right\}\end{array}}{\begin{array}{l}\left\{\left[4(\epsilon/\hbar)^2 + [\Gamma_L(1-f_L) + \Gamma_R(1-f_R) + \Gamma_i]^2\right]\right. \\ \times\left[\Gamma_L\Gamma_R(1 - f_L f_R) + \Gamma_i\Gamma_R(\theta + f_R\bar{\theta}) + \Gamma_i\Gamma_L(\bar{\theta} + f_L\theta)\right] \\ \left. +4g^2\left[\Gamma_L(1-f_L) + \Gamma_R(1-f_R) + \Gamma_i\right]\left[\Gamma_L(1+f_L) + \Gamma_R(1+f_R)\right]\right\}\end{array}}. \tag{7.6}$$

Here, g is the (elastic) tunnel coupling between the two dots, ϵ is the energy difference between the (2,0) charge configuration and the (1,1) charge configuration, f_L and f_R are the Fermi functions for the two leads L and R (they of course depend on energy, but this dependence is suppressed in the notation for brevity), Γ_L is the tunnel coupling between the left lead L and dot 1, Γ_R is the tunnel coupling between the right lead R and dot 2, Γ_i is the inelastic interdot coupling, and θ and $\bar{\theta}$, which account for the fact that phonon emission is much more likely than phonon absorption at low temperatures, are taken here to be Heaviside step functions: $\theta = \Theta(\epsilon)$ and $\bar{\theta} = \Theta(-\epsilon)$, with $\Theta(\epsilon) = 0$ when $\epsilon < 0$, $\Theta(\epsilon) = 1/2$ when $\epsilon = 0$, and $\Theta(\epsilon) = 1$ when $\epsilon > 0$. The inelastic interdot tunnel coupling Γ_i is a weak, even function of ϵ. Below, we show that our data are consistent with $\Gamma_i = (\text{constant})$ throughout most of the bias triangle. When the singlet and triplet channels are fully decoupled, as we assume here, the total current is expressed as a sum of terms like Eq. (7.6), one for each channel. For the case of triplet states that are triply degenerate, the total triplet current is therefore the sum of three terms, one for each state.

7.8 Analysis of data yielding information about energy-dependent tunneling

In this section, we first perform a fitting analysis using Eq. (7.6) to obtain estimates for the various tunneling parameters, including the energy dependent tunneling. We then go on to discuss the prominent features in the current map. We finish up by checking the self-consistency of our LET assumption of decoupling between the single and triplet channels,

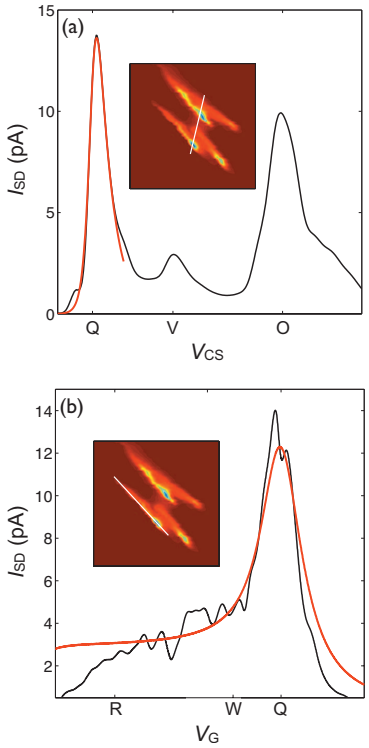

Figure 7.5: Fits to data cuts. (a) Black curve: a cut through the data obtained along the line segment QVO, as indicated in the inset. Red curve: a fit to the 1D data cut, using the theoretical formula in Eq. (7.11). (b) Black curve: a cut through the data along the line segment RWQ, as indicated in the inset. Red curve: a cut through the theoretical fit to the 2D data set, evaluated along the same line. The data were fit using the full theoretical model of Eq. (7.6).

and we discuss the implications for preferential loading of the excited states.

Fitting analysis of the tunnel parameters

We begin with an investigation of the various tunnel rates in the LET regime. The transport data of Fig. 7.2(g) will be analyzed along particular cuts. We first consider the cut QVO, which is along the base of the singlet triangle, as shown in Fig. 7.5(a). We also consider the data cut RWQ, which is along the high slope of the singlet triangle, as shown in Fig. 7.5(b). Along the latter cut, the data exhibit two prominent features: a Lorentzian peak, which is characteristic of resonant tunneling, and a relatively flat region to the left of the peak, which is characteristic of inelastic tunneling [119].

We first analyze the singlet inelastic transport current, which dominates the current flow

over most of the singlet bias triangle, except near the line QV. As we shall see, the tunnel coupling g has a characteristic magnitude of μeV, while the length of the bias triangle is on the order of hundreds of μeV, in energy units. Thus, away from line segment QV, the condition $\epsilon \gg \hbar t$ is true almost everywhere. Equation (7.6) then reduces to the expected form for sequential tunneling

$$I/e \simeq f_L(1-f_R)\left[\Gamma_L^{-1}+\Gamma_R^{-1}+\Gamma_i^{-1}\right]^{-1}, \tag{7.7}$$

where the tunneling between dots 1 and 2 is strictly inelastic.

To make further progress, it is useful to introduce a specific model for the tunneling rates between the dots and the leads. For simplicity, we consider square tunnel barriers, for which the leading order energy dependence of the tunnel rate is exponential and is given by [109]

$$\Gamma(E) = \Gamma_0 e^{-2W\sqrt{2m^*(U-E)/\hbar^2}}. \tag{7.8}$$

Here, W is the barrier width, U is its height, and E is the energy of the tunneling electron. Since our transport data do not exhibit enough structure to independently determine the parameters characterizing the tunnel barriers, we consider an alternative tunneling function by linearizing the argument of the exponential in Eq. (7.8) about one of the lead Fermi levels (see Refs. [43] and [32]). For the tunneling function between the left lead and dot 1, we perform our expansion around the Fermi energy of the left lead, obtaining

$$\Gamma_L(E_1) \simeq \Gamma_{L0} e^{(E_1-E_{LF})/E_{L0}}, \tag{7.9}$$

with the characteristic energy defined as $E_{L0} = [(U_L - E_{LF})\hbar^2/2m^*W_L^2]^{1/2}$. An analogous linearization can also be performed for the right lead.

We first consider the singlet triangle. We can make a rough comparison of the magnitudes of the different tunnel rates in Eq. (7.7), based on general observations of the data in Fig. 7.5. We first consider the flat region near point W in panel (b). To the left of this region, the bias triangle closes, due to the action of the Fermi functions. To the right, we observe the resonant peak at point Q. Along the line segment RQ, the chemical potential of the left dot is constant, so Γ_L must be constant, but Γ_R need not be. Since the data are

almost flat, Γ_R must not determine the shape of the current flow. For data cuts parallel to line segment QVO, the detuning parameter ϵ is a constant, so Γ_i must be almost constant. However, the current has a strong energy dependence, which cannot be due to Γ_i. Together, these facts suggest that the energy dependence of Γ_L controls the shape of the current in the inelastic tunneling regime, although not necessarily its magnitude. We conclude that the functions Γ_R and Γ_i must either be much larger than Γ_L or constants in the inelastic tunneling regime.

We now perform a more quantitative analysis by considering the line QV, defined by the resonant condition $\epsilon = 0$. Because of the resonance, terms involving g must be dominant in Eq. (7.6). Away from the long edges of the triangle, Eq. (7.6) then reduces to

$$I/e \simeq (\Gamma_L^{-1} + 2\Gamma_R^{-1})^{-1}. \tag{7.10}$$

As expected, we find that the inelastic tunneling contribution, Γ_i, is irrelevant in the resonant regime. This fact makes it possible to independently determine the parameters Γ_R and Γ_i. By comparing Eqs. (7.7) and (7.10) and noting that the current in Fig. 7.5(b) is much larger at point Q than point W, we conclude that $\Gamma_i \ll \Gamma_R$ in the inelastic tunneling regime. This fact is not affected by the resonance condition. Since Γ_L corresponds to the bottleneck process in the resonant tunneling regime, we find that $\Gamma_L, \Gamma_i \ll \Gamma_R$. Equation (7.6) then reduces to

$$I/e \simeq \Gamma_L(f_L - f_R). \tag{7.11}$$

We can fit Eq. (7.11) to the data cut along QV, as shown in Fig. 7.5(a). This gives a direct estimate for the temperature and the energy dependent tunneling parameters in the linearized function Γ_L. We can obtain the remaining singlet tunneling parameters by performing a 2D fit of the data to the full expression in Eq. (7.6). This provides estimates for the parameters Γ_i, Γ_R and g, with results shown in Table 7.5. We note that since Γ_R has been proven to be irrelevant in our LET data, it was not possible to discern any energy dependence in this parameter. Thus, we have treated Γ_R as a constant in our analysis. In Fig. 7.5(b), we show one result from our 2D fitting procedure, as evaluated along the line segment RWQ .

Table 7.5: Fitting parameters and singlet-triplet energy splittings for the Si/SiGe double quantum dot transport model presented in Eq. (7.6) for the data in Fig. 7.2(g). The energy dependent tunneling parameters and the singlet-triplet energy splittings are described in the text. Standard deviations are given in square brackets.

	Energy (μeV)
$h\Gamma_{L0S}$	0.62 [0.01]
E_{L0S}	40 [2]
$h\Gamma_{iS}$	0.125 [0.003]
$\hbar g_S$	3.2 [1.2]
$h\Gamma_{RS}$	38 [28]
$h\Gamma_{L0T}$	0.48 [0.01]
E_{L0T}	34 [3]
$h\Gamma_{iT}$	0.183 [0.003]
$\hbar g_T$	2.0 [0.1]
$h\Gamma_{RT}$	55 [8]
Temperature	145 [7] mK
E_{ST}, (2,0) state	174 [38]
E_{ST}, (1,1) state	4 [1]

Prominent features in the data

It is instructive to consider limiting cases of Eq. (7.6) that are relevant for our LET data, in order to gain a better physical understanding. We specifically consider the bright line of current adjacent to line segment RWQ. As apparent from Fig. 7.4(e), the Fermi function for the left lead is nearly saturated along this line, so that $f_L \simeq 1$ and $f_R \simeq 0$. In this regime, the transport current takes the form

$$\frac{I}{e} \simeq \frac{\Gamma_L \left[1 + \epsilon^2 \Gamma_i \theta/(\hbar g)^2 \Gamma_R\right]}{\left[1 + \epsilon^2 (\Gamma_L + \Gamma_i \theta)/(\hbar g)^2 \Gamma_R\right]}, \tag{7.12}$$

corresponding to a Lorentzian line-shape centered on the resonant condition $\epsilon = 0$. The half-width of the peak is given by $\epsilon_{1/2}^2 \simeq (\hbar g)^2 \Gamma_{Rp}/\Gamma_{Lp}$, where Γ_{Lp} and Γ_{Rp} correspond to barrier tunnel rates, evaluated at the peak value of the current. Along the line from Q to R, the functions Γ_L and g remain approximately constant. To the left of the peak, the data are nearly flat, as shown in Fig. 7.5(b), with asymptotic behaviors determined by the bottleneck rate Γ_i. (Note from Table 7.5 that $\Gamma_{iS} \lesssim \Gamma_{LS}$ along line segment RWQ.) We conclude that Γ_{iS} is nearly constant as a function of ϵ. The dips in the data between R

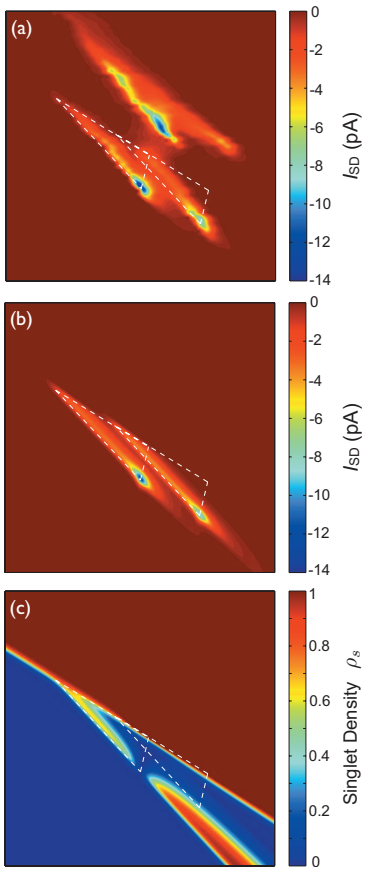

Figure 7.6: Comparison of the experimental data with calculations based on the fitting parameters of Table 7.5, obtained for the same range of gate voltages. (a) Current transport data, identical to Fig. 7.2g, with an overlay of the edges of the singlet and triplet lower bias triangles. (b) Theoretical reconstruction of the lower bias triangles, based on Eq. (7.6). (c) The computed singlet occupation density, $\rho_S = \rho_{1S} + \rho_{2S}$, shows that the singlet occuption falls off in the vicinity of the triplet triangle, as required for the observation of LET.

and W are due to drifts in the measurement. The suppression of the current to the left of R is probably caused by energy dependent variations of Γ_i, which are not included in our model. It is interesting to note that the general shape of the curve described in Eq. (7.12) is relatively insensitive to changes in Γ_R. This is consistent with the fact that tunneling from dot 2 to the right lead is the fastest of the tunnel rates, and it is therefore never a bottleneck.

To the right of the resonant peak in Fig. 7.5(b), the following conditions are satisfied: $\theta = 0$ and $-\epsilon \gg \hbar g$, so Eq. (7.12) is is no longer valid. The current in this region is more

strongly suppressed than the linearized theory we discuss here predicts.

Using the fitting parameters reported in Table 7.5, Eq. (7.6) can be used to reconstruct the singlet and triplet bias triangles corresponding to the electron transport data shown in Figs. 7.2(g) and 7.6(a). The resulting theoretical fits are presented in Fig. 7.6(b). The fits are quite satisfactory, and they provide strong support for the double dot theory described above.

Self-consistency check

In Sec. 7.7, we noted that the singlet and triplet transport channels should approximately decouple, if our theory is valid. As a self-consistency test, we should check whether this statement is consistent with the tunneling parameters obtained from the fitting procedure. Specifically, we want to show that the singlet density, $\rho_S = \rho_{S1} + \rho_{S2}$, is small wherever the triplet density, $\rho_T = \rho_{T1} + \rho_{T2}$, is appreciable, and vice versa.

The formalism developed in Appendix F.3 and Sec. 7.7 allows us to compute the steady-state occupations for dots 1 and 2, as a function of the tunneling coefficients. For either the singlet or the triplet triangles, the formalism of Sec. 7.7 leads to

$$\rho_1 + \rho_2 = \frac{\begin{array}{l}\big\{[4(\epsilon/\hbar)^2 + [\Gamma_L(1-f_L) + \Gamma_R(1-f_R) + \Gamma_i]^2] \\ \times [\Gamma_L\Gamma_R(f_L + f_R - 2f_Lf_R) + \Gamma_i(\Gamma_R f_R + \Gamma_L f_L)] \\ +8g^2[\Gamma_L(1-f_L) + \Gamma_R(1-f_R) + \Gamma_i][f_L\Gamma_L + f_R\Gamma_R]\big\}\end{array}}{\begin{array}{l}\big\{\big[4(\epsilon/\hbar)^2 + [\Gamma_L(1-f_L) + \Gamma_R(1-f_R) + \Gamma_i]^2\big] \\ \times \big[\Gamma_L\Gamma_R(1-f_Lf_R) + \Gamma_i\Gamma_R(\theta + f_R\bar{\theta}) + \Gamma_i\Gamma_L(\bar{\theta} + f_L\theta)\big] \\ +4g^2[\Gamma_L(1-f_L) + \Gamma_R(1-f_R) + \Gamma_i][\Gamma_L(1+f_L) + \Gamma_R(1+f_R)]\big\}\end{array}}. \tag{7.13}$$

In Fig. 7.6(c), we plot $\rho_S = \rho_{1S} + \rho_{2S}$ using the fitting parameters from Table 7.5. We conclude that the singlet density does indeed vanish inside the triplet triangle, in the portions of the triangle where current flow is appreciable. Below the singlet and triplet triangles, in the lower-right portion of Fig. 7.6(c), the theoretical model indicates an anomalous region of singlet occupation. Such behavior is spurious, and it is a consequence of using energy dependent tunneling models outside their range of validity.

Triplet relaxation and loading of excited states

We first address the question of triplet-to-singlet relaxation. In many experimental situa-

tions, the current is blockaded outside the singlet triangle [108, 19]. We have shown that in the LET regime, the triplet channel is not necessarily blockaded. However when the triplet loading is favored, if a (2,0) triplet decays to a (2,0) singlet faster than the singlet can unload, then current through the triplet triangle will be effectively blockaded. We have also shown that the condition for this blockade to be lifted is that the total singlet loading rate, including loading via triplet decay, should be of the same order or smaller than the singlet unloading rate [115]. The observation of current flow in the triplet tail indicates that these conditions are met in our sample.

In this Chapter, we did not explicitly consider the triplet-to-singlet decay channel. However, the decay 'current' must be bounded by the total loading current for the singlet. As reported in Ref. [115], we can fit the resonance in Fig. 7.5(a) close to the peak, to avoid spurious structure possibly related to cotunneling. In this way, we obtain a bound on the triplet-singlet decay rate, given by $\Gamma_{TS} < 1.45 \times 10^6$ s^{-1}. This bound differs from that published previously, because it depends exponentially on the singlet-triplet splitting and the gate voltage-to-energy calibration, both of which have been determined to a greater accuracy in this Chapter. The actual value of Γ_{TS} is expected to be much smaller than this current estimate or that published previously in Ref. [115].

Finally, we can investigate selective tunneling into the triplet and singlet states. We have shown that there is a very strong energy dependence for tunneling into the double dot. Tunneling into a singlet state proceeds at a very different rate than tunneling into a triplet, even when they are at the same energy. However, our analysis shows that the (2,0) triplet state is split off from the (2,0) singlet by a large amount: $E_{ST} = 173\,\mu$eV. Electrons tunneling into these two states therefore experience very different barriers. Based on our analysis of the transport data, we can estimate this difference by comparing the ratio of the singlet vs. triplet loading rates, as

$$\frac{\Gamma_{S,\mathrm{load}}}{\Gamma_{T,\mathrm{load}}} = \frac{f_L(E_1)\Gamma_{LS}(E_1)}{f_L(E_1+E_{ST})\Gamma_{LT}(E_1+E_{ST})}. \tag{7.14}$$

When the triplet lies above the Fermi level of the left lead, there will be a very strong suppression of the triplet loading. On the other hand, when both the singlet and triplet lie

below the Fermi level, we observe a very strong enhancement of the triplet, as compared to the singlet. For the tunneling parameters extracted above, this enhancement factor is on the of order 100. However, this is actually an under-estimate, owing to our use of linearized tunnel functions. Comparison of Figs. 7.6(a) and 7.6(b) shows that, in regions with low current flow, the experimental transport current is more strongly suppressed than the theoretical prediction. In general, the suppression of singlet tunneling in this regime should be enhanced for materials like silicon, which have relatively large effective masses. For example, by using linearized tunneling functions and setting the Fermi functions to 1 in Eq. (7.14), we obtain

$$\frac{\Gamma_{LS}(E_1)}{\Gamma_{LT}(E_1+E_{ST})} \propto \exp\left[E_{ST}\sqrt{2m^*W^2/(U-E_{LF})}\right]. \tag{7.15}$$

Here, we see that the effective mass appears inside the exponential.

7.9 Discussion

In this Chapter we performed a detailed analysis of eight sets of data measuring current through a double quantum dot. A striking feature of the data in reverse bias is the presence of a strong tail of current that extends outside the boundaries of the usual bias triangle and that we attribute to lifetime-enhanced transport (LET). The data also contain features that are difficult to explain using the conventional double dot transport theory, which assumes a single bias triangle. Yet, they are explained quite naturally when the data are fit to a pair of bias triangles, corresponding to distinct singlet and the triplet channels, as presented in columns 2 and 4 of Fig. 7.2. In Fig. 7.2(b), the region with strong current is broader on the electron-triangle side than on the hole-triangle side. The region with strong current on the electron-triangle side lies largely within the triplet triangle shown in red. It is clear throughout that tunneling through the $T_{1,1} \rightarrow T_{2,0}$ channel is very strong in the reverse bias (LET) direction, and this resonance appears to show up in the forward bias (spin blockade) direction as well.

It is worth noting that the tunnel rate between the two dots in this experiment was quite

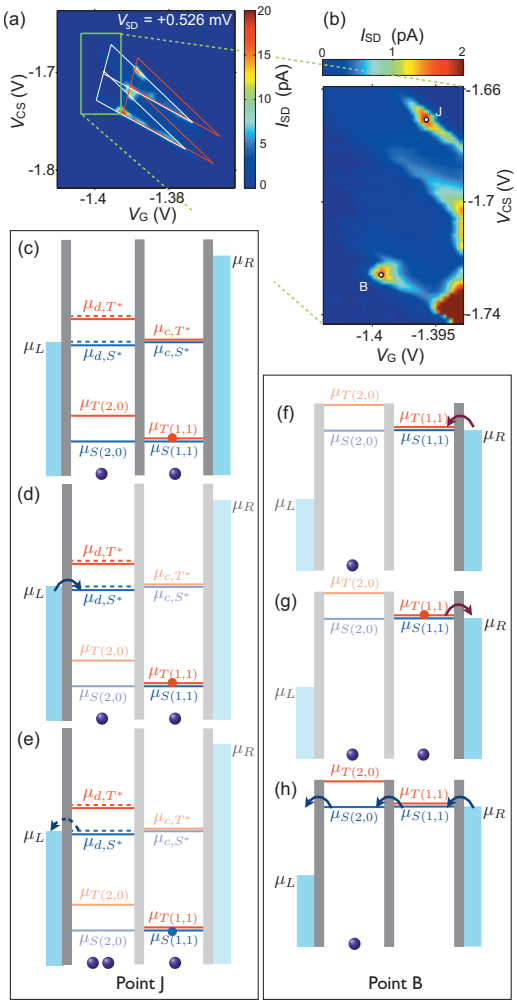

Figure 7.7: Description of the spin exchange processes between a dot and a lead at points B and J in Fig. 7.3(a). (a) Transport data at source-drain bias of $V_{\mathrm{SD}} = 0.526$ mV. (b) A blow-up of the data inside the green box in panel (a). The color scale is expanded to show the current at points B and J, which are important for determining the base slope, as discussed in Sec. 7.5. (c) Configuration in which the $T_{1,1}$ state is spin blockaded, in the three electron or 'hole triangle' regime. (d) An electron can tunnel into the left dot from the left lead, forming a singlet-like (2,1) state. (e) The singlet-like (2,1) state can emit an electron to the left lead, leaving the system in the $S_{1,1}$ state, and lifting spin blockade. (f) In the 'electron triangle' regime with two electrons, loading of the $T_{1,1}$ state from the right lead results in spin blockade. (g) The electron in the right dot can tunnel back to the right lead, allowing the right dot to be reloaded into the $S_{1,1}$ state. (h) When the $S_{1,1}$ state is loaded from the right lead, transport can resume through the double dot.

high. This rate was not easily tuned, because the device was not specifically designed with a gate for this purpose. However, this is not a limiting factor for future experiments. In other recent work, a double dot in Si/SiGe was specifically designed with tunable couplings, and the corresponding tunnel rates were found to be highly tunable [77]. As described in Sec. 7.4, the electron occupation of our double dot could not be absolutely determined here. However, recently, a double dot with a known one-electron occupation has been demonstrated in a different Si/SiGe experiment [88].

The ability to control energy dependent tunneling is an important tool for measuring spin qubits [44]. Here, we observe energy dependent tunneling so strong that in many cases it deforms a bias triangle into a thin line. Our fitting analysis indicates that the tunnel rates to the leads can change by a factor of $1/e$ when the dot chemical potential is varied by as little as 30-40 μeV.

The consistency of the analysis of all the data sets provides strong evidence that lifetime-enhanced transport occurs in a Si/SiGe double dot. The demonstration that quantum dots can be fabricated in Si/SiGe heterostructures that exhibit high-quality spin blockade as well as a new transport channel that only occurs when spin relaxation times are long is evidence that this materials system has promise for the manufacture of devices requiring spin coherence.

Chapter 8

Transport II: Unconventional three-electron regime

8.1 Introduction

Understanding spin-dependent transport [106, 105, 115, 108, 114] is important for using the spin degree of freedom in a double dot qubit. In the previous Chapter, we analyzed transport in the two-electron regime, and explained how spin blockade and lifetime-enhanced transport gave rise to characteristic features of the data. Here, we show that transport data taken in the three-electron regime of a double dot in a Si/SiGe heterostructure have features that are qualitatively inconsistent with the conventional model of 'hole' transport [110], because this model does not account for transport through excited states. Using the Configuration Interaction (CI) formalism with singly excited configurations [127], together with relevant CI parameters extracted from the transport data (see Chapter 7 and Ref. [24]), we demonstrate that the striking features in the data arise from a novel spin-flip cotunneling process in which the multi-electron nature of the system enters fundamentally.

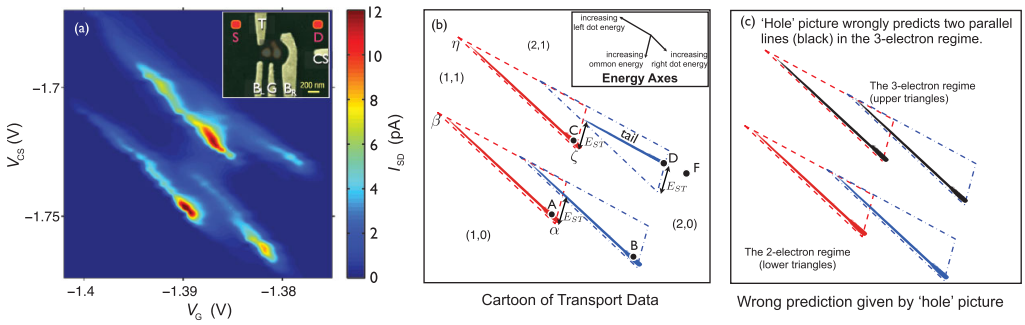

Figure 8.1: (a) Transport current $I_{\rm SD}$ in a Si/SiGe double quantum dot (color scale) as a function of controlling gate voltages, $V_{\rm G}$ (V) and $V_{\rm CS}$ (V), reported in Ref. [115]. Inset shows an SEM image of the gates with a numerically simulated double dot overlayed. White letters (T, $\rm B_L$, G, $\rm B_R$ and CS) label gates and red letters (S, D) label the source and drain. For this data, electrons flow from left to right. (b) A cartoon of the bias triangles and lines of high current. Inset shows the energy axes of the dots. The lower (upper) features are the electron (hole) triangles. Red dashed lines represent current through the singlet (singlet-like) channel of the electron (hole) bias triangle and blue dot-dashed lines the triplet (triplet-like) triangle. A and B are resonant peaks of the singlet and triplet electron triangles. C is the resonant peak of the singlet-like hole triangle. A and C are the triple points at the boundary of the (1,0), (1,1), (2,0) and (1,1), (2,0), (2,1) charge occupations. F lies along the line extending from the tail; it is a representative point where cotunneling is dominant. E_{ST} is the (2,0) singlet-triplet energy splitting. Data are obtained at a reverse-bias source-drain voltage, $V_{\rm SD} = -0.274$ mV, first published in Ref. [115] as -0.3 mV. Ref. [24] details the quantitative fits to identify the triangles. (c) The prediction using the conventional hole picture in the three-electron regime is shown as two parallel lines (black), which is inconsistent with the tail observed in the data.

8.2 Validity of conventional model

Several experiments have probed charge transport through double quantum dots in the few-electron regime and investigated effects such as energy-dependent tunneling and spin-dependent transport [106, 105, 115, 108, 114]. Transport in the three-electron regime is well-described in terms of holes when all the intra-dot relaxation rates are much faster than the interdot tunnel rate, so that the dominant transport channels are through the lowest energy states of each dot, as is typically the case in GaAs devices [108, 110].

Our theoretical work is based on data [115], in which a lateral double quantum dot was formed by electrostatic gating of a Si/SiGe heterostructure, as shown in the inset of Fig. 8.1(a). Fig. 8.1(a) shows source-drain current versus controlling gate voltages at a fixed

source-drain bias voltage. Transport through the two dots is energetically favorable within triangular regions whose size is determined by the source-drain bias. Lines of high current in these bias triangles are associated with fast tunneling between the dots and between the dots and the leads [110]. From the orientation of the line $\alpha\beta$ in Fig. 8.1(b), we deduce that it is associated with the resonance of an energy level in the 'left' dot with the chemical potential in the left lead. Quantitative fits allow the edges of the triangles to be determined and are reported in detail in Ref. [24] (see Chapter 7). Fig. 8.1(b) is a schematic diagram of the bias triangles, with energy axes shown in the inset. The lower features arise from transport when the double dot contains either one or two-electrons ('two-electron' regime), while the upper features reflect transport when the dot contains either two or three-electrons ('three-electron' regime, also conventionally termed 'hole' regime).

There are two regions of current flow in each transport regime, shown in Fig. 8.1(a). Each of these regions of current is contained in a triangle, shown in either blue or red in Fig. 8.1(b). The presence of current in the blue triangle implies that there is significant transport through excited states of the dots [115, 24], something that has recently been observed in transport through a single phosphorous donor in silicon as well [116].

Because the effective electronic mass in Si is much larger than in GaAs, transport is energetically favorable within each bias triangle, but the triangle is not entirely filled because the electron tunneling rate is strongly energy-dependent [106, 105, 115]. The two parallel lines of high current that are observed along the left edges of the singlet and triplet triangles in the two-electron regime (lower feature) indicate that energy-dependent tunneling across the left barrier is the bottleneck in the total tunneling rate [24].

In the three-electron regime, the conventional picture that describes the conduction in terms of holes predicts that there should be two parallel lines of high current (Fig. 8.1(c)). This is because, in the two-electron regime, electron occupancy cycles through the states (1,0) $\rightarrow$ (2,0) $\rightarrow$ (1,1), and the three-electron regime is modeled conventionally [110] as hole transport in the opposite direction: (1,1) $\rightarrow$ (0,2) $\rightarrow$ (0,1), where the numbers represent electron or hole occupancy in the left and right dots. Due to particle-hole symmetry, the

hole picture predicts parallel lines of high current similar to the data in the two-electron regime (Fig. 8.1(c)).

The transport data in Fig. 8.1(a) is inconsistent with a picture in terms of holes, as it shows two lines of high current in the three-electron regime (upper feature) that are clearly not parallel. In this regime, there is a line of high current at the left edge of the bias triangle (line $\zeta\eta$) for ground state transport, which is expected since the left barrier is observed to be the bottleneck in the two-electron regime. However, in the bias triangle for excited state transport, there is a 'tail' parallel to the right edge but away from it, which the hole picture completely fails to describe.

8.3 Configuration Interaction approach

To understand the problem theoretically, we formulate it in terms of chemical potentials and use the Configuration Interaction (CI) approximation with singly excited configurations to determine the spin eigenfunctions and energy levels of each of the double dot states involved in the three-electron regime. The relevant parameters in the CI formulation are extracted from the transport data as detailed in Ref. [24]. From the energy levels and possible transitions between states, we calculate the electrochemical potentials for charging or discharging a dot by one electron (see Appendix G). The four relevant electrochemical potentials for the dots are shown for the two-electron case in Fig. 8.2(a,b). For the three-electron case, the full set of ten electrochemical potentials, shown in Fig. 8.2(c,d), is clearly greater than the four electrochemical potentials for transport modeled on two holes. The many-electron nature of the problem thus enters our analysis of transport naturally.

Without going into the details of the CI calculations, we can gain some insight into the possible (2,1) states using qualitative arguments. The pure singlet and triplet states, $S(2,0)$ and $T(2,0)$, are no longer orthogonal when we include a weak coupling to a third electron in the right dot. The perturbation leads to a 'singlet-like' ground state $S^*(2,1)$, whose spin configuration in the left dot is mainly $S(2,0)$ with a small admixture of $T(2,0)$. The $S^*(2,1)$ state has spin $S_z = \pm 1/2$ and is doubly degenerate. The perturbation also

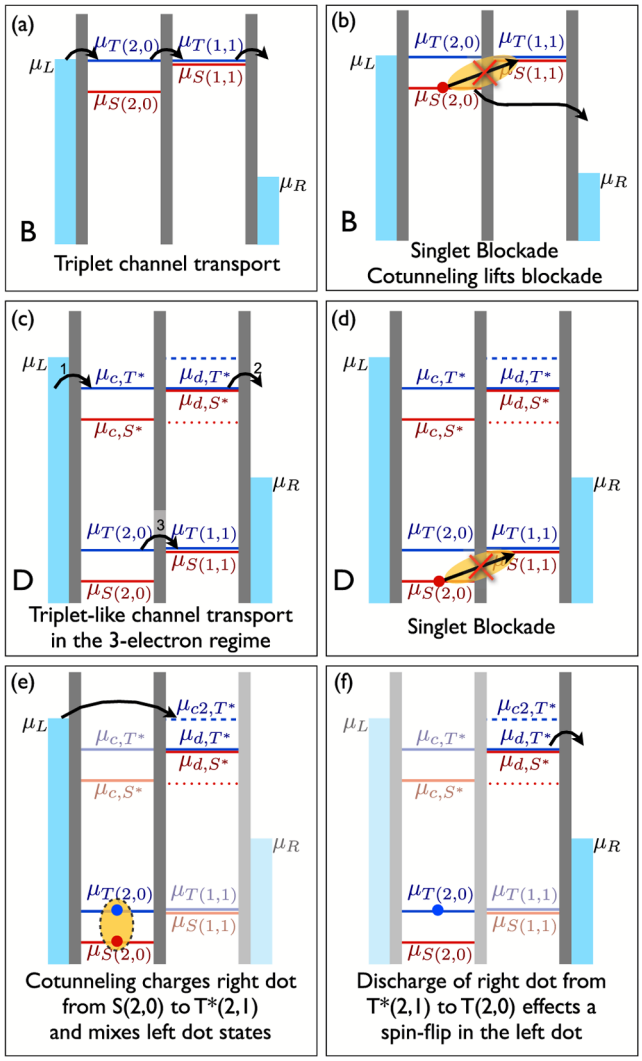

Figure 8.2: Diagrams for transport through excited states and the process of 'spin-flip cotunneling.' (a) Triplet channel transport in the two-electron regime. At B, the resonant peak of the triplet channel, transport is allowed through the triplet levels, $\mu_{T(2,0)}$ and $\mu_{T(1,1)}$. (b) When the singlet level $\mu_{S(2,0)}$ is loaded, transport is energetically uphill and blockaded. Cotunneling of a left dot electron out to the right lead lifts the blockade to resume triplet channel transport. (c) In the three-electron regime, transport occurs in the following cycle: step 1, $(1,1) \rightarrow (2,1)$; step 2, $(2,1) \rightarrow (2,0)$; step 3, $(2,0) \rightarrow (1,1)$. At D, these occur through the triplet-like channel (blue). (d) Because of the loading of the singlet-like μ_{c,S^*} level (red) at D, the system ends up in the $S(2,0)$ state, whereby transport is blockaded. (e) When an electron cotunnels from the left lead into the right dot to form a triplet-like state, it puts the left dot into an admixture of singlet and triplet. (f) The right dot discharges from μ_{d,T^*}, leaving a triplet state in the left dot, thus causing a spin-flip and resuming transport.

leads to 'triplet-like' states $T^*(2,1)$, for which spin addition gives $S_z = \pm 1/2$ or $\pm 3/2$. The $S_z = \pm 1/2$ states contain mainly triplet $T(2,0)$ with a small admixture of $S(2,0)$. The $S_z = \pm 3/2$ states have spins that are either all up or all down; they are doubly degenerate without any admixture of singlet states. The triplet degeneracies are lifted due to the fact that exchange energies are different for different three-electron spin configurations. The energy splittings arise from inter-dot interactions, which are much smaller than intra-dot interactions. Thus, the splittings within the triplet-like manifold are much finer than the splitting between the singlet- and triplet-like manifolds. These arguments are borne out by our calculations (See Appendix G).

8.4 Transport in the three-electron regime

From the energy levels calculated with the CI Hamiltonian, we can explain how the electrochemical potentials, shown in Fig. 8.2(c), are obtained. In the three-electron regime, electron occupancy cycles through $(1,1) \rightarrow (2,1) \rightarrow (2,0)$. The first transition corresponds to charging of the left dot from a (1,1) to a (2,1) state. For clarity, we do not distinguish between the two closely spaced (1,1) energies, nor do we distinguish between the three closely spaced $T^*(2,1)$ energies. We therefore obtain two distinct electrochemical potentials, μ_{c,T^*} and μ_{c,S^*}, shown in Fig. 8.2(c), which are the energies needed to charge the left dot from a (1,1) state to the $T^*(2,1)$ and $S^*(2,1)$ states respectively. The second transition represents the discharge of an electron from a (2,1) to a (2,0) state. Electrochemical potentials, μ_{d,T^*} and μ_{d,S^*}, drawn on the right dot, represent the discharge of the right dot from $T^*(2,1)$ to $T(2,0)$ and $S^*(2,1)$ to $S(2,0)$ respectively. These are the continuous lines (blue and red) on the right dot in Fig. 8.2(c). Due to singlet-triplet mixing in the left dot, two other transitions of much smaller likelihood are possible. They are the $S^*(2,1)$ to $T(2,0)$ and $T^*(2,1)$ to $S(2,0)$ transitions, represented by the red dotted and blue dashed levels respectively, in the same figures. The last step in the cycle is the inter-dot transition, $(2,0) \rightarrow (1,1)$. The chemical potentials in this step are identical to the two-electron case (Fig. 8.2(a,b)) and are labeled as $\mu_{S,T(2,0)}$ and $\mu_{S,T(1,1)}$.

We can now explain the tail in the transport data, which, as described above, is a prominent feature that is qualitatively inconsistent with a description in terms of holes. At point D in Fig. 8.2(c), transport is allowed through the blue triplet-like levels. However, it is also possible to load the red singlet-like μ_{c,S^*} level. In this case, as the right dot discharges, the system is likely to end up in the $S(2,0)$ state, where transport is energetically uphill and therefore blockaded (Fig. 8.2(d)). We call this a 'singlet blockade.' The lifting of the singlet blockade along the tail is shown in sequence in Figs. 8.2(e) and (f). Starting from $S(2,0)$, the double dot forms a triplet-like $T^*(2,1)$ state when an electron from the left lead cotunnels into the right dot, as shown in Fig. 8.2(e). The charging of the right dot in this transition requires the same energy as its reverse discharging process ($T^*(2,1)$ to $S(2,0)$), represented by the blue dashed line in Fig. 8.2(c). It is labeled by μ_{c2,T^*} in Figs. 8.2(e) and (f). Because the triplet-like state contains an admixture of singlet and triplet states in the left dot, when the right dot discharges from the μ_{d,T^*} level, the left dot ends up in the triplet (2,0) state, thus causing a spin-flip. With the singlet blockade lifted, the system then completes the cycle into the triplet (1,1) state and transport resumes as shown in Fig. 8.2(c). We term this process 'spin-flip cotunneling.'

The tail in the transport data in Fig. 8.1(a) is bright along its entire length because the chemical potentials for the right dot and the left lead are the same. Point D is the brightest point along the tail because of the fast inter-dot tunneling when $\mu_{T(2,0)}$ is aligned with $\mu_{T(1,1)}$.

The spacing of the tail away from the edge of the triangle is consistent with the energy difference between the μ_{c2,T^*} and μ_{d,T^*} levels on the right dot (Fig. 8.2(e)) being equal to E_{ST}, the (2,0) singlet-triplet energy splitting. To understand how this is consistent with the transport data, we start from point C in Fig. 8.1(b) and note that when both dot energies fall by E_{ST}, the blue, dashed μ_{c2,T^*} level of the right dot lines up with the Fermi level of the left lead. This measure of E_{ST} is also consistent with other measures of ST splitting [24].

8.5 Discussion

The significant role cotunneling plays in the triplet and triplet-like transport channels of the two and three-electron regime is interesting. In both cases, cotunneling by itself does not contribute significantly to the current, but plays the role of allowing transport to resume by lifting the singlet blockade.

Current will flow through the triplet-like channel when the loading rate is comparable to the unloading rate in the singlet-like channel (see Appendix G). In Appendix G, we estimate these rates and find that they are indeed the same order of magnitude. The blockade is therefore lifted about as quickly as it is encountered. In this way, spin-flip cotunneling enables transport through the triplet-like channel. The resulting current is that of the unblockaded, triplet-like channel, reduced by a factor of ~ 2 (Appendix G).

Interestingly, transport via the triplet channel was not observed in the experiments reported in Ref. [106]. In that study, a conventional hole model was sufficient to describe transport in the three-electron regime, as consistent with the fact that transport occurred through the ground states in the two-electron regime.

It is also interesting to compare the intra-dot spin-flip times with inter-dot tunneling times for GaAs and Si. In GaAs devices, spin-flip times range from $\sim$200 μs for a two-electron dot [128], to $\sim$0.85 ms (at 8 T [92]) and $>$ 1 s (at 1 T and 120 mK [129]) for single electron dots. Recent experiments report spin-flip times in single electron dots in Si [6, 7, 91, 8] ranging from 40 ms (at 2 T [6]) to 6 s (at 1 T [7]), at low temperatures. The tunnel coupling for the same Si double dot studied here was found to be 10 ns (25 ns) in the elastic (inelastic) tunneling regime [24]. However, tunnel couplings for electrostatically gated semiconductor double dots are tunable and can be both larger or smaller than spin-flip times.

We note that a pulsed gate experiment [108] exhibiting phenomena arising from singlet-triplet mixing, as described above, is presented in Appendix G.

In summary, we have shown that the conventional hole model of transport in the three-electron regime fails qualitatively because of the importance of excited state transport.

The Configuration Interaction formalism, with relevant parameters fitted to transport data, leads to the description of a model which explains all of the features of the transport data, including a novel process of spin-flip cotunneling.

Chapter 9

Conclusions

9.1 Summary

In summary, this thesis considered several aspects of quantum dot qubits in silicon. In Chapters 2 to 4, we considered double quantum dot spin qubits. Here, we presented a novel spin qubit architecture, termed hybrid spin qubit, and showed that implementing it in silicon is feasible. We developed a high speed pulsed-gating protocol for the hybrid spin qubit by utilizing the level crossings afforded to it by its charge degree of freedom. We found the optimal fidelities achievable using different gating protocols. We analyzed the merits of each gating scheme by comparing each of the schemes for the hybrid qubit with another double dot spin qubit – the singlet-triplet qubit.

The next two chapters, 5 and 6, we focussed our attention on decoherence in silicon quantum devices. We extracted charge dephasing rates from coherent charge oscillations using a double quantum dot charge qubit, and showed that the internal electronic states of the qubit enhanced charge coherence. We also extracted long spin relaxation times in a single spin single dot, which was of the order of 3 s. The enhanced coherence times hold substantial promise for coherent, high fidelity quantum manipulation of silicon qubits. In addition, we demonstrated tunable spin loading of more than an order of magnitude, which is particularly promising for spin initialization and readout.

Another aspect of interest to the silicon quantum dot qubit community is that of electronic transport. We described in detail transport through a double dot and explained features of spin-blockade, lifetime-enhanced transport and spin-flip cotunneling, using a theoretical approach that allowed the important parameters of the double dot device to be extracted from data.

9.2 Outlook

The realization of a full-scale quantum computer for quantum information processing tasks remain very much a promise of the future. Different potential technologies [130] are being developed by different research groups around the world to take advantage of the speed-up offered by quantum computation. In order to evaluate any type of hardware platform, one has to examine the complete package that each type of platform has to offer in terms of the resources required to complete various quantum algorithms with negligible error. In general, any hardware platform needs to offer long coherence times, fast coherent control of qubits, high connectivity between qubits, good signal-to-noise ratios, high fidelity initialization and measurement, scalablity, and so on. In this light, quantum dot qubits in silicon have demonstrated some of the desirable properties for a quantum computer platform. However, much work remains to be done in order to fulfill the ambitious goal of building a working quantum computer. In approaching this goal, we will have to learn how to control quantum mechanical systems to the exquisite precision required for quantum information processing. In so doing, we may continue asking the right questions and approach, not just a more sophisticated technological world, but also a richer and more profound understanding of the quantum mechanical nature of reality.

Appendix A

Supplemental material for Chapter 2

This Appendix presents details for four topics in Chapter 2: (1) the calculation, performed using a canonical transformation technique, that shows that transitions between the qubit states can be driven by modulating the tunnel couplings, which can be done by application of appropriate gate voltages; (2) a discussion of the "effective connections" for the qubit geometries shown in Fig. 2.1(d) and Fig. 2.1(e); (3) the presentation of gates of two logical qubits that are equivalent to CNOT up to local unitary operations using gate sequences of 14 and 16 operations for two hybrid qubits implemented in four dots in a linear array. These sequences have fewer operations than for two three-spin qubits implemented in six dots in a linear array, for which the shortest sequence known requires 18 operations; and (4) the presentation of the details of the experiments performed to measure the lifetime of the T_- triplet state in a Si/SiGe quantum dot.

A.1 Derivation of effective Hamiltonian

This section presents the derivation of an effective Hamiltonian that describes the quantum behavior of the hybrid double quantum dot spin qubit in the regime of low energy excitations. Gate voltages control the detuning and the tunnel barrier of the dots. We will

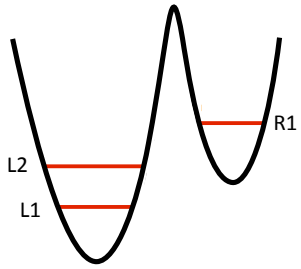

Figure A.1: Schematic of the hybrid spin qubit. Here, levels L1 and L2 refer to the lowest single particle energies of the left, doubly occupied dot and R1 is the lowest single particle energy of the right, singly occupied dot. We assume that changing appropriate gate voltages changes the detuning, or relative energies of the states in the two dots (though always with the (2,1) charge configurations having the lowest energy), and that gates can be used to change the tunnel barrier between the quantum dots.

assume that the gate voltages applied to the quantum dots are kept in the regime in which the the (2,1) charge configuration has lowest energy. Fig. A.1 shows the detuned double quantum dot system with the lowest single particle energies of each dot labeled by 1 and 2.

Before presenting the details of our calculations, we recall the cartoon presented in Fig. 2.1(a) that illustrates why introducing tunneling between dots induces transitions between the singlet and triplet states of the doubly occupied dot. When tunneling is allowed, there is a matrix element between the (2,1) state with the two electrons in the left dot in a singlet and the virtual (1,2) state in which the two electrons in the right dot are in a singlet, which in turn is coupled to the (2,1) state with the two electrons in a triplet state. The coupling between the (2,1) singlet and (2,1) triplet states is of order $g^2/\Delta E$, where g is the tunnel coupling and ΔE is the energy difference between the (2,1) state and the (1,2) excited state.

Here we provide a more detailed calculation of the couplings between the states of the hybrid qubit. The Hamiltonian describing interacting electrons, in general, can be written in the Hubbard-like form

$$\begin{aligned}\hat{H} &= \sum_{\alpha,i,s}(e_{\alpha i}+\mu_\alpha)\ \hat{n}_{\alpha i s}+\sum_{\alpha\neq\beta}\sum_{i,j}\sum_{s} g_{\alpha i,\beta j}\ \hat{c}^\dagger_{\alpha i s}\hat{c}_{\beta j s} \\ &\quad +\frac{1}{2}\sum_{\alpha,\beta,\gamma,\delta}\sum_{i,j,k,l}\sum_{s,s'}\Lambda^{\alpha\beta\gamma\delta}_{ijkl}\ \hat{c}^\dagger_{\alpha i s}\hat{c}^\dagger_{\beta j s'}\hat{c}_{\gamma k s'}\hat{c}_{\delta l s},\end{aligned} \tag{A.1}$$

where we have used Greek indices $\alpha, \beta, \gamma, \delta$ to refer to the quantum dots, Roman indices i, j, k, l to refer to the orbitals of a quantum dot, and s, s' are spin indices. In this notation, operator $\hat{c}^{\dagger}_{\alpha is}$ ($\hat{c}_{\alpha is}$) creates (annihilates) an electron with spin s in the i-th orbital of the α-th quantum dot, and $\hat{n}_{\alpha is} = \hat{c}^{\dagger}_{\alpha is}\hat{c}_{\alpha is}$ is the number operator.

In the Hamiltonian of Eq. A.1, the single particle energy of the i^{th} orbital in the α^{th} quantum dot is given by $e_{\alpha i}$, and the energy shift of the quantum dot is given by μ_{α}. This energy shift can be controlled experimentally by application of some gate voltage. The second term on the right-hand side of Eq. A.1 is the tunneling operator, which describes the tunneling of an electron with spin s between the j-th orbital of the β^{th} quantum dot and the i^{th} orbital of the α^{th} quantum dot, where α and β refer to different quantum dots. Orbital and tunneling energies can be calculated by single particle integrals between quantum dot orbital wavefunctions $\phi_{\alpha i}(\mathbf{r})$,

$$e_{\alpha i} = \int d\mathbf{r}\ \phi^{*}_{\alpha i}(\mathbf{r}) \left[\frac{1}{2m^{*}}\hat{\mathbf{p}}^2 + V_p(\mathbf{r})\right] \phi_{\alpha i}(\mathbf{r}), \tag{A.2}$$

$$g_{\alpha i,\beta j} = \int d\mathbf{r}\ \phi^{*}_{\alpha i}(\mathbf{r}) \left[\frac{1}{2m^{*}}\hat{\mathbf{p}}^2 + V_p(\mathbf{r})\right] \phi_{\beta j}(\mathbf{r}), \tag{A.3}$$

where $V_p(\mathbf{r})$ is the model quantum dot confinement potential, m^{*} is the effective mass of an electron in the conduction band, q is the electronic charge and $\hat{\mathbf{p}}$ is the momentum operator.

The prefactor of the third term in the Hamiltonian in Eq. A.1 is a two-electron Coulomb integral between quantum dot orbital wavefunctions $\phi(\mathbf{r})$, given by

$$\Lambda^{\alpha\beta\gamma\delta}_{ijkl} = \iint\ d\mathbf{r}\ d\mathbf{r}'\ \phi^{*}_{\alpha i}(\mathbf{r})\phi^{*}_{\beta j}(\mathbf{r}')\frac{q^2}{4\pi e_r e_0 |\mathbf{r}-\mathbf{r}'|}\phi_{\gamma k}(\mathbf{r}')\phi_{\delta l}(\mathbf{r}), \tag{A.4}$$

where ϵ_0 is the permittivity of free space and ϵ_r the relative permittivity of the material.

When the quantum dot indices refer to the same dot ($\alpha = \beta = \gamma = \delta$), we get the intra-dot Coulomb energies. This can be further categorized into the direct and exchange Coulomb energies. When the orbital indices $i = l$ and $j = k$, we obtain the direct Coulomb energy, $\Lambda^{\alpha\alpha\alpha\alpha}_{ijji} \equiv C_{\alpha i,\alpha j}$. When the orbital indices $i = k$ and $j = l$, we get the exchange Coulomb energy, $\Lambda^{\alpha\alpha\alpha\alpha}_{ijij} \equiv K_{\alpha i,\alpha j}$. When the quantum dot indices refer to the different dots ($\alpha = \delta,\ \beta = \gamma,\ \alpha \neq \beta$), we obtain the direct and exchange Coulomb energies between the electrons localized in the different quantum dots, i.e. $\Lambda^{\alpha\beta\beta\alpha}_{ijji} \equiv C_{\alpha i,\beta j}$ and $\Lambda^{\alpha\beta\beta\alpha}_{ijij} \equiv K_{\alpha i,\beta j}$.

These direct and exchange Coulomb energies are given by

$$C_{\alpha i,\beta j} = \iint d\mathbf{r}\ d\mathbf{r}'\ \phi^*_{\alpha i}(\mathbf{r})\phi^*_{\beta j}(\mathbf{r}')\frac{q^2}{4\pi e_r e_0|\mathbf{r}-\mathbf{r}'|}\phi_{\beta j}(\mathbf{r}')\phi_{\alpha i}(\mathbf{r}), \tag{A.5}$$

$$K_{\alpha i,\beta j} = \iint d\mathbf{r}\ d\mathbf{r}'\ \phi^*_{\alpha i}(\mathbf{r})\phi^*_{\beta j}(\mathbf{r}')\frac{q^2}{4\pi e_r e_0|\mathbf{r}-\mathbf{r}'|}\phi_{\beta i}(\mathbf{r}')\phi_{\alpha j}(\mathbf{r}). \tag{A.6}$$

Because of the non-vanishing overlap of the orbital wavefunctions between different quantum dots in the regime where the dots are coupled, other integrals also yield nonzero contributions. In general, for a system of two quantum dots, the integrals $\Lambda^{\alpha\beta\beta\alpha}_{ijkl}$ and $\Lambda^{\beta\alpha\beta\alpha}_{ijkl}$ may be non-zero for different orbitals i, j, k and l, due to the overlap between orbitals centered on different quantum dots α and β. On the other hand, for a single quantum dot, if we assume a symmetric confinement potential $V_p(\mathbf{r})$, such terms vanish.

By categorizing these energies into intra-dot, inter-dot and tunneling energies, we can transform the Hamiltonian of Eq. A.1 into a more familiar form [131] with intra-dot energy, inter-dot energy and tunneling operators $\hat{U}_0$, $\hat{U}_1$ and $\hat{T}$, respectively:

$$\hat{H} = \hat{U}_0 + \hat{U}_1 + \hat{T}, \tag{A.7}$$

where

$$\begin{aligned}\hat{U}_0 &= \sum_{\alpha,i,s}(e_{\alpha i}+\mu_\alpha)\ \hat{n}_{\alpha i s} \\ &\quad +\frac{1}{2}\sum_{\alpha}\sum_{i,j}\sum_{s,s'}\Big(\ C_{\alpha i,\alpha j}\ \hat{c}^\dagger_{\alpha i s}\hat{c}^\dagger_{\alpha j s'}\hat{c}_{\alpha j s'}\hat{c}_{\alpha i s} + K_{\alpha i,\alpha j}\ \hat{c}^\dagger_{\alpha i s}\hat{c}^\dagger_{\alpha j s'}\hat{c}_{\alpha i s'}\hat{c}_{\alpha j s}\Big), \qquad \text{(A.8)}\\ \hat{U}_1 &= \frac{1}{2}\sum_{\alpha\neq\beta}\sum_{\gamma\neq\delta}\sum_{i,j,k,l}\sum_{s,s'}\Lambda^{\alpha\beta\gamma\delta}_{ijkl}\ \hat{c}^\dagger_{\alpha i s}\hat{c}^\dagger_{\beta j s'}\hat{c}_{\gamma k s'}\hat{c}_{\delta l s}, \qquad \text{(A.9)}\\ \hat{T} &= \sum_{\alpha\neq\beta}\sum_{i,j}\sum_{s} g_{\alpha i,\beta j}\ \hat{c}^\dagger_{\alpha i s}\hat{c}_{\beta j s}. \qquad \text{(A.10)}\end{aligned}$$

The Hilbert space of a system of three electrons confined in a double quantum dot potential spans the space of states with charge configurations (3,0), (0,3), (2,1) and (1,2). Here, number pairs (n, m) denote the number of electrons in the left (n) and right (m) dots. We shall denote by $\mathcal{A}^{(2,1)}$, $\mathcal{A}^{(1,2)}$, $\mathcal{A}^{(3,0)}$ and $\mathcal{A}^{(0,3)}$ the set of states spanning the subspaces of (2,1), (1,2), (3,0) and (0,3) states respectively. The Hilbert space of the hybrid qubit is given by direct sum of these subspaces, and will be denoted by $\mathcal{A} \equiv \mathcal{A}^{(2,1)} \oplus \mathcal{A}^{(1,2)} \oplus \mathcal{A}^{(3,0)} \oplus \mathcal{A}^{(0,3)}$.

In the Hilbert space $\mathcal{A}$, the inter-dot tunneling operator $\hat{T}$ describes the coherent tunneling of electrons between states of the distinct subspaces whereas the intra-dot and inter-dot energy operators $\hat{U}_0$ and $\hat{U}_1$ do not couple these subspaces.

We can treat the tunneling matrix elements perturbatively and block-diagonalize the Hamiltonian by using the Schrieffer-Wolff transformation [36, 37, 38]. In this way we can transform the Hubbard-like Hamiltonian into a spin Hamiltonian $\hat{H}'$ by a unitary transformation,

$$\begin{aligned} \hat{H}' &= e^{i\hat{S}}\hat{H}e^{-i\hat{S}} \\ &= \hat{H} + [i\hat{S}, \hat{H}] + \dots \\ &= (\hat{U}_0 + \hat{U}_1) + \hat{T} + [i\hat{S}, (\hat{U}_0 + \hat{U}_1)] + [i\hat{S}, \hat{T}] + \dots \end{aligned} \tag{A.11}$$

We note that $i\hat{S}$ can be chosen such that $\hat{T} + [i\hat{S}, (\hat{U}_0 + \hat{U}_1)] = 0$, yielding an effective Hamiltonian for states with a fixed number of electrons on each dot. The transformed Hamiltonian becomes, in the lowest order, $\hat{H}' \approx \hat{U}_0 + \hat{U}_1 + [i\hat{S}, \hat{T}]$. Ref. [37] provides an explicit expression for the choice of $i\hat{S}$, given by

$$i\hat{S} = \sum_{n,m} |\varphi_n\rangle \frac{\langle\varphi_n|\hat{T}|\varphi_m\rangle}{\langle\varphi_n|\hat{U}|\varphi_n\rangle - \langle\varphi_m|\hat{U}|\varphi_m\rangle} \langle\varphi_m|, \tag{A.12}$$

where the states $|\varphi_n\rangle \in \mathcal{A}$ are eigenstates of $\hat{U} \equiv \hat{U}_0 + \hat{U}_1$. Since $|\varphi_n\rangle$ are eigenstates of $\hat{U}$, from the eigenvalue equation, $\hat{U}|\varphi_n\rangle = U_n|\varphi_n\rangle$, the orthogonality condition $\langle\varphi_n|\varphi_m\rangle = \delta_{nm}$, and the completeness relation, $\sum_n |\varphi_n\rangle\langle\varphi_n| = \hat{\mathbf{1}}$, one obtains

$$[i\hat{S}, \hat{U}] = -\hat{T}. \tag{A.13}$$

The first order commutator $[i\hat{S}, \hat{T}]$ gives

$$\begin{aligned} &\langle\varphi_k|[i\hat{S}, \hat{T}]|\varphi_{k'}\rangle \\ &= \sum_m \frac{\langle\varphi_k|\hat{T}|\varphi_m\rangle\langle\varphi_m|\hat{T}|\varphi_{k'}\rangle}{U_k - U_m} - \sum_m \frac{\langle\varphi_k|\hat{T}|\varphi_m\rangle\langle\varphi_m|\hat{T}|\varphi_{k'}\rangle}{U_m - U_{k'}} \ . \end{aligned} \tag{A.14}$$

Therefore, the first order commutator contains terms describing the second order hopping of an electron between states in the subspaces. These second order processes produce

hoppings between the subspaces as follows: $\mathcal{A}^{(0,3)} \rightarrow \mathcal{A}^{(1,2)} \rightarrow \mathcal{A}^{(0,3)}, \mathcal{A}^{(3,0)} \rightarrow \mathcal{A}^{(2,1)} \rightarrow \mathcal{A}^{(3,0)}, \mathcal{A}^{(1,2)} \rightarrow \mathcal{A}^{(0,3)} \rightarrow \mathcal{A}^{(1,2)}, \mathcal{A}^{(2,1)} \rightarrow \mathcal{A}^{(3,0)} \rightarrow \mathcal{A}^{(2,1)}, \mathcal{A}^{(1,2)} \rightarrow \mathcal{A}^{(2,1)} \rightarrow \mathcal{A}^{(1,2)}$ and $\mathcal{A}^{(2,1)} \rightarrow \mathcal{A}^{(1,2)} \rightarrow \mathcal{A}^{(2,1)}$.

Eq. A.14 shows that second order processes have coefficients that are are inversely proportional to the magnitude of the intra-dot energy difference $|U_m - U_k|$ between states $|\varphi_m\rangle$ and $|\varphi_k\rangle$. Since intra-dot energies of the states in subspaces $\mathcal{A}^{(0,3)}$ and $\mathcal{A}^{(3,0)}$ are larger than those of the states in subspaces $\mathcal{A}^{(2,1)}$ and $\mathcal{A}^{(1,2)}$ because of the much larger Coulomb repulsion between electrons in triply-occupied quantum dots, second order hopping processes involving triply-occupied states are virtual processes with much smaller probability compared to hoppings between states in the subspaces $\mathcal{A}^{(2,1)}$ and $\mathcal{A}^{(1,2)}$. As we are interested in the low-lying energy states of the system, we can restrict our basis to the states in the subspace of $\mathcal{A}^{(2,1)} \oplus \mathcal{A}^{(1,2)}$ and ignore triply-occupied states.

Because the qubit states are encoded in the $S = \frac{1}{2}, S_z = -\frac{1}{2}$ two-level subspace belonging to $\mathcal{A}^{(2,1)}$, we can preserve the (2,1) charge configuration of the qubit by adjusting the gate voltages that define the dots so that the lowest energy $\mathcal{A}^{(1,2)}$ configuration has higher energy than both of the qubit states in $\mathcal{A}^{(2,1)}$. The energy coefficient of the n-th order of the commutators in Eq. A.11 is proportional to $\frac{g^{n+1}}{(U_m - U_k)^n}$ and the series in Eq. A.11 can be truncated to desired order when $g \ll |U_m - U_k|$. Here, we keep only the lowest order contribution.

The effective Hamiltonian that describes the low-lying energy states can then be projected onto the subspace $\mathcal{A}^{(2,1)}$ by the projection operator $\hat{P}^{(2,1)} \equiv \sum_k |\varphi_k^{(2,1)}\rangle\langle\varphi_k^{(2,1)}|$, where the set of states $\{|\varphi_k^{(2,1)}\rangle\}$ span $\mathcal{A}^{(2,1)}$. The effective Hamiltonian is given by

$$\begin{aligned} \hat{H}_{\text{eff}} &= \hat{P}^{(2,1)} \hat{H}' \hat{P}^{(2,1)} \\ &= \hat{P}^{(2,1)} \left(\hat{U} + [i\hat{S}, \hat{T}] \right) \hat{P}^{(2,1)} \ . \end{aligned} \tag{A.15}$$

With the understanding that we are restricting our basis to the $\mathcal{A}^{(2,1)}$ subspace, we drop the projection operators $\hat{P}^{(2,1)}$. Using the bilinear spin identity $\vec{\mathbf{S}}_i = \frac{1}{2} \sum_{s,s'} \hat{c}_{is}^\dagger \vec{\sigma}_{ss'} \hat{c}_{is'}$, we

cast the effective Hamiltonian into the form

$$\hat{H}_{\text{eff}}^{(\text{t-J})} = \hat{U} + \hat{H}_J + \hat{H}_{J'}, \tag{A.16}$$

reminiscent of the t-J model [132]. The terms $\hat{H}_J$ and $\hat{H}_{J'}$ are in the form of inter-dot and intra-dot Heisenberg-like exchange interactions, and are given explicitly by

$$\begin{aligned}
\hat{H}_J &= \frac{1}{2}\sum_i J_i \left[\left(\sum_{s,s'} \hat{c}^\dagger_{\text{L}is} \vec{\sigma}_{ss'} \hat{c}_{\text{L}is'} \right) \cdot \left(\sum_{s,s'} \hat{c}^\dagger_{\text{R1}s} \vec{\sigma}_{ss'} \hat{c}_{\text{R1}s'} \right) - \hat{n}_{\text{L}i} \hat{n}_{\text{R1}} \right] \\
&= \frac{1}{2}\sum_i J_i (4\vec{\mathbf{S}}_{\text{L}i} \cdot \vec{\mathbf{S}}_{\text{R1}} - \hat{n}_{\text{L}i}\hat{n}_{\text{R1}}), \qquad \text{(A.17)} \\
\hat{H}_{J'} &= \frac{1}{2}\sum_{i\neq j} J'_{ij} \left[\left(\sum_{s,s'} \hat{c}^\dagger_{\text{L}is} \vec{\sigma}_{ss'} \hat{c}_{\text{L}js'} \right) \cdot \left(\sum_{s,s'} \hat{c}^\dagger_{\text{R1}s} \vec{\sigma}_{ss'} \hat{c}_{\text{R1}s'} \right) \right. \\
&\quad \left. - \left(\sum_s \hat{c}^\dagger_{\text{L}is} \hat{c}_{\text{L}js} \right) \hat{n}_{\text{R1}} \right] \qquad \text{(A.18)}
\end{aligned}$$

Labels L and R denote the left and right quantum dots and $i, j = 1, 2$ refer to the lowest two orbitals of a quantum dot. The meaning of these operators are as follows. $\hat{H}_J$ is the Heisenberg exchange coupling between electron spin in the i^{th} orbital of the left quantum dot and the electron spin in the ground orbital of the right quantum dot (R1). $\hat{H}_{J'}$ is the exchange coupling between the electron spins in the i^{th} and j^{th} orbital of the left quantum dot, mediated by the spin in the ground orbital of the right quantum dot.

Here, we note that the difference in the energy eigenvalues U_m and U_k, of the total intra- and inter-dot energy operator $\hat{U} \equiv \hat{U}_0 + \hat{U}_1$ in the subspaces of $\mathcal{A}^{(2,1)}$ and $\mathcal{A}^{(1,2)}$ appear in the denominator of each of the terms in Eq. A.14. If m and k refer to the ground eigenstates of these subspaces, the biggest contribution to the energy difference in the denominator would be due to the detuning or energy shift differences between the dots, followed contributions from differences in intra-dot energies, and finally, from differences in inter-dot energies in states m and k. Therefore, one could omit the inter-dot energy operator $\hat{U}_1$ from the Hubbard-like Hamiltonian (Eq. A.7) from the start, without changing the physical processes described by the t-J Hamiltonian (Eq. A.16) as it contributes only a small correction to the Heisenberg coupling constants J_i and J'_{ij}. In order to make our model less complicated without losing the essential physics, we make the approximation

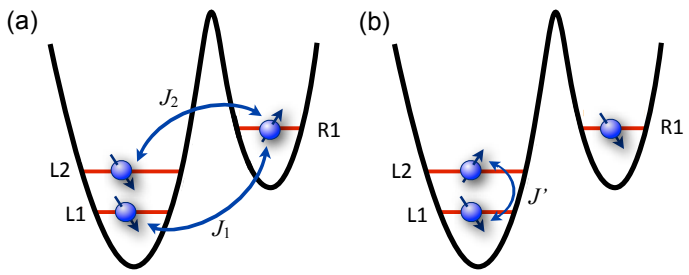

Figure A.2: Schematic of the Heisenberg exchange couplings as given by Eqs. A.17 and A.18. Levels L1 and L2 refer to the lowest single particle energies of the left quantum dot, and R1 refers to the lowest single particle energy of the right dot. (a) J_1 and J_2 are respectively, the Heisenberg exchange couplings between electron spins in the ground (1) and first excited (2) orbitals of the left quantum dot and the electron spin in the ground orbital of the right quantum dot. (b) J' is the exchange coupling between the electron spins in the lowest two orbitals of the left quantum dot, mediated by the spin in the ground orbital of the right quantum dot. Explicit forms of J_1, J_2 and J' are given in Eqs. A.19 assuming equal tunneling energies between the orbitals of the two quantum dots.

of neglecting these inter-dot contributions. We also assume that tunneling energies for different orbitals in Eq. A.10 are equal, $g_{\alpha i,\beta j} \equiv g$.

Noting that the ground state of two electrons in a quantum dotat low magnetic fields is a singlet and the next three higher energy states are triplets and denoting the energies of the singlet (S) and triplet (T) states of the left (L) and right (R) quantum dot by $E^{L/R}_{\mathrm{S/T}}$, we can then write the forms of J_i and J'_{ij} in terms of the tunneling energies and singlet and triplet energies. They are given by

$$\begin{aligned} J_1 \approx \frac{2g^2}{E^{\mathrm{R}}_S - E^{\mathrm{L}}_S}, \qquad & J_2 \approx \frac{2g^2}{E^{\mathrm{R}}_S - E^{\mathrm{L}}_T}, \\ J'_{12} = J'_{21} \quad = \quad & \frac{J_1 + J_2}{2} \equiv J'. \end{aligned} \tag{A.19}$$

The couplings due to these exchange terms are shown schematically in Fig. A.2. Here, we assume that $E^{\mathrm{R}}_S - E^{\mathrm{L}}_T > 0$ is satisfied due to detuning, tighter right quantum dot confinement or some experimental scheme that is employed. Then, $E^{\mathrm{R}}_S - E^{\mathrm{L}}_S > 0$ follows because the triplet states are higher in energy than the singlet state, $E^{\mathrm{L}}_T > E^{\mathrm{L}}_S$. Note that in truncating the series in Eq. A.11, we also implicitly assumed that $g < (E^{\mathrm{R}}_S - E^{\mathrm{L}}_T)$.

For the form of intra-dot energy operator given in Eq. A.8, the singlet and triplet energies

are

$$\begin{aligned} E_S^{\rm L} &= 2e_{\rm L1} + C_{\rm L1,L1} + 2\mu_{\rm L}, \\ E_S^{\rm R} &= 2e_{\rm R1} + C_{\rm R1,R1} + 2\mu_{\rm R}, \\ E_T^{\rm L} &= e_{\rm L1} + e_{\rm L2} + C_{\rm L1,L2} - K_{\rm L1,L2} + 2\mu_{\rm L}, \\ E_T^{\rm R} &= e_{\rm R1} + e_{\rm R2} + C_{\rm R1,R2} - K_{\rm R1,R2} + 2\mu_{\rm R}. \end{aligned} \tag{A.20}$$

The logical basis given in Chapter 2 is in spin form. To make it consistent with the notations introduced here, we explicitly write them out below. Here, the three-electron kets are the usual Slater determinants.

$$|0\rangle_L \equiv |S\rangle|\downarrow\rangle = |\phi_{\rm L1\uparrow}(\mathbf{r}_1)\ \phi_{\rm L1\downarrow}(\mathbf{r}_2)\ \phi_{\rm R1\downarrow}(\mathbf{r}_3)\rangle, \tag{A.21}$$

$$\begin{aligned} |1\rangle_L &\equiv \sqrt{\frac{1}{3}}|T_0\rangle|\downarrow\rangle - \sqrt{\frac{2}{3}}|T_-\rangle|\uparrow\rangle \\ &= \sqrt{\frac{1}{6}}\left[|\phi_{\rm L1\uparrow}(\mathbf{r}_1)\ \phi_{\rm L2\downarrow}(\mathbf{r}_2)\ \phi_{\rm R1\downarrow}(\mathbf{r}_3)\rangle + |\phi_{\rm L1\downarrow}(\mathbf{r}_1)\ \phi_{\rm L2\uparrow}(\mathbf{r}_2)\ \phi_{\rm R1\downarrow}(\mathbf{r}_3)\rangle\right] \\ &\quad -\sqrt{\frac{2}{3}}\left[|\phi_{\rm L1\downarrow}(\mathbf{r}_1)\ \phi_{\rm L2\downarrow}(\mathbf{r}_2)\ \phi_{\rm R1\uparrow}(\mathbf{r}_3)\rangle\right]. \end{aligned} \tag{A.22}$$

The effective Hamiltonian in the logical basis $\{|0\rangle_{\rm L}, |1\rangle_{\rm L}\}$ is given by

$$\hat{H}_{\rm eff}^{\rm (t\text{-}J)} = \begin{pmatrix} -J_1 & \sqrt{\frac{3}{2}}J' \\ \sqrt{\frac{3}{2}}J' & E_{ST} - \frac{3}{2}(J_1 + J_2) \end{pmatrix}, \tag{A.23}$$

with $E_{ST} \equiv E_T^{\rm L} - E_S^{\rm L}$ being the singlet-triplet splitting of the two electrons in the left quantum dot. Of significance is the exchange term J' whose expression is given in Eq. A.19, which couples the two logical states of the qubit and can be modulated by means of electrically controlling the tunnel barrier between the quantum dots.

A.2 Connectivity between two hybrid qubits

This section discusses why the connectivity of two hybrid qubits composed of six electrons in four dots arranged in a linear array (Fig. 2.1(d) and Fig. 2.1(f) of Chapter 2) is higher

than the connectivity of two qubits that consist of electrons in six dots arranged in a linear array (shown in Fig. 2.1(e)). We have calculated the number of independently controllable interactions using the methods described in the previous section of this Appendix and find that there are two independent interdot couplings when one dot has two electrons and the other has one, and that there are three independent interdot couplings when both dots have two electrons. The coupling strengths are tunable as a function of the top-gate voltages that define the quantum dots. As discussed in the previous section, the control parameters include the height of the tunnel barrier, the energy splitting between the ground and excited states in each dot, and the energy detuning between the two dots. Here we present intuitive arguments that the electrons in the dots have at least two independently tunable interdot couplings for both cases. Note that our searches for CNOT gate sequences, described in the following section, require only two independent interdot couplings, for either of the connectivities shown in Figs. 2.1(d) and (f).

We first consider the case of Fig. 2.1(d), where one dot has two electrons and the other dot has one electron. Here, since the geometry of the connections between hybrid qubits is the same as the connections between the dots comprising a single logical qubit, the analysis presented in the previous section of this Appendix can be applied straightforwardly. Fig. A.3 is a visualization of configurations of the two dots that have different effective exchange couplings, because they involve overlaps of different orbital states of the doubly occupied dot. (One can view the diagram as indicating the energies and extents of single-particle orbitals for the possible electron states of the dot.) Note that configuration (3) in Fig. A.3(a) does not occur during single-qubit manipulation, but it becomes accessible when two qubits are coupled. Fig. A.3(b) shows a similar schematic when the connection between qubits is between two dots, each with two electrons. Because the two dots are not identical, configurations (1) and (2) are independently tunable. Configuration (3) contributes because of tunneling to excited states. Configuration (4) is a configuration that cannot occur for a single qubit, but which can appear during two-qubit manipulation. Because the number of configurations with different exchange couplings is larger than for the case shown in (a),

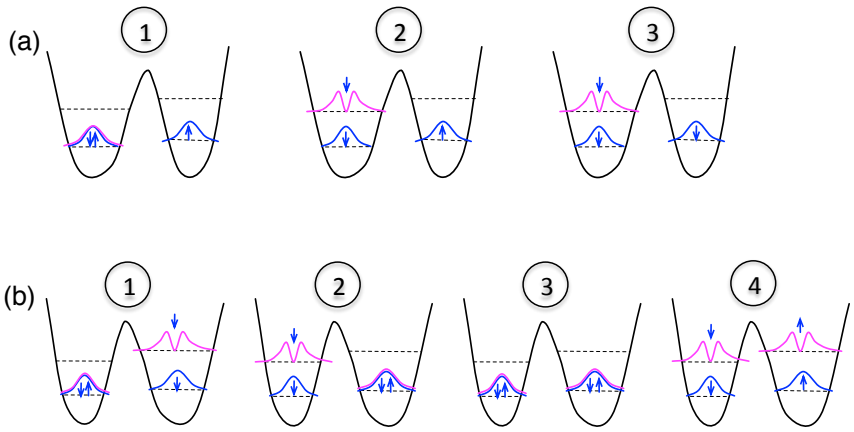

Figure A.3: (a) Schematic diagram of the (2,1) electron configurations of one doubly occupied dot and one singly occupied dot that have separately tunable tunnel couplings. Configuration 3, on the right, does not arise when manipulating a single qubit, but can arise during two-qubit manipulations. Using the methods presented in the first section of this appendix, we have performed calculations with properly symmetrized wavefunctions, showing that the (2,1) configuration has two independently tunable exchange couplings. (b) Schematic diagram of the (2,2) electron configurations of two doubly occupied dots that have separately tunable tunnel couplings. Configuration 4, on the right, does not arise when manipulating a single qubit, but can arise during two-qubit manipulations. The number of distinct tunnel couplings is greater than for the (2,1) case shown in (a), so it is plausible that the number of tunable interdot exchange couplings is at least as great as in (a). Detailed calculations show that the (2,2) arrangement has three independently tunable exchange couplings. Our calculations of gate sequences presented in the next section assume only two independently tunable interdot exchange couplings.

it is extremely plausible that the number of independently tunable interactions is at least as great. This expectation is borne out by detailed calculations using methods similar to those used in the previous section.

A.3 CNOT gates for qubits with increased connectivities

This section presents gate sequences that implement gates that are equivalent to CNOT, up to local unitary transformations, for two logical qubits that consist of the two eigenstates of three spins with $S = 1/2$, $S_z = -1/2$. As noted in Chapter 2, the spin symmetries of the hybrid qubit proposed here and the triple-dot qubit of Ref. [21] are the same. However, two hybrid qubits consisting of six electrons in four dots arranged in a linear array has more spin-

spin couplings than two logical qubits consisting of six electrons in six dots arranged in a linear array, as shown in Fig. 2.1. Here we present evidence that this increased connectivity can be exploited to reduce the number of gate operations needed to implement gates of two logical qubits, by presenting two-spin gate sequences that are equivalent to a CNOT gate, up to local unitary operations, for different connectivities of the spin-1/2 particles that make up the logical qubits. This result is not unexpected, since Ref. [21] shows that for single qubit operations, at most three gates are needed when all three spins are coupled (e.g. in a triangular quantum dot configuration), and at most four gates are necessary when the spins are coupled only to nearest neighbors in a linear array.

The quantum dot geometries we considered are shown in panel (a) of Figs. A.4 and A.5. We implemented a search algorithm similar to the one described in Ref. [31], which is a combination of Nelder-Mead [133] and genetic [134] algorithms. We parallelized the program and exploited the resources of the University of Wisconsin Center for High Throughput Computing (CHTC) [135] grid using Condor [136] to improve the speed of the calculations. As in Ref. [31], the numerical results could be used to deduce exact gate times, which points to the power of the algorithm and perhaps some underlying hidden symmetry of the $S = 1, S_z = 1$ subspace in which the two logical qubits reside. The exact gate sequences are presented schematically in Fig. A.4(b) and Fig. A.5(b).

We also obtained the local unitary operations necessary for obtaining the exact CNOT gate for the geometry of Fig. A.5(a), and the exact times and spin couplings are presented in Fig. A.5(b). Note that in this coded qubit scheme, the local unitary operations are implemented as exchange gates.

A.4 Details of the experimental measurements

This section presents the details of the experimental measurements shown in Fig. 2.2 of Chapter 2. The data in Fig. 2.2 correspond to a single electron tunneling between the left dot and the left reservoir, as shown in the insets to Fig. 2.2(b–d). Charge sensing is performed by measuring the current I_{QPC} using a bias voltage of 500 μV. We measure

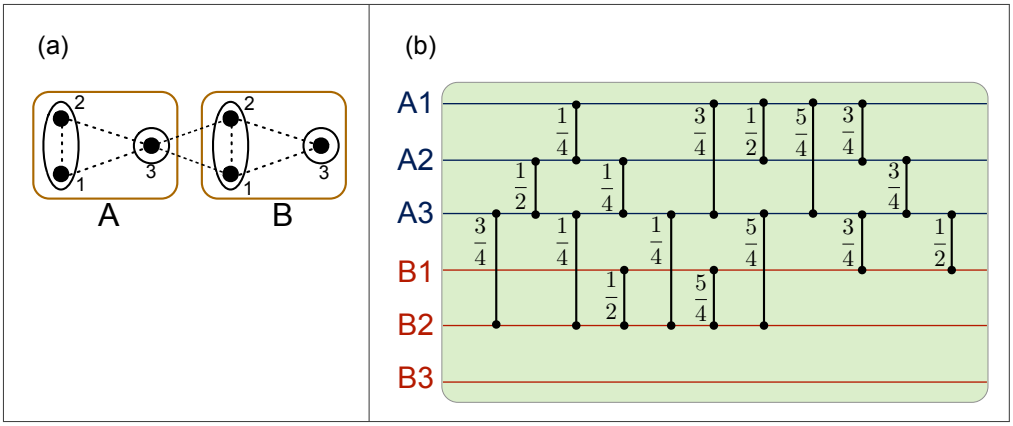

Figure A.4: (a) Schematic of qubit-qubit couplings used to implement a gate that is equivalent to CNOT, up to local unitary operations [137]. Each logical qubit A and B, is encoded in three spins 1, 2 and 3, with spins 1 and 2 both in one quantum dot. (b) A 16 gate sequence, with gate times indicated, that implements a gate that is equivalent to CNOT up to local unitary transformations between logical qubits A and B, in 11 time steps. The order of gate couplings run from left to right. Each coupling between the i^{th} and j^{th} spins represents the unitary evolution $U_{ij}(t) = \exp\left(-\frac{i}{\hbar}tJ\vec{\mathbf{S}}_i \cdot \vec{\mathbf{S}}_j\right)$. Gate times are in units of h/J, so that gate times of $\frac{1}{4}$ and $\frac{1}{2}$ correspond to $\sqrt{\text{SWAP}}$ and SWAP operations respectively.

the electron loading and unloading rates by applying a small amplitude square wave pulse to one of the gates defining the quantum dot and observing the electron tunneling events, which are manifested as steps in I_{QPC}. We report the amplitude of the square wave pulse as generated by the arbitrary waveform generator (AWG); there is attenuation between the AWG and the sample. To measure the tunnel rate into the dot, we start with one electron in the left dot and apply a step increase in voltage of 80 mV to the experimental wiring leading to gate PL, causing an electron to tunnel from the lead into the dot. By averaging 300 single-shot traces of I_{QPC} versus time, we obtain the curves shown in Fig. 2.2(b–c), which show an exponential decay (increase) for electron loading (unloading) events. By fitting these curves to exponentials, we extract the tunnel rates for electron loading and unloading. To study the singlet and triplet states independently, we apply an in-plane magnetic field B. At small B, the singlet state S is the ground state, whereas at large B the triplet state T_- is the ground state. Applying a small amplitude voltage pulse will

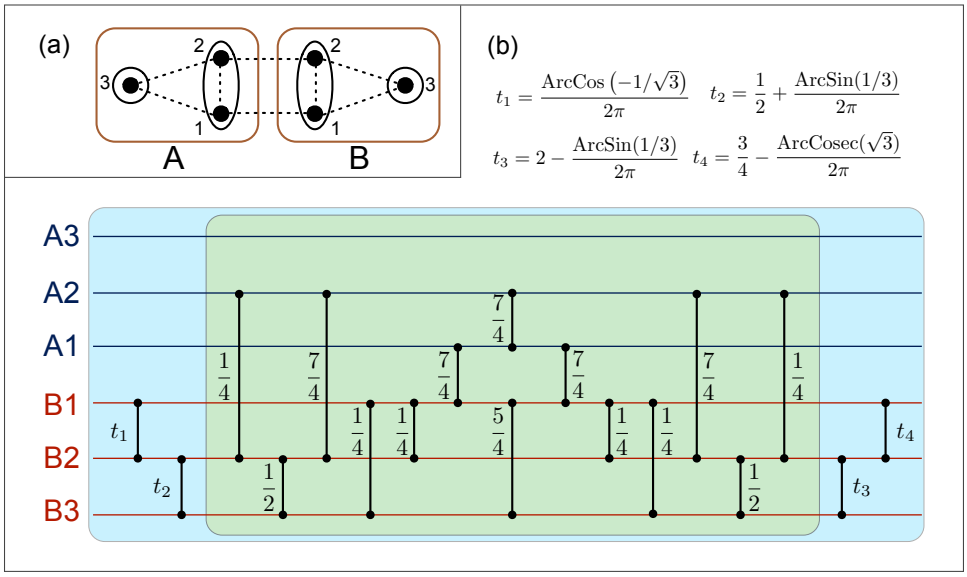

Figure A.5: (a) Schematic of qubit-qubit couplings used to implement a CNOT gate of two logical qubits. Each logical qubit A and B, is encoded in three spins 1,2 and 3, with spins 1 and 2 both in one quantum dot. (b) Gate sequence, with gate times indicated, that implements an exact CNOT gate between logical qubits A and B, with the order of the couplings running from left to right. The central block (in green) of 14 gates in 13 time steps give a CNOT, up to local unitary operations [137]. Together with the additional 4 local unitary operations (labelled by $g_{1,2,3,4}$) shown in the outer block (in light blue), an exact CNOT gate can be implemented by a total of 18 gates in 17 time steps. Each coupling between the i^{th} and j^{th} qubits represents the unitary evolution $U_{ij}(t) = \exp\left(-\frac{i}{\hbar}tJ\vec{\mathbf{S}}_i \cdot \vec{\mathbf{S}}_j\right)$. Gate times are in units of h/J, so that gate times of $\frac{1}{4}$ and $\frac{1}{2}$ correspond to $\sqrt{\text{SWAP}}$ and SWAP operations respectively.

enable loading of the ground state only. Thus, a measurement at both small and large B of the tunnel rate into or out of the dot with a small amplitude voltage pulse enables a measurement of the tunnel rates into and out of both the singlet and the triplet states. As discussed in Chapter 2, we find these tunnel rates to be quite different, enabling readout of the spin state.

The difference in the unloading rate of the singlet S and the triplet T_- can be used to measure the triplet-singlet relaxation time at magnetic fields B small enough that the singlet S is the ground state [44]. We enable loading of both state S and state T_- by applying a voltage pulse to the dot, as described in Chapter 2. We choose a pulse amplitude that brings T_- into resonance with the Fermi level of the lead, preferentially loading that state.

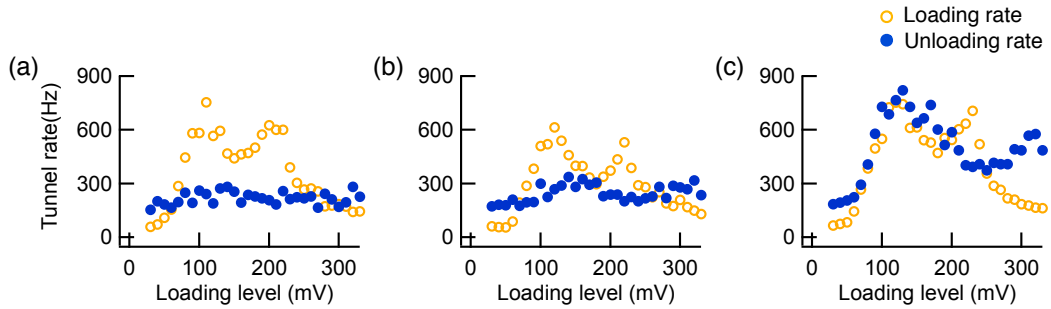

Figure A.6: Measurement of loading and unloading rates into and out of the quantum dot as a function of loading depth. The unloading level is kept at -150 mV. The unloading time is 40ms for all three panels and the loading times are 600 ms, 300 ms and 40 ms for panel (a), (b), and (c), respectively. For long loading times, as in panel (a), the unloading rate is slow because the states T_- and T_0 relax to the singlet state S during the loading period; for short loading times and loading voltages around 120 mV, as in panel (c), the unloading rate is fast, indicating that the state T_- does not relax to the singlet S before the electron tunnels out of the dot. The loading and unloading voltage levels correspond to voltages generated by the arbitrary wave generator and applied to the experimental wiring leading to gate PL.

With this initial condition, we then measure the unloading rate of the dot as a function of the dwell time Δt between the steps in voltage that induce loading and unloading of an electron. The unloading rate shows an exponential decay as a function of dwell time, as reported in Fig. 2.2(d). The unloading rate is fast when the electron stays in the T_- state throughout the dwell time, so that the electron tunnels out of the dot from the T_- state; the unloading rate is slow when the electron decays to the singlet state before exiting the dot. A measurement of the characteristic time of this decay is thus a measurement of T_1 for the triplet-to-singlet relaxation process.

To perform this measurement, it is useful to find the loading voltage that corresponds to resonance with the T_- state, by measuring the loading and unloading tunnel rates as a function of the amplitude of the loading pulse. As shown in Fig. A.6, the loading rate develops two peaks as we increase the amplitude of this pulse. We identify the two peaks as T_- and T_0 states coming into resonance with the Fermi level. These states have fast tunnel rates because the triplet wavefunction is more strongly coupled to the lead. The splitting between the peaks, when converted to energy using a lever arm measured in [8]

($\alpha = 0.00144 \pm 0.00013\,\mathrm{eV/V}$), is $144 \pm 13\,\mu\mathrm{eV}$ between triplet T_0 and T_-, a value that is in good agreement with the Zeeman splitting at $B = 1.5\,\mathrm{T}$, $\Delta E_B = 138\,\mu\mathrm{eV}$, where we have used the g-factor measured in [8]: $g = 1.585$ at $B = 1.5\,\mathrm{T}$. The unloading rate, when the pulse amplitude is such that the T_- state is in resonance with the Fermi level, is fast when the loading time is short, and slow when the loading time is long. This behavior indicates that during a long loading period the electron loads into state T_- and then relaxes to state S. As shown in Fig. A.6(c), for short loading times the electron remains in state T_- until it unloads.

Appendix B

Supplemental material for Chapter 3

This Appendix presents details for two topics in Chapter 3: (1) the calculation of the parameters of the gate sequence required to implement a qubit rotation by an arbitrary angle about an arbitrary axis on the Bloch sphere, and (2) a description of the device modeled to demonstrate the feasibility of capacitive coupling for implementing two-qubit operations.

B.1 Details of the derivations of Eqs. (3.2 – 3.4).

Here, we outline the calculations of the control parameters ϕ_1, ϕ_2, θ for the single-qubit gate shown in Fig. 3.1(c).

A general rotation of a two-component spinor around the axis $\hat{\mathbf{n}}$ with angle ϕ is given by

$$e^{-i\boldsymbol{\sigma}\cdot\hat{\mathbf{n}}\phi/2} = \cos(\phi/2) - i\boldsymbol{\sigma}\cdot\hat{\mathbf{n}}\,\sin(\phi/2), \tag{B.1}$$

where $\boldsymbol{\sigma} = (\sigma_x, \sigma_y, \sigma_z)$ are Pauli matrices. The B gate corresponds to an x rotation of angle π in the $\{|1\rangle_L, |E\rangle\}$ subspace of the full Hilbert space spanned by $\{|0\rangle_L, |1\rangle_L, |E\rangle\}$. During the course of the operation, states $|1\rangle_L$ and $|E\rangle$ gain a phase of $e^{i\phi_B}$. Throughout

this analysis, we define all phases relative to $|0\rangle_L$. The phase of $|0\rangle_L$ therefore remains constant.) Thus,

$$B = \begin{pmatrix} 1 & 0 & 0 \\ 0 & 0 & -ie^{i\phi_B} \\ 0 & -ie^{i\phi_B} & 0 \end{pmatrix}. \tag{B.2}$$

The A gate corresponds to an x rotation of angle θ in the $\{|0\rangle_L, |E\rangle\}$ subspace. During this operation, state $|1\rangle_L$ gains a phase of $e^{i\alpha_A}$. Thus,

$$A = \begin{pmatrix} \cos(\theta/2) & 0 & -i\sin(\theta/2) \\ 0 & e^{i\alpha_A} & 0 \\ -i\sin(\theta/2) & 0 & \cos(\theta/2) \end{pmatrix}. \tag{B.3}$$

The P_1 and P_2 gates are phase gates. During the P_1 operation, state $|E\rangle$ gains a phase of $e^{i\phi_1}$ relative to $|0\rangle_L$, while state $|1\rangle_L$ gains a phase of $e^{i\alpha_1}$. Similar considerations apply to P_2. Thus,

$$P_{1,2} = \begin{pmatrix} 1 & 0 & 0 \\ 0 & e^{i\alpha_{1,2}} & 0 \\ 0 & 0 & e^{i\phi_{1,2}} \end{pmatrix}. \tag{B.4}$$

Computing the composite gate $U = BP_2AP_1B$, we obtain the following rotation in the $\{|0\rangle_L, |1\rangle_L\}$ subspace:

$$R = \begin{pmatrix} \cos(\theta/2) & -e^{i(\phi_1+\phi_B)}\sin(\theta/2) \\ -e^{i(\phi_2+\phi_B)}\sin(\theta/2) & -e^{i(\phi_1+\phi_2+2\phi_B)}\cos(\theta/2) \end{pmatrix}. \tag{B.5}$$

We can decompose this into a sum of Pauli matrices using $R = \sum_{j=0,x,y,z} C_j\sigma_j$, where $\sigma_0 = I$ is the identity matrix, and $C_j = \mathrm{Tr}[\sigma_j R]/2$. Comparing this result to Eq. B.1, above, we identify the appropriate rotations angles shown in Eqs. 3.2–3.4 of Chapter 3, up to an overall phase.

We note that an alternative and equivalent pulse sequence is obtained when $\epsilon_P < \epsilon_B$, corresponding to the gate sequence $U = P_2BABP_1$. For this gate sequence, we obtain identical results after making the substitutions $\alpha_{0,1} \leftrightarrow \phi_{0,1}$.

B.2 Description of the modeled device.

The Thomas-Fermi calculations are performed on a realistic quadruple quantum dot gate geometry for an accumulation-mode device. Fig. 3.3(b) shows the primary gate pattern, in which metallic gates sit on a 10 nm thick Al_2O_3 layer on top of a $Si/Si_{0.7}Ge_{0.3}$ heterostructure containing a Si quantum well 35 nm beneath its surface. The $Si_{0.7}Ge_{0.3}$ layer is modeled as a dielectric with a relative dielectric constant of $\epsilon = 13.19$. The accumulation gates are positively biased, resulting in electron accumulation as indicated schematically on the diagram. The depletion gates provide tunability of tunnel barriers between the dots themselves and between each dot and its reservoir. Two large top gates sit on top of an additional 70 nm of Al_2O_3. The first, positively biased, establishes the reservoirs on the left-hand side of Fig. 3.3(b); the second, negatively biased, prevents any undesired accumulation on the right-hand side of Fig. 3.3(b).

Appendix C

Supplemental material for Chapter 4

In this Supplemental Material, we address the details of the following: (1) the definition of gate fidelity, (2) the derivation of the analytical expressions for optimal fidelity and optimal detuning in the logical qubit resonance (LQR) gating protocol, (3) STIRAP gating and the scaling law of its fidelity, and (4) DC pulsed gating.

C.1 Definition of gate fidelity

Our definition of gate fidelity $f(\rho, \sigma)$ is based on the measure of distance between two density matrices, ρ and σ, first defined in Ref. [79], given by

$$f(\rho, \sigma) = \left(\mathrm{Tr} \left(\sqrt{\sqrt{\sigma}\rho\sqrt{\sigma}} \right) \right)^2 . \tag{C.1}$$

(We note that Ref. [2] gives a similar definition which some authors refer to, the only difference being the absence of the square on the right hand side.) If one of the density matrices describes a pure state, $\sigma = |\phi\rangle\langle\phi|$, then the fidelity (Eq. C.1) can be written as

$$f = \langle\phi|\rho|\phi\rangle. \tag{C.2}$$

In our work, the system is initially in the pure state $|a\rangle \equiv |\uparrow\downarrow\rangle$ for the ST qubit, and $|0\rangle_L$ for the hybrid qubit. We then implement an exchange gate for a time τ to perform a π

rotation about the $x-$axis. A perfect π rotation would yield pure states $|b\rangle \equiv |\downarrow\uparrow\rangle$ and $|1\rangle_L$ for the ST and hybrid qubits, respectively. However, dephasing causes the ST and hybrid qubits to end up in mixed states given by the respective density matrices $\rho^{\mathrm{ST}}(\tau)$ and $\rho^{\mathrm{hy}}(\tau)$. The probability of finding state $|b\rangle$ for the ST qubit and state $|1\rangle_L$ for the hybrid qubit are given by density matrix elements $\rho_{bb}(\tau) \equiv \langle b|\rho^{\mathrm{ST}}(\tau)|b\rangle$ and $\rho_{11}(\tau) \equiv_L \langle 1|\rho^{\mathrm{hy}}(\tau)|1\rangle_L$, respectively.

We make use of the distance measure in Eq. C.2 and define the gate fidelity for a π rotation with gate time τ for the ST and hybrid qubits as

$$f_{\mathrm{ST}} \equiv \rho_{bb}(\tau), \tag{C.3}$$

$$f_{\mathrm{hy}} \equiv \rho_{11}(\tau). \tag{C.4}$$

This definition provides a simple, intuitive understanding of fidelity as the probability of finding the target state $|b\rangle \equiv |\downarrow\uparrow\rangle$ for the ST qubit and $|1\rangle_L$ for the hybrid qubit. The ideal gate fidelity f is unity, and we define the gate *infidelity* as $1 - f$.

C.2 Derivation of optimal fidelity for Logical Qubit Resonance (LQR) gating

The interaction picture

In time-dependent quantum mechanical problems, it is often useful to separate the Schrodinger picture Hamiltonian $H(t)$ into a time-independent part H_0 and a time-dependent part $V(t) \equiv H(t) - H_0$. If the dynamics of the system under H_0 are known, it is natural to transform into the interaction frame, where the states incorporate the time-evolution due to H_0 and the time-dependent part $V(t)$ induces transitions between the states. The interaction picture is formally exact, but it provides a natural reference frame that allows a complicated time-dependent problem to be simplified. With appropriate simplifications like the rotating wave approximation (RWA) [70], the interaction picture [74] becomes a good choice of representation for efficient numerical simulations.

The transformation from the Schrödinger picture into the interaction picture Hamiltonian is, in general, given by $H^i(t) = U^\dagger(t)H(t)U(t) - i\hbar U^\dagger(t)\frac{dU(t)}{dt}$, where $U(t) \equiv \exp\left(-\frac{i}{\hbar}\int_0^t H_0(t')dt'\right)$. For the special case where H_0 is time-independent, the transformation simplifies into

$$H^i(t) = U^\dagger(t)V(t)U(t). \tag{C.5}$$

Operators in the interaction picture, such as the density matrix $\rho(t)$, transform similarly:

$$\rho^i(t) = U^\dagger(t)\rho(t)U(t), \tag{C.6}$$

In the interaction picture, the master equation, (Eq. 4.1), of the Chapter 4 reads

$$\dot{\rho}^i(t) = -\frac{i}{\hbar}[H^i(t), \rho^i(t)] - D^i, \tag{C.7}$$

where D^i is the phenomenological term describing Markovian dephasing in the interaction picture.

In LQR and STIRAP gating, tunnel couplings are time-dependent. Because tunnel couplings depend on the overlap of electronic wavefunctions centered on adjacent quantum dots, their magnitudes depend on the height of the inter-dot tunnel barrier and the distance between the dots, both of which can be controlled via electrical voltages applied to appropriate top-gates. The sign of the tunnel couplings, however, depend on the definition of basis states used in the problem and are fixed.

We model the tunnel couplings realistically in the LQR protocol as the sum of a constant DC component g_0 and an AC component, also with amplitude g_0, so that the tunnel coupling to oscillate between zero and amplitude $2g_0$. For the ST qubit, the tunnel coupling is

$$g(t) = g_0\left(1 + \cos(\omega_B t/2)\right), \tag{C.8}$$

where t is time, $\omega_B \equiv \Delta E_B/\hbar$, and g_0 is the tunnel coupling amplitude. For the hybrid qubit, the tunnel couplings g_1 and g_2 that apply to tunneling of electrons in each of the two orbitals in the doubly occupied dot are assumed to be independently tunable [18], and are

similarly modeled as

$$g_1(t) = g_0\left(1+\cos(\omega_{01}t/2)\right), \tag{C.9}$$

$$g_2(t) = g_0\left(1+\cos(\omega_{01}t/2)\right), \tag{C.10}$$

where $\omega_{01} \equiv \Delta E_{01}/\hbar$.

To transform into the interaction picture, we first define the time-independent part of the Hamiltonian.

For the ST qubit, we define

$$H_{\mathrm{ST},0} = \begin{pmatrix} -\hbar\omega_B/2 & 0 & 0 \\ 0 & \hbar\omega_B/2 & 0 \\ 0 & 0 & 0 \end{pmatrix}, \tag{C.11}$$

and for the hybrid qubit,

$$H_{\mathrm{hy},0} = \begin{pmatrix} -\hbar\omega_{01}/2 & 0 & 0 \\ 0 & \hbar\omega_{01}/2 & 0 \\ 0 & 0 & 0 \end{pmatrix}. \tag{C.12}$$

Using $U_{\mathrm{ST}}(t) \equiv \exp\left(-i\,tH_{\mathrm{ST},0}/\hbar\right)$ for the ST qubit and $U_{\mathrm{hy}}(t) \equiv \exp\left(-i\,tH_{\mathrm{hy},0}/\hbar\right)$ for the hybrid qubit, we obtain the interaction picture Hamiltonians for the two qubit systems using Eq. C.5:

$$H^i_{\mathrm{ST}}(t) = \begin{pmatrix} 0 & 0 & \frac{1}{2}g_0\left(1+2e^{-i\omega_B t/2}+e^{-i\omega_B t}\right) \\ 0 & 0 & -\frac{1}{2}g_0\left(1+2e^{i\omega_B t/2}+e^{i\omega_B t}\right) \\ \frac{1}{2}g_0\left(1+2e^{i\omega_B t/2}+e^{i\omega_B t}\right) & -\frac{1}{2}g_0\left(1+2e^{-i\omega_B t/2}+e^{-i\omega_B t}\right) & -\epsilon \end{pmatrix}, \tag{C.13}$$

$$H^i_{\mathrm{hy}}(t) = \begin{pmatrix} 0 & 0 & \frac{1}{2}g_0\left(1+2e^{-i\omega_{01} t/2}+e^{-i\omega_{01} t}\right) \\ 0 & 0 & -\frac{1}{2}g_0\left(1+2e^{i\omega_{01} t/2}+e^{i\omega_{01} t}\right) \\ \frac{1}{2}g_0\left(1+2e^{i\omega_{01} t/2}+e^{i\omega_{01} t}\right) & -\frac{1}{2}g_0\left(1+2e^{-i\omega_{01} t/2}+e^{-i\omega_{01} t}\right) & -\epsilon \end{pmatrix}. \tag{C.14}$$

Up till this point, the transformation into the interaction picture is exact. In the following section, we make appropriate approximations to the interaction Hamiltonians in order to simplify the problem.

Rotating wave approximation

The off-diagonal matrix elements of the interaction picture Hamiltonians in Eqs. C.13 and C.14 represent the time-dependent tunnel couplings in the rotating frame. They consist of a constant term $g_0/2$ and two fast oscillating terms.

The constant term $g_0/2$ represents the condition where tunnel couplings oscillate at resonance with the frequency that corresponds to half of the energy difference between the qubit states. The rotating wave approximation (RWA) consists of neglecting the non-resonant, quickly oscillating terms in the interaction Hamiltonian [70]. The RWA is a good approximation in the case of resonance and the limit of weak coupling, $g_0 \ll |\epsilon|$. The weak coupling assumption is essential because the fast oscillating terms are of the same magnitude as the resonant, constant term. It is also a reasonable assumption because the AC gating of the qubits is implemented in the far detuned regime, which is exactly the weak coupling limit. In this limit, the exchange coupling is $J_{\mathrm{AC}} \propto g_0^2/|\epsilon|$.

The fast oscillating terms can be neglected because they average to zero over a long time scale, $\omega_{B,01}\Delta t \gg 1$. Since the operation is a π rotation about the exchange gate axis, the gate time over which the averaging is done is $\Delta t \propto \hbar/J_{\mathrm{AC}} \propto \hbar|\epsilon|/g_0^2$. This condition can be written as $g_0 \ll \sqrt{\hbar\omega_B|\epsilon|}$, and $g_0 \ll \sqrt{\hbar\omega_{01}|\epsilon|}$ for the ST and hybrid qubits respectively.

The above condition implies that a large energy separation of the qubit states – essential for fast gating in the axis perpendicular to the exchange gate axis – is not only advantageous but crucial for the success of AC gating. This means that AC gating has the huge advantage that both exchange and phase accumulation single-qubit gates can be made fast.

Within the RWA, the problem is time-independent in the interaction picture. The RWA, interaction picture Hamiltonians for the ST and hybrid qubits are given by

$$H_{\mathrm{ST}}^{i,\mathrm{rwa}} = \begin{pmatrix} 0 & 0 & \frac{1}{2}g_0 \\ 0 & 0 & -\frac{1}{2}g_0 \\ \frac{1}{2}g_0 & -\frac{1}{2}g_0 & -\epsilon \end{pmatrix}, \tag{C.15}$$

$$H_{\rm hy}^{i,\rm rwa} = \begin{pmatrix} 0 & 0 & \frac{1}{2}g_0 \\ 0 & 0 & -\frac{1}{2}g_0 \\ \frac{1}{2}g_0 & -\frac{1}{2}g_0 & -\epsilon \end{pmatrix}. \tag{C.16}$$

We use the RWA interaction picture Hamiltonians of Eqs. C.15 and C.16 in the interaction picture master equation C.7 for numerical simulations in this work.

Description of slow and fast dephasing regimes

Based on measurements of decoherence times in semiconducting qubits [4, 27, 56, 23], we identify two regimes in which a particular dephasing mechanism dominates. At small detuning, fast dephasing Γ from double occupation is dominant, while at large detuning, slow dephasing γ of the logical qubit states dominates. In the following sections, we derive analytical expressions for the fidelities of the qubit systems in each of these regimes. We then explain how the optimal fidelity is deduced.

Fast Dephasing Γ Dominant Regime

In this section, we solve for the density matrix elements for the hybrid qubit in the regime in which fast dephasing dominates. In this regime, the solution for the ST qubit can be mapped onto the solution for the hybrid qubit by a one to one mapping of basis states: $|0\rangle_L \leftrightarrow |\uparrow,\downarrow\rangle, |1\rangle_L \leftrightarrow |\downarrow,\uparrow\rangle, |E\rangle \leftrightarrow |S_{02}\rangle$ – and will not be repeated here.

In the double quantum dot system, the fast dephasing rate Γ is much greater than the slow dephasing rate γ, so $\Gamma \gg \gamma$. In the regime where fast dephasing noise dominates the effect on the fidelity of a quantum gate, we make the approximation $\gamma \simeq 0$. In this regime, it is useful to change the basis in which the master equation 7 is analyzed to:

$$|u\rangle \equiv \frac{1}{\sqrt{2}}\left(|0\rangle_L - |1\rangle_L\right), \tag{C.17}$$

$$|v\rangle \equiv \frac{1}{\sqrt{2}}\left(|0\rangle_L + |1\rangle_L\right), \tag{C.18}$$

$$|w\rangle \equiv |E\rangle. \tag{C.19}$$

The gate fidelity in terms of the density matrix elements in the new basis is given by

$$\begin{aligned} f_{\rm hy} &\equiv \rho_{11}(\tau) = \rho^i_{11}(\tau) \\ &= \frac{1}{2}\left(\rho^i_{uu}(\tau) + \rho^i_{vv}(\tau) - \rho^i_{uv}(\tau) - \rho^i_{vu}(\tau)\right). \end{aligned} \tag{C.20}$$

The hybrid and ST qubits work in the region of large and negative detuning, so $-\epsilon$ is a positive quantity. To make the signs explicit so as to avoid confusion, we write $|\epsilon|$ whenever appropriate.

The master equation for the hybrid qubit yields six differential equations:

$$\dot{\rho}^i_{vv} = 0, \tag{C.21}$$

$$\dot{\rho}^i_{vu} = \frac{i}{\hbar}\frac{g_0}{\sqrt{2}}\rho^i_{vw}, \tag{C.22}$$

$$\dot{\rho}^i_{vw} = \frac{i}{\hbar}\left(\frac{g_0}{\sqrt{2}}\rho^i_{vu} + |\epsilon|\rho^i_{vw}\right) - \Gamma\rho^i_{vw}, \tag{C.23}$$

$$\dot{\rho}^i_{uu} = \frac{i}{\hbar}\frac{g_0}{\sqrt{2}}(\rho^i_{uw} - \rho^{i*}_{uw}), \tag{C.24}$$

$$\dot{\rho}^i_{uw} = \frac{i}{\hbar}\left(\frac{g_0}{\sqrt{2}}(\rho^i_{uu} - \rho^i_{ww}) + |\epsilon|\rho^i_{uw}\right) - \Gamma\rho^i_{uw}, \tag{C.25}$$

$$\dot{\rho}^i_{ww} = -\frac{i}{\hbar}\frac{g_0}{\sqrt{2}}(\rho^i_{uw} - \rho^{i*}_{uw}). \tag{C.26}$$

Eq. C.21 is trivially decoupled from the other equations, Eqs. C.22 and C.23 are coupled to each other, and Eqs. C.24, C.25 and C.26 are coupled with each other. Following Ref. [61], we parameterize the set of three density matrix elements ρ^i_{uu}, ρ^i_{uw} and ρ^i_{ww} in terms of a Bloch vector $\vec{n}$ on the $\{|u\rangle, |w\rangle\}$ Bloch sphere using

$$\begin{pmatrix} \rho^i_{uu} & \rho^i_{uw} \\ \rho^{i\,*}_{uw} & \rho^i_{ww} \end{pmatrix} = \frac{1}{2}\left(I + \vec{n}\cdot\vec{\sigma}\right). \tag{C.27}$$

From this, we obtain an equation describing the damped precession dynamics of the Bloch vector about a pseudo-magnetic field $\vec{\Omega}$,

$$\dot{\vec{n}} = \vec{\Omega}\times\vec{n} - \Gamma\vec{n}_t. \tag{C.28}$$

Here $\vec{n}_t \equiv \{n_x, n_y, 0\}$ is the transverse component of the Bloch vector and the pseudo-magnetic field vector is $\vec{\Omega} = \{\sqrt{2}g_0/\hbar, 0, |\epsilon|/\hbar\}$. The first term describes the precession of

the Bloch vector about the pseudo-magnetic field vector $\vec{\Omega}$. The second term describes the damping of the transverse component of the Bloch vector. If the gate is turned on sufficiently adiabatically and the dephasing rate is weak ($\hbar\Gamma \ll |\epsilon|$), the Bloch vector precesses around the pseudo-magnetic field vector $\vec{\Omega}$, making a small angle with the latter [61].

Taking the dot product on both sides of Eq. C.28 with $\vec{\Omega}$, and making the small angle approximation for the angle between $\vec{n}$ and $\vec{\Omega}$, we obtain

$$\dot{n} \simeq -\Gamma \sin^2\theta \; n, \tag{C.29}$$

where θ is the angle the pseudo-magnetic field vector $\vec{\Omega}$ makes with the $z-$axis of the Bloch sphere. It is related to the experimental quantities g_0 and ϵ by

$$\begin{aligned} \sin^2\theta &= \frac{2g_0^2}{2g_0^2+\epsilon^2} \\ &\simeq \frac{2g_0^2}{\epsilon^2} \ll 1, \end{aligned} \tag{C.30}$$

where the weak coupling or far-detuned regime of $g_0 \ll |\epsilon|$ was applied to the last step of Eq. C.30. Averaged over many precession cycles, the Bloch vector $\vec{n}$ makes an angle of approximately θ with the $z-$axis. Since angle θ is small, we take $n_z \simeq n$. Solving Eq. C.29 and using the small angle approximation for θ, we obtain

$$n_z(t) \simeq n(t) = \exp\left(-\frac{2g_0^2}{\epsilon^2}\Gamma t\right). \tag{C.31}$$

By making use of the condition where the initial state of our system is $|0\rangle_L$, we have the initial density matrix elements, $\rho^i_{uu}(0) = \rho^i_{vv}(0) = 1/2$, and $\rho^t_{ww}(0) = 0$. Using the initial conditions and the formal solution of $\rho^i_{uu}(t)$ from Eq. C.28, we have

$$\begin{aligned} \rho^i_{uu}(t) &= \frac{1}{2}\rho^i_{uu}(0)\left(1+n_z(t)\right), \\ &\simeq \frac{1}{2}\rho^i_{uu}(0)\left[1+\exp\left(-\frac{2g_0^2}{\epsilon^2}\Gamma t\right)\right]. \end{aligned} \tag{C.32}$$

In addition, Eq. C.21 gives us trivially,

$$\rho^i_{vv}(t) = \rho^i_{vv}(0). \tag{C.33}$$

Next, Eqs. C.22 and C.23 can be solved to give an exact solution for the interaction picture density matrix element:

$$\begin{aligned}\rho^i_{vu}(t) &= \frac{\rho^i_{vu}(0)}{2\xi} e^{\frac{1}{2}t(\xi+\Gamma-i|\epsilon|/\hbar)} \\ &\quad \times \left[\left(\xi - \Gamma + \frac{i|\epsilon|}{\hbar}\right) + e^{\xi t}\left(\xi + \Gamma - \frac{i|\epsilon|}{\hbar}\right)\right], \end{aligned} \tag{C.34}$$

where

$$\xi \equiv \sqrt{\left(\Gamma - \frac{i|\epsilon|}{\hbar}\right)^2 - 2\left(\frac{g_0}{\hbar}\right)^2} \tag{C.35}$$

$$\simeq \frac{i|\epsilon|}{\hbar}\left(1 - \frac{g_0^2}{\epsilon^2}\right) - \Gamma\left(1 - \frac{2g_0^2 + \hbar^2\Gamma^2}{\epsilon^2}\right). \tag{C.36}$$

Using Eq. C.36, Eq. C.34 can be further simplified to give a more instructive form:

$$\rho^i_{vu}(t) \simeq \frac{1}{2}\rho^i_{vu}(0) e^{-(\tilde{\Gamma} - iJ_{\rm AC}/\hbar)t}\left(1 + \mathcal{A}e^{-(\Gamma - i|\epsilon|/\hbar)t}\right), \tag{C.37}$$

which comprises of two oscillating terms. The quantities in Eq. C.37 above are defined as

$$\tilde{\Gamma} \equiv \Gamma\frac{(2g_0^2 + \hbar^2\Gamma^2)}{\epsilon^2} \simeq \Gamma\frac{2g_0^2}{\epsilon^2}, \tag{C.38}$$

$$J_{\rm AC} \equiv \frac{g_0^2}{2|\epsilon|}, \tag{C.39}$$

$$\mathcal{A} \equiv -2i\frac{\hbar\Gamma}{|\epsilon|}. \tag{C.40}$$

After expanding the terms in the parentheses in Eq C.37, the first term describes the large oscillation between the $|u\rangle$ and $|v\rangle$ states due to the exchange interaction $J_{\rm AC}$, at an angular frequency $J_{\rm AC}/\hbar$ and a dephasing rate $\tilde{\Gamma}$. The second term describes the rapid beating between the angular frequencies $|\epsilon|/\hbar$ and $J_{\rm AC}/\hbar$ due to the coupling of the qubit states $|u\rangle$ and $|v\rangle$ to the excited state $|w\rangle$. The amplitude of this beating is smaller than the primary oscillations by a factor of $|\mathcal{A}|$. We note that $|\mathcal{A}| \ll 1$, and drop the tiny beating term henceforth. With Eqs. C.32, C.33 and C.37, we can deduce the fidelity of a gate in the charge dephasing dominant regime using Eq. C.20. With a gate time of $\tau = \pi\hbar/J_{\rm AC}$ for a π rotation, we find that the fidelity in this regime is

$$f^{\rm f}_{\rm hy} \simeq \frac{3}{8} + \frac{1}{8}e^{-4\pi\hbar\Gamma/|\epsilon|} + \frac{1}{2}e^{-\pi\hbar\Gamma/|\epsilon|}. \tag{C.41}$$

By a one to one mapping of hybrid qubit to ST qubit basis states : $|0\rangle_L \leftrightarrow |\uparrow,\downarrow\rangle, |1\rangle_L \leftrightarrow |\downarrow,\uparrow\rangle, |E\rangle \leftrightarrow |S_{02}\rangle$, we can derive the fidelity in the same regime for the ST qubit in exactly the same manner as described above. The expression is identical to Eq. C.41:

$$f_{\rm ST}^{\rm f} \simeq \frac{3}{8} + \frac{1}{8}e^{-4\pi\hbar\Gamma/|\epsilon|} + \frac{1}{2}e^{-\pi\hbar\Gamma/|\epsilon|}. \tag{C.42}$$

From these results, it is clear that the fidelity of an exchange gate in the regime in which charge dephasing is dominant is independent of the tunnel coupling; it only depends on the ratio of the charge dephasing rate to the detuning, $\hbar\Gamma/|\epsilon|$. For any given charge dephasing rate, the fidelity can be improved by increasing the magnitude of the detuning. The physics behind this is that, at small absolute values of detuning, the state of the qubit contains a large fraction of the excited state which experiences fast dephasing from charge noise, resulting in reduced fidelity. As detuning increases, this fraction gets smaller, the effect of fast dephasing is reduced and fidelity increases.

There is a limit to the improvement in fidelity by simply slowing the gate speed through increasing detuning, since the gate speed is bounded from below by the ST dephasing rate. In the next section, we examine the fidelity in the regime of slow gate speeds, where ST dephasing becomes dominant.

Slow Dephasing γ Dominant Regime

At the other extreme is the regime where the exchange gate speeds are slow enough (at large absolute values of detuning) that the fidelity is limited by the dephasing between the singlet and triplet states of the qubit. Here, we make the approximation of $\Gamma \simeq 0$ so that the three-state systems can be described with effective two-state Hamiltonians. For the hybrid qubit, we write the effective interaction picture Hamiltonian in the logical basis $\{|0\rangle_L, |1\rangle_L\}$, and for the ST qubit, we write the effective interaction picture Hamiltonian in the ST basis $\{|S\rangle, |T_0\rangle\}$. The effective Hamiltonians are given by

$$H_{\rm hy}^{i,\rm eff} = \frac{1}{2}\begin{pmatrix} 0 & J_{\rm AC} \\ J_{\rm AC} & 0 \end{pmatrix}, \tag{C.43}$$

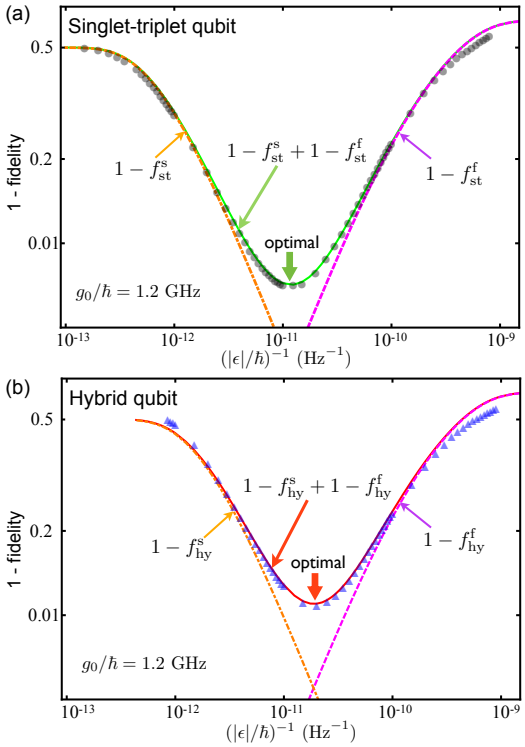

Figure C.1: Plots of infidelity (1-fidelity) against the reciprocal of detuning $(|\epsilon|/\hbar)^{-1}$ with a fixed value of tunnel coupling $g_0/\hbar = 1.2$ GHz, for LQR of the ST qubit (panel a) and the hybrid qubit (panel b). These plots were shown as the inset of Fig. 2 of the Chapter 4. Data from numerical simulations are plotted as gray circles and light blue triangles for the ST and hybrid qubits. For each qubit, data within the fast dephasing dominant regime (right side of each plot) are in good agreement with the corresponding analytical expression for infidelity $1 - f^{\mathrm{f}}$, shown as the magenta dashed lines. Also, data within the ST dephasing dominant regime (left side of each plot) agree very well with their corresponding analytical expression for infidelity $1 - f^{\mathrm{s}}$, shown as the orange dotted-dashed lines. We found that the optimized infidelity (minimum infidelity, Eqs. C.60 and C.61) correspond to the sum of the two infidelities, shown as the green and red bold curves on the ST and hybrid qubit plots respectively. Furthermore, the optima occur at approximately the value of detuning (Eqs. C.58) corresponding to the intersection of $1 - f^{\mathrm{f}}$ and $1 - f^{\mathrm{s}}$.

$$H_{\rm ST}^{i,\rm eff} = \begin{pmatrix} 0 & 0 \\ 0 & J_{\rm AC} \end{pmatrix}, \tag{C.44}$$

where $J_{\rm AC} = g_0^2/2|\epsilon|$ is the effective exchange energy for AC resonant gating.

In their respective bases, the dephasing terms in Eq. C.7 for the qubits are given by

$$D_{\rm hy}^{i,\rm eff} = \begin{pmatrix} 0 & \gamma_{\rm hy}\rho_{01}^i \\ \gamma_{\rm hy}\rho_{10}^i & 0 \end{pmatrix}, \tag{C.45}$$

$$D_{\rm ST}^{i,\rm eff} = \begin{pmatrix} 0 & \gamma_{\rm ST}\rho_{st}^i \\ \gamma_{\rm ST}\rho_{ts}^i & 0 \end{pmatrix}. \tag{C.46}$$

Using the master equation (Eq. C.7) in the interaction picture, we obtain two coupled differential equations for the density matrix elements for the ST qubit as

$$\dot{\rho}_{ss}^i = 0, \tag{C.47}$$

$$\dot{\rho}_{st}^i = \frac{iJ_{\rm AC}}{\hbar}\rho_{st}^i - \gamma_{\rm ST}\rho_{st}^i. \tag{C.48}$$

These yield exact solutions,

$$\rho_{ss}^i(t) = \rho_{ss}^i(0), \tag{C.49}$$

$$\rho_{st}^i(t) = \rho_{st}^i(0)e^{-(\gamma_{\rm ST}+iJ_{\rm AC}/\hbar)t}, \tag{C.50}$$

from which the fidelity of the ST qubit can be derived. Using $\tau = \pi\hbar/J_{\rm AC}$, we obtain the fidelity in the ST dephasing dominant regime for the ST qubit as

$$\begin{aligned} f_{\rm ST}^{\rm s} &\equiv \rho_{bb}(\tau) = \rho_{bb}^i(\tau) \\ &= \frac{1}{2}\left(\rho_{ss}^i(\tau) + \rho_{tt}^i(\tau) - \rho_{st}^i(\tau) - \rho_{ts}^i(\tau)\right) \\ &= \frac{1}{2}\left[1 + \exp\left(-\frac{2\pi\hbar\gamma_{\rm ST}|\epsilon|}{g_0^2}\right)\right]. \end{aligned} \tag{C.51}$$

The master equation for the hybrid qubit gives the following differential equations

$$\dot{\rho}_{11}^i = -\frac{iJ_{\rm AC}}{2\hbar}\left(\rho_{01}^i - \rho_{01}^{i*}\right), \tag{C.52}$$

$$\dot{\rho}_{01}^i = -\frac{iJ_{\rm AC}}{2\hbar}\left(2\rho_{11}^i - 1\right) - \gamma_{\rm hy}\rho_{01}^i. \tag{C.53}$$

These yield an approximate solution to zeroth order in $\hbar\gamma_{\rm hy}/J_{\rm AC}$ for the appropriate density matrix element,

$$\rho_{11}^{i}(t) \simeq \frac{1}{2}\left(1 + e^{-(\gamma_{\rm hy}/2 + iJ_{\rm AC}/\hbar)t}\right), \tag{C.54}$$

from which the fidelity of the hybrid qubit can be derived:

$$\begin{aligned} f_{\rm hy}^{\rm s} &\equiv \rho_{11}(\tau) = \rho_{11}^{i}(\tau) \\ &\simeq \frac{1}{2}\left[1 + \exp\left(-\frac{\pi\hbar\gamma_{\rm hy}|\epsilon|}{g_0^2}\right)\right]. \end{aligned} \tag{C.55}$$

Optimal fidelity

In the regime of slow exchange gates, ST dephasing dominates, and the fidelity increases when the magnitude of the detuning is decreased. In the regime in which fast dephasing dominates, increasing the magnitude of the detuning improves fidelity. Therefore, there is some optimal value of detuning for which the fidelity is maximum.

We find that the net infidelity $(1 - f)$ obtained from simulated data are in excellent agreement with a simple sum of the infidelities in the two regimes. This allows us to write

$$f_{\rm ST} = f_{\rm ST}^{\rm f} + f_{\rm ST}^{\rm s} - 1, \tag{C.56}$$

$$f_{\rm hy} = f_{\rm hy}^{\rm f} + f_{\rm hy}^{\rm s} - 1. \tag{C.57}$$

Also, we find empirically, across a wide range of values of dephasing rates, detuning and tunnel coupling, that the optimal values of detuning and fidelity occur when the curves for fidelity in the two regimes, f^c and f^q, intersect. Expanding the exponential terms in terms of small quantities $\hbar\Gamma/|\epsilon|$ and $\hbar\gamma/J_{\rm AC}$, we deduce the value of detuning which gives the optimal fidelity for each qubit,

$$|\epsilon_{\rm ST}^{\rm opt}| \simeq g_0\sqrt{\Gamma/\gamma_{\rm ST}}, \tag{C.58}$$

$$|\epsilon_{\rm hy}^{\rm opt}| \simeq g_0\sqrt{2\Gamma/\gamma_{\rm hy}}. \tag{C.59}$$

From these results, we deduce simple expressions for the optimal fidelities in terms of either tunnel coupling amplitude g_0:

$$f_{\rm ST}^{\rm opt} \simeq 1 - \frac{2\pi\hbar\sqrt{\Gamma\gamma_{\rm ST}}}{g_0}, \tag{C.60}$$

$$f_{\rm hy}^{\rm opt} \simeq 1 - \frac{2\pi\hbar\sqrt{\Gamma\gamma_{\rm hy}/2}}{g_0}. \tag{C.61}$$

C.3 STIRAP Gating

STIRAP tunnel coupling pulses

For STIRAP [68] gating, the tunnel coupling is the sum of two Gaussian envelopes, each modulated at the frequency of the transition between a qubit state and the intermediate state. The pulses are applied in a counter-intuitive sequence, with the Stokes pulse that couples the target qubit state and the intermediate state, applied before the pump pulse that couples the initial qubit state and the intermediate state.

$$g_s(t) = g_0 \exp\left[-\left(\frac{t + t_{\text{delay}}/2}{t_{\text{width}}}\right)^2\right], \tag{C.62}$$

$$g_p(t) = g_0 \exp\left[-\left(\frac{t - t_{\text{delay}}/2}{t_{\text{width}}}\right)^2\right]. \tag{C.63}$$

For the ST qubit, the time dependence of the tunnel coupling in STIRAP gating is given as

$$g(t) = g_s(t)\left(1 + \cos(\omega_s t)\right) + g_p(t)\left(1 + \cos(\omega_p t)\right), \tag{C.64}$$

where $\omega_s \equiv |\epsilon|/\hbar + \frac{1}{2}\omega_B$ is the angular frequency corresponding to the energy difference between the initial state $|\uparrow,\downarrow\rangle$ and the excited charge state $|S_{02}\rangle$, and $\omega_p \equiv |\epsilon|/\hbar - \frac{1}{2}\omega_B$ is the angular frequency corresponding to the energy difference between the final state $|\downarrow,\uparrow\rangle$ and the excited charge state $|S_{02}\rangle$.

For the hybrid qubit, the time-dependence of the tunnel couplings in STIRAP gating is given by

$$g_1(t) = g_s(t)\left(1 + \cos(\omega_s t)\right) + g_p(t)\left(1 + \cos(\omega_p t)\right), \tag{C.65}$$

$$g_2(t) = g_s(t)\left(1 + \cos(\omega_s t)\right) + g_p(t)\left(1 + \cos(\omega_p t)\right), \tag{C.66}$$

where $\omega_s \equiv |\epsilon|/\hbar + \frac{1}{2}\omega_{01}$ is the angular frequency corresponding to the energy difference between the initial state $|0\rangle_L$ and the excited charge state $|E\rangle$, and $\omega_p \equiv |\epsilon|/\hbar - \frac{1}{2}\omega_{01}$ is the angular frequency corresponding to the energy difference between the final state $|1\rangle_L$ and the excited charge state $|E\rangle$.

In our numerical study we cut off the Gaussian tails by taking a hard limit on the start and end times of STIRAP gating by taking the product of Eqs. C.64 and C.65 with a

rectangular unit step function that is zero outside of times $t > |t_{\rm delay} + t_{\rm width}|$. We define as the gating speed, $\frac{1}{2}(t_{\rm delay} + t_{\rm width})^{-1}$, indicated by the top panel of Fig. 2 in the Chapter 4.

To transform into the interaction picture, we take $U_{\rm ST} \equiv \exp\left(-\frac{it}{\hbar}{\rm diag}\left\{H_{\rm ST}\right\}\right)$ and $U_{\rm hy} \equiv \exp\left(-\frac{it}{\hbar}{\rm diag}\left\{H_{\rm hy}\right\}\right)$, we obtain the interaction picture Hamiltonians in the rotating wave approximation as

$$H_{\rm ST}^{i,{\rm rwa}} = \begin{pmatrix} 0 & 0 & \frac{1}{2}g_p(t) \\ 0 & 0 & -\frac{1}{2}g_s(t) \\ \frac{1}{2}g_p(t) & -\frac{1}{2}g_s(t) & 0 \end{pmatrix}, \tag{C.67}$$

$$H_{\rm hy}^{i,\ {\rm rwa}} = \begin{pmatrix} 0 & 0 & \frac{1}{2}g_p(t) \\ 0 & 0 & -\frac{1}{2}g_s(t) \\ \frac{1}{2}g_p(t) & -\frac{1}{2}g_s(t) & 0 \end{pmatrix}. \tag{C.68}$$

We use the master equation in the interaction picture (Eq. C.7) to compute the fidelity, and then optimize the fidelity for STIRAP with pulse parameters $t_{\rm delay}$ and $t_{\rm width}$ for each value of tunnel coupling amplitude g_0.

Scaling of STIRAP fidelity

It was shown in the previous section, how the optimal fidelity for LQR scales with the amplitude of tunnel coupling g_0 and the fast and slow dephasing rates Γ, γ.

We have strong numerical evidence that the optimal fidelity for STIRAP gating follows the same scaling law, given in Eqs. C.60 and C.61.

The first piece of numerical evidence can be seen in Fig. 2 of the Chapter 4, where the optimal fidelities obtained for both STIRAP and LQR are in excellent agreement with the scaling laws for both qubits, over a range of tunnel coupling amplitudes g_0, for fixed dephasing rates Γ and γ.

In addition, we calculated the optimal fidelities for STIRAP and for LQR over a range of fast dephasing rates Γ, for fixed γ and g_0. This is shown in Fig. C.2, where good agreement with the scaling laws of Eqs. C.60 and C.61 (bold lines), are demonstrated for both STIRAP (open symbols) and LQR (filled symbols).

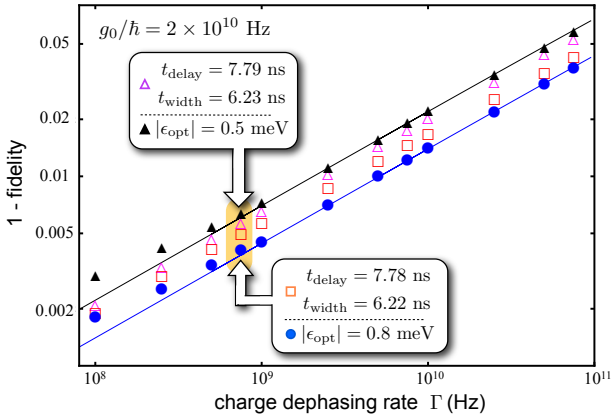

Figure C.2: Plot of infidelity (1 - fidelity) against charge dephasing rate Γ for LQR and STIRAP gating at a fixed tunnel coupling amplitude $g_0/\hbar = 2 \times 10^{10}$ Hz, and for ST dephasing rates of $\gamma_{\rm ST} = 2 \times 10^5$ Hz and $\gamma_{\rm hy} = 1 \times 10^6$ Hz. The black line is the analytical result for the optimal infidelity (Eq. C.61) for the hybrid qubit and the blue line is the analytical result for the optimal infidelity (Eq. C.60) for the ST qubit. Numerical results for LQR are plotted as solid black triangles and solid blue circles for the hybrid and ST qubits respectively. They follow their corresponding analytical results (Eqs. C.60 and C.61) very closely. Optimal infidelities for STIRAP gating are plotted in empty triangles and empty squares for the hybrid and ST qubits respectively. The results show that the infidelities for STIRAP agree very closely with those of LQR over a wide range of charge dephasing rates. The optimized pulse parameters for STIRAP gating as well as the optimal detuning for LQR are given in the boxes for a charge dephasing rate of $\Gamma = 7.5 \times 10^8$ Hz.

To further support our claim that the optimal fidelity for STIRAP follows the scaling law that was derived for LQR, we optimized STIRAP over a range of dephasing rates and tunnel coupling amplitudes, while keeping as a constant the quantities: $\frac{\hbar\sqrt{\Gamma\gamma_{\rm ST}}}{g_0}$ for the ST qubit, and $\frac{\hbar\sqrt{\Gamma\gamma_{\rm hy}/2}}{g_0}$ for the hybrid qubit. This is shown in Fig. C.3, where the optimal fidelities for both qubits follow the scaling laws (bold line).

C.4 DC pulsed gating

In DC pulsed gating, tunnel couplings are fixed while detuning ϵ is controlled by the application of electrical voltages to appropriate top-gates. Detuning pulses are modeled as instantaneous, i.e. nonadiabatic. In our model, tunnel couplings are defined to be a real-

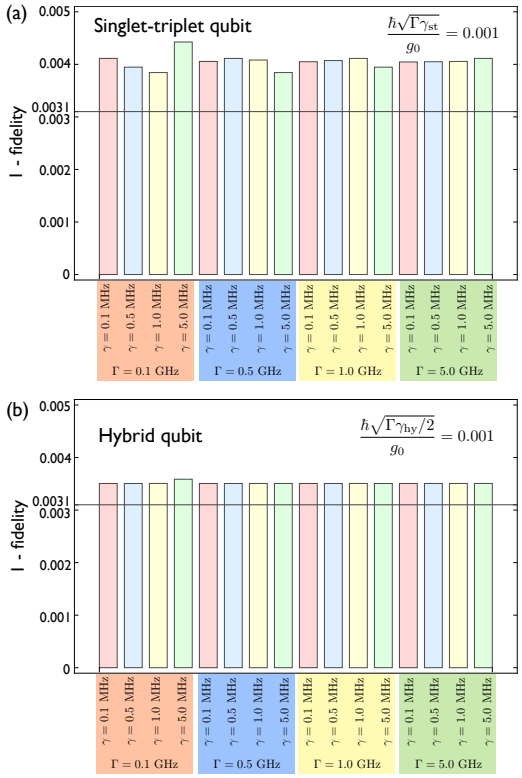

Figure C.3: Optimal infidelity (1-fidelity) of STIRAP for a range of fast and slow dephasing rates, Γ and γ, and tunnel coupling amplitude g_0, while keeping as a constant the quantities: $\hbar\sqrt{\Gamma\gamma_{\rm ST}}/g_0 = 0.001$ for the ST qubit (panel a), and $\hbar\sqrt{\Gamma\gamma_{\rm hy}/2}g_0 = 0.001$ for the hybrid qubit (panel b). With these quantities fixed, the fidelities as given by the scaling laws in Eqs. C.60 and C.61 are constant. The bold horizontal lines at 0.0031 in both panels are the optimal infidelities calculated from the above equations. The optimized STIRAP fidelities show close agreement with the analytical result, with maximum deviations of less than 40% for the ST qubit (panel a) and 15% for the hybrid qubit.

valued constant value, $g \equiv g_0$ for the ST qubit, and $|g_1| \equiv |g_2| \equiv g_0$ for the hybrid qubit.

The Hamiltonians used in the DC pulsed gating sequences are

$$H_{\rm ST} = \begin{pmatrix} -E_B/2 & 0 & g_0 \\ 0 & E_B/2 & -g_0 \\ g_0 & -g_0 & -\epsilon(t) \end{pmatrix}, \tag{C.69}$$

$$H_{\rm hy} = \begin{pmatrix} -E_{01}/2 & 0 & g_0 \\ 0 & E_{01}/2 & -g_0 \\ g_0 & -g_0 & -\epsilon(t) \end{pmatrix}. \tag{C.70}$$

In the limit of zero energy separation between qubit states, i.e. $E_B = 0$ and $E_{01} = 0$, the exchange interaction of DC gating is $J_{\rm DC} = 2g_0^2/|\epsilon|$, which is 4 times larger than the AC exchange interaction $J_{\rm AC}$ due to the factor of 1/2 in the Hamiltonians for AC gating (Eqs. C.15 and C.16). This implies that the optimal fidelity for DC pulsed gating in the limit of zero energy separation can be derived in the same way as that for LQR, by a simple substitution of $g_0 \to 2g_0$ in Eqs C.60 and C.61. This gives, for the ST qubit,

$$\lim_{\Delta E_B \to 0} f_{\rm ST}^{\rm DC} \simeq 1 - \frac{\pi\hbar\sqrt{\Gamma\gamma_{\rm ST}}}{g_0}. \tag{C.71}$$

Fig. 3 of the Chapter 4 shows a plot of the optimal fidelities from the 3-step DC pulse sequence of Hanson and Burkard (HB) [75] at two inter-dot magnetic field differences. These plateau at larger tunnel couplings because of the bottleneck from the slow magnetic gate in the second step of the HB sequence..

We plot the optimal DC gating fidelity for simple one step pulse sequence in Fig. C.4 and compare it with the fidelity from the HB 3-step sequence plotted in the inset of the same figure. We find that the one step pulse sequence provides a significant improvement to the fidelity obtained from the HB sequence at large tunnel couplings. The reason for this is due to the fact that large enough tunnel couplings, the exchange interaction can be made much larger than the qubit energy separation, $J \gg E_B$, leading to a fast rotation tilted only slightly away from the $x-$axis. In comparison, the 3-step HB procedure corrects this tiny tilt, but at the cost of a slow gate. The horizontal lines represents the fidelity of the magnetic gate for the two inter-dot magnetic fields plotted and correspond to the plateaus of the HB sequence.

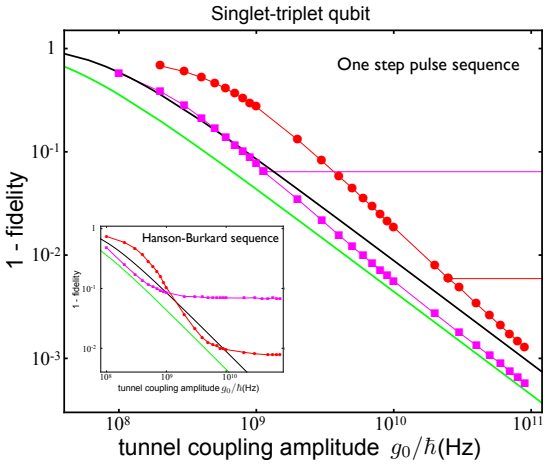

Figure C.4: Main panel: Infidelity (1-fidelity) of DC pulsed gating for the ST qubit using a one step pulse sequence for isotopically purified silicon with an inter-dot magnetic field difference of 0.03 mT (magenta squares) and 0.3 mT (red circles). Inset: plot of infidelity of the HB [94] 3-step sequence for the same inter-dot field differences. The one step pulse sequence provides a significant improvement to the fidelity obtained from the HB sequence at large tunnel couplings, due to the fact that large enough tunnel couplings, the exchange interaction can be made much larger than the qubit energy separation, $J \gg E_B$, leading to a fast rotation tilted only slightly away from the $x-$axis. In comparison, the 3-step HB procedure corrects this tiny tilt, but at the cost of a slow gate. The horizontal lines represents the fidelity of the magnetic gate for the two inter-dot magnetic fields plotted and correspond to the plateaus of the HB sequence. The optimal AC fidelity (Eq. C.60) is shown as the black bold line, while the optimal DC fidelity for the asymptotic limit of $E_B \to 0$ (Eq. C.71) is shown as the green bold line. The fidelities using the one-step sequence tend asymptotically to the latter as tunnel coupling increases.

Appendix D

Supplemental material for Chapter 5

We present details of the numerical simulation presented in Chapter 5. We explain the choice of parameters by discussing simulations with several choices of the parameters and with one instead of two anticrossings. The results indicate two anticrossings are required to explain the data.

D.1 Numerical simulation of charge oscillation data

We model the dynamical evolution of the density matrix ρ of the three electron, double quantum dot system by the master equation [2, 78] approach. The master equation, $\dot{\rho} = -\frac{i}{\hbar}[H, \rho] - D$, is explained in Eq. 3.5 in Chapter 3 and again in Eq. **??** in Chapter 4. The Hamiltonian is given by H; D is a phenomenological term that describes pure dephasing of the charge state under the assumption of Markovian dynamics, as appropriate for the

double dot system. In the $\{|a\rangle \equiv |G(2,1)\rangle, |b\rangle \equiv |G(1,2)\rangle, |c\rangle \equiv |E(1,2)\rangle\}$ basis, they are

$$H = \begin{pmatrix} \epsilon/2 & g_1 & g_2 \\ g_1 & -\epsilon/2 & 0 \\ g_2 & 0 & \delta\epsilon - \epsilon/2 \end{pmatrix}, \tag{D.1}$$

$$D = \begin{pmatrix} 0 & \Gamma_{ab}\ \rho_{ab} & \Gamma_{ac}\ \rho_{ac} \\ \Gamma_{ab}\ \rho_{ba} & 0 & 0 \\ \Gamma_{ac}\ \rho_{ca} & 0 & 0 \end{pmatrix}, \tag{D.2}$$

where g_1 and g_2 are tunnel coupling matrix elements, ϵ is the detuning, $\delta\epsilon$ is the energy separation of the ground and excited (1,2) states ($|b\rangle$ and $|c\rangle$), and Γ_{ab} and Γ_{ac} are dephasing rates ($1/T_2^*$) that describe the exponential decay of the coherences between different charge states of the qubit, presumably caused by charge noise. We note that the existence of the low-lying excited state E(1,2) is consistent with experimental magnetospectroscopy measurements showing that the right dot has a very small or negative singlet-triplet splitting in the two-electron state (data not shown). In contrast, the first excited state of the left dot is large in energy (approximately 200 μeV) [33] and therefore can be neglected.

From the data, the dephasing rates show a dependence on detuning. Dephasing rates increase away from a minimum of $\Gamma_i = 0.48$ GHz at detuning $\epsilon = 0$, corresponding to the position of the first anticrossing. Similar behavior of noise in the detuning parameter has been observed in GaAs double dot charge qubits with one anticrossing [50, 56].

We use the T_2^* value of 179 ps at a detuning of -63 μeV derived from the Ramsey experiment, combined with the intrinsic minimum observed in the Larmor oscillations to model the dephasing rates. They are given as a quadrature sum of the intrinsic rate Γ_i and a detuning dependent rate $\alpha\Gamma_\epsilon$:

$$\Gamma_{ab} = \sqrt{\Gamma_i^2 + (\alpha_{ab}\ \Gamma_\epsilon)^2}, \tag{D.3}$$

$$\Gamma_{ac} = \sqrt{\Gamma_i^2 + (\alpha_{ac}\ \Gamma_\epsilon)^2}, \tag{D.4}$$

where Γ_ϵ is a parameter that is determined by experimental values of T_2^* at two values of detuning as described above. The variables α_{ab} and α_{ac} play the role of describing the

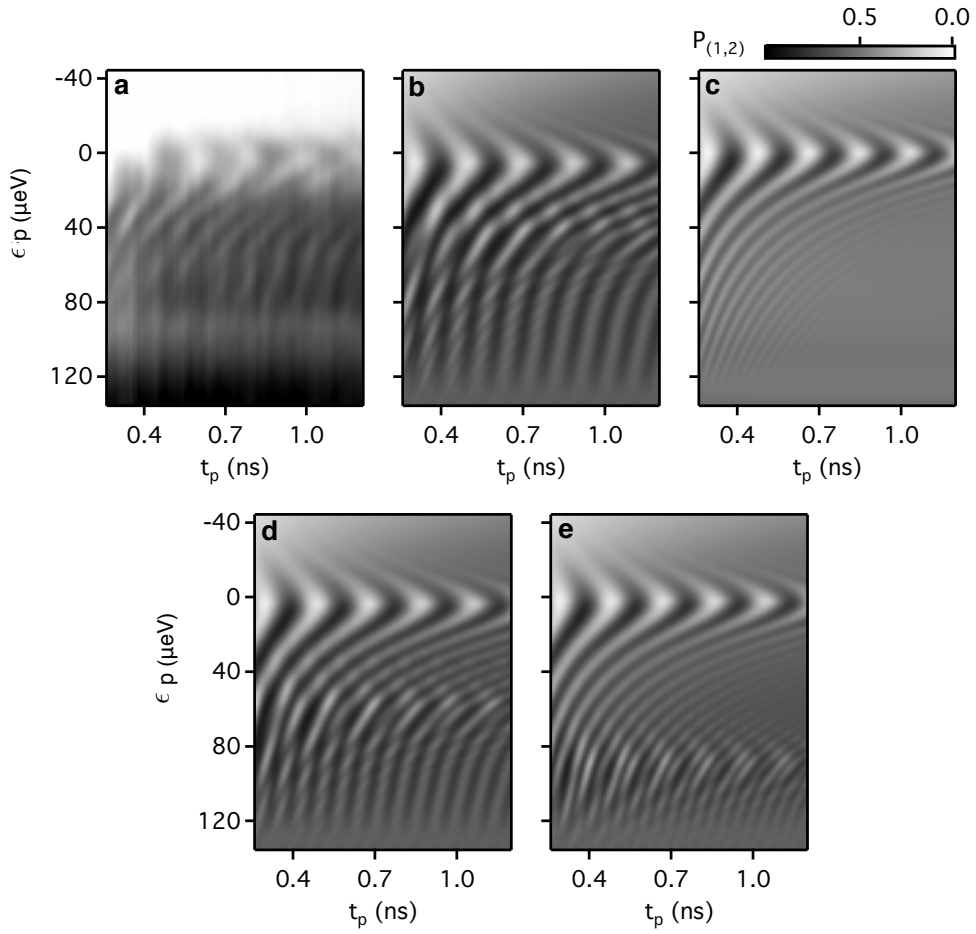

Figure D.1: Comparison between experimental Larmor oscillation data (panel (a)) and simulations (rest of panels). (a) Larmor oscillation data (reproduced from Fig. 2c of the main paper). (b) Simulation using optimal values of parameters: $g_1/h = 2.7$ GHz, $g_2/h = 3.5$ GHz, $\delta\epsilon = 45$ μeV and $\Gamma_\epsilon = 5.98$ GHz. (c) Simulation, using optimal parameters as in b, but with only a single anticrossing (a two-state model). It is clear that a single anticrossing is insufficient to explain the data, as a single anticrossing does not result in the nearly parallel fringes in the lower half of the plot. Panels (d) and (e) are simulations with the optimal values of all the parameters as in b, except for the anticrossing separation $\delta\epsilon$. In (d) and (e), $\delta\epsilon = 60$ μeV and 90 μeV, respectively. Comparing (b), (d) and (e), it is clear that as the displacement $\delta\epsilon$ between the first and the second anticrossing increases, the frequency of oscillations at far positive detuning increases as well. Thus, the frequency of these oscillations essentially fixes $\delta\epsilon$.

relative fluctuations in energy between different charge states due to changes in detuning. In terms of the slopes of energy versus detuning, they are

$$\alpha_{ab}(\epsilon_j) \equiv \left| \frac{dE_a}{d\epsilon} - \frac{dE_b}{d\epsilon} \right|_{\epsilon=\epsilon_j}, \tag{D.5}$$

$$\alpha_{ac}(\epsilon_j) \equiv \left| \frac{dE_a}{d\epsilon} - \frac{dE_c}{d\epsilon} \right|_{\epsilon=\epsilon_j}. \tag{D.6}$$

Eqs. D.3 and D.4 produce dephasing that decreases as the relative slopes of a pair of energy-detuning curves gets flatter, and vice versa, as observed in the data.

Electrical pulses applied to gate L control the detuning ϵ as a function of time, and this is modeled as a smooth trapezoid with a rise time of 80 ps (from the specifications for the Agilent 81134A pulse generator) and pulse amplitude of 127 μeV.

D.2 Simulation results

The tunable parameters that go into our simulation are the values of the tunnel couplings g_1 and g_2, and the energy separation $\delta\epsilon$ between the ground and excited (1,2) charge states. Using Eq. (D.3), the detuning-dependent dephasing parameter Γ_ϵ is determined by experimentally extracted dephasing rates at two detuning values, namely the intrinsic dephasing rate $\Gamma_i = 0.48$ GHz at $\epsilon = 0$, and the T_2^* value of 179 ps at $\epsilon = -63$ μeV, which yields $\Gamma_\epsilon = 5.98$ GHz. Optimal values of the other parameters can then be found to give the best fit to the data. We found that the optimal values of the parameters that give the best fit to the data are: $g_1/h = 2.7$ GHz, $g_2/h = 3.5$ GHz, and $\delta\epsilon = 45$ μeV.

Here, we briefly explain how the parameters were obtained. The frequency of oscillations at the first anticrossing at $\epsilon = 0$ is very sensitive to the value of the first tunnel coupling and sets the value of g_1, as is consistent with the usual Larmor dynamics of two-level systems. Because the pulse is not entirely abrupt, detuning pulses that reach beyond the first anticrossing (that is, to $\epsilon > 0$) necessarily induce Landau-Zener-Stuckelberg interference effects [84, 85, 86, 87]. For the energy level structure we study here, the presence and proximity of the second anticrossing to the first results in population of both G(1,2) and E(1,2), states $|b\rangle$ and $|c\rangle$. The frequency of oscillations at far positive detuning is strongly

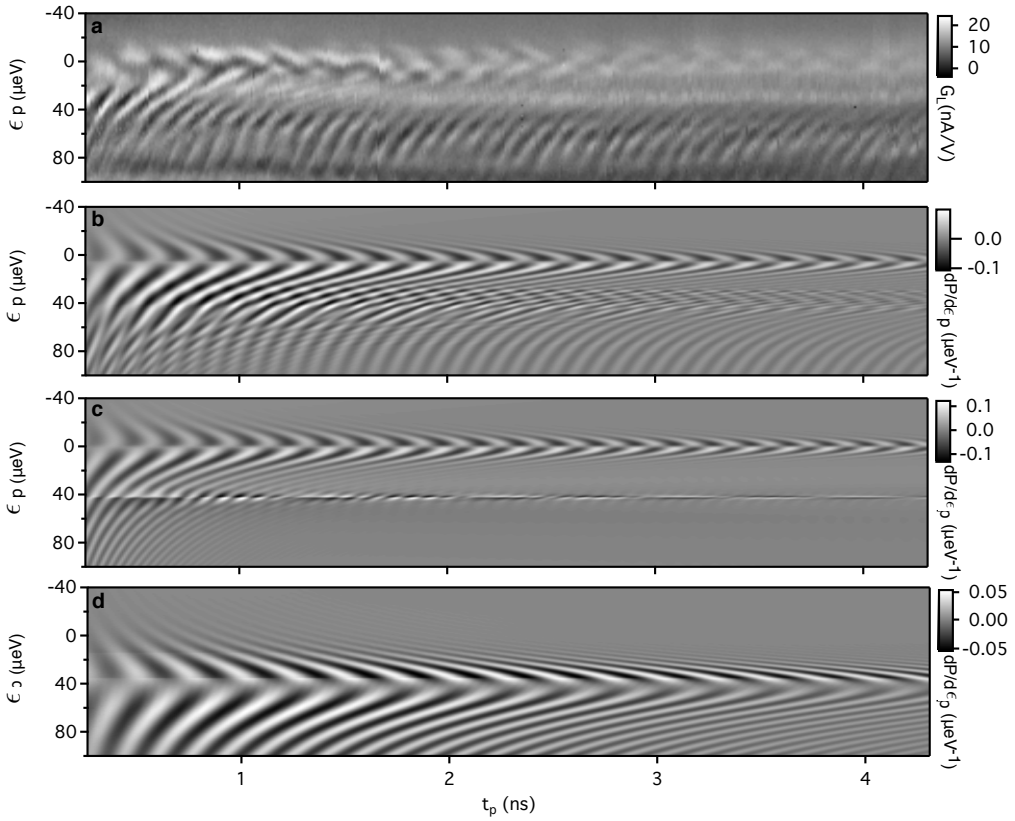

Figure D.2: Explanation of the determination of g_2. (a) Experimental QPC transconductance $G_{\rm L}$, from Fig. 5.2(a), as a function of both detuning and pulse width. Here, for comparison to theory, we have shifted each vertical line scan to compensate for the increasing pulse duration, as described in the caption for Fig. 5.2(c–e). (b) Simulation of $G_{\rm L}$ with the same parameters as in Fig. D.1 above: $g_1/h = 2.7$ GHz, $g_2/h = 3.5$ GHz, $\delta\epsilon = 45\mu$eV, and $\Gamma_\epsilon = 5.98$ GHz. The simulation shows good agreement with the data. Note in particular the nearly vertical lines in the bottom half of panels (a) and (b). (c) Simulation with the same parameters except $g_2/h = 0.6$ GHz. The small value of g_2 results in fringes that are essentially unresolvable in the lower half of the plot for times larger than 1 ns or so. (d) Simulation with the same parameters except $g_2/h = 10$ GHz. For large g_2 the second anticrossing dominates the energy level spectrum the effect of the first anticrossing (at $\epsilon = 0$) is not visible in the simulation, in stark contrast to the experimental data in panel a.

dependent on the anticrossing separation $\delta\epsilon$, and that frequency essentially fixes $\delta\epsilon$. The precise value of the tunnel coupling g_2 at the second anticrossing is not critical; nonetheless, we show below it must be of order 3.5 GHz; if it is dramatically different, the parallel fringes from $\epsilon = 50$ to 100 μeV do not appear in the simulations.

Fig. D.1 shows a comparison of simulated data using various parameters. Panel a shows the experimental Larmor oscillation data (reproduced from Fig. 5.2(c) of Chapter 5). Panel b shows the simulated data using the optimal parameters, displaying excellent agreement with the main features of the data shown in panel a.

In order to ascertain whether the oscillations at far positive detuning can be explained by having only one anticrossing, simulated data, shown in Panel c, show the result for a two-state model with one anticrossing. This simulation with a single anticrossing shows clear discrepancies with the data at large positive detuning, even though there is a good match at zero detuning. It is clear that in order to consistently explain the data — especially the prominent nearly parallel lines at $\epsilon > 0$ — a single anticrossing is insufficient.

The frequency of oscillations at far positive detuning is affected by the proximity of the second anticrossing to the first. Panels d and e are simulations using all of the optimal values of the parameters, except for the anticrossing separation $\delta\epsilon$. In panel b, $\delta\epsilon = 45$ μeV, while in panels d and e $\delta\epsilon = 60$ μeV and 90 μeV respectively. Comparing these panels, it is clear that the proximity of the second anticrossing plays an important role in determining the number of secondary oscillations at far positive detuning, allowing us to fix $\delta\epsilon$.

Fig. D.2 shows a comparison between a the experimentally measured Larmor oscillations and b–d simulations with three different values of g_2. For clarity the lock-in data G_{L} is plotted in a and the simulations are differentiated with respect to ϵ_{p} to correspond to this data. The agreement between simulations using the optimal value of $g_2/h = 3.5$ GHz, plotted in b and the data in a is very good. Modest variations in g_2 from this value do not produce large changes in the simulated results. Panels c and d show that large changes from the optimal value can clearly be ruled out. In c, $g_2/h = 0.6$ GHz is too small, and the fringes in the lower half of the plot are missing. In d, $g_2/h = 10$ GHz is too large, and the affect of the first anticrossing at $\epsilon = 0$ is overwhelmed by the influence of the second anticrossing.

Appendix E

Supplemental material for Chapter 6

E.1 Analysis of real-time electron counting data

All of the single-shot counting experiments in the paper required detecting single electron tunneling events, as indicated by changes in the quantum point contact (QPC) current I_{QPC}. Two different algorithms were employed for this determination. The first algorithm used wavelets to determine transition edges and, subsequently, levels in the QPC signal. All of the data in the paper were analyzed with this wavelet algorithm. In the second algorithm, the data were inspected using a thresholding technique. Instead of detecting edges of transitions in the signal, this method compares the value of the QPC signal to a threshold value and thereby infers the state of the dot. Both algorithms are described in greater detail below, and we show that the results of the two approaches to the analysis are consistent.

Electron tunnel event detection using wavelets

A single electron tunneling onto or off of the quantum dot causes changes in the magnitude of I_{QPC}, leading to steps or "edges" in $I_{\mathrm{QPC}}(t)$. Wavelet analysis is a useful tool to determine the significance of edges. In fact, the classic Canny edge detection algorithm [138] can be

interpreted in the context of wavelets. Based on observation of the real wavelet transform of our data and its noise characteristics, a robust edge detection algorithm was constructed based on the Stanford Wavelab library [139]. The algorithm has strong similarities to the Canny algorithm. First derivative of Gaussian wavelets [140] are used, implemented under the name "DerGauss" in Wavelab. Significant edges are indicated by (i) the presence of a modulus maxima track over many scales of the wavelet transform, and (ii) the amplitude of the wavelet transform (A_W) at the location of its track [140].

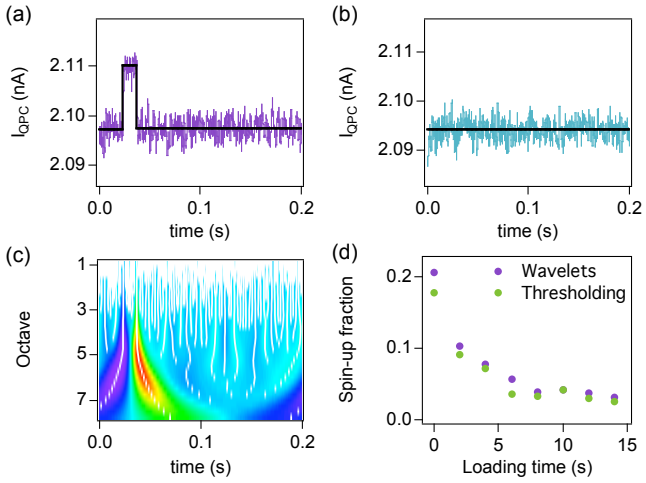

Figure E.1: (a and b) Raw data and reconstructed signals (shown in black) using the real wavelet transform for the two single-shot traces presented in Fig. 6.2(a, b). (c) Real wavelet transform and modulus maxima (shown in white) for the trace shown in (a). (d) Results of the T_1 measurement presented in the inset to Fig. 6.3(b), analyzed using both wavelet and thresholding algorithms. Exponential fits yield $T_1 = 2.75 \pm 0.33$ s for the wavelet analysis results and $T_1 = 2.72 \pm 0.37$ s for the thresholding analysis results.

The design of the algorithm and the tuning of its parameters were initially accomplished by the selection of a set of single-shot traces displaying a wide variety of inputs. These inputs included traces with events on short, middle, and long time scales; traces with no, few, or several events; and traces with a variety of significant features that did not correspond to actual events. The wavelet transforms of all traces in this set were observed, which allowed the construction of the algorithm and the initial tuning of detection parameters. Subsequently, a few thousand traces were analyzed and verified by hand, and parameters

were tweaked to approach a detection rate of 98%. It should be noted that, in all steps of the algorithm but the last, we try to err in the direction of selecting too many (possibly spurious) edges, waiting until the last step to reject spurious events.

The sampling rate employed in this experiment was 40 kHz, much higher than the 1 ms rise time of the current amplifier. To speed up processing, bins of ten data points were averaged, which did not result in a loss of significant features. The "DerGauss" real wavelet transform was computed using four scales per octave, which provides adequate resolution in the wavelet domain to make real features stand out visually. The modulus maxima of this wavelet transformation is then computed. A sample plot of a wavelet transformation with its modulus maxima superimposed can be seen in Fig. E.1(c) for the trace shown in (a).

The algorithm then iterates from the coarsest to the finest scale of the wavelet transform. At each scale, the wavelet amplitude squared (A_W^2) for each modulus maxima track is computed. Tracks for which this value reaches ten times the median value of all tracks at that scale are stored for further processing. The purpose of this step is to select edges that are significantly larger than all other edges at the time scale under examination, which is reasonable because few events are expected in any particular trace. For the results presented in this paper, increasing or decreasing the cutoff value by a factor of two results in less than a 5% change in the correct detection ratio.

The stored tracks are then followed to the next finer time scale, a procedure which is repeated until the best estimate of position for an edge is obtained at the finest time scale. For each modulus maxima track this is accomplished by finding the closest track for which the wavelet amplitude has the same sign on both scales. Some tracks representing spurious features, such as an insignificant change in the base level of the signal, or the remainder of a crosstalk edge at the beginning or end of the data, may fall off the edge of the wavelet transform. For this reason, all tracks that come to within 2.5 rise times of the edge are rejected. If cross talk from the applied pulse sequence were not significant, this parameter could be set much less aggressively, as in that case only tracks that truly fall off the edge

need to be rejected. Halving or doubling this parameter causes up to a 10% change in correct detections. At each time scale in the iteration, new tracks that suddenly reach the cutoff discussed in the previous paragraph are stored and considered in all subsequent iterations. For each track followed, A_W^2 is summed from the scale at which it is detected until the finest scale.

When the finest time scale is reached, any edges for which the cumulative A_W^2 does not meet a secondary cutoff are rejected. This cutoff is set by finding the typical maximum value of A_W^2 for a feature of interest by hand for a few traces, and requiring a sum of at least four times this amplitude. This corresponds to a significant presence of the edge over at least one octave. This will accept, for example, short tracks that are very strong, such as sharp spikes in the signal, but also longer tracks that are a bit weaker, such as long pulses with more gently sloping edges. Halving or doubling this parameter causes approximately a 10% change in the correct detection ratio.

All cutoffs up to this point were set to risk acceptance of edges of spurious features rather than to risk rejection of edges of weaker, true features. The last step in the algorithm calculates the levels between edges found, and uses this information to perform a final rejection based on the physics of interest. This step can have a large impact on which features are detected. While the algorithm used for this last step works well for the data in this pa- per, a completely different approach may be necessary for data with vastly different noise or signal characteristics. For these particular experiments, edges that do not border significant changes in I_{QPC} are rejected. This is accomplished by rejecting level changes that are less than five times the standard deviation of the signal between all edges. This standard deviation is a good measure of high frequency noise present in the signal. The sensitivity to this parameter is rather large, resulting in up to a 30% change in correct detection ratio when the parameter is increased or decreased by one standard deviation, but once set, it is robust to the variation in high frequency noise encountered in the extensive quantity of data analyzed for the current experiments.

Figure E.1(a) and (b) show results from using this wavelet edge detection algorithm for

the readout phase of the two single-shot traces presented in Fig. 6.2(a, b). The reconstructed signals using the real wavelet transform are shown in black superimposed on the data. An up-edge and a down-edge are detected in (a), corresponding to the unloading of a spin-↑ electron followed by the reloading of a spin-↓ electron, and no edges are detected in (b).

Electron tunnel event detection using thresholding

In this algorithm, the QPC signal is compared to a threshold. A tunneling event is detected if I_{QPC} crosses the threshold. If the signal remains below the threshold, zero tunneling events are assumed. While simple in concept, the thresholding analysis is complicated by the need to account for signal drift and high frequency noise.

First, the data are corrected for slow drifting of the QPC signal by subtracting the value of I_{QPC} corresponding to the electron located on the quantum dot (loaded) from every trace in a given experimental run. The value to subtract from each trace is determined in one of two ways, depending on the variance of the signal. If the variance is small (as for traces with zero tunnel events), then the loaded QPC signal is determined as the mean of the data. If the variance is large (as for traces containing tunneling events), then a histogram of the data is produced. This histogram contains a noise-broadened double peak, with the peaks centered on the values of I_{QPC} corresponding to the electron on or off the quantum dot. Least-squares fitting of a sum of two Gaussians identifies the centers of the peaks, and the lower of the two center values is taken as the loaded I_{QPC} value.

After the drift correction, the threshold value can be determined. A combined histogram of the QPC signal for many single-shot traces is produced. This histogram contains a double peak where, again, the two peaks are centered on the loaded and unloaded values of I_{QPC}. The histogram is fit to a sum of two Gaussian peaks, and the threshold value is chosen as the location of the minimum between the fitted peaks.

Once the threshold is established, every single-shot trace can be identified as containing tunnel events (the signal crosses the threshold), or containing no tunnel events (the signal remains below the threshold). To reduce the probability that short, noise-induced spikes in the signal are misidentified as real tunnel events, only above-threshold signals that last

longer than twice the time constant of measurement amplifier are counted.

Comparison of wavelet and thresholding analysis

All relevant data were analyzed employing both wavelet and thresholding methods. The results show good quantitative agreement (see Figure E.1(d)). The advantage of the wavelet algorithm is that it allows each trace to be interpreted independently of all other traces. It is therefore uniquely suited for live, real-time analysis.

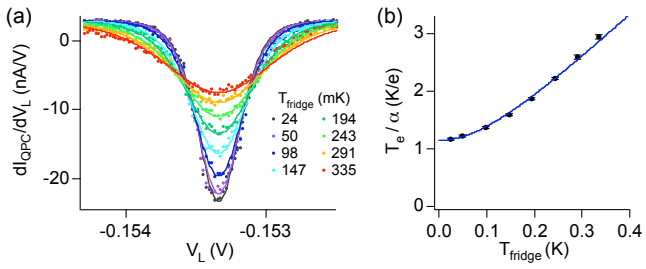

Figure E.2: Measurement of α and electron temperature. (a) A charge transition peak measured with fridge temperatures ranging from 24 mK to 335 mK. (b) The width of the charge transitions for each of the temperature traces shown in (a) determined from a global fit. Error bars for each data point are determined from the uncertainties in the fit.

E.2 Measurement of voltage lever arms, electron temperature and Zeeman energy

As described in Chapter 6, the dot was fabricated from a Si/SiGe heterostructure. The carrier density n and mobility μ were obtained from Shubnikov de Haas measurements and were $n = 4 \times 10^{-11}$ cm^{-2} and $\mu = 50,000$ cm^2/Vs. The dot was tuned to the few-electron regime, and we estimate that we measured transitions between two-and three-electron occupation of the dot. Two of the electrons formed a "closed shell" [141] and were essentially inert, and our measurements were sensitive to the state of the third electron moving into and out of the dot. Pulsed gate voltages were supplied using a Tektronix AFG3022B arbitrary waveform generator.

The spectroscopy in Fig. 6.1(c,d) show the electron response to an 800 kHz square wave

pulse applied to gate L (see [93] for details of the spectroscopy technique). The rate for an electron to tunnel onto the quantum dot is tuned to be slow compared to this pulse frequency. A lock-in signal with a carrier frequency of 97 Hz applied to gate L is used to measure $\mathrm{d}I_{\mathrm{QPC}}/dV_{\mathrm{L}}$ in response to the square wave pulse. The dark lines indicate when additional energy levels become accessible resulting in a sudden increase in the electron tunneling rate. In both (c) and (d), the dark contrast of the excited orbital state indicates that it is more strongly coupled to the reservoir than the ground orbital state, because it causes a larger increase in the electron tunnel rate and thus the electron response. Only the lower energy of the strongly coupled orbital excited states, $|\downarrow e\rangle$, is clearly visible in this spectroscopy, because once this state is accessible the tunnel rate is comparable to the pulse frequency and additional energy levels have no effect on the electron response.

In order to translate the spectroscopy data into energy levels on the dot, it is necessary to determine the lever arm, α, for gate L. The width of a charge transition peak in gate voltage is determined by both α and the electron temperature [142]. In order to determine these variables independently, we fit the width of a charge transition as a function of temperature by increasing the temperature of the dilution refrigerator. The results for fridge temperatures (T_{fridge}) ranging from 24 mK (base temperature) to 335 mK are plotted in Fig. E.2(a). The peak indicating the charge transition clearly decreases in amplitude and increases in width as the temperature is increased.

We extract the width of each peak in Fig. E.2(a) in terms of T_e/α by performing a global fit to the data. Each peak is fit with the equation,

$$dI_{\mathrm{QPC}}/dV_{\mathrm{L}}(V_L) = \frac{B}{4k_BT_e}\cosh^{-2}\left(\frac{\alpha(V_0 - V_L)}{2k_BT_e}\right) + D \tag{E.1}$$

where B, D and V_0 are fit parameters that are the same for all the peaks, and T_e/α is a fit parameter that is optimized for each peak independently. The fit results for T_e/α for each of the peaks in Fig. E.2(a) are shown in (b). As expected, at high temperatures T_e/α is linear in T_{fridge}, while at low temperatures T_e/α saturates. We fit this cross-over using the functional form $T_e = \sqrt{T_0^2 + T_{\mathrm{fridge}}^2}$. This fit is shown as the solid blue fridge line in

Fig. E.2(b), and the results for the two fit parameters, α and T_0 give $\alpha = 0.125 \pm 0.006$ eV/V for gate L and $\alpha = 143 \pm 10$ mK at base temperature.

With a measure of the electron temperature, it is possible to determine the lever arm for additional gates by performing a single fit. We used gate PL to sweep through the same charge transition at base temperature, and the resulting fit gives 0.00144 ± 0.00013 eV/V for α multiplied by the attenuation (note: the voltage on gate PL is attenuated by a factor of 50).

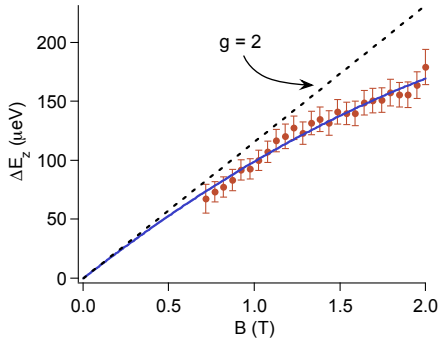

Figure E.3: Zeeman splitting versus B-field. Zeeman splitting as a function of magnetic field determined from the data presented in Fig. 6.1(d). Error bars are due to a combination of uncertainty in the peak separation, ΔV_L, and uncertainty in the lever arm, α, for gate L. The dashed black line indicates $g = 2$ and the solid blue line is the result of a fit using a second-order polynomial.

Using the above results for α for gate L, it is possible to extract the Zeeman energy as a function of magnetic field, B, for the ground orbital state from the excited state spectroscopy data presented in Fig. 6.1(d). We take vertical line cuts to determine the separation, ΔV_L, between the peaks corresponding to the states $|\downarrow g\rangle$ and $|\uparrow g\rangle$ for $B \approx 0.7$ to 2 T. The results, after correcting for the gate voltage lever arm, are plotted in Fig. E.3.

Similar to the results for a GaAs quantum dot presented in [143], at high magnetic fields we observe a clear deviation from the bulk silicon g-factor of 2 (black dashed line). Following the method in [143], we fit the Zeeman splitting data with a second-order polynomial restricted to pass through the origin. The result gives

$$g = (1.96 \pm 0.15) - (0.25 \pm 0.05)B(T). \tag{E.2}$$

The B-independent contribution of this result is in good agreement with the value for an electron spin in bulk silicon.

E.3 Global fit of loading rates and spin-↑ fraction

In this section, we give details of the modeling of the loading rates and the spin-↑ fraction as a function of the loading gate voltage.

Modeling of the loading rates

We perform a global fit to the data for loading rate and the spin-↑ fraction as functions of the loading level, shown in Fig. 6.3(a) and (b). Fig. 6.3(a) shows two pairs of peaks that correspond to the loading of the Zeeman-split ground $|\uparrow g\rangle, |\downarrow g\rangle$ and excited $|\uparrow e\rangle, |\downarrow e\rangle$ orbital states, as well as a shallow minimum on the right that we believe is due to a contribution from the loading of a higher orbital $|\uparrow h\rangle, |\downarrow h\rangle$. Fig. 6.3(b) shows two peaks as a function of loading level that correspond to the measurement of an increased fraction of spin-↑ electrons. Tables E.1 and E.2 provide the numerical results and parameters for the global fit.

In fitting to the loading rate data of Fig. 6.3(a), we model the loading rate taking into account energy-dependent tunneling across the barrier [43] as well as the lifetime broadening of energy states of the dot, modeled using a Lorentzian function. The overall loading rate Γ_{load} as a function of loading level V is given by $\Gamma_{\text{load}}(V) = \sum_i \Gamma_i(V)$, where the sum is over all possible transport channels $i \in \{\downarrow, \uparrow; g, e, h\}$.

For each of these channels, the loading rate is given by the convolution of the Fermi-Dirac distribution, the energy dependent tunneling function, and the Lorentzian function [103]. It is given by

$$\Gamma_i(V) = \int_{-\infty}^{\infty} \left(\frac{\Gamma_{0i}\, e^{-\alpha y/E_i}}{1 + e^{-\alpha y/k_B T}} \right) \frac{\gamma_i/2\pi}{(\gamma_i/2)^2 + (\delta V_i - y)^2}\, \mathrm{d}y, \tag{E.3}$$

where E_i is the linearized energy dependent tunneling coefficient that relates to the transparency of the barrier [43]; γ_i is the full width at half maximum of the Lorentzian; Γ_{0i} is the amplitude; V is the loading voltage; and $\delta V_i = V - V_i$, where V_i is the position of the state.

In the fitting, the Zeeman splitting for each pair of states was identical, and initial guesses were made for the overall scale, position and Lorentzian width for the higher orbital states ($|\uparrow h\rangle, |\downarrow h\rangle$), with the leveling off of Γ_{load} at about 600 mV as a guide. These contributions are plotted as dotted lines in Fig. 6.3(a). After each fitting run, the parameter estimates for $|\uparrow h\rangle$ and $|\downarrow h\rangle$ were revised such that the ratio of overall scaling of the rates and the fit repeated so that self-consistency is achieved.

Following the observations in Ref. [32], the amplitudes of the loading rates for different spin states were allowed to differ; we find, for each orbital, that $\Gamma_{\uparrow} < \Gamma_{\downarrow}$.

We note that, while the energy dependent coefficients for the ground orbital states gave a good fit when they were constrained to be equal, this was not the case for the excited orbital states. It was necessary to have $E_{\downarrow e} > E_{\uparrow e}$, as can be seen from the fact that the downward slope on the right of the highest peaks, which is strongly dependent on $E_{\uparrow e}$, is much steeper than those of the ground orbital states.

The ground orbital states were modeled as delta functions, while the excited orbital states were modeled with a finite energy width as fit parameters, as consistent with the hypothesis of short-lived excited states. However, due to the fact that the temperature broadening of the Fermi function limits the resolution with which we can extract any energy information, only an upper bound on the energy width due to lifetime broadening could be obtained, giving a lifetime of at least 4×10^2 ps.

Calculation of spin-↑ fraction

In the limit of infinite loading and unloading rates, and no spin-↑ decay, the fraction, $n_{\uparrow}$, of spin-↑ electrons measured as a function of loading level V is simply

$$n_{\uparrow}(V) = \frac{\Gamma_{\text{load}\uparrow}(V)}{\Gamma_{\text{load,total}}(V)}, \tag{E.4}$$

where the loading rates $\Gamma_i(V)$ are functions of the voltage V at which the dot is loaded, $\Gamma_{\text{load}\uparrow}$ is the combined rate for loading all spin-↑ channels, and $\Gamma_{\text{load,total}}$ is the total loading rate for all spin channels. This quantity is plotted as the dashed red line in Fig. 6.3(b).

So that the modeled spin-↑ fraction correctly takes into account finite rates of loading, unloading and spin-↑ decay, we set up rate equations for the load and readout phases and

solve for the fraction of spin-↑ at the end of each phase.

Given a pair of spin-↑ and spin-↓ states, the rate equations can be written as

$$\frac{dn_\uparrow(t)}{dt} = -T_1^{-1}n_\uparrow + \Gamma_{\text{load}\uparrow}(1-n_\uparrow-n_\downarrow) - \Gamma_{\text{unload}\uparrow}n_\uparrow, \tag{E.5}$$

$$\frac{dn_\downarrow(t)}{dt} = T_1^{-1}n_\uparrow + \Gamma_{\text{load}\uparrow}(1-n_\uparrow-n_\downarrow) - \Gamma_{\text{unload}\downarrow}n_\downarrow. \tag{E.6}$$

where $n_\uparrow(t)$ and $n_\downarrow(t)$ are the fractions of spin-↑ and spin-↓ respectively. They are explicit functions of time, and implicit functions of loading voltage V via the loading rates $\Gamma_i(V)$.

With the dot empty initially, we impose initial conditions $n_\uparrow(0) = n_\downarrow(0) = 0$ and solve to obtain the solution, which is a complicated function of the rates and time. However, during the load phase, both the spin-↑ and spin-↓ states are below the Fermi level of the lead, so the unloading rates are much smaller than the loading rates and can be neglected: i.e. $\Gamma_{\text{unload}\uparrow} = \Gamma_{\text{unload}\downarrow} = 0$. This assumption leads to a simplified solution that offers more physical insight, given by

$$n_\uparrow(t) = \frac{\Gamma_{\text{load}\uparrow}}{\Gamma_{\text{load}\uparrow}+\Gamma_{\text{load}\downarrow}-T_1^{-1}} e^{-tT_1^{-1}} \left(1 - e^{-(\Gamma_{\text{load}\uparrow}+\Gamma_{\text{load}\downarrow}-T_1^{-1})t}\right), \tag{E.7}$$

$$n_\downarrow(t) = \frac{(\Gamma_{\text{load}\downarrow}-T_1^{-1})(1-e^{-t(\Gamma_{\text{load}\downarrow}+\Gamma_{\text{load}\uparrow})} + \Gamma_{\text{load}\uparrow}\left(1-e^{-tT_1^{-1}}\right)}{\Gamma_{\text{load}\uparrow}+\Gamma_{\text{load}\downarrow}-T_1^{-1}}. \tag{E.8}$$

It is clear that, in the limit of loading rates fast compared to the decay rate, the approximation $n_\uparrow \approx e^{-tT_1^{-1}}(\Gamma_{\text{load}\uparrow}/\Gamma_{\text{load,total}})$ holds. If the rates are comparable, then the last term in brackets in Eq. S7 contributes significantly.

We can generalize to include the loading of other spin states whose population comes from the tunneling in of electrons from the lead and not from the decay of the spin-↑ state in question. This is necessary as the spin-↑ states in question are each sandwiched between two spin-↓ states and a higher orbital state. The solution to the spin-↑ fraction then includes the total tunneling rate into all states, $\Gamma_{\text{total}} = \Gamma_{\text{load all}\downarrow} + \Gamma_{\text{load all}\uparrow}$, given by

$$n_\uparrow(t) = \frac{\Gamma_{\text{load}\uparrow}}{\Gamma_{\text{total}}-T_1^{-1}} e^{-tT_1^{-1}} \left(1 - e^{-(\Gamma_{\text{total}}-T_1^{-1})}\right). \tag{E.9}$$

Next, we consider the correction to the spin-↑ fraction during the readout phase. During this phase, because the spin-↑ state is above the Fermi level and the spin-↓ state is below

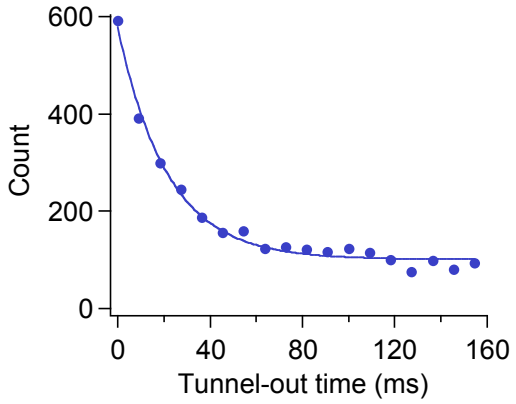

Figure E.4: Measurement of the spin-↑ unloading rate. Histogram of the times at which an up-edge is detected in the readout phase of the single-shot traces for the data presented in Fig. 6.3(b). The exponential fit gives the rate at which a spin-↑ electron tunnels off the dot, $\Gamma^{-1}_{\mathrm{unload}\uparrow} = 21.6 \pm 1.3$ ms.

it, we neglect the spin-↑ loading rate as well as the spin-↓ unloading rate. Because the quantity measured in the experiment is the number of spin-↑ electrons that tunnel out to the lead $n_{c\uparrow}$, we solve the following rate equations for $n_{\mathrm{c}\uparrow}(t)$,

$$\frac{dn_{\uparrow}(t)}{dt} = -T_1^{-1} n_{\uparrow} - \Gamma_{\mathrm{unload}\uparrow} n_{\uparrow}, \tag{E.10}$$

$$\frac{dn_{\downarrow}(t)}{dt} = T_1^{-1} n_{\uparrow} + \Gamma_{\mathrm{load}\uparrow} \left(1 - n_{\uparrow} - n_{\downarrow}\right), \tag{E.11}$$

$$\frac{dn_{\mathrm{c}\uparrow}(t)}{dt} = \Gamma_{\mathrm{unload}\uparrow} n_{\uparrow}. \tag{E.12}$$

The rate $\Gamma_{\mathrm{unload}\uparrow}$ at which a spin-↑ electron tunnels off the dot during the readout phase is determined by fitting to a histogram of the times at which up-edge is detected in the single-shot traces. The results for the data presented in Fig. 6.3(b) are shown in Fig. E.4, where 0 corresponds to the start of the readout phase. The exponential fit gives $\Gamma^{-1}_{\mathrm{unload}\uparrow} = 21.6 \pm 1.3$ ms.

With the initial condition of a loaded spin-↑ state, $n_{\uparrow}(0) = 1$, we obtain the measured spin-↑ fraction as

$$n_{\mathrm{c}\uparrow}(t) = \frac{\Gamma_{\mathrm{unload}\uparrow}}{T_1^{-1} + \Gamma_{\mathrm{unload}\uparrow}} \left(1 - e^{-t(T_1^{-1} + \Gamma_{\mathrm{unload}\uparrow})}\right). \tag{E.13}$$

Table E.1: Results of fit

Fit Parameter	Value [Unc.]
Energy dependent coefficient $\|\downarrow g\rangle, \|\uparrow g\rangle$ (meV)	0.148 [27]
Energy dependent coefficient $\|\downarrow e\rangle$ (meV)	0.195 [30]
Energy dependent coefficient $\|\uparrow e\rangle$ (meV)	0.064 [23]
Position $\|\uparrow g\rangle$ (meV)	0.186 [18]
Position $\|\downarrow e\rangle$ (meV)	0.456 [42]
Position $\|\uparrow e\rangle$ (meV)	0.585 [58]
Amplitude $\|\downarrow g\rangle$ (Hz)	116 [8]
Amplitude $\|\uparrow g\rangle$ (Hz)	110 [7]
Amplitude $\|\downarrow e\rangle$ (Hz)	1,916 [62]
Amplitude $\|\uparrow e\rangle$ (Hz)	610 [33]
Lorentzian width for $\|e\rangle$ (meV)	5×10^{-6}
Quantities derived from fit parameters	
Position $\|\downarrow g\rangle$ (meV)	0.057 [9]
Zeeman splitting (meV)	0.129 [17]
g-factor	1.20 [16]
Lifetime of $\|e\rangle$ (ps)	440

With an independent determination of the spin-↑ detection fidelity and the dark count rate (92% and 3% respectively, as described in the next section), the measured spin-up fraction $\kappa_\uparrow$, fully corrected for finite tunnel rates during the load and readout phases of the 3-level pulse sequence and for spin-↑ decay, is given by

$$\kappa_\uparrow = 0.03 + 0.92 \times n_\uparrow(t_{\text{load}}) \times n_{\text{c}\uparrow}(t_{\text{readout}}), \tag{E.14}$$

where t_{load} and t_{readout} are the durations for the load and readout phases (100 ms and 200 ms respectively for the data in Fig. 6.3(b)). This result is plotted as the bold, black line in Fig. 6.3(b).

Single-shot spin readout visibility

We determine the visibility of our spin readout using the method in [92]. Since our g-factor is positive, spin-↓ is the lower energy spin state in our case, and we therefore analogously define α as the probability that a spin-↓ is detected as "up" and β as the probability that a spin-↑ is detected as "down", and we use corresponding definitions for the two contributions to β: β_1 and β_2. The visibility of the spin readout is then given by $1 - \alpha - \beta$.

Due to the finite electron temperature, it is possible, although rare, for a spin-↓ electron to tunnel off the dot during the readout phase even though its energy is below E_F , causing

Table E.2: Constants and independent parameters

temperature T (mK)	143 [10]
magnetic field (T)	1.85
alpha $\times$ attenuation (eV / V)	0.00144 [13]
$T_{1,g}$ (ms)	136 [22]
$T_{1,e}$ (ms)	2.8[3] $\times 10^3$
Parameters for $\|\downarrow h\rangle$	
Position (meV)	1.146
Lorentzian width (meV)	0.433
Amplitude (Hz)	3100
Parameters for $\|\uparrow h\rangle$	
Position (meV)	1.275
Lorentzian width (meV)	0.433
Amplitude (Hz)	310

a spin-$\downarrow$ electron to be misidentified as spin-$\uparrow$. This 'dark count' is determined by the saturation value of the exponential fit in the inset to Fig. 6.3(b) in Chapter 6. The result gives $\alpha = 0.031$.

During the readout phase, if a spin-$\uparrow$ electron tunnels off the dot and is replaced by a spin-$\downarrow$ electron at a rate comparable to the bandwidth of the measurement electronics, then the resulting step in I_{QPC} will be too small to detect, causing a spin-$\uparrow$ to be misidentified as spin-$\downarrow$. As in [92], we determine the spin-$\uparrow$ detection fidelity by applying the 3-level pulse sequence in reverse, and we find it to be 91.8%. This gives $\beta_2 = 1 - 91.8\% = 0.082$.

Due to the finite time for an spin-$\uparrow$ electron to tunnel off the quantum dot during the readout phase, it is possible that an electron that is spin-$\uparrow$ at the start of the readout might decay to a spin-$\downarrow$ before it tunnels off the dot. This contribution to the spin readout fidelity is given by $\beta_1 = 1/(1 + T_1\Gamma_{\mathrm{unload}\uparrow})$. From the exponential fit in Fig. E.4, we find $\Gamma^{-1}_{\mathrm{unload}\uparrow} = 21.6$ ms. This result combined with the measured value of $T_1 = 2.75$ s gives $\beta_1 = 0.0078$.

Finally, we determine a spin-$\downarrow$ detection fidelity of $1 - \alpha \approx 0.97$ and a spin-$\uparrow$ detection fidelity of $1 - \beta \approx 0.91$, and this amounts to a total single-shot readout visibility of 88%. This visibility is notably improved from the 65% reported in [92], and the majority of the improvement is due to the long spin lifetime compared to the relatively fast electron

tunneling time.

Appendix F

Supplemental material for Chapter 7

F.1 Spin exchange with leads in the spin blockade regime

In Sec. 7.5, we described a method for determining the base slope by fitting a line to the points labelled B and J in Fig. 7.3. Fig. 7.7(b) is an expanded view of one of the spin blockade data sets, showing that points B and J are indeed clearly visible in the raw data. At these points, and in fact along the entire segments BA and JI in Fig. 7.3, spin exchange with the leads lifts spin blockade. In this appendix we briefly discuss this spin exchange process. Figs. 7.7(f)-(h) describe this spin exchange process between the right dot and the right lead at point B, while Figs. 7.7(c)-(e)describe the spin exchange process between the left dot and the left lead at point J.

In the three electron regime at point J, the transport cycle goes from (1,1) to (2,0) to (2,1) and back to (1,1). At point J, transport is spin blockaded, because $\mu_{T(1,1)}$ lies below $\mu_{T(2,0)}$. The set of chemical potentials labeled μ_{d,S^*}, shown by the blue dashed and solid lines in Figs. 7.7(c)-(e), refer to the energy involved in discharging the left dot from the ground, singlet-like (2,1) state to the $S_{1,1}$ and $T_{1,1}$ states, respectively. At point J, when the system is blockaded in the $T_{1,1}$ state, an electron can tunnel from the left lead to the left

dot. This corresponds to a tunneling event that is in the direction opposite to the overall electron motion under the effect of the transport bias V_{SD}. Such a tunneling event can enable the formation of a singlet-like (2,1) state from the $T_{1,1}$ state, because electrons with either spin orientation are available in the left lead. This transition occurs at an energy given by the blue μ_{d,S^*} level (solid line). The left dot is allowed to discharge from any one of the two μ_{d,S^*} levels. If it discharges from the higher of the two chemical potentials, the system relaxes to the singlet (1,1) state. The two μ_{d,S^*} levels are separated by the singlet-triplet splitting of the (1,1) state and are therefore very closely spaced.

F.2 Chemical potentials of electron and hole triangles

Figure F.1 shows the chemical potentials corresponding to the full set of labelled points in Fig. 7.3.

F.3 Theoretical model for quantitative energy-dependent tunneling effects

In this appendix we present our theoretical treatment of energy-dependent tunneling effects that uses the Lindblad formalism to account for both resonant and incoherent processes.

In our calculations, we treat the S and T transport channels independently. Our reference state has one fixed electron in dot 1, and we consider transport that involves just three different states: $|0\rangle$, $|1\rangle$, and $|2\rangle$. Here, $|0\rangle$ refers to the state with no additional electrons, $|1\rangle$ refers to the state with one additional electron on dot 1 [the (2,0) charge configuration], and $|2\rangle$ refers to the state with one additional electron on dot 2 [the (1,1) charge configuration]. Coherent evolution is controlled by the Hamiltonian

$$H = \frac{1}{2}\epsilon(|1\rangle\langle 1| - |2\rangle\langle 2|) + \hbar g(|1\rangle\langle 2| + |2\rangle\langle 1|), \tag{F.1}$$

where g is the tunnel coupling between the two dots.

We now couple this system to the environment, using the Lindblad formalism.[73, 2] Tunneling from the left lead to dot 1 is described by the Lindblad operator

$$L_{L1} = \sqrt{f_L(E_1)\Gamma_L(E_1)}\,|1\rangle\langle 0|, \tag{F.2}$$

where $f_L(E_1) = f(E_1 - E_{LF})$ is the Fermi function of the left lead, and Γ_L is the tunnel coupling between the lead L and dot 1. Both f_L and Γ_L depend on energy, but, for brevity, we will suppress the energy dependence in the notation. The other relevant Lindblad operators are given by

$$\begin{aligned}
L_{1L} &= \sqrt{(1-f_L)\Gamma_L}\,|0\rangle\langle 1|, &\text{(F.3)}\\
L_{2R} &= \sqrt{(1-f_R)\Gamma_R}\,|0\rangle\langle 2|, &\text{(F.4)}\\
L_{R2} &= \sqrt{f_R\Gamma_R}\,|2\rangle\langle 0|, &\text{(F.5)}\\
L_{12} &= \sqrt{\theta\Gamma_i}\,|2\rangle\langle 1|, &\text{(F.6)}\\
L_{21} &= \sqrt{\bar{\theta}\Gamma_i}\,|1\rangle\langle 2|. &\text{(F.7)}
\end{aligned}$$

Note that reverse processes (from right to left), such as L_{1L}, are also included here. The latter play a role along the edges of the bias triangle. For example, an electron may enter dot 1 from lead L and then exit back to lead L. Such processes do not directly affect the steady-state current, but they do affect the current indirectly, because, while the dot is occupied, it cannot be occupied by a second, right-moving electron.

In Eqs. (F.6) and (F.7), the incoherent tunneling between the two dots involves phonon emission or absorption processes. We have accounted for these phonon effects through the θ-functions. At high temperatures, the θ-functions may possess considerable structure. However for low temperature applications, we assume that $\theta = \Theta(\epsilon)$ and $\bar{\theta} = \Theta(-\epsilon)$, where the step function $\Theta(\epsilon)$ takes the values 0, when $\epsilon < 0$, 1/2 when $\epsilon = 0$, and 1 when $\epsilon > 0$. More general forms for θ can be substituted, as appropriate. We also note that the inelastic, interdot tunnel coupling Γ_i is a weak, even function of ϵ. Below, we show that our data are consistent with $\Gamma_i =$ (constant) throughout most of the bias triangle.

The evolution of the density operator is described by the rate equation

$$\dot{\hat{\rho}} = -\frac{i}{\hbar}[H, \hat{\rho}] + \sum_j \left[L_j \hat{\rho} L_j^\dagger - \frac{1}{2} \left\{ \hat{\rho}, L_j^\dagger L_j \right\} \right], \tag{F.8}$$

where $\hat{\rho}$ is the density matrix. In general, $\hat{\rho}$ must satisfy the normalization condition $1 = \rho_0 + \sum_k (\rho_{1k} + \rho_{2k})$, where the diagonal terms ρ_0, ρ_{1k}, and ρ_{2k} describe the probability of being in a given occupation state, and the sum over k includes the singlet and three triplet channels. In the absence of any decay processes between the triplet and singlet states, this normalization condition is the only coupling between the singlet and triplet sectors, since it ensures that a triplet cannot be formed when a singlet state is occupied, and vice versa. However, in the LET regime, we have shown that the $(2,0)$ singlet state unloads much faster than it loads, and that the unloading of the (1,1) singlet is similarly fast (or faster).[115] These conditions are equivalent to the statement that $\rho_{1S} + \rho_{2S} \ll 1$ wherever $\rho_{1T} + \rho_{2T}$ is appreciable, and vice versa. Since LET behavior is observed in our samples, we make a singlet-triplet decoupling approximation, such that the normalization

$$1 \simeq \rho_0 + \rho_1 + \rho_2, \tag{F.9}$$

applies to both the singlet and triplet channels. The resulting rate equations are correspondingly simplified.

Since there is no coherent coupling between state $|0\rangle$ and states $|1\rangle$ and $|2\rangle$, the density operator for a single channel can be defined as

$$\hat{\rho} = \rho_0 |0\rangle\langle 0| + \rho_1 |1\rangle\langle 1| + \rho_2 |2\rangle\langle 2| + \rho_{12} |1\rangle\langle 2| + \rho_{21} |2\rangle\langle 1|. \tag{F.10}$$

We may then use Eq. (F.9) to eliminate ρ_0 from the rate equations defined in Eq. (F.8). Steady-state solutions are obtained by requiring that $\dot{\hat{\rho}} = 0$.

The current operator is defined as

$$\hat{I}/e = ig(|1\rangle\langle 2| - |2\rangle\langle 1|) + \Gamma_i(\theta |1\rangle\langle 1| - \bar{\theta} |2\rangle\langle 2|), \tag{F.11}$$

and it involves both coherent and incoherent components. The steady-state current is given by $I = \mathrm{Tr}(\rho \hat{I})$. Using the steady-state rate equations, the result can be expressed in terms

of density coefficients:

$$I/e = (1 - f_R)\Gamma_R\rho_2 - f_R\Gamma_R\rho_0. \tag{F.12}$$

In this form, the current is simply expressed as the net tunneling rate between dot 2 and lead R.

By solving for the density coefficients, Eq. (F.12) can be expressed entirely in terms of tunneling rates and Fermi functions, yielding the following result for single-channel transport in a two-electron double dot:

$$\frac{I}{e} = \Gamma_L\Gamma_R \frac{\begin{array}{c}\{4g^2(f_L - f_R)[\Gamma_L(1-f_L) + \Gamma_R(1-f_R) + \Gamma_i] \\ +\Gamma_i\left(4(\epsilon/\hbar)^2 + [\Gamma_L(1-f_L) + \Gamma_R(1-f_R) + \Gamma_i]^2\right)[f_L(1-f_R)\theta - f_R(1-f_L)\bar{\theta}]\}\end{array}}{\begin{array}{c}\left\{\left[4(\epsilon/\hbar)^2 + [\Gamma_L(1-f_L) + \Gamma_R(1-f_R) + \Gamma_i]^2\right][\Gamma_L\Gamma_R(1 - f_Lf_R) + \Gamma_i\Gamma_R(\theta + f_R\bar{\theta}) + \Gamma_i\Gamma_L(\bar{\theta} + f_L\theta)]\right. \\ \left. +4g^2[\Gamma_L(1-f_L) + \Gamma_R(1-f_R) + \Gamma_i][\Gamma_L(1+f_L) + \Gamma_R(1+f_R)]\right\}\end{array}}. \tag{F.13}$$

When the singlet and triplet channels are fully decoupled, as we assume here, the total current is expressed as a sum of terms like Eq. (F.13), one for each channel.

As an initial check on our result, we consider a known limit. For the case of pure coherent tunneling between dots 1 and 2, we take the limit $\Gamma_i \to 0$. In the interior of the bias triangle where $f_L \simeq 1$ and $f_R \simeq 0$, Eq. (F.13) immediately reproduces the resonant tunneling results obtained in Refs. [117] and [118].

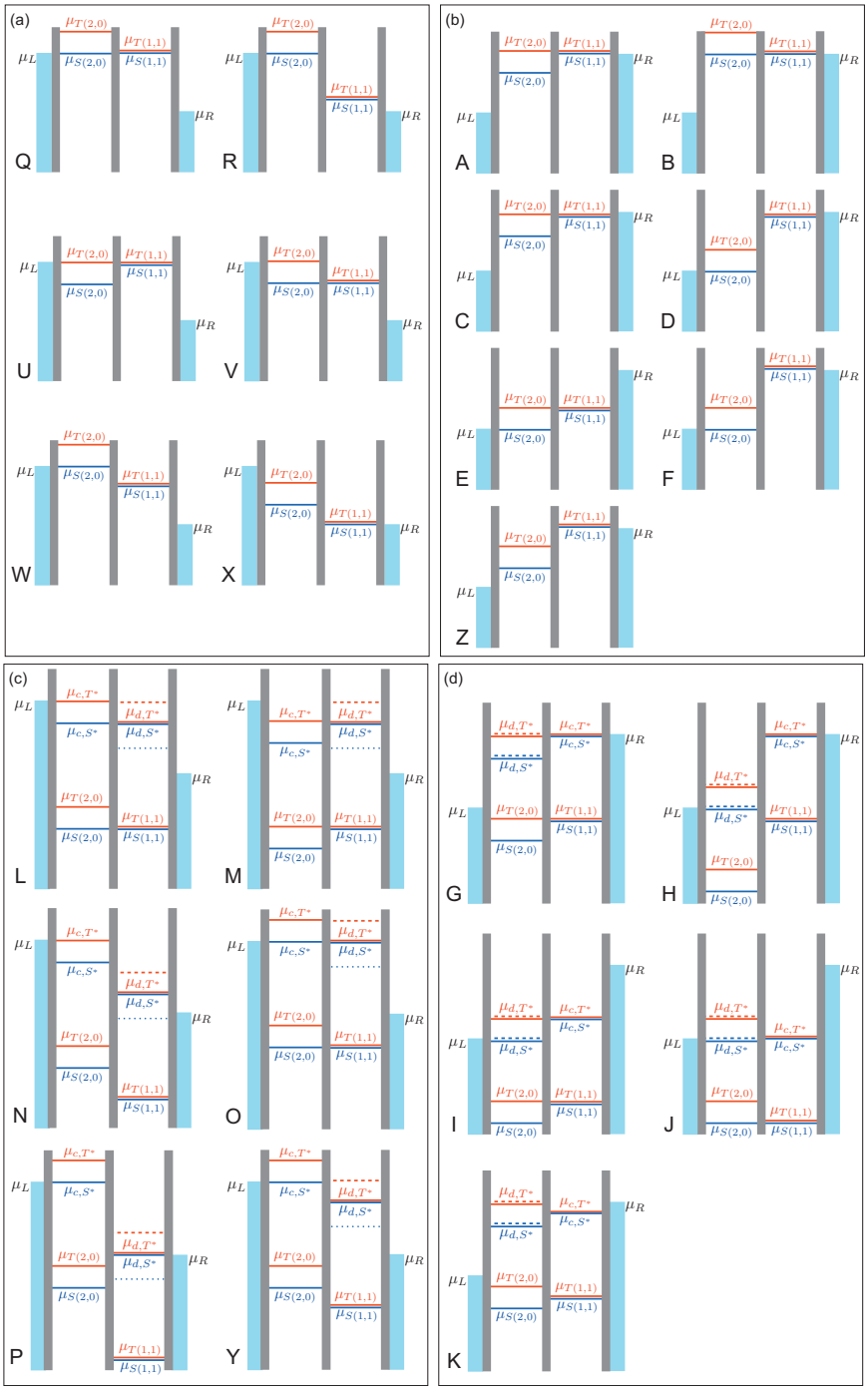

Figure F.1: Chemical potentials corresponding the the labelled points in Fig. 7.3. (a) Chemical potentials corresponding to the two-electron regime for reverse bias, which shows LET. (b) The two-electron regime for forward bias, which shows spin-blockade. (c) The three-electron or 'hole' regime for reverse bias (LET). (d) The three-electron or 'hole' regime for forward bias (spin blockade).

Appendix G

Supplemental material for Chapter 8

This Appendix presents our detailed calculations of the Configuration Interaction approximation and electrochemical potentials relevant for reverse bias transport in the three electron regime. We estimate the spin-flip cotunneling occurrence rate, quantify the effect spin-flip cotunneling has on transport current in the triplet-like triangle, and show that it is consistent with the data. We propose an experiment to verify the singlet-triplet mixing mechanism and also present a detailed analysis showing that at forward bias, transport data has a feature associated with the process of spin-flip cotunneling, as discussed in the main paper.

G.1 Configuration Interaction Hamiltonian

The Configuration Interaction (CI) Hamiltonian used in our calculations is given by [127]

$$H = \sum_{i,j} \langle i|h|j\rangle a_i^\dagger a_j + \frac{1}{2} \sum_{i,j,k,l} \langle ij|V_C|kl\rangle a_i^\dagger a_j^\dagger a_l a_k, \tag{G.1}$$

where the sums run over the spin orbitals chosen to form the basis of the problem. Operators $a_i^\dagger$ and a_i create and annihilate an electron in the i-th spin-orbital respectively. The first term contains the one electron operator, $h \equiv \sum -1/2\nabla_\alpha^2 + V(\vec{x}_\alpha - \vec{x}_{dot})$, the sum of

Table G.1: Basis states used for the (2,1) configuration.

Basis states		Spin
(*in spin-orbital notation*)	(*in S,T notation*)	S_z
$\|123\rangle$	$\|T_+(2,0)\rangle \otimes \|3\rangle$	3/2
$\|12\bar{3}\rangle$	$\|T_+(2,0)\rangle \otimes \|\bar{3}\rangle$	1/2
$(\|\bar{1}23\rangle + \|1\bar{2}3\rangle)/\sqrt{2}$	$\|T_0(2,0)\rangle \otimes \|3\rangle$	1/2
$(\|\bar{1}23\rangle - \|1\bar{2}3\rangle)/\sqrt{2}$	$\|S_1(2,0)\rangle \otimes \|3\rangle$	1/2
$\|1\bar{1}3\rangle$	$\|S_0(2,0)\rangle \otimes \|3\rangle$	1/2
(and their spin reversed counterparts)		

the kinetic and potential energies of each α-th non-interacting electron in a quantum dot centered at $\vec{x}_{dot}$. We note that the parabolic well approximation is a reasonable form of the potential for our geometry. The second term contains the two electron Coulomb operator, $\langle ij|V_C|kl\rangle \equiv \int d\mathbf{x}_\alpha d\mathbf{x}_\beta \chi_i^*(\mathbf{x}_\alpha)\chi_j^*(\mathbf{x}_\beta) r_{\alpha\beta}^{-1} \chi_k(\mathbf{x}_\alpha)\chi_l(\mathbf{x}_\beta)$, where $\chi_i(\mathbf{x}_\alpha)$ denotes the i-th spin-orbital wave-function of the α-th electron, following the notation of Ref. [127].

We define the quantities $s_{ij} \equiv \langle i|j\rangle$, the overlap between the i-th and j-th spin orbitals; $e_i \equiv \langle i|h|i\rangle$, the single particle energy; $C_{ij} \equiv \langle ij|V_C|ij\rangle$ and $K_{ij} \equiv \langle ii|V_C|jj\rangle$, the Coulomb and exchange interactions respectively. $g_{ij} \equiv \langle i|h|j\rangle$ and $\Lambda_{lk}^{ij} \equiv \langle ij|V_C|kl\rangle$ govern coherent tunneling between dots and are first and second order in the overlap integral, respectively.

Singly-excited configurations that form the basis for the (2,1) Hamiltonian matrix, are constructed from dot-centered single particle spatial orbitals $\{1,2\}$ and $\{3,4\}$, centered on the left and right dots respectively. The two sets of spatial orbitals are not orthogonal to each other, due to the overlap across the finite barrier between the dots. Within each set, however, the spatial orbitals are orthonormal. The corresponding spin orbitals are denoted by $\{1,\bar{1},2,\bar{2}\}$ and $\{3,\bar{3},4,\bar{4}\}$ where the overbar (or lack of) denote spin down (up). Table G.1 shows the basis states used to construct the 10×10 Hamiltonian matrix.

The (2,1) Hamiltonian consists of four block diagonals: two 1×1 blocks corresponding to a total spin of $S_z = \pm 3/2$, and two 4×4 blocks corresponding to $S_z = \pm 1/2$. In the $S_z = \pm 1/2$ blocks, off-diagonal matrix elements are second order in the overlap between spin orbitals centered on different dots and represent the amount of mixing of the singlet and triplet states in the left dot. As such, we term the ground state, 'singlet-like', and

denote it as $S^*(2,1)$. It contains mainly singlet $S(2,0)$ with some admixture of triplet $T(2,0)$ in the left dot, coupled to the third electron in the right dot. The first excited state is the pure $S_z = \pm 3/2$ state with all spins either up or down, which does not have any singlet-triplet mixing. The next two higher states, which are closely spaced with each other as well as with the first excited state, contain a small admixture of singlet with mainly triplet states in the left dot, coupled to the right dot. For brevity, we term the three excited states triplet-like $T^*(2,1)$ states, and do not distinguish between them henceforth, as the energy separation between the triplet-like states is of second order in the overlap integral and is small compared to the spacing between the ground and first excited state. The next higher state is well separated from these and does not enter into our analysis.

The $S_z = 1/2$ block of the Configuration Interaction Hamiltonian for the (2,1) state is

$$\hat{H}^{S_z=1/2}_{(2,1)} = \begin{pmatrix} 2e_1 + e_3 + C_{11} + 2C_{13} & (\Lambda^{13}_{23} + s_{13}g_{23} + s_{23}g_{13})/\sqrt{2} & (2\Lambda^{11}_{12} - \Lambda^{13}_{23} + 2\Lambda^{13}_{32} & -\Lambda^{13}_{23} - s_{13}g_{23} - s_{23}g_{13} \\ -K_{13} + 2s_{13}g_{13} & & -s_{13}g_{23} - s_{23}g_{13})/\sqrt{2} & \\ (\Lambda^{13}_{23} + s_{13}g_{23} + s_{23}g_{13})/\sqrt{2} & e_1 + e_2 + e_3 + C_{12} + C_{13} + C_{23} & (K_{23} - K_{13})/2 & -(K_{13} + K_{23} \\ & -K_{12} - (K_{13} + K_{23})/2 & -s_{13}g_{13} + s_{23}g_{23} & +2s_{13}g_{13} + 2s_{23}g_{23})/\sqrt{2} \\ & -s_{13}g_{13} - s_{23}g_{23} & & \\ (2\Lambda^{13}_{32} - \Lambda^{13}_{23} + 2\Lambda^{11}_{12} & (K_{23} - K_{13})/2 & e_1 + e_2 + e_3 + C_{12} + C_{13} + C_{23} & (K_{13} - K_{23} \\ -s_{13}g_{23} - s_{23}g_{13})/\sqrt{2} & -s_{13}g_{13} + s_{23}g_{23} & +K_{12} - (K_{13} + K_{23})/2 & +2s_{13}g_{13} - 2s_{23}g_{13})/\sqrt{2} \\ & & -s_{13}g_{13} - s_{23}g_{23} & \\ -\Lambda^{13}_{23} - s_{13}g_{23} - s_{23}g_{13} & -(K_{13} + K_{23} & (K_{13} - K_{23} & e_1 + e_2 + e_3 + C_{12} \\ & +2s_{13}g_{13} + 2s_{23}g_{23})/\sqrt{2} & +2s_{13}g_{13} - 2s_{23}g_{13})/\sqrt{2} & +C_{13} + C_{23} - K_{12} \end{pmatrix}, \tag{G.2}$$

in the basis $|S_0(2,0)\rangle \otimes |3\rangle, |T_0(2,0)\rangle \otimes |3\rangle, |S_1(2,0)\rangle \otimes |3\rangle, |T_+(2,0)\rangle \otimes |\bar{3}\rangle$.

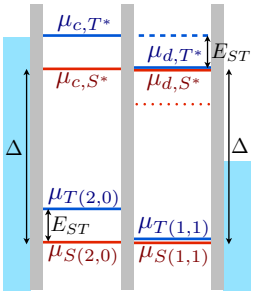

Figure G.1: Electrochemical potentials μ for different states relevant to transport in the three electron regime. Here, the label E_{ST} is the (2,0) singlet-triplet splitting. Δ is the spacing between the chemical potentials of the two and three electron regimes, as defined in Eq. G.11, and is equal to the energy spacing between points A and C in the transport data in Fig. 8.1(b) of Chapter 8. Both quantities are extracted from the transport data as detailed in Chapter 7 and Ref. (see Chapter 7 and Ref. [24]), giving $E_{ST(2,0)} \approx 174$ μeV for (2,0) singlet-triplet splitting and $\Delta \approx$ 500 μeV.

The off-diagonal elements are second order in the overlap integral and therefore small, so the problem can be treated perturbatively. The energies, to first order approximation, are given in Table G.2. The splitting between the singlet-like and triplet-like states is approximately equal to the singlet-triplet splitting of the (2,0) state, $E_{ST(2,0)}$. We apply the CI Hamiltonian (Eq. G.2) to calculate the singlet and triplet energies of the two electron states, which are necessary for the calculation of electrochemical potentials. Similar analyses using molecular and dot-centered orbitals have been done elsewhere [144], so we do not reproduce the calculations here. We refer the reader to Section III. D of Ref. [144] for calculations using dot-centered orbitals. We caution the reader that, in this previous study, the double dot geometry and material are different, so their numerical results will not be applicable for our case. However, the expressions for energy levels in terms of dot-centered single-particle, direct and exchange Coulomb energies in Eq. (18–21) of Ref. [144] are relevant for our two electron double dot case.

Once the expressions for the energies are known, it is straightforward to calculate the relevant expressions for electrochemical potentials. For clarity, we neglect the singlet-triplet splitting in the (1,1) states and the energy spacing between the three triplet-like (2,1) states and obtain two distinct electrochemical potentials. The electrochemical potentials

Table G.2: Energies and characteristics of the (2,1) states.

Energy (ascending order)	State	Spin S_z
$2e_1 + e_3 + C_{11} + 2C_{13}$ $-K_{13} + 2s_{13}g_{13}$	Singlet-like, Mixed	$\pm 1/2$
$e_1 + e_2 + e_3 + C_{12} + C_{13}$ $+C_{23} - (K_{12} + K_{13} + K_{23})$	Triplet-like, Pure	$\pm 3/2$
$e_1 + e_2 + e_3 + C_{12} + C_{13} + C_{23} - K_{12}$ $-(K_{13} + K_{23})/2 - (s_{13}g_{13} + s_{23}g_{23})$	Triplet-like, Mixed	$\pm 1/2$
$e_1 + e_2 + e_3 + C_{12} + C_{13} + C_{23} - K_{12}$	Triplet-like, Mixed	$\pm 1/2$

for charging the left dot from a (1,1) state to the $S^*(2,1)$ and $T^*(2,1)$ states are, respectively,

$$\mu_{c,S^*} = e_1 + C_{11} + C_{13} - E_{ST(1,1)} + E_{\mathrm{Ldot}}, \tag{G.3}$$

$$\mu_{c,T^*} \approx \mu_{c,S^*} + E_{ST(2,0)}. \tag{G.4}$$

E_{Rdot} (E_{Ldot}) is the electrostatic energy of the right (left) quantum dot. The electrochemical potentials for discharging the right dot from the triplet-like $T^*(2,1)$ to the triplet $T(2,0)$ state and from the singlet-like $S^*(2,1)$ to singlet $S(2,0)$ state are

$$\mu_{d,T^*} \approx \mu_{d,S^*} = e_3 + 2C_{13} - K_{13} + E_{\mathrm{Rdot}}. \tag{G.5}$$

There are two more electrochemical potentials involved in the discharge of the right dot from the (2,1) states, due to the mixing of the singlet and triplet (2,0) states. These are associated with the discharge from $T^*(2,1)$ to $S(2,0)$ and $S^*(2,1)$ to $T(2,0)$, and are shown by the blue dashed and red dotted lines on the right dot in Fig. G.1. They are separated from μ_{d,T^*} and μ_{d,S^*} by the (2,0) singlet-triplet splitting $E_{ST(2,0)}$.

The last set of electrochemical potentials needed are those for the two electron regime,

which are given by

$$\mu_{S(2,0)} = e_1 + C_{11} + E_{\mathrm{Ldot}}, \tag{G.6}$$

$$\mu_{T(2,0)} = \mu_{S(2,0)} + E_{ST(2,0)}, \tag{G.7}$$

$$\mu_{T(1,1)} = e_3 + C_{13} - K_{13} + E_{\mathrm{Rdot}}, \tag{G.8}$$

$$\mu_{S(1,1)} = \mu_{T(1,1)} - E_{ST(1,1)}. \tag{G.9}$$

The chemical potentials for the two and three electron regimes satisfy the relation

$$\mu_{c,S^*} - \mu_{S(2,0)} \approx \mu_{d,S^*} - \mu_{S(1,1)}, \tag{G.10}$$

and we therefore define

$$\Delta \equiv \mu_{d,S^*} - \mu_{S(1,1)}. \tag{G.11}$$

Here, we point out that it is the relative positions of the electrochemical potentials that are important in order to build the transport model shown in Fig. G.1. The important energy quantities are therefore, the (2,0) and (1,1) singlet-triplet energy splittings $E_{ST(2,0)} \approx 174$ μeV and $E_{ST(1,1)} \approx 4$ μeV, and the spacing $\Delta \approx 500$ μeV between the two and three electron triangles. These energies are extracted from the transport data as detailed in Chapter 7 (Ref. (see Chapter 7 and Ref. [24])).

G.2 Effect of spin-flip cotunneling on transport current

In this section, we show that current can flow through the triplet channel in the 'hole' transport regime when certain conditions are met for the singlet channel. Specifically, the singlet unloading rate should be equal to or larger than the singlet loading rate. We then show that these conditions are met in our data.

Conditions on the singlet tunnel rates

We first obtain the conditions on the singlet transport rates by developing rate equations, in analogy with those found in Ref. [115].

We consider the contribution of loading and unloading rates of each channel to the total transport rate through the channel. Starting from the (1,1) state, the double dot is loaded

into one of the (2,1) states from the left lead. The mean loading rate is given by

$$\begin{aligned}\Gamma_{\text{load}} &\equiv 1/T_{\text{load}} \\ &= \Gamma_{S\ \text{load}} + \Gamma_{T\ \text{load}},\end{aligned} \tag{G.12}$$

where $\Gamma_{S/T\ \text{load}}$ are the loading rates into the singlet-like and triplet-like states from the left lead respectively.

The total time required for a complete transport cycle is

$$T = T_{\text{load}} + p_T/\Gamma_{T\ \text{unload}} + p_S/\Gamma_{S\ \text{unload}}, \tag{G.13}$$

where $\Gamma_{S/T\ \text{unload}}$ are the unloading rates of the singlet-like and triplet-like channels respectively, and

$$p_S = \frac{\Gamma_{S\ \text{load}}}{\Gamma_{S\ \text{load}} + \Gamma_{T\ \text{load}}}, \tag{G.14}$$

$$p_T = \frac{\Gamma_{T\ \text{load}}}{\Gamma_{S\ \text{load}} + \Gamma_{T\ \text{load}}}, \tag{G.15}$$

are the probabilities of loading the singlet-like and triplet-like channels.

In the triplet-like transport regime, the singlet-like channel is strongly suppressed by energy dependent tunneling. If we assume that the loading and unloading rates for the triplet-like channel are much faster than the loading and unloading rates for the singlet-like channel, and if we also assume that the unloading rate of the triplet-like channel is much faster than its loading rate due to asymmetric tunnel barriers (see Ref. [115] for a discussion), then Eq. G.13 reduces to

$$\begin{aligned}T &\approx \left(1 + \frac{\Gamma_{S\ \text{load}}}{\Gamma_{S\ \text{unload}}}\right)\frac{1}{\Gamma_{T\ \text{load}}} + \frac{1}{\Gamma_{T\ \text{unload}}} \\ &\approx \left(1 + \frac{\Gamma_{S\ \text{load}}}{\Gamma_{S\ \text{unload}}}\right)\frac{1}{\Gamma_{T\ \text{load}}}.\end{aligned} \tag{G.16}$$

In the limit of only one fast triplet-like channel, the total tunneling time is $T \approx 1/\Gamma_{T\ \text{load}}$. This implies that if $\Gamma_{S\ \text{load}} \ll \Gamma_{S\ \text{unload}}$, then the current through the double dot is essentially a triplet-like channel current. Therefore, it is important to determine the ratio of the loading to unloading rates of the singlet-like channel.

Loading rates

We now estimate the loading rates for the singlet-like and triplet-like channels at point D on the 'tail' of the transport data (Fig. 8.1, Chapter 8). Starting from the (1,1) charge configuration, the loading rates into the (2,1) states are strongly energy-dependent at the left barrier (see Chapter 7 and Ref. [24]) and are given by

$$\Gamma_{S/T,\,\mathrm{load}} = \Gamma_0 e^{-E_{S/T}/E_L}, \tag{G.17}$$

where the amplitude $\Gamma_0 \approx 1.5 \times 10^8$ s^{-1}, the energy dependent coefficient $E_L \approx 40$ μeV, $E_T \approx E_{ST(2,0)} \approx 174$ μeV (see Chapter 7 and (see Chapter 7 and Ref. [24])) and $E_S \approx 2E_{ST(2,0)}$ at point D.

The loading rates of the triplet-like and singlet-like states at point D are therefore

$$\Gamma_{T,\,\mathrm{load}} \approx 1.9 \times 10^6 \text{ s}^{-1}, \tag{G.18}$$

$$\Gamma_{S,\,\mathrm{load}} \approx 2.5 \times 10^4 \text{ s}^{-1}. \tag{G.19}$$

Unloading rates

We now estimate the unloading rates for the singlet-like and triplet-like channels at point D. Unloading of the triplet-like (2,1) state occurs when the electron in the right dot tunnels out across the right barrier, followed by interdot tunneling from the (2,0) to the (1,1) state. The tunneling rate across the right barrier $\Gamma_R \approx 9.2 \times 10^9$ s^{-1} and the coherent interdot tunneling rate $\Gamma_i \approx 7.7 \times 10^8$ s^{-1} (see Chapter 7 and Ref. [24]). The unloading rate for the triplet-like channel is therefore given by

$$\Gamma_{T,\,\mathrm{unload}} = (\Gamma_R^{-1} + \Gamma_i^{-1})^{-1} \approx 7.1 \times 10^8 \text{ s}^{-1}. \tag{G.20}$$

The unloading rate of the singlet-like state is dominated by spin-flip cotunneling, which involves two low-probability processes: the spin-flip and the cotunneling. The spin-flip can be understood as the small probability p_m that the T^* state contains the $(2,0)$ singlet. We then have

$$\Gamma_{S,\,\mathrm{unload}} = p_m \Gamma_C, \tag{G.21}$$

where Γ_C is the total cotunneling rate.

We can estimate p_m from the (2,1) Hamiltonian of Eq. G.2 by considering the subspace spanned by the states $|S_0(2,0)\rangle \otimes |3\rangle$ and $|T_0(2,0)\rangle \otimes |3\rangle$. The Hamiltonian within this subspace is given by the top-leftmost 2×2 matrix block in the right-hand side of Eq. G.2. The off-diagonal element in this subspace is $(\Lambda_{23}^{13} + s_{13}g_{23} + s_{23}g_{13})/\sqrt{2} \approx \Lambda_{23}^{13}/\sqrt{2}$. The singlet-triplet mixing probability is therefore

$$p_m \approx \left[\frac{\Lambda_{23}^{13}}{2E_{ST(2,0)}}\right]^2. \tag{G.22}$$

We do not have a direct experimental estimate for the quantity Γ_{23}^{13}. However, we can estimate it using the parabolic well approximation, where the eigenstates of each dot are those of the 2-dimensional harmonic oscillator [109]. For a dot size of approximately 100 nm and an interdot distance of approximately 200 nm [115], we obtain $\Gamma_{23}^{13} \approx 0.15$ meV when there is maximum overlap between the first excited eigenstate ('2') of the left dot with the ground eigenstate ('3') of the right dot. This corresponds to the axis of the wavefunction of the first excited eigenstate being aligned with the axis of the double dot. A more realistic estimate where the angle between the wavefunction axis and the axis of the double dot is 45 degrees, gives

$$\Lambda_{23}^{13} \approx 0.073 \text{ meV}. \tag{G.23}$$

Given that $E_{ST(2,0)} \approx 174$ μeV (see Chapter 7 and Ref. [24]), the singlet-triplet mixing probability is

$$p_m \approx 0.044. \tag{G.24}$$

The cotunneling rate Γ_C from the left lead into the right dot and out to the right lead, can be estimated from point F of the transport data (Fig. G.2 and Fig. 8.1(b) of Chapter 8). This cotunneling has contributions from both the singlet and triplet channels. The singlet-like channels, $S, T(2,0) \rightarrow S^*(2,1)$, are suppressed by energy dependent tunneling, as is one of the triplet-like channels, $T(2,0) \rightarrow T^*(2,1)$. The other triplet-like channel, $S(2,0) \rightarrow T^*(2,1)$ is suppressed by the slow spin-flip process. In principle, we cannot separate these contributions at point F. However, we can consider a worst case scenario where the cotunneling current at point F is dominated by the channels without spin-flip,

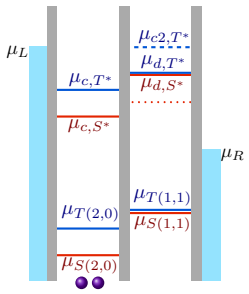

Figure G.2: Electrochemical potentials at point F of the transport data shown in Fig. 8.1 of Chapter 8. The dominant current contribution is from cotunneling from the left lead into the right dot and out to the right lead.

$S(2,0) \rightarrow S^*(2,1)$ and $T(2,0) \rightarrow T^*(2,1)$, with very little energy dependent tunneling. In this case, the cotunneling rate through the triplet-like spin-flip channel, $S(2,0) \rightarrow T^*(2,1)$, is given by Eq. (S26), where $e\Gamma_C$ is the total current measured at point F. In this way, we obtain

$$\Gamma_C \approx 5.0 \times 10^5 \text{ s}^{-1}, \tag{G.25}$$

$$\Gamma_{S,\text{ unload}} \approx 2.2 \times 10^4 \text{ s}^{-1}. \tag{G.26}$$

Conclusions

It is clear from the preceding analysis that the loading and unloading rates satisfy the conditions for Eq. G.16 to be valid, i.e. $\Gamma_{T\text{ unload}} \gg \Gamma_{T\text{ load}} \gg \Gamma_{S\text{ load/unload}}$. Since the ratio $\Gamma_{S\text{ load}}/\Gamma_{S\text{ unload}} \approx 1$, the current along the tail is of the same order of magnitude as the current in the singlet-like triangle away from the resonant left edge.

Below the tail, cotunneling is energetically unfavorable, while above the tail, cotunneling is suppressed through energy dependent tunneling. $\Gamma_{S\text{ unload}}$ is therefore much smaller on both sides of the tail. Loading of the singlet-like channel, which is strongly energy dependent, increases below the tail, further suppressing current. However, suppression of the singlet-like channel loading rate above the tail could mitigate the decrease in the unloading rate, so that the ratio $\Gamma_{S\text{ load}}/\Gamma_{S\text{ unload}}$ remains small, allowing some current flow. That there is small current above the tail is observed in transport data at larger biases (see Chapter 7 and Ref. [24]), where the loading of the singlet-like channel can be

more strongly suppressed as it moves lower in the bias window.

Therefore, although spin-flip cotunneling involves two mechanisms of lower probability, namely cotunneling and triplet-singlet mixing, the dampening effect on the tunnel rate is mitigated by the small loading probability into the singlet-like channel. The effect of spin-flip cotunneling is to open a thin window in the triplet-like bias triangle to allow triplet-like channel current.

G.3 Proposed experiment to verify singlet-triplet mixing mechanism

In this section, we propose an experiment to verify the singlet-triplet mixing mechanism described in Chapter 8. We note that in the spin-flip process described in the text, the loading of the third electron into the right dot is through cotunneling from the left lead. Since it is the singlet-triplet mixing mechanism that we are interested in, this loading can also be from the tunneling of an electron from the right lead, as described below.

Using pulsed gate techniques such as those described in Ref. [105], the double dot could be first loaded into the (2,0) singlet state (a), then pulsed such that the μ_{c2,T^*} level of the right dot is below the Fermi level of the right lead (b), allowing for the loading of an electron into the right dot from the right lead. Loading of the μ_{d,S^*} level will not cause singlet-triplet mixing but this is suppressed because of energy dependent tunneling. Next, a gate pulse can then be applied such that the triplet-like level μ_{c,T^*} is above the Fermi level of the left lead (c). A singlet-triplet spin-flip will lead to a tunneling out of an electron via this level. Tunneling events can be detected by charge sensing via an adjacent quantum point contact [105]. These three pulse stages, a to c, are shown schematically in Fig. G.3.

G.4 Transport through the singlet-like channel

The strong line on the left edge of the singlet-like triangle in Fig. 8.1 of Chapter 8 can be explained by Fig. G.4. At C, the μ_{c,S^*} level of the left dot is resonant with the Fermi level

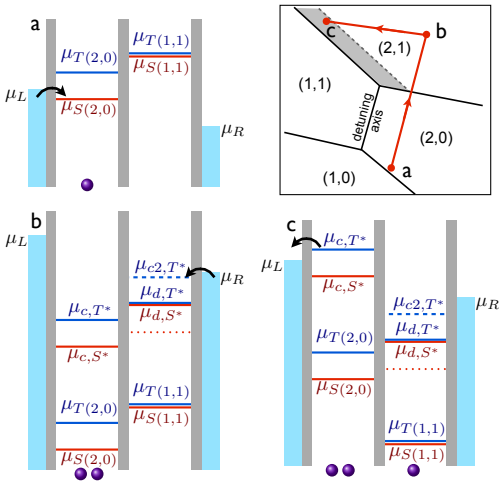

Figure G.3: Proposed experimental verification of the singlet-triplet spin-flip process. The boxed panel shows a schematic of the honeycomb charge stability diagram [110], showing the regions in which the ground (singlet and singlet-like) states of the various charge configurations are stable. Points a, b and c are the positions to which the double dot should be pulsed. The dotted line indicates the boundary between the (1,1) and triplet-like (2,1) regions, i.e. within the shaded region, a (1,1) state is more stable than the triplet-like (2,1) state. Panels a, b and c show the electrochemical potentials, with the circles at the bottom of each diagram indicating the number of electrons at the start of each pulse. Black arrows indicate the tunneling of an electron, which can be detected via charge sensing using an adjacent quantum point contact. Detection of a tunneling out process at 'c' would indicate a singlet-triplet spin-flip.

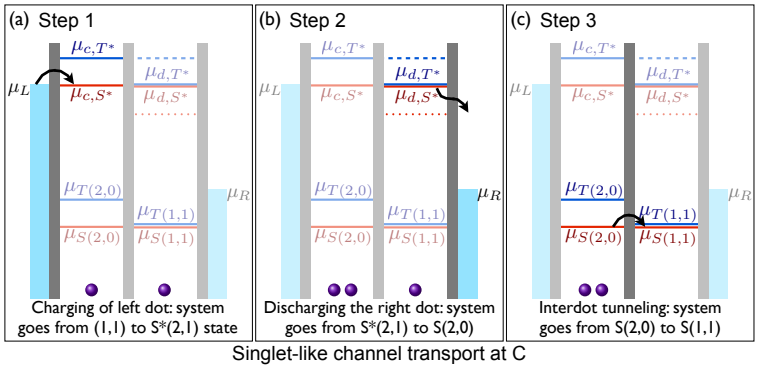

Figure G.4: Diagrams of singlet-like channel transport at point C. Purple dots at the bottom of each diagram indicate the electron number at the beginning of each step in the transport cycle. (a) Starting from a (1,1) state, charging of the left dot from the μ_{c,S^*} level brings the system to the $S^*(2,1)$ state. (b) From the $S^*(2,1)$ state, the left dot ends up in the $S(2,0)$ state as the right dot discharges from the μ_{d,S^*} level. (c) Inter-dot tunneling from (2,0) to (1,1) completes the cycle.

of the left lead, μ_L, as shown in Fig. G.4(a). Also, $\mu_{S(2,0)}$ and $\mu_{S(1,1)}$ are aligned with each other as shown in Fig. G.4(c). These two resonance conditions lead to a sharp current peak at C. Going away from C along the left edge of the triangle (Fig. 8.1, Chapter 8), the right dot falls in energy but the left dot maintains its resonance with the left lead, giving rise to a bright line along the left edge. In the direction where both dot energies fall in tandem, loading of the left dot into μ_{c,S^*} from the left lead is suppressed due to the exponential energy dependence in tunneling (see Chapter 7 and Ref. [24]).

G.5 Spin-flip cotunneling in forward bias data

Here we discuss the interpretation of transport data taken at forward bias of $V_{\rm SD} = +0.526$mV, originally reported in Ref. (see Chapter 7 and Ref. [24]) and shown in Fig. G.6 and show that certain features of the data arise because of spin-flip cotunneling.

In the three-electron regime, transport at forward bias cycles from $(1,1) \rightarrow (2,0) \rightarrow (2,1)$. The bias triangles for forward bias are shown in Fig. G.5(b). In this regime, transport is spin blockaded within the region bounded by $\gamma\delta\sigma\omega$ of Fig. G.5(b), due to the fact that $\mu_{T(1,1)}$ is below the $\mu_{T(2,0)}$ level as shown in Fig. G.6(c). Any mechanism that allows spin relaxation to the $S(1,1)$ state lifts the spin blockade, and typical relaxation mechanisms are expected to give rise to uniform current over the entire blockade region $\gamma\delta\sigma\omega$. However, we observe a line of high current, shown by the dotted line in Fig. G.5, which indicates that there is a preferentially high relaxation rate along this feature. We explain this line of strong current by a spin-flip cotunneling process.

Point E (Fig. G.5) lies along the line of high current in the spin blockade region. At this point, the lower (solid line) of the two μ_{d,T^*} levels of the left dot are lined up with the right lead. This allows cotunneling of an electron from the right lead into the left dot to form the triplet-like $T^*(2,1)$ state. (Fig. G.6(d)). Discharging of the left dot from the higher (dashed line) of the μ_{d,T^*} chemical potential results in the singlet $S(1,1)$ state, which is not blockaded. The double dot is then able to complete the transport cycle until the next time the double dot gets spin blockaded.

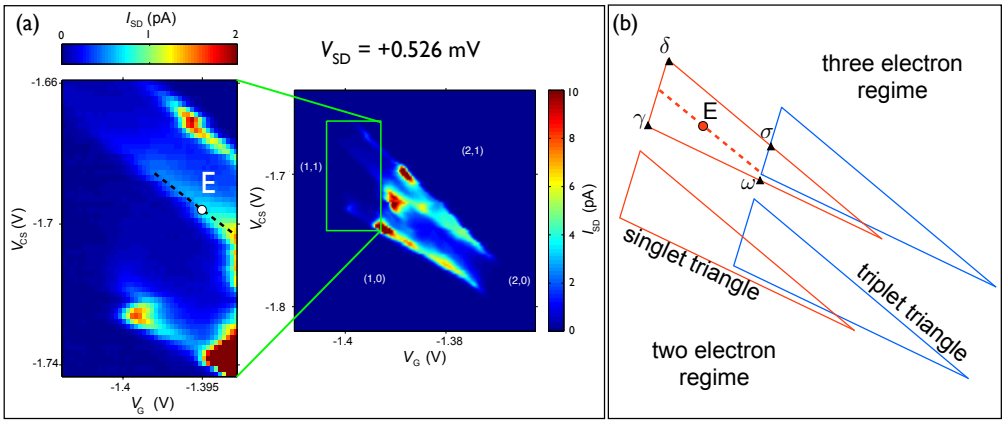

Figure G.5: Transport data and schematic of bias triangles at forward bias. (a) Transport current I_{SD} as a function of two gate voltages, V_{G} (V) and V_{CS} (V), taken at a forward bias source-drain voltage of $V_{\mathrm{SD}} = +0.526\mathrm{mV}$. These data were reported originally in Ref. (see Chapter 7 and Ref. [24]). The feature shown by the dotted line is explained by the spin-flip cotunneling process. (b) Schematic of the bias triangles of transport data taken at the forward bias. Bias triangles corresponding to transport through ground (excited) states are shown in the red (blue) on the left (right). In the three electron regime (upper triangles), the dotted line lies in the region $\gamma\delta\sigma\omega$, where the triplet $T(1,1)$ state is spin blockaded. Spin relaxation to the $S(1,1)$ state lifts the spin blockade and allows transport to resume. This is possible within the region bounded by $\gamma\delta\sigma\omega$ and should give rise to a uniform current within the region. However, the presence of the line of high current (dotted) within $\gamma\delta\sigma\omega$ suggests a preferentially high spin relaxation rate which is explained by the spin-flip cotunneling process shown below in Fig. G.6.

It is because the dotted line in Fig. G.5 lies in the right dot energy axis that the spin blockade is lifted at a much faster rate. This is due to the fact that the left dot energy is aligned with the Fermi level of the right lead, allowing cotunneling to occur at a fast rate. As a result, spin relaxation happens at a much higher rate along this line.

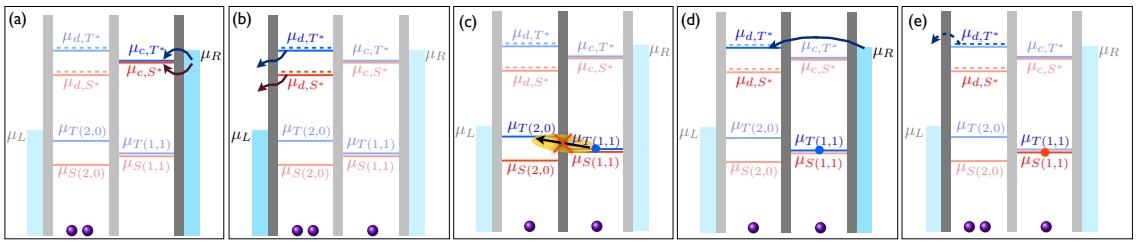

Figure G.6: Processes involved in the lifting of the triplet $T(1,1)$ spin blockade through cotunneling induced spin flip at point E. In the three-electron regime (upper triangles) of Fig. G.5(b), transport is spin blockaded within the region bounded by $\gamma\delta\sigma\omega$. Purple dots at the bottom of each diagram indicate the electron number at the beginning of each step in the transport cycle. (a) Starting from any one of the two (2,0) states, the $S^*(2,1)$ or $T^*(2,1)$ state is loaded from the right lead onto the left dot at the μ_{c,S^*} or μ_{c,T^*} chemical potential respectively. (b) The left dot may discharge from the lower (solid line) of the μ_{d,S^*} or μ_{d,T^*} chemical potential, resulting in a $T(1,1)$ triplet. (Discharge from any one of the two dashed levels is also possible, but it results in a singlet $S(1,1)$ that is not spin blockaded.) (c) The $T(1,1)$ triplet state is spin blockaded as the $\mu_{T(1,1)}$ chemical potential lies below the $\mu_{T(2,0)}$ level. (d) Along the dashed line of Fig. G.5, the lower (solid line) of the two μ_{d,T^*} chemical potentials is lined up with the Fermi level of the right lead, allowing the loading of the excited (2,1) state through cotunneling from the right lead. (e) Subsequent discharge of a left dot electron could be from either one of the μ_{d,T^*} levels, with discharge from the upper (dashed line) of the μ_{d,T^*} levels resulting in the singlet $S(1,1)$ state which can then complete the transport cycle by going into the $S(2,0)$ state through inter-dot tunneling. Transport thus resumes until the next triplet (1,1) spin blockade. The key is that from either the singlet-like or triplet-like (2,1) states, discharge from the left dot at the chemical potentials indicated by the dashed or solid lines results in a singlet or triplet (1,1) state respectively. The former allows transport to resume, whereas the latter results in a spin blockade. The dotted line of Fig. G.5 lies in the direction where the left dot energy is fixed, leading to the line of high current.

Bibliography

[1] D. Loss and D. P. DiVincenzo, "Quantum computation with quantum dots," *Phys. Rev. A*, vol. 47, p. 120, 1998.

[2] M. A. Nielsen and I. L. Chuang, *Quantum Computation and Quantum Information*. Cambridge: Cambridge University Press, 2000.

[3] F. A. Zwanenburg, A. S. Dzurak, A. Morello, M. Y. Simmons, L. C. L. Hollenberg, G. Klimeck, S. Rogge, S. N. Coppersmith, and M. A. Eriksson, "Silicon quantum electronics." Preprint at http://arxiv.org/abs/1206.5202.

[4] J. R. Petta, A. C. Johnson, J. M. Taylor, E. A. Laird, A. Yacoby, M. D. Lukin, C. M. Marcus, M. P. Hanson, and A. C. Gossard, "Coherent manipulation of coupled electron spins in semiconductor quantum dots," *Science*, vol. 309, p. 2180, 2005.

[5] B. E. Kane, "A silicon-based nuclear spin quantum computer," *Nature*, vol. 393, p. 133, 1998.

[6] M. Xiao, M. G. House, and H. W. Jiang, "Measurement of the spin relaxation time of single electrons in a silicon metal-oxide-semiconductor-based quantum dot," *Phys. Rev. Lett.*, vol. 104, p. 096801, 2010.

[7] A. Morello, F. Z. J. Pla, K. Chan, K. Tan, H. Huebl, M. Mottonen, C. Nugroho, C. Yang, J. van Donkelaar, A. Alves, D. Jamieson, C. Escott, L. Hollenberg, R. Clark, and A. Dzurak, "Single-shot readout of an electron spin in silicon," *Nature*, vol. 467, p. 687, 2010.

[8] C. B. Simmons, J. R. Prance, B. J. van Bael, T. S. Koh, Z. Shi, D. E. Savage, M. G. Lagally, R. Joynt, M. Friesen, S. N. Coppersmith, and M. A. Eriksson, "Tunable spin loading and T_1 of a silicon spin qubit measured by single-shot readout," *Phys. Rev. Lett.*, vol. 106, p. 156804, 2011.

[9] C. Tahan, M. Friesen, and R. Joynt, "Decoherence of electron spin qubits in Si-based quantum computers," *Phys. Rev. B*, vol. 66, p. 035314, 2002.

[10] R. de Sousa and S. Das Sarma, "Electron spin coherence in semiconductors: Considerations for a spin-based solid-state quantum computer architecture," *Phys. Rev. B*, vol. 67, p. 033301, 2003.

[11] A. M. Tyryshkin, S. Tojo, J. J. L. Morton, H. Riemann, N. V. Abrosimov, P. Becker, H.-J. Pohl, T. Schenkel, M. L. W. Thewalt, K. M. Itoh, and S. A. Lyon, "Electron spin coherence exceeding seconds in high-purity silicon," *Nature Materials*, vol. 11, p. 143, 2012.

[12] D. P. DiVincenzo, "Quantum computation," *Science*, vol. 270, p. 255, 1995.

[13] J. Preskill, "Quantum computing: Pro and con," *Proc. R. Soc. Lond. A*, vol. 454, p. 469, 1998.

[14] A. J. Fisher, "Quantum computing in the solid state: The challenge of decoherence," *Philos. Trans. Roy. Soc. A*, vol. 361, p. 1441, 2003.

[15] J. K. Gamble, X. Hu, M. Friesen, and S. N. Coppersmith, "Two-electron dephasing in single Si and GaAs quantum dots," *Phys. Rev. B*, vol. 86, p. 035302, 2012.

[16] D. Vion, A. Aassime, A. Cottet, P. Joyez, H. Potheir, C. Urbina, D. Esteve, and M. H. Devoret, "Manipulating the quantum state of an electrical circuit," *Science*, vol. 296, p. 886, 2002.

[17] O. Astafiev, Y. Pashkin, Y. Nakamura, T. Yamamoto, and J. Tsai, "Quantum noise in the Josephson charge qubit," *Phys. Rev. Lett.*, vol. 93, p. 267007, 2004.

[18] Z. Shi, C. B. Simmons, J. R. Prance, J. K. Gamble, T. S. Koh, Y.-P. Shim, X. Hu, D. E. Savage, M. G. Lagally, M. A. Eriksson, M. Friesen, and S. N. Coppersmith, "Fast hybrid silicon double quantum-dot qubit," *Phys. Rev. Lett.*, vol. 108, p. 140503, 2012.

[19] F. H. L. Koppens, C. Buizert, K. J. Tielrooij, I. T. Vink, K. C. Nowack, T. Meunier, L. P. Kouwenhoven, and L. M. K. Vandersypen, "Driven coherent oscillations of a single electron spin in a quantum dot," *Nature*, vol. 442, p. 766, 2006.

[20] J. Levy, "Universal quantum computation with spin-1/2 pairs and Heisenberg exchange," *Phys. Rev. Lett.*, vol. 89, p. 147902, 2002.

[21] D. P. DiVincenzo, D. Bacon, J. Kempe, G. Burkard, and K. B. Whaley, "Universal quantum computation with the exchange interaction," *Nature*, vol. 408, p. 339, 2000.

[22] T. S. Koh, J. K. Gamble, M. Friesen, M. A. Eriksson, and S. N. Coppersmith, "Pulse-gated quantum dot hybrid qubit." To appear in Phys. Rev. Lett. (Preprint at http://arxiv.org/abs/1207.5581).

[23] Z. Shi, C. B. Simmons, D. R. Ward, J. R. Prance, T. S. Koh, J. K. Gamble, X. Wu, D. E. Savage, M. G. Lagally, M. Friesen, S. N. Coppersmith, and M. A. Eriksson, "Coherent quantum oscillations in a silicon charge qubit." Preprint at http://arxiv.org/abs/1208.0519.

[24] C. B. Simmons, T. S. Koh, N. Shaji, M. Thalakulam, L. J. Klein, H. Qin, H. Luo, D. E. Savage, M. G. Lagally, A. J. Rimberg, R. Joynt, R. Blick, M. Friesen, S. N. Coppersmith, and M. A. Eriksson, "Pauli spin blockade and lifetime-enhanced transport in a Si/SiGe double quantum dot," *Phys. Rev. B*, vol. 82, p. 245312, 2010.

[25] T. S. Koh, C. B. Simmons, M. A. Eriksson, S. N. Coppersmith, and M. Friesen, "Unconventional transport in the "hole" regime of a Si double quantum dot," *Phys. Rev. Lett.*, vol. 106, p. 186801, 2011.

[26] E. A. Laird, J. M. Taylor, D. P. DiVincenzo, C. M. Marcus, M. P. Hanson, and A. C. Gossard, "Coherent spin manipulation in an exchange-only qubit," *Phys. Rev. B*, vol. 82, p. 075403, 2010.

[27] H. Bluhm, S. Foletti, I. Neder, M. Rudner, D. Mahalu, V. Umansky, and A. Yacoby, "Dephasing time of GaAs electron-spin qubits coupled to a nuclear bath exceeding 200 μs," *Nature Physics*, vol. 7, p. 109, 2011.

[28] D. A. Lidar, I. L. Chuang, and K. B. Whaley, "Decoherence-free subspaces for quantum computation," *Phys. Rev. Lett.*, vol. 81, p. 2594, 1998.

[29] E. I. Rashba, "Theory of electric dipole spin resonance in quantum dots: Mean field theory with Gaussian fluctuations and beyond," *Phys. Rev. B*, vol. 78, p. 195302, 2008.

[30] V. N. Golovach, M. Borhani, and D. Loss, "Electric-dipole-induced spin resonance in quantum dots," *Phys. Rev. B*, vol. 74, p. 165319, 2006.

[31] B. Fong and S. Wandzura, "Universal quantum computation and leakage reduction in 3-qubit decoherence free subsystem," *Quantum Information and Computation*, vol. 11, p. 1003, 2011.

[32] S. Amasha, K. MacLean, I. P. Radu, D. M. Zumbühl, M. A. Kastner, M. P. Hanson, and A. C. Gossard, "Spin-dependent tunneling of single electrons into an empty quantum dot," *Phys. Rev. B*, vol. 78, p. 041306(R), 2008.

[33] Z. Shi, C. B. Simmons, J. Prance, J. K. Gamble, M. Friesen, D. E. Savage, M. G. Lagally, S. N. Coppersmith, and M. A. Eriksson, "Tunable singlet-triplet splitting in a few-electron Si/SiGe quantum dot," *Appl. Phys. Lett.*, vol. 99, p. 233108, 2011.

[34] T. B. Boykin, G. Klimeck, M. Friesen, S. N. Coppersmith, P. von Allmen, F. Oyafuso, and S. Lee, "Valley splitting in low-density quantum-confined heterostructures studied using tight-binding models," *Phys. Rev. B*, vol. 70, p. 165325, 2004.

[35] A. L. Saraiva, M. J. Calderon, X. Hu, S. Das Sarma, and B. Koiller, "Physical mechanisms of interface-mediated intervalley coupling in Si," *Phys. Rev. B*, vol. 80, p. 081305(R), 2009.

[36] J. R. Schrieffer and P. A. Wolf, "Relation between the Anderson and Kondo Hamiltonians," *Physical Review*, vol. 149, p. 491, 1966.

[37] C. Gros, R. Joynt, and T. M. Rice, "Antiferromagnetic correlations in almost-localized Fermi liquids," *Phys. Rev. B*, vol. 36, p. 381, 1987.

[38] A. H. MacDonald, S. M. Girvin, and D. Yoshioka, "t/U expansion for the Hubbard model," *Phys. Rev. B*, vol. 37, p. 9753, 1988.

[39] S. Goswami, K. A. Slinker, M. Friesen, L. M. McGuire, J. L. Truitt, C. Tahan, L. J. Klein, J. O. Chu, P. M. Mooney, D. W. van der Weide, R. Joynt, S. N. Coppersmith, and M. A. Eriksson, "Controllable valley splitting in silicon quantum devices," *Nature Physics*, vol. 3, p. 41, 2007.

[40] M. G. Borselli, R. S. Ross, A. A. Kiselev, E. T. Croke, K. S. Holabird, P. W. Deelman, L. D. Warren, I. Alvarado-Rodriguez, I. Milosavljevic, F. C. Ku, W. S. Wong, A. E. Schmitz, M. Sokolich, M. F. Gyure, and A. T. Hunter, "Measurement of valley splitting in high-symmetry Si/SiGe quantum dots," *Appl. Phys. Lett.*, vol. 98, p. 123118, 2011.

[41] J. R. Petta, A. C. Johnson, C. M. Marcus, M. P. Hanson, and A. C. Gossard, "Manipulation of a single charge in a double quantum dot," *Phys. Rev. Lett.*, vol. 93, p. 186802, 2004.

[42] J. A. Jones and E. Knill, "Efficient refocusing of one-spin and two-spin interactions for NMR quantum computation," *J. Magn. Res.*, vol. 141, p. 322, 1999.

[43] K. MacLean, S. Amasha, I. P. Radu, D. M. Zumbühl, M. A. Kastner, M. P. Hanson, and A. C. Gossard, "Energy-dependent tunneling in a quantum dot," *Phys. Rev. Lett.*, vol. 98, p. 036802, 2007.

[44] R. Hanson, L. H. W. van Beveren, I. T. Vink, J. M. Elzerman, W. J. M. Naber, F. H. L. Koppens, L. P. Kouwenhoven, and L. M. K. Vandersypen, "Single-shot readout of electron spin states in a quantum dot using spin-dependent tunnel rates," *Phys. Rev. Lett.*, vol. 94, p. 196802, 2005.

[45] M. Prada, R. Blick, and R. Joynt, "Singlet-triplet relaxation in two-electron silicon quantum dots," *Phys. Rev. B*, vol. 77, p. 115438, 2008.

[46] L. Wang and M. W. Wu, "Singlet-triplet relaxation in SiGe/Si/SiGe double quantum dots," *J. Appl. Phys.*, vol. 110, p. 043716, 2011.

[47] X. Hu, B. Koiller, and S. Das Sarma, "Charge qubits in semiconductor quantum computer architecture: Tunnel coupling and decoherence," *Phys. Rev. B*, vol. 71, p. 235332, 2005.

[48] X. Hu, "Two-spin dephasing by electron-phonon interaction in semiconductor double quantum dots," *Phys. Rev. B*, vol. 83, p. 165322, 2011.

[49] D. Culcer, X. Hu, and S. Das Sarma, "Dephasing of Si spin qubits due to charge noise," *Appl. Phys. Lett.*, vol. 95, p. 073102, 2009.

[50] T. Hayashi, T. Fujisawa, H. D. Cheong, Y. H. Jeong, and Y. Hirayama, "Coherent manipulation of electronic states in a double quantum dot," *Phys. Rev. Lett.*, vol. 91, p. 226804, 2003.

[51] J. M. Martinis, S. Nam, and J. Aumentado, "Rabi oscillations in a large Josephson-junction qubit," *Phys. Rev. Lett.*, vol. 89, p. 117901, 2002.

[52] M. Pioro-Ladriere, T. Obata, Y. Tokura, Y.-S. Shin, T. Kubo, K. Yoshida, T. Taniyama, and S. Tarucha, "Electrically driven single-electron spin resonance in a slanting Zeeman field," *Nature Physics*, vol. 4, p. 776, 2008.

[53] J. Gorman, D. G. Hasko, and D. A. Williams, "Charge-qubit operation of an isolated double quantum dot," *Phys. Rev. Lett.*, vol. 95, p. 090502, 2005.

[54] J. R. Petta, A. C. Johnson, J. M. Taylor, A. Yacoby, M. D. Lukin, C. M. Marcus, M. P. Hanson, and A. C. Gossard, "Charge and spin manipulation in a few-electron double dot," *Physica E*, vol. 34, p. 42, 2006.

[55] G. Shinkai, T. Hayashi, T. Ota, and T. Fujisawa, "Correlated coherent oscillations in coupled semiconductor charge qubits," *Phys. Rev. Lett.*, vol. 103, p. 056802, 2009.

[56] K. D. Petersson, J. R. Petta, H. Lu, and A. C. Gossard, "Quantum coherence in a one-electron semiconductor charge qubit," *Phys. Rev. Lett.*, vol. 105, p. 246804, 2012.

[57] L. Gaudreau, G. Granger, A. Kam, G. C. Aers, S. A. Studenikin, P. Zawadzki, M. Pioro-Ladriere, Z. R. Wasilewski, and A. S. Sachrajda, "Coherent control of three-spin states in a triple quantum dot," *Nature Physics*, vol. 8, p. 54, 2012.

[58] M. D. Shulman, O. E. Dial, S. P. Harvey, H. Bluhm, V. Umansky, and A. Yacoby, "Demonstration of entanglement of electrostatically coupled singlet-triplet qubits," *Science*, vol. 336, p. 202, 2012.

[59] B. M. Maune, M. G. Borselli, B. Huang, T. D. Ladd, P. W. Deelman, K. S. Holabird, A. A. Kiselev, I. Alvarado-Rodriguez, R. S. Ross, A. E. Schmitz, M. Sokolich, C. A. Watson, M. F. Gyure, and A. T. Hunter, "Coherent singlet-triplet oscillations in a silicon-based double quantum dot," *Nature*, vol. 481, p. 344, 2012.

[60] L. Viola, E. Knill, and S. Lloyd, "Dynamical decoupling of open quantum systems," *Phys. Rev. Lett.*, vol. 82, p. 2417, 1999.

[61] S. D. Barrett and C. H. W. Barnes, "Double-occupation errors induced by orbital dephasing in exchange-interaction quantum gates," *Phys. Rev. B*, vol. 66, p. 125318, 2002.

[62] L. V. C. Assali, H. M. Petrilli, R. B. Capaz, B. Koiller, X. Hu, and S. Das Sarma, "Hyperfine interactions in silicon quantum dots," *Phys. Rev. B*, vol. 83, p. 165301, 2011.

[63] Y. Nakamura, *Nonadiabatic Transition: Concepts, Basic Theories and Applications*. London: World Scientific, 2001.

[64] M. Stopa, "Quantum dot self-consistent electronic structure and the Coulomb blockade," *Phys. Rev. B*, vol. 54, p. 13767, 1996.

[65] T. Yamamoto, Y. A. Pashkin, O. Astafiev, Y. Nakamura, and J. S. Tsai, "Demonstration of conditional gate operation using superconducting charge qubits," *Nature*, vol. 425, p. 941, 2003.

[66] I. van Weperen, B. D. Armstrong, E. A. Laird, J. Medford, C. M. Marcus, M. P. Hanson, and A. C. Gossard, "Charge-state conditional operation of a spin qubit," *Phys. Rev. Lett.*, vol. 107, p. 030506, 2011.

[67] C. P. Poole, *Electron Spin Resonance*. New York: Wiley, 2nd ed., 1983.

[68] K. Bergmann, H. Theuer, and B. W. Shore, "Coherent population transfer among quantum states of atoms and molecules," *Rev. Mod. Phys.*, vol. 70, p. 1003, 1998.

[69] S. Schiemann, A. Kuhn, S. Steuerwald, and K. Bergmann, "Efficient coherent population transfer in NO molecules using pulsed lasers," *Phys. Rev. Lett.*, vol. 71, p. 3637, 1993.

[70] B. W. Shore, *The Theory of Coherent Atomic Excitation.* New York: Wiley, 1990.

[71] J. R. Petta, J. M. Taylor, A. C. Johnson, A. Yacoby, M. D. Lukin, C. M. Marcus, M. P. Hanson, and A. C. Gossard, "Dynamic nuclear polarization with single electron spins," *Phys. Rev. Lett.*, vol. 100, p. 067601, 2008.

[72] S. Foletti, H. Bluhm, D. Mahalu, V. Umansky, and A. Yacoby, "Universal quantum control of two-electron spin quantum bits using dynamic nuclear polarization," *Nature Physics*, vol. 5, p. 903, 2009.

[73] J. Preskill. Lecture Notes at http://theory.caltech.edu/preskill/.

[74] D. J. Tannor, *Introduction to Quantum Mechanics: A Time-Dependent Perspective.* California: University Science Books, 2006.

[75] R. Hanson and G. Burkard, "Universal set of quantum gates for double-dot spin qubits with fixed interdot coupling," *Phys. Rev. Lett.*, vol. 98, p. 050502, 2007.

[76] X. Hu and S. Das Sarma, "Charge-fluctuation-induced dephasing of exchange- coupled spin qubits," *Phys. Rev. Lett.*, vol. 96, p. 100501, 2006.

[77] C. B. Simmons, M. Thalakulam, B. M. Rosemeyer, B. J. van Bael, E. K. Sackmann, D. E. Savage, M. G. Lagally, R. Joynt, M. Friesen, S. N. Coppersmith, and M. A. Eriksson, "Charge sensing and controllable tunnel coupling in a Si/SiGe double quantum dot," *Nano Lett.*, vol. 9, p. 3234, 2009.

[78] H.-P. Breuer and F. Petruccione, *The Theory of Open Quantum Systems.* USA: Oxford University Press, 2002.

[79] R. Jozsa, "Fidelity of mixed quantum states," *J. Mod. Optics*, vol. 41, p. 2315, 1994.

[80] I. Neder, M. S. Rudner, H. Bluhm, S. Foletti, B. I. Halperin, and A. Yacoby, "Semiclassical model for the dephasing of a two-electron spin qubit coupled to a coherently evolving nuclear spin bath," *Phys. Rev. B*, vol. 84, p. 035441, 2011.

[81] Y. Nakamura, Y. A. Pashkin, and J. S. Tsai, "Coherent control of macroscopic quantum states in a single-Cooper-pair box," *Nature*, vol. 398, p. 786, 1999.

[82] K. C. Nowack, F. H. L. Koppens, Y. V. Nazarov, and L. M. K. Vandersypen, "Coherent control of a single electron spin with electric fields," *Science*, vol. 318, p. 1430, 2007.

[83] R. Vrijen, E. Yablonovitch, K. Wang, H. W. Jiang, A. Balandin, V. Roychowdhury, T. Mor, and D. DiVincenzo, "Electron-spin-resonance transistors for quantum computing in silicon-germanium heterostructures," *Phys. Rev. A*, vol. 62, p. 012306, 2000.

[84] L. D. Landau, "On the theory of transfer of energy at collisions II," *Phys. Z. Sowjetunion*, vol. 2, p. 46, 1932.

[85] C. Zener, "Non-adiabatic crossing of energy levels," *Proc. R. Soc. London Ser. A*, vol. 137, p. 696, 1932.

[86] E. C. G. Stückelberg, "Theory of inelastic collisions between atoms, using two simultaneous differential equations," *Helv. Phys. Acta*, vol. 5, p. 369, 1932.

[87] J. R. Petta, H. Lu, and A. C. Gossard, "A coherent beam splitter for electronic spin states," *Science*, vol. 327, p. 669, 2010.

[88] M. Thalakulam, C. B. Simmons, B. M. Rosemeyer, D. E. Savage, M. G. Lagally, M. Friesen, S. N. Coppersmith, and M. A. Eriksson, "Fast tunnel rates in Si/SiGe one-electron single and double quantum dots," *Appl. Phys. Lett.*, vol. 96, p. 183104, 2010.

[89] Y. Dovzhenko, J. Stehlik, K. D. Petersson, J. R. Petta, H. Lu, and A. C. Gossard, "Nonadiabatic quantum control of a semiconductor charge qubit," *Phys. Rev. B*, vol. 84, p. 161302, 2011.

[90] S. Harvey, M. Shulman, O. Dial, H. Bluhm, V. Umansky, and A. Yacoby, "Fast exchange oscillations in quantum dot spin qubits." APS March Meeting 2012 (Abstract BAPS.2012.MAR.L29.8).

[91] R. R. Hayes, A. A. Kiselev, M. G. Borselli, S. S. Bui, E. T. Croke III, P. W. Deelman, B. M. Maune, I. Milosavljevic, J.-S. Moon, R. S. Ross, A. E. Schmitz, M. F. Gyure, and A. T. Hunter, "Lifetime measurements (T1) of electron spins in Si/SiGe quantum dots," 2009. Preprint at http://arxiv.org/abs/0908.0173.

[92] J. M. Elzerman, R. Hanson, L. H. W. van Beveren, B. Witkamp, L. M. K. Vandersypen, and L. P. Kouwenhoven, "Single-shot read-out of an individual electron spin in a quantum dot," *Nature*, vol. 430, p. 431, 2004.

[93] J. M. Elzerman, R. Hanson, L. H. W. van Beveren, L. M. K. Vandersypen, and L. P. Kouwenhoven, "Excited-state spectroscopy on a nearly closed quantum dot via charge detection," *Appl. Phys. Lett.*, vol. 84, p. 4617, 2004.

[94] R. Hanson, L. P. Kouwenhoven, J. R. Petta, S. Tarucha, and L. M. K. Vandersypen, "Spins in few-electron quantum dots," *Rev. Mod. Phys.*, vol. 79, p. 1217, 2007.

[95] T. B. Boykin, G. Klimeck, M. A. Eriksson, M. Friesen, S. N. Coppersmith, P. von Allmen, F. Oyafuso, and S. Lee, "Valley splitting in strained silicon quantum wells," *Appl. Phys. Lett.*, vol. 85, p. 115, 2004.

[96] N. Kharche, M. Prada, T. B. Boykin, and G. Klimeck, "Valley splitting in strained silicon quantum wells modeled with 2^{o} miscuts, step disorder, and alloy disorder," *Appl. Phys. Lett.*, vol. 90, p. 092109, 2007.

[97] G. P. Lansbergen, R. Rahman, C. J. Wellard, I. Woo, J. Caro, N. Collaert, S. Biesemans, G. Klimeck, L. C. L. Hollenberg, and S. Rogge, "Gate-induced quantum-confinement transition of a single dopant atom in a silicon FinFET," *Nature Physics*, vol. 4, p. 656, 2008.

[98] D. Culcer, L. Cywinski, Q. Li, X. Hu, and S. Das Sarma, "Realizing singlet-triplet qubits in multivalley Si quantum dots," *Phys. Rev. B*, vol. 80, p. 205302, 2009.

[99] M. Friesen and S. N. Coppersmith, "Theory of valley-orbit coupling in a Si/SiGe quantum dot," *Phys. Rev. B*, vol. 81, p. 115324, 2010.

[100] M. Fuechsle, S. Mahapatra, F. A. Zwanenburg, M. Friesen, M. A. Eriksson, and M. Y. Simmons, "Spectroscopy of few-electron single-crystal silicon quantum dots," *Nature Nanotech.*, vol. 5, p. 502, 2010.

[101] A. Khaetskii and Y. Nazarov, "Spin relaxation in semiconductor quantum dots," *Phys. Rev. B*, vol. 61, p. 12639, 2000.

[102] M. Friesen, C. Tahan, R. Joynt, and M. A. Eriksson, "Spin readout and initialization in a semiconductor quantum dot," *Phys. Rev. Lett.*, vol. 92, p. 037901, 2004.

[103] S. Datta, *Electronic Transport in Mesoscopic Systems*. Cambridge: Cambridge University Press, 1995.

[104] A. B. Vorontsov and M. G. Vavilov, "Spin relaxation in quantum dots due to electron exchange with leads," *Phys. Rev. Lett.*, vol. 101, p. 226805, 2008.

[105] J. R. Petta, A. C. Johnson, A. Yacoby, C. M. Marcus, M. P. Hanson, and A. C. Gossard, "Pulsed-gate measurements of the singlet-triplet relaxation time in a two-electron double quantum dot," *Phys. Rev. B*, vol. 72, p. 161301, 2005.

[106] K. Ono, D. G. Austing, Y. Tokura, and S. Tarucha, "Current rectification by Pauli exclusion in a weakly coupled double quantum dot system," *Science*, vol. 297, p. 1313, 2002.

[107] A. C. Johnson, J. R. Petta, J. M. Taylor, A. Yacoby, M. D. Lukin, C. M. Marcus, M. P. Hanson, and A. C. Gossard, "Triplet-singlet spin relaxation via nuclei in a double quantum dot," *Nature*, vol. 435, p. 925, 2005.

[108] A. C. Johnson, J. R. Petta, C. M. Marcus, M. P. Hanson, and A. Gossard, "Singlet-triplet spin blockade and charge sensing in a few-electron double quantum dot," *Phys. Rev. B*, vol. 72, p. 165308, 2005.

[109] J. H. Davies, *The Physics of Low-Dimensional Semiconductors: An Introduction.* Cambridge: Cambridge University Press, 1998.

[110] W. G. van der Wiel, S. D. Franceschi, J. M. Elzerman, T. Fujisawa, S. Tarucha, and L. P. Kouwenhoven, "Electron transport through double quantum dots," *Rev. Mod. Phys.*, vol. 75, p. 1, 2002.

[111] L. P. Rokhinson, L. J. Guo, S. Y. Chou, and D. C. Tsui, "Magnetically induced reconstruction of the ground state in a few-electron Si quantum dot," *Phys. Rev. Lett.*, vol. 87, p. 166802, 1998.

[112] A. K. Hüttel, H. Qin, A. W. Holleitner, R. H. Blick, K. Neumaier, D. Weinmann, K. Eberl, and J. P. Kotthaus, "Spin blockade in ground-state resonance of a quantum dot," *Europhys. Lett.*, vol. 62, p. 712, 2003.

[113] J. M. Taylor, H.-A. Engel, W. Dür, A. Yacoby, C. M. Marcus, P. Zoller, and M. D. Lukin, "Fault-tolerant architecture for quantum computation using electrically controlled semiconductor spins," *Nature Physics*, vol. 1, p. 177, 2005.

[114] H. W. Liu, T. Fujisawa, Y. Ono, H. Inokawa, A. Fujiwara, K. Takashina, and Y. Hirayama, "Pauli-spin-blockade transport through a silicon double quantum dot," *Phys. Rev. B*, vol. 77, p. 073310, 2008.

[115] N. Shaji, C. B. Simmons, M. Thalakulam, L. J. Klein, H. Qin, H. Luo, D. E. Savage, M. G. Lagally, A. J. Rimberg, R. Joynt, M. Friesen, R. H. Blick, S. N. Coppersmith, and M. A. Eriksson, "Spin blockade and lifetime-enhanced transport in a few-electron Si/SiGe double quantum dot," *Nature Physics*, vol. 4, p. 540, 2008.

[116] G. P. Lansbergen, R. Rahman, J. Verduijn, G. C. Tettamanzi, N. Collaert, S. Biesemans, G. Klimeck, L. C. L. Hollenberg, and S. Rogge, "Lifetime-enhanced transport in silicon due to spin and valley blockade," *Phys. Rev. Lett.*, vol. 107, p. 136602, 2011.

[117] Y. V. Nazarov, "Quantum interference, tunnel junctions and resonant tunneling interferometer," *Physica B*, vol. 189, p. 57, 1993.

[118] T. H. Stoof and Y. V. Nazarov, "Time-dependent resonant tunneling via two discrete states," *Phys. Rev. B*, vol. 53, p. 1050, 1996.

[119] T. Fujisawa, T. H. Oosterkamp, W. G. van der Wiel, B. W. Broer, R. Aguado, S. Tarucha, and L. P. Kouwenhoven, "Spontaneous emission spectrum in double quantum dot devices," *Science*, vol. 282, p. 932, 1998.

[120] K. A. Slinker, K. L. M. Lewis, C. C. Haselby, S. Goswami, L. J. Klein, J. O. Chu, S. N. Coppersmith, R. Joynt, R. H. Blick, M. Friesen, and M. A. Eriksson, "Quantum dots in Si/SiGe 2DEGs with Schottky top-gated leads," *N. J. Phys.*, vol. 7, p. 246, 2005.

[121] T. Berer, D. Pachinger, G. Pillwein, M. Muehlberger, H. Lichtenberger, G. Brunthaler, and F. Schaeffler, "Single-electron transistor in strained Si/SiGe heterostructures," *Physica E*, vol. 34, p. 456, 2006.

[122] L. J. Klein, D. E. Savage, and M. A. Eriksson, "Coulomb blockade and Kondo effect in a few-electron silicon/silicon-germanium quantum dot," *Appl. Phys. Lett.*, vol. 90, p. 033103, 2007.

[123] C. B. Simmons, M. Thalakulam, N. Shaji, L. J. Klein, H. Qin, R. H. Blick, D. E. Savage, M. G. Lagally, S. N. Coppersmith, and M. A. Eriksson, "Single-electron quantum dot in Si/SiGe with integrated charge sensing," *Appl. Phys. Lett.*, vol. 91, p. 213103, 2007.

[124] T. B. Boykin, G. Klimeck, P. von Allmen, S. Lee, and F. Oyafuso, "Valley splitting in V-shaped quantum wells," *J. Appl. Phys.*, vol. 97, p. 113702, 2005.

[125] M. Friesen, M. A. Eriksson, and S. N. Coppersmith, "Magnetic field dependence of valley splitting in realistic Si/SiGe quantum wells," *Appl. Phys. Lett.*, vol. 89, p. 202106, 2006.

[126] M. Friesen, S. Chutia, C. Tahan, and S. N. Coppersmith, "Valley splitting theory of SiGe/Si/SiGe quantum wells," *Phys. Rev. B*, vol. 75, p. 115318, 2007.

[127] A. Szabo and N. Ostlund, *Modern Quantum Chemistry*. New York: Dover, 1996.

[128] T. Fujisawa, D. G. Austing, Y. Tokura, Y. Hirayama, and S. Tarucha, "Allowed and forbidden transitions in artificial hydrogen and helium atoms," *Nature*, vol. 419, p. 278, 2002.

[129] S. Amasha, K. MacLean, I. P. Radu, D. M. Zumbühl, M. Kastner, M. Hanson, and A. Gossard, "Electrical control of spin relaxation in a quantum dot," *Phys. Rev. Lett.*, vol. 100, p. 046803, 2008.

[130] T. D. Ladd, F. Jelezko, R. Laflamme, Y. Nakamura, C. Monroe, and J. L. OBrien, "Quantum computers," *Nature*, vol. 464, p. 45, 2010.

[131] S. Das Sarma, X. Wang, and S. Yang, "Hubbard model description of silicon spin qubits: Charge stability diagram and tunnel coupling in Si double quantum dots," *Phys. Rev. B*, vol. 83, p. 235314, 2011.

[132] A. Auerbach, *Interacting Electrons and Quantum Magnetism*. New York: Springer-Verlag, 1998.

[133] J. A. Nelder and R. Mead, "A simplex method for function minimization," *Computer Journal*, vol. 7, p. 308, 1965.

[134] D. E. Goldberg, *Genetic Algorithms in Search Optimization and Machine Learning*. Boston: Addison Wesley, 1989.

[135] http://chtc.cs.wisc.edu/.

[136] http://www.cs.wisc.edu/condor/.

[137] Y. Makhlin, "Nonlocal properties of two-qubit gates and mixed states, and the optimization of quantum computations," *Quantum Information Processing*, vol. 1, p. 243, 2002.

[138] J. Canny, "A computational approach to edge detection," *IEEE Transactions on Pattern Analysis and Machine Intelligence*, vol. 8, p. 679, 1986.

[139] J. B. Buckheit and D. L. Donoho, "Wavelab architecture." http://www-stat.stanford.edu/∼wavelab/ftp/WaveLabArch.ps.Z.

[140] S. Mallat, *A Wavelet Tour of Signal Processing*. Academic Press, 2nd ed., 1995.

[141] L. P. Kouwenhoven, T. H. Oosterkamp, M. W. S. Danoesastro, M. Eto, D. G. Austing, T. Honda, and S. Tarucha, "Excitation spectra of circular, few-electron quantum dots," *Science*, vol. 278, p. 1788, 1997.

[142] H. van Houten, C. Beenakker, and A. Staring, "Coulomb-blockade oscillations in semiconductor nanostructures." Preprint at http://arxiv.org/abs/cond-mat/0508454.

[143] R. Hanson, B. Witkamp, L. M. K. Vandersypen, L. H. W. van Beveren, J. M. Elzerman, and L. P. Kouwenhoven, "Zeeman energy and spin relaxation in a one-electron quantum dot," *Phys. Rev. Lett.*, vol. 91, p. 196802, 2003.

[144] L. He, G. Bester, and A. Zunger, "Singlet-triplet splitting, correlation, and entanglement of two electrons in quantum dot molecules," *Phys. Rev. B*, vol. 72, p. 195307, 2005.